Airborne UHF Radar for Fine Resolution Mapping of Near-Surface Accumulation Layers in Greenland and West Antarctica

by

Cameron Lewis

B.S. Atmospheric Science (with Honors, 2006)

B.S. Electrical Engineering (with Honors, 2007)

University of Kansas

Submitted to the graduate degree program in Electrical Engineering and Computer Science and the Graduate Faculty of the University of Kansas School of Engineering in partial fulfillment of the requirements for the degree of Master of Science.

_____

Chairperson: Prasad Gogineni

_____

Carl Leuschen

_____

Fernando Rodriguez-Morales

Date Defended: September 29, 2010

This Thesis Committee for Cameron Lewis certifies that this is the approved version of the following thesis:

Airborne UHF Radar for Fine Resolution Mapping of Near-Surface Accumulation Layers in Greenland and West Antarctica

_____
Chairperson: Prasad Gogineni

_____
Carl Leuschen

_____
Fernando Rodriguez-Morales

Date Approved _____

Table of Contents

List of Figures

List of Tables

Abstract

The usefulness of accurate, fine resolution accumulation layer measurements over central Greenland and West Antarctica is significant for the improvement of ice sheet models. These models are critical to both global climate models as well as understanding sea level rise. Previously developed accumulation layer radars were used as templates for the current single channel system. Improvements were incorporated including increased output power, increased receiver sensitivity, single antenna operation, and reduced susceptibility to external noise sources. Steps were also taken to reuse previously purchased components to reduce development costs. Externally developed Vivaldi and elliptical dipole antennas were utilized. Collected data shows the system is capable of measuring layering to a depth of nearly 300 m in most dry snow regions of Greenland and West Antarctica with a resolution of ~0.5 m. Future revisions will focus on reducing size and weight, as well as incorporate multiple receive channels to allow for clutter rejection algorithms to be applied; this will allow for viable data collection in percolation and wet snow zone of major ice sheets.

Acknowledgments

I would like to thank the following individuals and organizations for their contributions to this research. I would like to express my appreciation of the National Science Foundation (NSF) and the Center for Remote Sensing of Ice Sheets (CReSIS) for providing the financial support and facilities necessary to support this research. I would like to thank Dr. Prasad Gogineni for accepting me as one of his undergraduate research assistants and later as a graduate research assistant. Your patience, insight, and intellect have been essential to both my academic and research success over the past five years. Providing me with the opportunity to attend conference and participate in field campaigns has significantly enriched my educational and personal experience; for this, I am very grateful. Collectively, I would like to thank the faculty and staff at CReSIS for their dedication to our research objectives. Your hard work and enthusiasm makes the research process bearable, dare I say enjoyable. Individually, I would like to thank Dr. Fernando Rodriguez-Morales and John Ledford for acting as mentors. You both have always been there to answer my questions and defuse my anxieties. Also, I would like to thank Jackie St. Aubyn and Jennifer Laverentz for their support with paperwork, purchase orders, travel arrangements, and a whole host of other administrative items. Your hard work and positive attitude help make life as a graduate student simpler. Also, I would like to thank Dennis Sundermeyer for your assistance in the machine shop. While I've done my best to avoid last minute milling issues, your patience and willingness to help with them has been greatly appreciated. Additionally, I would like to thank all the students of CReSIS for their help and camaraderie over the years. Specifically, I want to recognize Victor Jara-Olivares, Logan Smith, William Blake, Ben Panzer, and Kevin Player. Your knowledge and dedication will always be a source of inspiration. Further, I would like to thank all my friends outside of CReSIS and the University. You have provided me with much needed emotional support. Your patience and enthusiasm empower me to continue both on my educational path and my path in life; I would not have made it this far without you. Finally, I want to thank my parents, Angelia and Jeff. You are responsible for instilling in me the importance of education from the beginning. You incessantly remind me to work hard, be responsible, be patient, and do not give up. You have dedicated your lives to making sure I had every opportunity to excel and grow. You accept and support me for who I am and the paths I choose in my education and my life. For all this I am truly grateful and forever indebted; therefore, I dedicate this thesis research to my parents.

Chapter 1: Introduction

1.1 Motivation

Recent satellite observations show that the disintegration of the Arctic and Antarctic ice sheets is proceeding rapidly; exacerbated by multiple positive feedbacks. The summer melt area in Greenland has been increasing at a rate of ~40,000 km^2/year since 1992; this trend is somewhat enhanced by volcanic cooling due to the eruption of Mount Pinatubo in 1991. QuickSCAT observations have also confirmed increasing summer melt areas and an increase in the length of the melt season in West Antarctica since 1999 [13]. The Intergovernmental Panel on Climate Change (IPCC) estimated that sea level would likely increase between 18 and 59 cm over the next century [35]. Nearly 100 million people live within 1 m of current mean sea level (MSL) and nearly 37% of the world's population lives within 100 km of the coast, making our understanding of how sea level rise is affected by changes in the planet's major ice sheets critical to society and the economy [7].

Positive feedback mechanisms responsible for the recent acceleration in ice sheet melting can occur on and under the ice sheets as well as in adjacent oceans [13]. Key feedbacks, such as decreased ice sheet albedo due to surface melting and increased ice stream and outlet glacier velocities due to basal lubrication and loss of buttressing ice shelves, have led to an overall negative mass balance [5] [12]. The mass balance of both the Greenland and Antarctic ice sheets can be defined, in simple terms, as the difference between precipitation - the addition of mass - and the combination of evaporation, runoff, and ice discharge - the removal of mass [41]. All of these processes are directly affected by temperature increases in both the air and ocean surrounding the ice sheets. The ocean surrounding an ice sheet is vital to its stability. Recent dramatic increases in anthropogenic greenhouse gases have made the troposphere more opaque

to infrared radiation. This increase in opacity has hindered the ability of the atmosphere to radiate heat to space, creating an energy imbalance. This additional energy, sufficient to melt enough ice to raise sea level by one meter per decade, is mostly absorbed by the ocean. Higher ocean surface temperatures can be linked to higher precipitation rates and the accelerated melting of ice shelves and free sea ice [13].

The IPCC reported that models used to generate sea level rise estimates did not include dynamic processes and significant changes in mass balance known to be associated with the recent changes seen in the Arctic and Antarctic [35]. Three techniques can be employed to measure the mass balance of an ice sheet. A budgeting approach can be used, comparing accumulation input with ice flow and melting output; repeat altimetry measures volume changes; and temporal mass changes can be inferred from gravity measurements [37]. Many satellite, airborne, and *in situ* measurements have been taken in an effort to better understand the mass balance of the ice sheets using the budget approach. While satellite missions such as GRACE, ICESat, and Cryosat seek to understand both sides of the mass balance equation, they are only capable of collecting data with relatively coarse temporal and spatial resolutions [40] [41] The poor spatial resolution and coverage of these satellites renders them useless for accurately measuring important small scale features such as outlet glaciers (i.e. Jakobshavn). Satellite observations alone are not sufficient to fully understand all the mechanisms responsible for changes in the overall ice sheet mass balance. Advanced fine-resolution measurements are necessary for the improvement of ice sheet models. Airborne platforms, especially autonomous platforms, allow for larger areas of the ice sheet to be measured with fine-resolution remote sensing instruments. These platforms provide more accurate ice thickness estimates, internal layer mapping, and ice-bedrock interface imaging. To address the gap in the observations, a

wideband UHF radar has been developed to measure ice sheet and glacial ice layering from an airborne platform.

1.2 Document Organization

This document is organized into seven chapters. A brief history of the accumulation radar development at the University of Kansas and fundamental FM radar concepts are discussed in Chapter 2. A detailed description of the radar system is addressed in Chapter 3. Laboratory testing procedures and results are discussed in Chapter 4. Instrument installation and field testing are focused on in Chapter 5. Field data collection campaigns and results are presented in Chapter 6. Finally, Chapter 7 provides a summary. Additional discussions, calculations, antenna simulations, the radar operation manual and loop-back testing instructions are presented in the Appendixes.

Chapter 2: Background

2.1 Previous Accumulation Radar Development

Numerous VHF, UHF, and microwave remote sensing system for measuring accumulation rates and ice sheet layering have been introduced since the 1970's [10] [15] [33]. During the late 1990's a team of radar engineers and researchers at the University of Kansas developed an ultra-wideband, frequency-modulated, continuous-wave (FM-CW) radar to map near-surface internal layers within polar ice [18] [19] [29]. This radar operated over the frequency range from 170-2000 MHz. Data were collected and analyzed by Kanagaratnam et al. [18] during the summer 1998 and summer 1999 Greenland surface experiments. The data showed that choosing an operating frequency range of 600-900 MHz maximized the sensitivity of the radar for mapping near-surface internal layers while minimizing potential interference

from the aircraft navigation and communication systems on the chosen future airborne platform: a P-3 Orion.

A prototype radar system was developed operating over the above frequency range. Data were collected using this prototype system during airborne experiments conducted in Greenland during the summers of 2001, 2002, and 2003. Analysis of the data showed that the system was capable of mapping internal layering with a vertical resolution better than 50 cm to a depth of at least 100 meters in the dry snow zone.

This prototype system operated as a single-channel transmit, single-channel receive radar. While a system of this configuration is capable of capturing useful data over the dry snow zones of the ice sheet where the surface roughness is low and layering variations are minimal across the ground footprint (defined by the antenna pattern, expected to be wide with a single horn antenna, roughly 1000 m diameter circle for this prototype system [18]), the limitations of such a system are quickly realized within the percolation and wet snow zones where the surface roughness is very high and layering variations can be significant within the radar footprint. These conditions often make it difficult to distinguish between targets that are directly under the aircraft and those targets that are off to the left or right of the aircraft. We refer to these off-angle targets as clutter, and they are responsible for masking the information of interest, such as internal layering and the ice/bedrock interface, directly below the aircraft.

To overcome the limitations of a single-channel receiver radar, a multi-channel receiver version of the radar was developed by Parthasarathy [29]. A multi-channel receiver allows for the use of digital beamforming techniques that can be employed to reduce or null out clutter that would otherwise mask returns of interest from internal layers.

The multi-channel system as presented by Parthasarathy [29] was extensively tested in the laboratory, but was never used in the field. Modifications were made during the fall of 2008 and spring of 2009 to ready the system for field testing during the spring 2009 Twin Otter survey mission. The modifications are discussed in the section 3.2. The limitations of the modified system, particularly the lack of adequate multi-channel digital hardware, led to the development of the improved single-channel system that is the focus of this document. Improvements to the previous design include a simpler transmitter topology, higher output power, better receiver sensitivity, and improved electromagnetic interference shielding. Further expansion to a multi-channel configuration for future systems is discussed in Section 7.3.

2.2 FM Radar Principles

In general, radars can be classified as one of three types: impulse radar, Doppler radar, or FM radar. Impulse radars rely on gathering information about the target of interest through the transmission of pulses at a single frequency. The amplitude of the received pulse is dependent on the distance between the radar and target, as well as the target's scattering characteristics. The received signal from a single target (point target) is a replica of the transmitted pulse whose amplitude is modulated. This point target is a single object (i.e. a building, a rock, etc.) whose largest dimension is on the order of, or smaller than, the horizontal spatial resolution of the radar. When attempted to image an area larger than a single horizontal resolution cell, the scene is referred to as a distributed target. The received signal from a distributed target is a superposition of all the point targets that exist in the radar footprint. For a distributed target, the amplitude of the received signal is modulated by the different scattering characteristics of each individual target. Since individual targets within the footprint are at different distances from the phase center of the radar's antenna, they will be received at varying instances in time, leading to a

return signal with a time duration much longer than the duration of the transmitted pulse [38]. Pulse radars are often limited by a handful of tradeoffs that limit their performance in terms of range resolution and accuracy. For a given transmit power level, a short duration pulse (large bandwidth) has a better range resolution than a longer duration pulse (smaller bandwidth), but the reduced time of illumination results in a low accuracy measurement. This is often compensated for by increasing the output power level, which can quickly become costly.

While a ranging radar's transmit signal must be modulated so that the time delay between the transmit and receive signal can be determined, this modulation may be forgone if only the radial speed of the target is to be determined. This is a Doppler radar in its simplest form. A Doppler radar operates by mixing a sample of the transmit continuous wave (CW) waveform with the received signal. Since the received signal is a different frequency than the transmitted signal, the output of the mixer consists of frequencies near the second harmonic of the CW oscillator and the Doppler frequency. Filters are used to select the Doppler frequency, which is directly proportional to the radial speed of the target by:

$$f_D = -\frac{2u_R}{\lambda} \tag{1}$$

where u_R is the radial speed of the target and λ is the wavelength [38].

A solution to the tradeoffs that exist with pulse radars is to modulate the transmit signal to gain bandwidth while increasing the pulse duration. This improves range resolution and accuracy without the need for increased transmit power. This modulation also gives us the advantage of simple CW radars by allowing for the ability to distinguish between multiple targets unambiguously. An FM radar accomplishes this modulation by linearly sweeping the frequency of the transmit waveform over both a defined bandwidth (B) and a defined time instance (τ). A copy of this transmit waveform is coupled into the receiver where it is mixed

with the received signal to generate a beat frequency (f_b). This beat frequency is proportional to the range between the radar and the target.

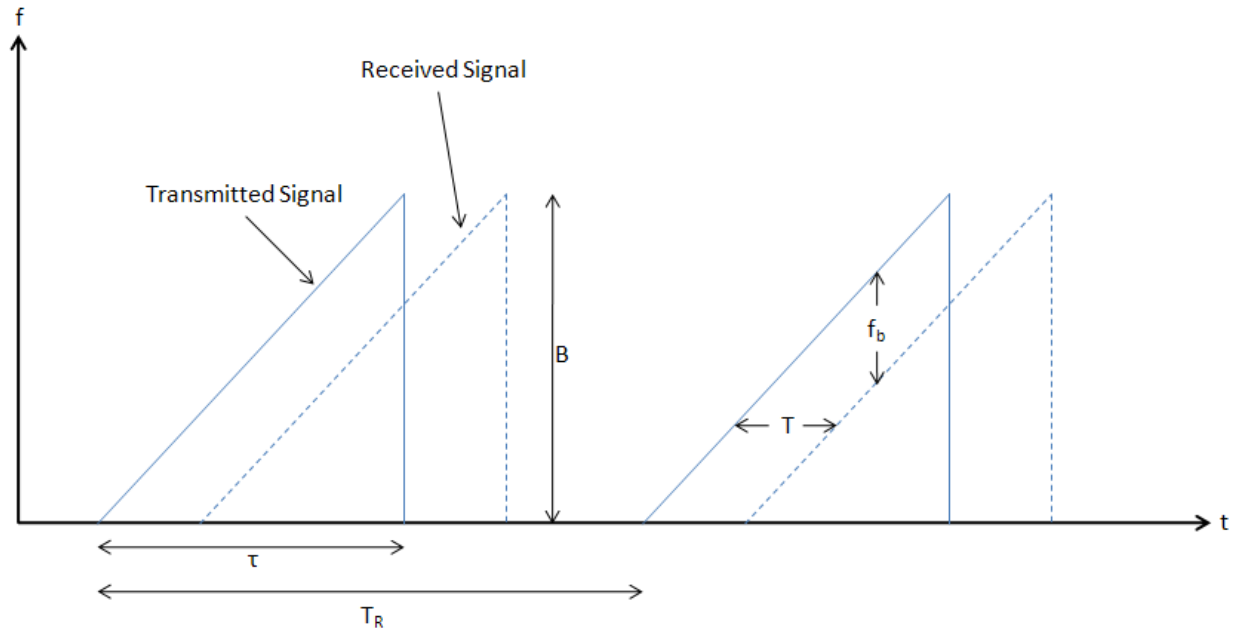

Figure 1. Instantaneous frequencies for point a target seen by FM radar.

As with the Doppler radar, the output of the receiver mixer contains the sum and difference of the input frequencies; the sum existing near the second harmonic of the transmitter is discarded and the difference frequency is the beat frequency. Since FM and Doppler radars compare transmit and receive signals, these radars are often referred to as coherent radars. Figure 1 shows the frequency content of the transmitted and received signals as a function of time.

From Figure 1 we can define the beat frequency as the multiplication of the slope of the transmitted signal and the time delay between the transmitted and received signals:

$$f_b = \frac{df}{dt} T \tag{2}$$

The slope of the transmitted signal can be further defined as the bandwidth divided by the sweep duration:

$$\frac{df}{dt} = \frac{B}{\tau} \tag{3}$$

The time delay (T) can also be further defined as the two-way range divided by the speed of the light within the medium:

$$T = \frac{2R}{c} \tag{4}$$

Combining Equations 2, 3, and 4 we can define the beat frequency using fundamental radar system parameters:

$$f_b = \frac{2BR}{c\tau} \tag{5}$$

Solving for the range (R), we can define the range to the target based on the received signal and the radar parameters:

$$R = \frac{c\tau f_b}{2B} \tag{6}$$

Typically, FM radars are presented as frequency-modulation continuous-waveform (FMCW). Radars that contain a combination of pulse and frequency modulation (as presented in Figure 1) are called chirp radars. Most synthetic aperture remote sensing radars fall into this category [38] [39].

The periodicity of the transmitted signal (this timing is typically referred to as the pulse repetition frequency or PRF) leads to an output spectrum that consists of harmonic components surrounding the beat frequency. These harmonics are spaced at the PRF frequency ($1/T_R$ from Figure 1). The existence of these harmonics is a result of the rectangular pulse train nature of the amplitude of the transmitted signal; that is, a signal with a rectangular amplitude shape translates to a spectrum with a sinc amplitude shape. These neighboring harmonics can interfere with accurate determination of the beat frequency, as well as mask beat frequencies generated by

other closely-spaced targets within the radar footprint. To reduce these harmonics, the amplitude of a transmit waveform is shaped so as to ease the transitions near the beginning and end of the chirp. For a rectangular amplitude shape, we expect the highest harmonic to be 13 dB below the carrier (dBc). Comparing this to a Hanning amplitude shape with harmonics of 23 dBc or a 25% Tukey amplitude shape with harmonics of 14 dBc, it is clear that the use of a windowed transmit signal is crucial for achieving near theoretical range resolution [14].

The need for the ability to map near-surface layering with fine resolution is the driving force behind choosing an FM radar over a pulsed radar system. The range resolution of a pulse radar system (ΔR) is defined by the ability to resolve separate targets in time. If the time delay between two adjacent echoes is greater than the pulse duration, then the two objects can be resolved individually [20]. Equation 7 describes this relationship:

$$\Delta R = \frac{c\tau}{2} \tag{7}$$

For FM radar systems, since the effective bandwidth of a signal is approximated by the inverse of the pulse duration, we can rewrite the above equation as:

$$\Delta R = \frac{c}{2B} \tag{8}$$

From Equation 8, we can see that range resolution improves with shorter pulses or higher bandwidths. As discussed before, generation of a short pulse with high power is difficult and costly. Additionally, using such a high-power system would likely lead to significant antenna feed-through (or T/R switch feed-through) and significant signal return from the surface reflection. These high-power returns would need to be gated from the layering returns to prevent receiver saturation; this adds complexity to the receiver. The additional complexity can be avoided with the use of an FM system, where the use of filters within the intermediate frequency (IF) subsection of the receiver can significantly reduce leakage signals. Additionally, mixing the

received signal to baseband before digitization allows for the use of a much lower bandwidth analog-to-digital converter (ADC); resulting in cost savings and reduced complexity.

2.3 Radar Range Equation

As discussed in the Section 1.1, accumulation rate measurements are crucial to understanding the mass balance of the planet's major ice sheets and, consequently, sea level rise. Estimates of yearly, decadal, and multi-decadal accumulation rates can be made from estimates of snow/firn/ice densities coupled with layer thickness. Measurements of this type can be done *in situ* via snow pits; however, these point measurements provide poor horizontal resolution and can usually only collect data to a depth of a few meters. Surface-based ice-penetrating radars can solve the depth issue by penetrating up to 100's of meters, but still lack adequate horizontal resolution. Airborne platforms provide a solution to both the depth and horizontal resolution limitations.

Seasonal changes in the polar regions lead to a yearly cycle of accumulation, melt, and refreeze. This cycle creates a layered profile where relatively sharp changes in density occur between yearly layers of accumulated snow. These density changes create dielectric contrasts, and it is these dielectric boundaries that reflect impinging radio waves. Dielectric contrasts can arise from changes in density, the presence of impurities, and changes in ice crystal orientation [11] [18] [29].

The radar range equation can be used to estimate the power received from the surface, internal layers, and the bedrock interface energy reflections that arise from these dielectric contrasts. We can estimate the reflection from internal layers or embedded inclusions assuming we can treat them as coherent reflectors (which we can) using Equation 9a. This equation can be generalized for a planar targets such as the ice surface and ice-bed interface (as well as distinct

internal layers whose properties remain nearly constant over a large area) as shown in Equation 9b.

$$P_r = \frac{P_t G^2 \lambda^2 \Gamma^2 L}{(4\pi)^2 (2R)^2} \tag{9a}$$

$$P_r = \frac{P_t G^2 \lambda^2 L \sigma^0 A}{(4\pi)^2 R^4} \tag{9b}$$

where P_t is the transmitted power, G is the antenna gain (same antenna for transmit and receive), λ is the wavelength of the transmitted waveform, σ^0 is the backscatter coefficient of the target of interest, A is the area illuminated by the radar (determined by the antenna pattern), and R is the one-way range between the radar and the target.

Chapter 3: System Description

3.1 Specifications

The radar system developed is expected to meet the following requirements:

1. Map internal layers to a depth of at least 200 m in dry snow zone
2. Map internal layers with sub-meter vertical resolution
3. Capable of operating at a nominal platform altitude of 1500 ft AGL
4. Operate with a surface return signal to noise ratio (SNR) of at least 10 dB
5. Capable of operating with an existing digital system using the AD9640 ADC and AD9910 direct digital synthesizer (DDS) from Analog Devices
6. Capable of operation on a DCH-6 Twin Otter and a P-3 Orion
7. Capable of easy upgrade to multiple receivers
8. Capable of operation using a single antenna

The first five requirements will be used to derive the remaining radar parameters. Requirements 6 and 7 will determine how the chassis is designed and built. Requirement 8 calls

for an elaborate transmission scheme that is discussed in detail in the transmitter section to follow. The DDS and ADC are collectively known as the digital hardware. The DDS subsystem was developed using the Analog Devices AD9910 [21]. The ADC uses an evaluation board from Analog Devices based on their AD9640.

The Analog Devices AD9640 has a 14-bit resolution with a 2-Vpp analog input span. For the 125-MHz sampling frequency version of this evaluation board, the effective number of bits (ENOB) is stated to be 11.7, which translates into roughly 72 dB maximum SNR. The maximum input power signal is defined by the following equation:

$$P_{max} = \frac{V_{pp}^2}{2R} = \frac{4}{100} = 0.04\,W = 16\,dBm \tag{10}$$

To prevent saturation and possible damage, it will be accepted that the maximum input power is 10 dBm. Combined with the maximum SNR, this gives an ADC noise floor of roughly -62 dBm.

This can be compared to the noise floor of the system, defined by the following equation:

$$N = kTBF \tag{11}$$

where k is the Boltzmann constant (1.38 x 10^{-23} J/K), T is the ambient system temperature (accepted to be 290 K), B is the receiver bandwidth (50 MHz for this receiver), and F is the noise figure of the receiver. The noise figure of super-heterodyne receivers is typically dominated by the front-end components. This calculation is presented in detail in section 3.3.3.1. The receiver noise figure is 2.55 (linear) or 4.06 dB. Plugging these values into the above equation produces a system noise floor of -93 dBm, the minimal detectable signal before pulse compression and signal processing gain. Since this value is significantly lower than the ADC noise floor of -62 dBm, the receiver chain must provide enough gain to amplify the received signal above the quantization noise floor of the ADC.

Using the radar range equation from Chapter 2, the expected received signal power can be calculated; this value can help define the needed receiver gain. From the requirements above, the platform height is accepted to be 1500 ft and the depth of ice penetration is accepted to be 200 m. Since these receive signal powers considered rough estimates, a simple transmission model will be adopted: only spherical spreading loss within the air, a specular air-snow/ice/water interface, and a homogeneous ice medium (constant loss). We can convert the radar range equation into logarithmic form:

$$P_r = P_t + 20log(\lambda) + 20log(G) + 20log(\Gamma) + L - 20log(4\pi) - 20log(2R) \qquad (12)$$

For this calculation, a transmit power of 5 W (37 dBm) and an antenna gain of 3 dB will be used. The air-snow interface reflection coefficient, Γ, can be calculated using the following equation:

$$\Gamma = \left| \frac{1 - \sqrt{\varepsilon_r / \varepsilon_0}}{1 + \sqrt{\varepsilon_r / \varepsilon_0}} \right|^2 \qquad (13)$$

where ε_r is the dielectric constant of snow (taken as 2) and ε_0 is the dielectric of air (taken as unity). This produces a reflection coefficient of roughly 0.029 (linear) or -15.3 dB. Based on calculations presented in [18] [29], the reflection coefficient from internal layering is expected to be roughly -55 dB with a propagation loss of roughly -6 dB for a depth of 200 m. Table 1 shows the expected received signal power from a depth of 200 m.

Table 1. Calculated received power from 200 m depth.

Frequency (MHz)	Wavelength (m)	Received Power (dBm)
600	0.5	-106
750	0.4	-108
900	0.333	-109.5

If we assume that the strongest received signal is from a specular water surface (Γ = 1) at R = 500 m with no path loss, the received signal power would be roughly -47 dB. Therefore the dynamic range of the received signals of interest is 62.5 dB, near the ADC spurious-free

dynamic range (SFDR) or 74 dB. The receiver chain should map the strongest expected receive signal to roughly 6 dB (one quantization bit) below the saturation level of the ADC and the system thermal noise floor to at least 6 dB (ideally 10 dB) above the ADC noise floor (quantization noise level). Since the stated quantization noise level of the ADC is -62 dBm and the SFDR is 74 dB, the expected saturation point would be +12 dBm (experimental found to be roughly 11 dBm). It will be assumed that the saturation point is +10 dBm. To map -47 dBm to +4 dBm requires a receiver chain gain of 51 dB. This gain would map the system noise floor of -93 dBm to -42 dBm, 20 dB above the ADC quantization noise level.

The receiver chain was designed to provide roughly 63 dB of gain, including losses due to the T/R switch, filters, attenuators, and mixer conversion. This gain was chosen based on original radar range equation calculations that were found to be erroneous. Since the current receiver chain has 12 dB more gain than necessary, strong returns can easily saturate the ADC. This is likely the cause of the surface return sidelobes seen in much of the collected data, especially over coastal Greenland.

A Gaussian high-pass filter was used prior to the intermediate frequency (IF) amplifier to prevent saturation caused by leakage of the transmit signal through the T/R switch and high-power reflections from antenna mismatches that leak through the receiver blanking switch. A Gaussian filter was chosen because its impulse response does not produce any overshoot. An overshoot in the filter response creates transients that degrade sidelobe performance. A low-pass filter with a 50-MHz cutoff was also used prior to the IF amplifier to prevent saturation from higher order products produced by the mixer. Typical FM radar operation would call for either direct hardware pulse compression (using the receiver mixer to generate the beat frequency) or direct sampling of the received signal. The latter is not an option due to the limitations of current

digital hardware. The former is the most often-used method; however, the transmission scheme used for this system calls for a more elaborate reception scheme. As discussed in the transmitter section below, this transmission scheme is necessary, as it allows for the use of a single antenna. The limiting factor is the sampling rate of the ADC. The timing scheme is discussed in detail in section 3.3.2; the basics will be described here to shed some light on the system specifications.

The 300-MHz transmit bandwidth is broken up into 16 overlapping 50-MHz bandwidth, 2-μs chirps (i.e. 600-650 MHz, 620-670 MHz, 640-690 MHz, etc.). These individual chirps need to be preserved so that they can be combined in post processing to generate the original 300 MHz bandwidth. In lieu of providing a chirp to the local oscillator (LO) port of the receiver mixer (as would be done to achieve hardware pulse compression), tones are provided that correspond to the start frequency of the transmitted chirp with a small 6 MHz offset so that zero range does not fall at DC (i.e. 606 MHz, 626 MHz, 646 MHz, etc.). Instead of performing hardware pulse compression, the receiver mixer translates the radio frequency (RF) band received signal to baseband (i.e. 5-55 MHz). Since our highest frequency of interest is defined by the IF low pass filter (3 dB cutoff at 55 MHz), the ADC sampling frequency of 125 MHz is adequate to satisfy the Nyquist sampling theorem.

To reduce data volume, eight coherent integrations are performed in hardware before the data are written to the hard drive; this provides a 9-dB improvement to the SNR. An additional four coherent integrations are performed in processing, providing another 6 dB of SNR improvement, and 10 incoherent integrations are performed in post-processing, providing another 5 dB of SNR improvement.

Additional gain exists due to pulse compression. Each received chirp is pulse compressed in software and then stacked together to recreate the original bandwidth. While each

chirp has a bandwidth of 50 MHz and duration of 2 μs, they overlap in frequency. After this overlap is accounted for, each chirp effectively has a bandwidth of 20 MHz and this bandwidth extends over a time of 0.8 μs. This time/bandwidth product is 16. Since it takes 16 chirps to recreate the original bandwidth, the effective time/bandwidth product is 256, or a compression gain of 24 dB.

Combining the coherent integration gain and the pulse compression gain produces a total processing gain of 39 dB. This means the minimum detectable signal is -132 dBm. Table 2 summarizes key radar parameters.

Table 2. Key system parameters.

System Parameter	Value
Operating Frequencies	600-900 MHz
Transmission Scheme	Stepped Chirp
Number of Sub-chirps	16
Chirp Bandwidth	50 MHz
Chirp Sweep Time	2.048 μs
Transmit Power	5 W (37 dBm)
PRF (Effective PRF)	50 kHz (3.125 kHz)
Receiver Gain	63 dB
Sampling Frequency	125 MHz
ADC Dynamic Range	74 dB
Antenna Type	Twin Otter: Vivaldi Array P-3 Orion: PC Board Elliptical Dipole Array
Hardware Integrations	8
Processing Integrations	Coherent: 4, Incoherent: 10

3.2 Previous Versions

Many versions of an "accumulation measuring radar" have been developed at the University of Kansas. The reader is directed to [18], [19], and [29] for detailed information regarding the development of early operational and prototype radars not developed by the author of this document. These radars provided the scientific basis for the current radar and defined many of its parameters, outlined in Table 2. The current system strives to provide increased sensitivity as well as provide a track for miniaturization.

Three versions of this radar system were developed in the context of this investigation. The first was an improved copy of the radar system discussed in [29]. This system used the previous receiver while operating with a new transmitter, antenna, and digital system. This system was fielded during the spring 2009 Greenland Twin Otter survey and will be the focus of the discussion to follow.

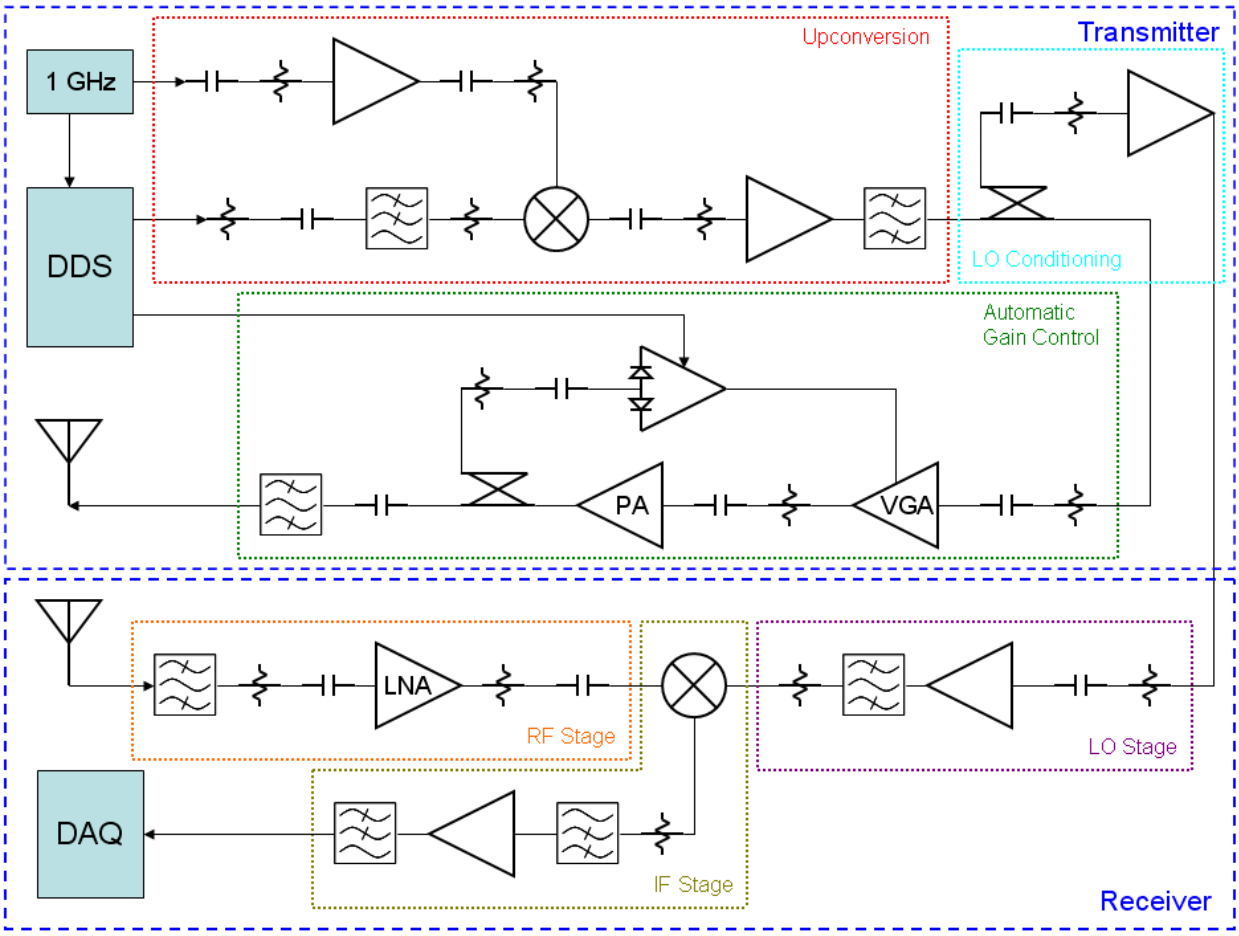

Figure 2. Spring 2009 Greenland survey accumulation radar block diagram.

The next two versions of the radar are considered the "current version" and are discussed in Section 3.3 below. This version was designed and built from scratch and seeks to resolve many of the issues discovered during the 2009 Greenland survey. Both versions use the same radar hardware, with the exception of the antenna. The second version of the radar system used a Vivaldi array and was fielded during the winter 2009-2010 Antarctica Twin Otter survey. The

third version used an elliptical dipole array and was fielded during the spring 2010 Greenland NASA Operation Ice Bridge (OIB) P-3 Orion survey.

The version of the radar fielded during the spring 2009 Greenland Twin Otter survey was a resurrected version of the system developed earlier [29]. This system was developed around previously-developed Compact PCI (CPCI) card. The original receiver module was kept intact, with minor modifications to the IF filter, which was removed and replaced with an external filter with wider bandwidth (MiniCircuits SLP-50+). The transmitter module was redesigned to incorporate an amplitude auto-leveling circuit and a high-power amplifier. Figure 2 shows the system block diagram and Figure 3 shows the assembled radar chassis with the CPCI chassis elevated to show the radar cards. A custom CPCI chassis with a custom CPCI backplane was used to provide power to the transmitter (top) and receiver (bottom) cards.

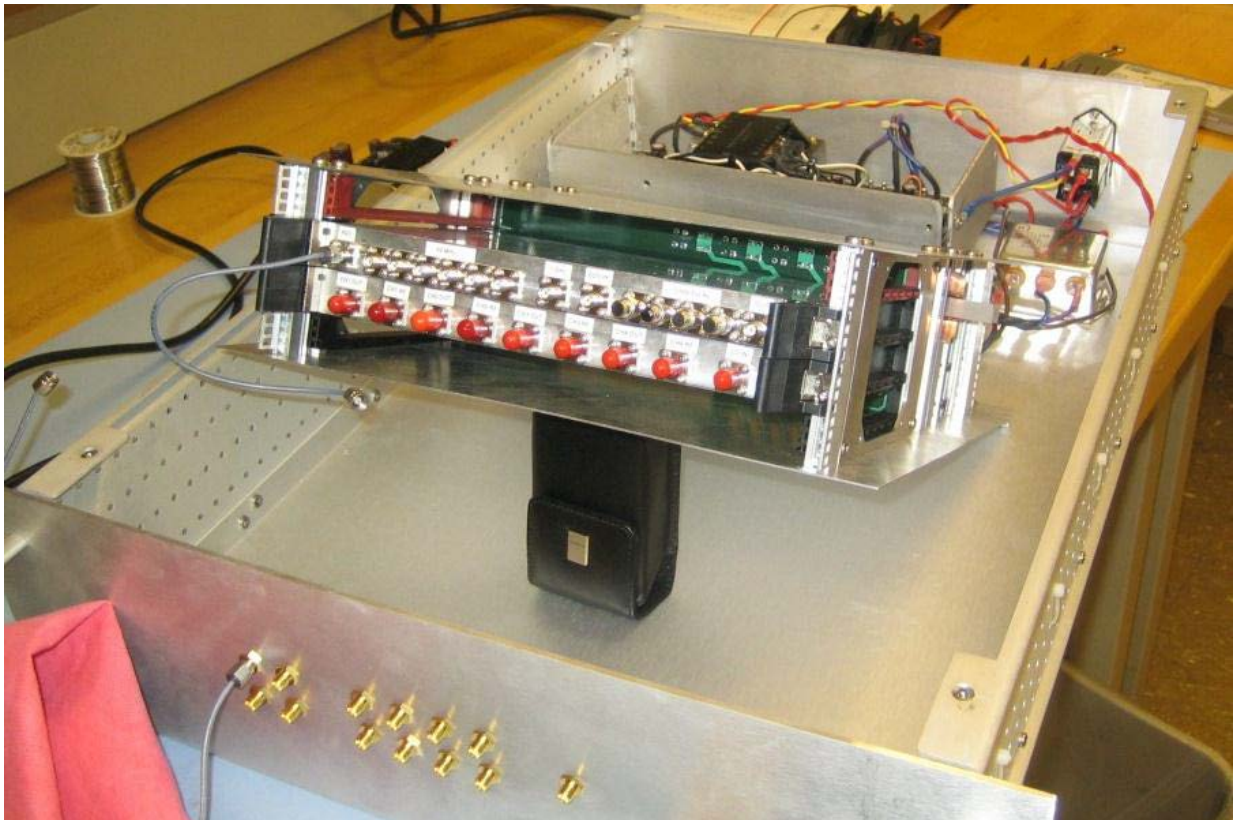

Figure 3. Photograph of the spring 2009 Greenland survey Accumulation radar.

As discussed in [29], the previous transmitter module housed a 1 GHz tone generation board; this 1-GHz tone was used to up-convert the 100-400 MHz output of the digital system to the needed 600-900 MHz via a separate circuit board. This up-converted signal was passed to a final circuit board where copy was generated for use as an LO by the receiver and a copy was amplified to 0.5 W for transmission. The new version bypassed the 1-GHz tone generator in favor of using a copy of the 1-GHz clock used by the digital hardware; this was done to reduce circuit redundancy and ensure better phase lock between the digital and RF hardware waveforms.

The power-amplifier stage was also replaced in the new version with amplitude-leveling circuitry (Analog Devices ADL5330 and AD8318) and a 1-W power amplifier (Hittite HMC452QS16G). The reader is referred to Analog Device Circuit Note CN0050: Stable, Closed-Loop Automatic Power Control for RF Applications [2], which discusses a closed loop circuit between the ADL5330 variable-gain amplifier (VGA) and the AD8318 log detector. For this application, the HMC452 power amplifier was added to the loop following the output of the ADL5330; additional attenuation is added to the log detector input to compensate for the additional power added to the loop. The purpose of the circuit was to provide an auto-sensing, auto-correcting power amplifier that would level the transmitter output, compensating for the unleveled response of the components preceding it and falling within the loop circuit.

A DC voltage was provided from the DDS that set the output power level. Figure 4 shows the automatically-leveled transmitter output. The closed-loop circuit was capable of leveling the output between 600-900 MHz with a maximum ripple of 0.87 dB.

Unlike the described transmission scheme used by the current radar system, this version of the radar typically followed FM radar design form by mixing the received signal with a copy of the transmitted waveform to produce a beat frequency in hardware, before digitization. The

proper system operation was confirmed using a synthetic target constructed with an optical delay line. The SNR obtained during this test was greater than 40 dB after roughly 105 dB of attenuation. Figure 5 shows the received beat frequency for a multiple target response.

Due to the short design timeline, it was decided to use the existing, wing-mounted folded dipole antennas used by the depth sounder, whose operating frequency is 140-160 MHz. A set of diplexers were developed to allow for both radars to transmit on the same antenna simultaneously using a small resonance in the folded dipole response at 750 MHz. Measurements of the antennas showed a reasonable resonance band between 600-900 MHz. Figure 6 shows the measured return loss response of the folded dipoles installed on the aircraft; this response was measured during flight and includes the diplexer.

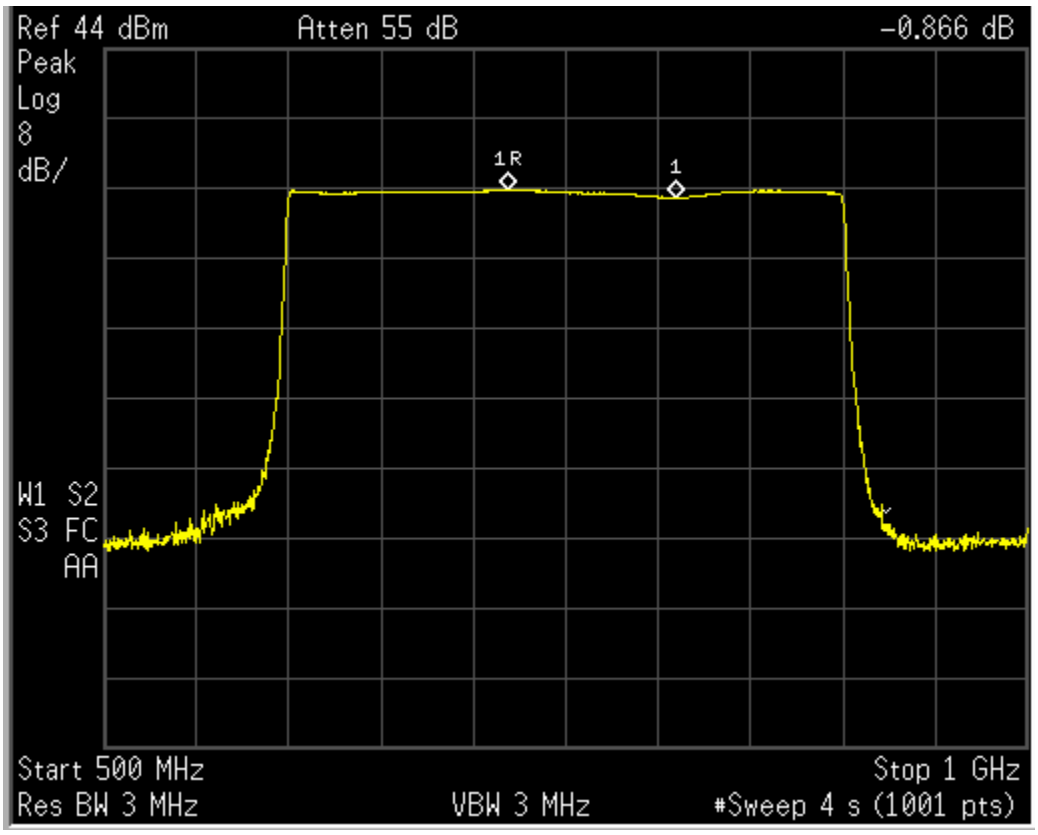

Figure 4. Automatically leveled transmitter output.

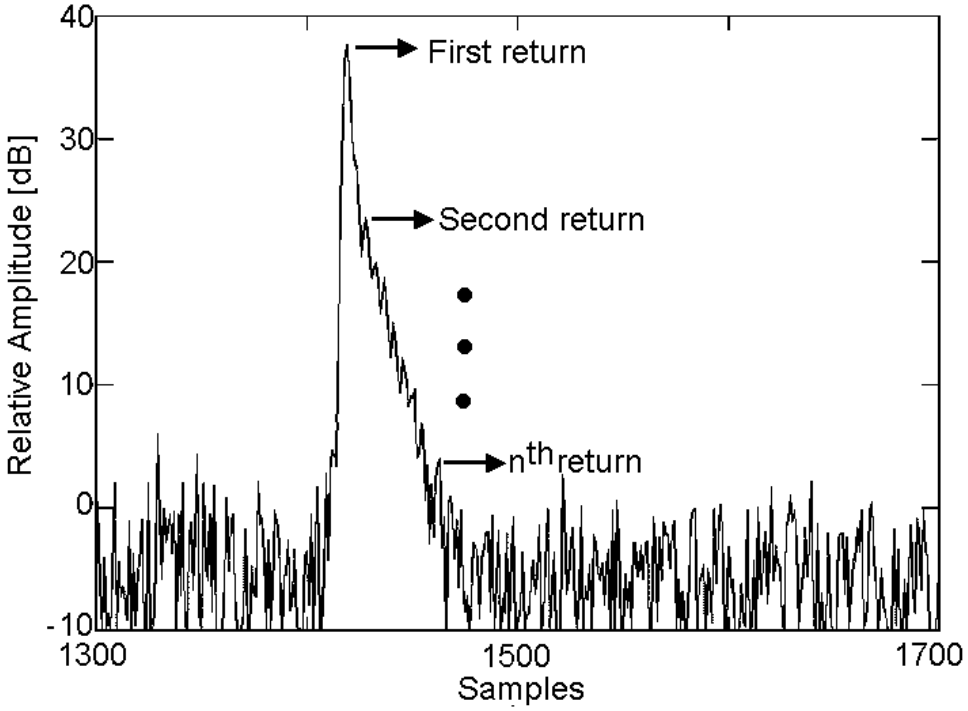

Figure 5. Delay line, multi-target response for spring 2009 accumulation radar. The total loss introduced during this test was roughly 105 dB.

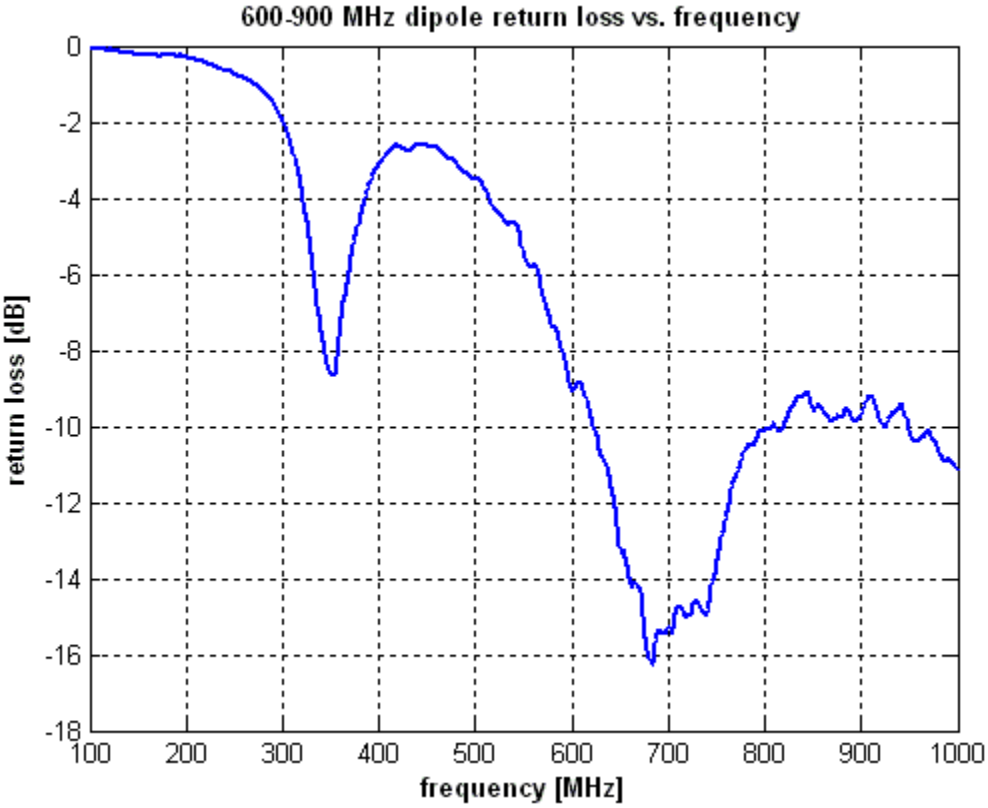

Figure 6. Folded dipole 750 MHz measured response, includes diplexer.

While the radar performed as expected during loop-back testing, field operation showed that the radar lacked the expected sensitivity. The radar performed consistently, but it was only able to pick up surface returns, not internal layering. An outlet glacier is not an ideal location for testing an accumulation radar. The often rough and wet surface of an outlet glacier leads to significant attenuation of radio waves resulting in very little penetration of the signal into the firn.

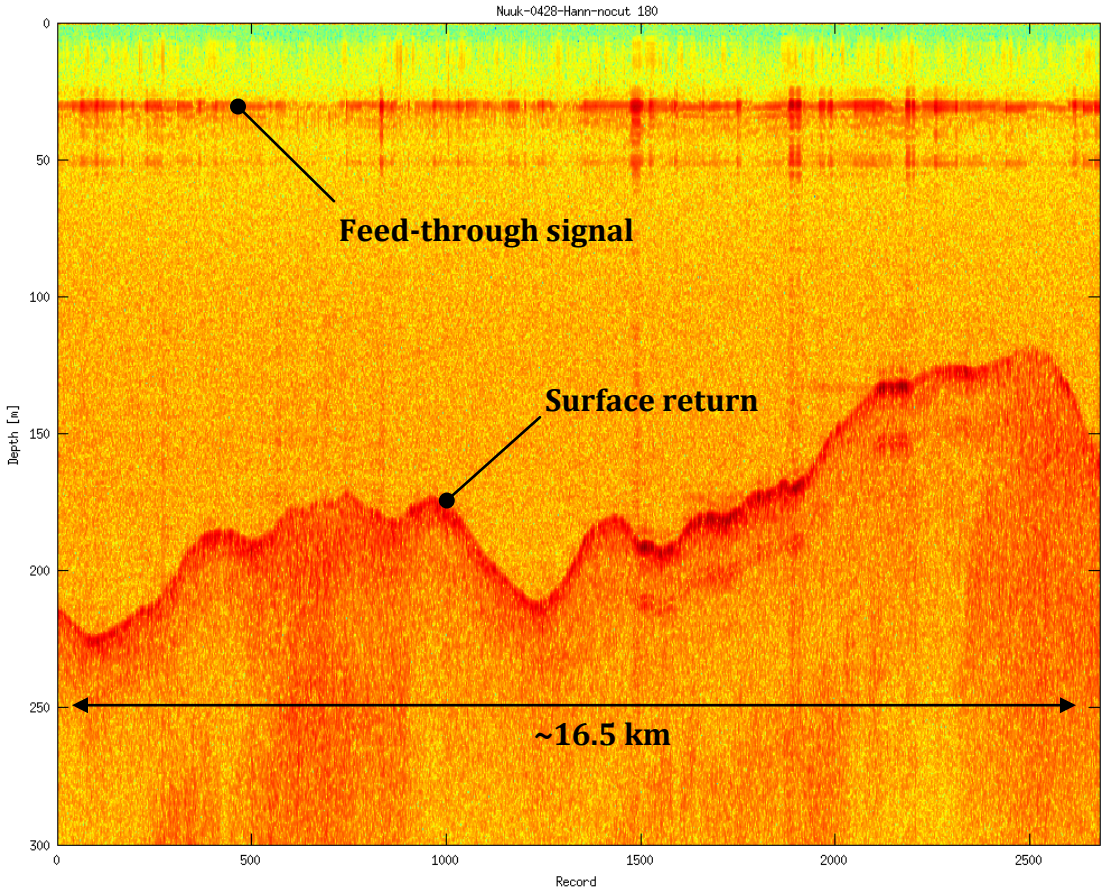

Figure 7. Echogram obtained over the Nuuk Glacier, collected in the spring of 2009.

Unfortunately, surveys during the spring 2009 campaign were limited to outlet glaciers. Figure 7 shows a sample echogram from the flight over the Nuuk Glacier during the spring 2009 survey. This image was collected as far in land as possible to minimize poor surface conditions (Figure 8). The surface return is prominent; additional returns occurring below the surface are likely multiples present due to receiver saturation. Significant changes in ice thickness and

movement in the percolation and wet zones of the ice sheets places great importance on characterizing the inputs to the mass balance of the ice in these regions. Subsequent versions of this radar seek to improve the radars ability to see layering in these regions.

Figure 8. Photograph of the lower portion of the Nuuk Glacier showing significant surface roughness.

3.3 Current Version

3.3.1 Digital Subsystems

The digital subsystem consists of two primary parts: a direct digital synthesizer (DDS) and a digital acquisition (DAQ) unit. The DDS is responsible for generating the signals conditioned by the transmitter for broadcast and is used by the receiver to generate signals that

can be digitized by the DAQ. The DAQ is responsible for digitizing down-converted radar returns that are received (after pre-conditioning).

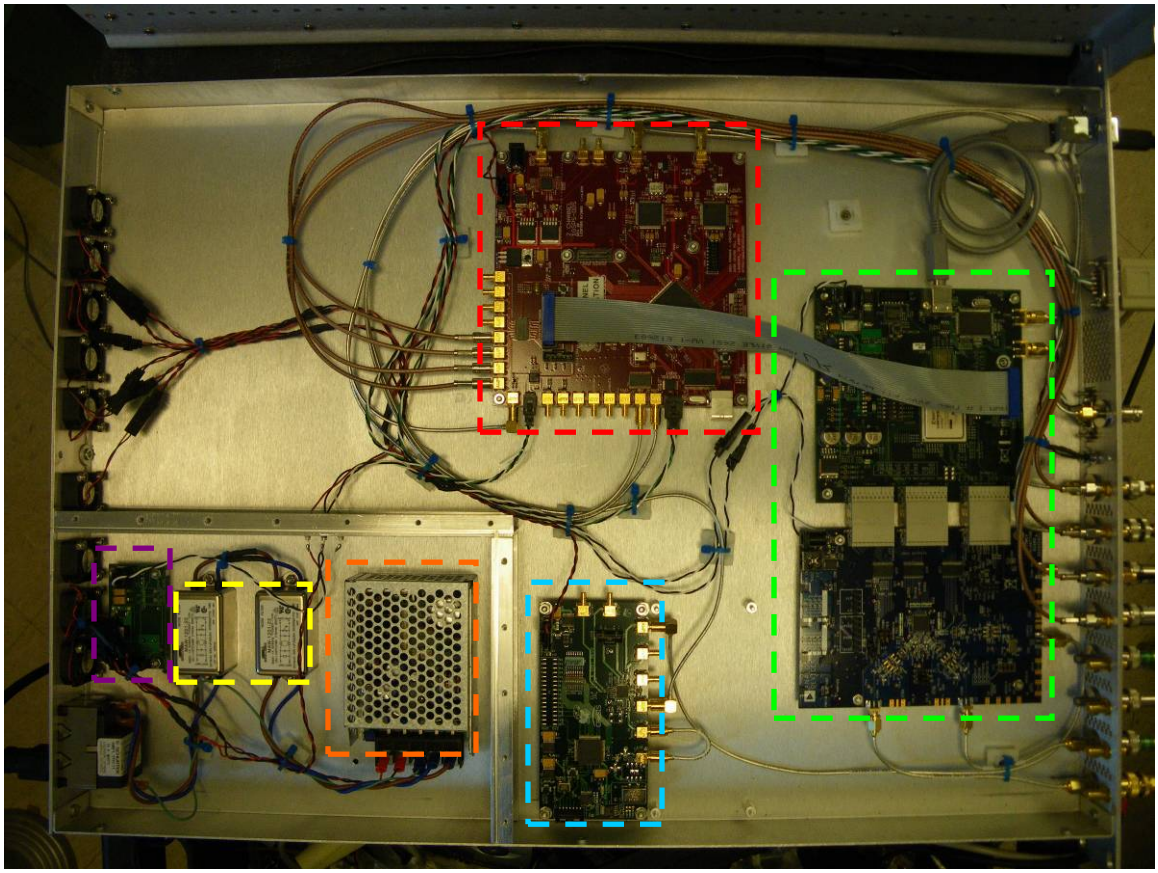

Figure 9. Photograph of the digital hardware (1UDAQ) interior. Red: DDS board, Green: DAQ boards, Blue: 1 GHz clock generator board, Orange: 5V supply, Purple: 5V to 6V step-up board, Yellow: A/C input EMI filters.

Essentially the DDS is a digital-to-analog converter and the DAQ is an analog-to-digital (A/D) converter with digital storage capabilities. Specifics about the DDS and DAQ, as they relate to the design and operation of the radar, are stated in section 3.1 above. The reader is referred to [21] for detailed information about the DDS board and [1] for detailed information about the ADC chip. Both subsystems are interfaced with a computer used to control and operate the radar through a graphical user interface (GUI). For convenience and better control of electromagnetic interference (EMI) generated by the digital subsystems, all digital hardware is housed inside a separate compact chassis. Figure 9 shows the internal layout of this chassis. It

contains the DDS circuit board, the DAQ mother and daughter circuit boards, the 1 GHz reference oscillator circuit board, and a power supply.

3.3.2 RF Transmitter

The RF transmitter for the current version of the accumulation radar is greatly simplified when compared to previous versions. Preceding versions relied on up-converting the output of the DDS (100-400 MHz) to the needed UHF band (600-900 MHz) using a 1-GHz reference. This configuration requires a phase-locked 1-GHz reference (phase-locked with the DDS output or the DDS clock), a mixer, and filters to reduce spurious signals. The aforementioned hardware can be eliminated by exploiting the properties of digitally-produced signals from the DDS.

Since the DDS uses a 1-GHz clock, the spectrum of the generated signal will not only include the fundamental signals in the 100-400 MHz band, but also their images (harmonics) in the required frequency range of 600-900 MHz. Since the output of the DDS has a sin(x)/x amplitude roll-off with frequency relative to the fundamental, the amplitude of the signals in the 600-900 MHz band will be smaller compared to that of the 100-400 MHz band and will roll-off faster with increasing frequency. This roll-off can be eliminated by digitally predistoring the output signal of the DDS. The unleveled output of Channel 1 (WFG1) of the DDS is shown in Figure 10.

This channel is referred to as the RF output of the DDS. Predistortion of the output is employed to obtain a leveled output. The output is leveled to the lowest power level occurring at 900 MHz (or 100 MHz at baseband), roughly -17 dBm. Figure 11 shows the leveled output after predistortion.

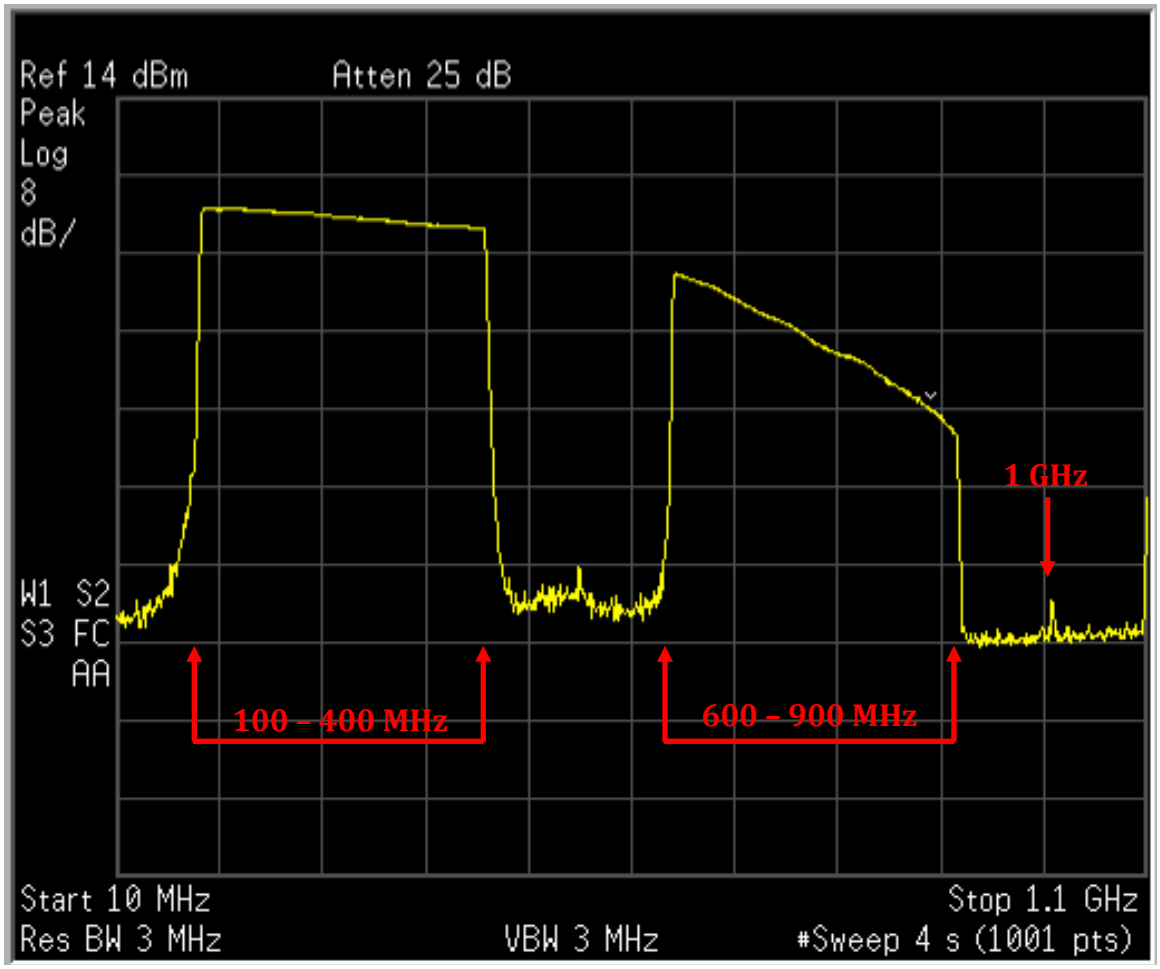

Figure 10. Unleveled output of DDS programmed for 100 - 400 MHz band

Assuming a nominal survey altitude of roughly 500 m above the surface, and limiting the depth of interest to 300 m in ice, the round trip time of a transmitted pulse through 500 m of air and 300 m of ice is calculated as follows:

$$\tau_{air} = 2 * \frac{500\ m}{3x10^8\ {}^{m}/_{s}} = 3.3\ \mu s$$
$$\tau_{ice} = 2 * \frac{300\ m}{3x10^8\ {}^{m}/_{s}} * \sqrt{3.15} = 3.5\ \mu s \quad (14)$$

This corresponds to a total two-way travel time of roughly 7 µs. For the 2009-2010 CReSIS Antarctic Survey mission, only the nadir port of a DCH-6 Twin Otter platform was available for antenna installation; this limited the system to a single-antenna configuration.

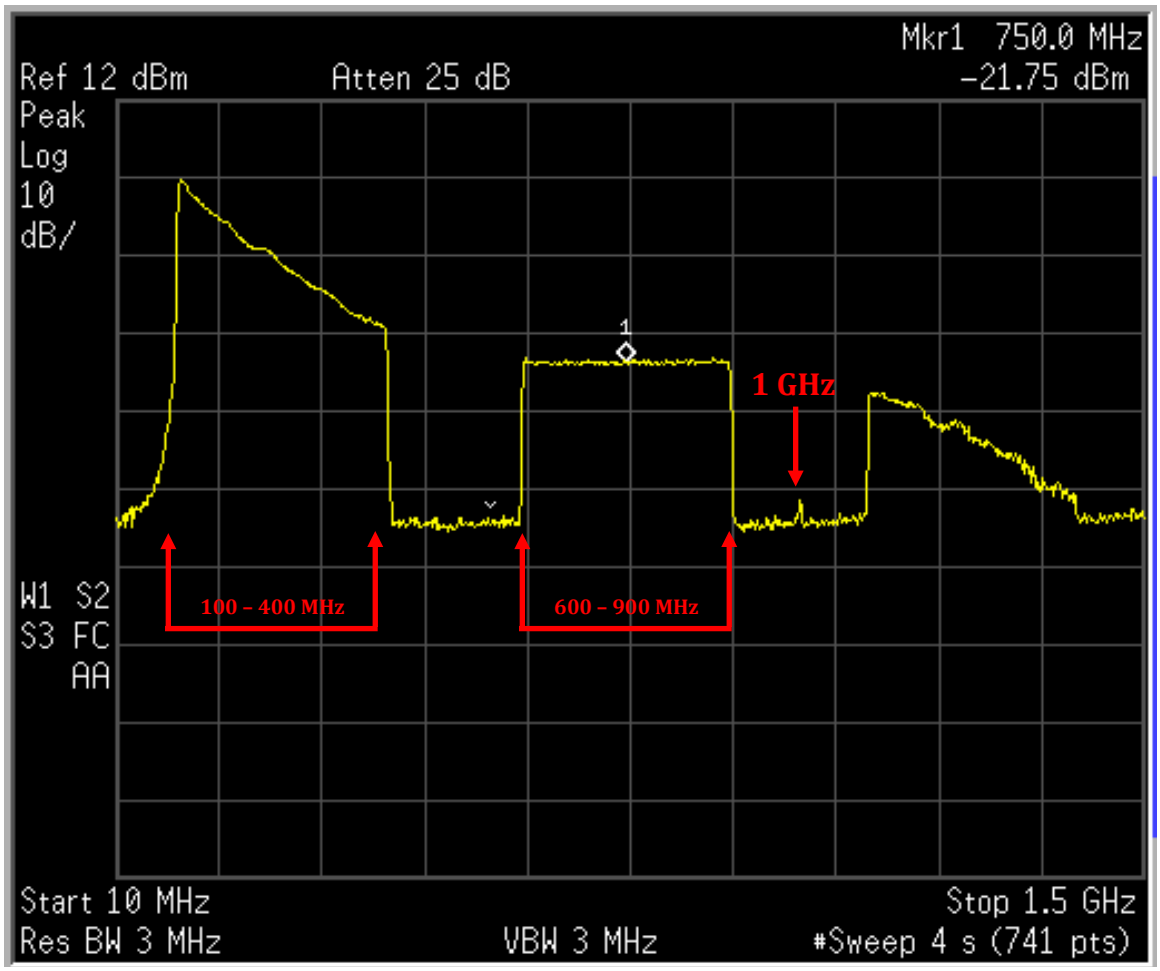

Figure 11. Output of DDS, predistorted to produce a flat 600-900 MHz chirp.

Operating the DDS at a 50-kHz pulse repetition frequency (PRF) provides 20 µs to transmit and receive a single waveform and reprogram the DDS to output the next waveform. Reprogramming the DDS requires at least 8 µs, leaving 12 µs available to be divided thus: 2 µs to transmit the waveform, 0.5 µs to allow for transients to settle following T/R switch toggling, and the remaining 9.5 µs dedicated to receive. This 9.5-µs window includes the necessary 7 µs for two-way air and ice travel time (previously calculated), plus the 2-µs pulse length, plus some margin.

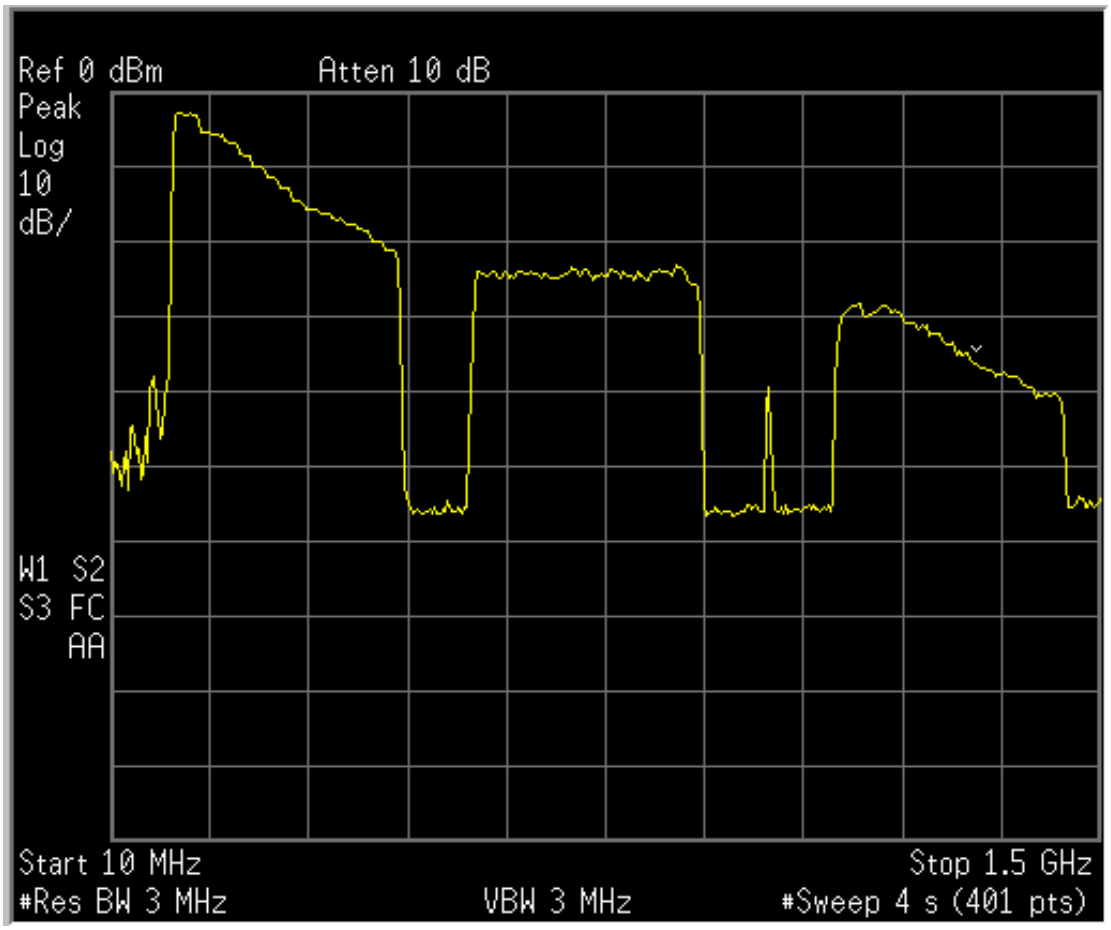

Figure 12. Leveled DDS output for 16 sub-chirp configuration (Stepped response is visible).

This scheme limits the pulse length to 2 µs. Let us consider the entire transmit bandwidth of 300 MHz being transmitted within this 2 µs (the DDS is capable of this). Equation 5 can be used to determine the beat frequency (f_b) bandwidth based on the ranges of interest (800 m minus 500 m platform height = 300 m). When transmitting 300 MHz over 2 µs, the beat frequency bandwidth is 300 MHz; this is much larger than the theoretical (Nyquist) maximum sampling rate of the ADC: 62.5 MHz. To overcome this limitation, it was chosen to divide the transmit signal into 16, 2 µs, 50 MHz bandwidth chirps as presented earlier. Using Equation 5, this reduces the beat frequency bandwidth (the IF bandwidth) to 50 MHz, well within the capabilities of the ADC to digitize. Another solution may have been to increase the pulse length (reducing the PRF), but the pulse length is limited by the two-way travel time of the surface

return: 3.3 µs, which is fixed by the platform height. Increasing the pulse length and reducing the PRF may be a useful solution if the platform height is increased to allow for a longer two-way travel time.

To avoid the use of this elaborate transmission scheme, an ADC with a higher sampling frequency is required; this may be implemented in future versions. In this case, changes to the hardware are not necessary. Providing a chirp to the LO chain, in lieu of the current tones, will simply move the pulse compression from software to hardware. Using an ADC capable of digitizing 300 MHz would also lend well to directly digitizing the received waveform. This could be achieved by providing the LO chain with a fixed tone (or replacing the LO chain with a fixed oscillator) to move the received frequency content to baseband. If an even wider bandwidth ADC is available, the received 600-900 MHz signal could be directly digitized. These additional solution schemes would greatly simplify the receiver chain, reducing (or eliminating) possible source of noise and improving received signal integrity.

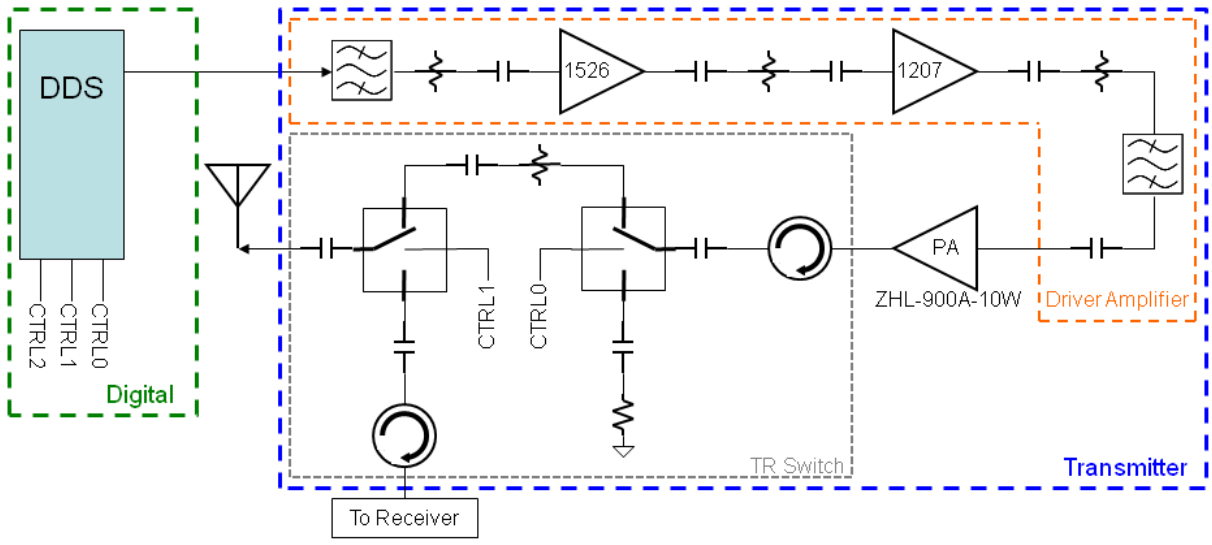

Figure 13. Winter 2009-2010 accumulation radar transmitter block diagram.

Figure 28 shows a graphical illustration of the transmit/receive windows as well as switch timing. Figure 12 shows the newly-leveled DDS output for the 16-waveform configuration.

With this configuration, the output of the DDS contains the frequencies of interest. All that remains is to condition this signal for transmission through filtering and amplifying. Figure 13 shows the block diagram for the transmitter. Excluding the digital hardware and antenna, the RF transmitter consists of three separate subsystems: the driver amplifier stage, the power amplifier, and the T/R switch.

3.3.2.1 Driver Amplifier Stage

The RF signal from the DDS (Channel 1, WFG1), shown in Figure 12, is first filtered using a 600-900 MHz bandpass filter (Lark Engineering MS750-X300-5CC). The response of this filter is shown in Figure 14. This filter is designed to reduce out-of-band noise as well as reduce the baseband and higher image frequencies produced by the DDS. This filter reduces the power of signals in the baseband frequency range of 100-400 MHz by at least 35 dB and reduces the 1-GHz clock feed-through by roughly 15 dB.

This filtered signal, with prominent frequencies only within the 600-900 MHz band, is amplified using two cascadable monolithic amplifier modules (Teledyne Cougar ARS1526 and ARS1207). DC-blocking capacitors and attenuators are employed between the amplifiers and filters to ensure isolation of biased and padded amplifiers. The amplifiers were padded with 3-dB attenuators to reduce the mismatch between them. The first amplifier is a high-gain amplifier (Teledyne Cougar ARS1526). This amplifier has a gain of 29 dB with a 1-dB compression of +14.5 dBm referenced to the output. Accepting 1 dB of loss in the bandpass filter, it amplifies the transmit signal to +8 dBm, well below the compression point. The second amplifier is a low gain, medium-power amplifier (Teledyne Cougar ARS1207). This amplifier has a gain of 11 dB with a 1-dB compression of +25.5 dBm. Accounting for attenuators, this amplifies the transmit signal to +16 dBm. The output of the amplifier is filtered again using

another Lark 600-900 MHz bandpass filter to reduce out-of-band noise and harmonics produced by the previous stages. Accounting for all gains and losses, the final output level should be +12 dBm.

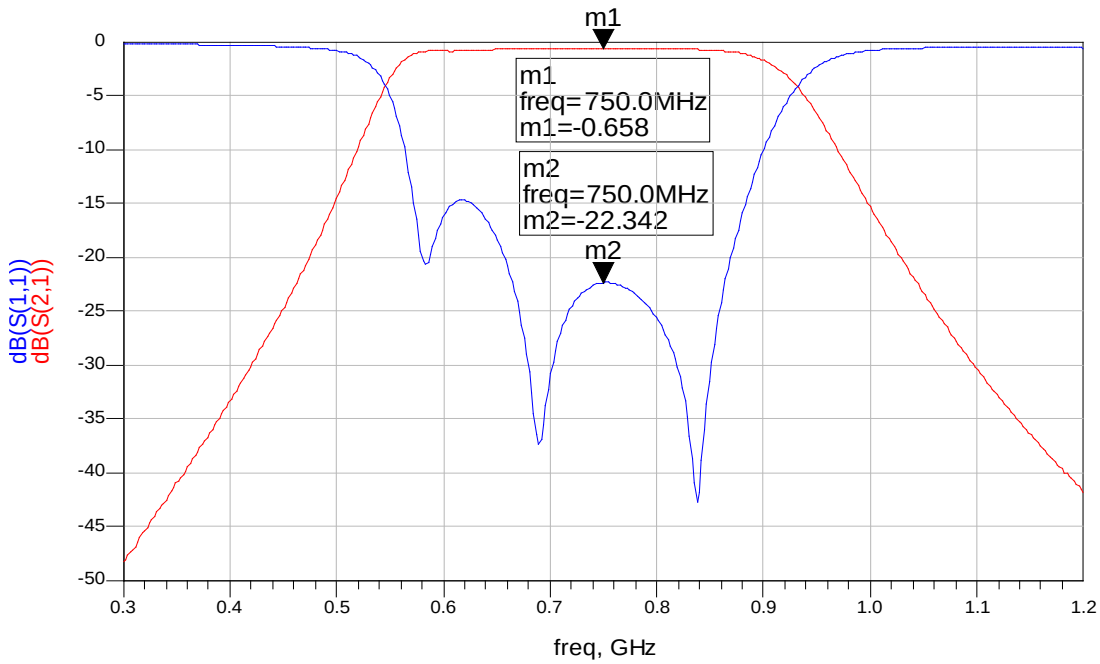

Figure 14. Bandpass filter response (Lark Engineering MS750-X300-5CC).

The Lark bandpass filters, ARS1526, ARS1207, and associated DC-blocking capacitors and attenuators are collectively referred to as the driver amplifier stage (orange highlighted section of Figure 13). These components are mounted on a circuit board designed using Altium Designer. The schematic and board layout are shown in Figure 15 and Figure 16, respectively.

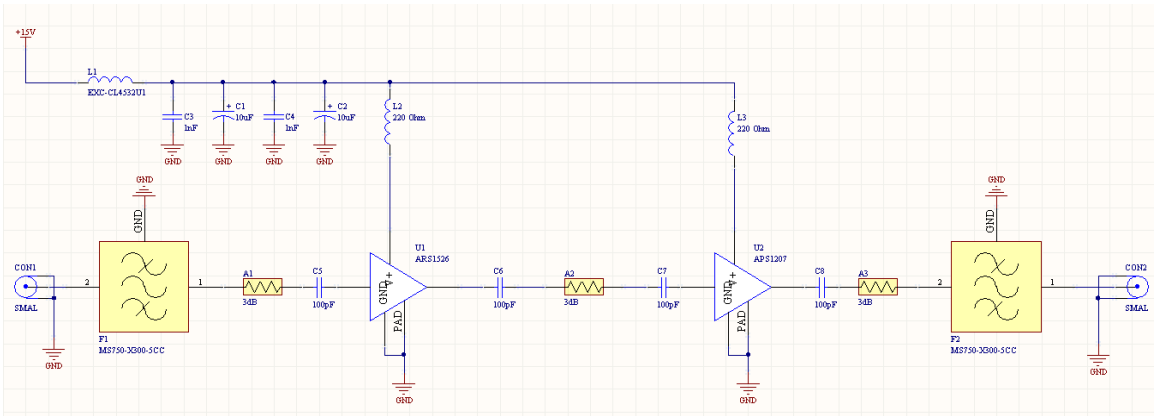

Figure 15. RF transmitter driver amplifier stage schematic diagram.

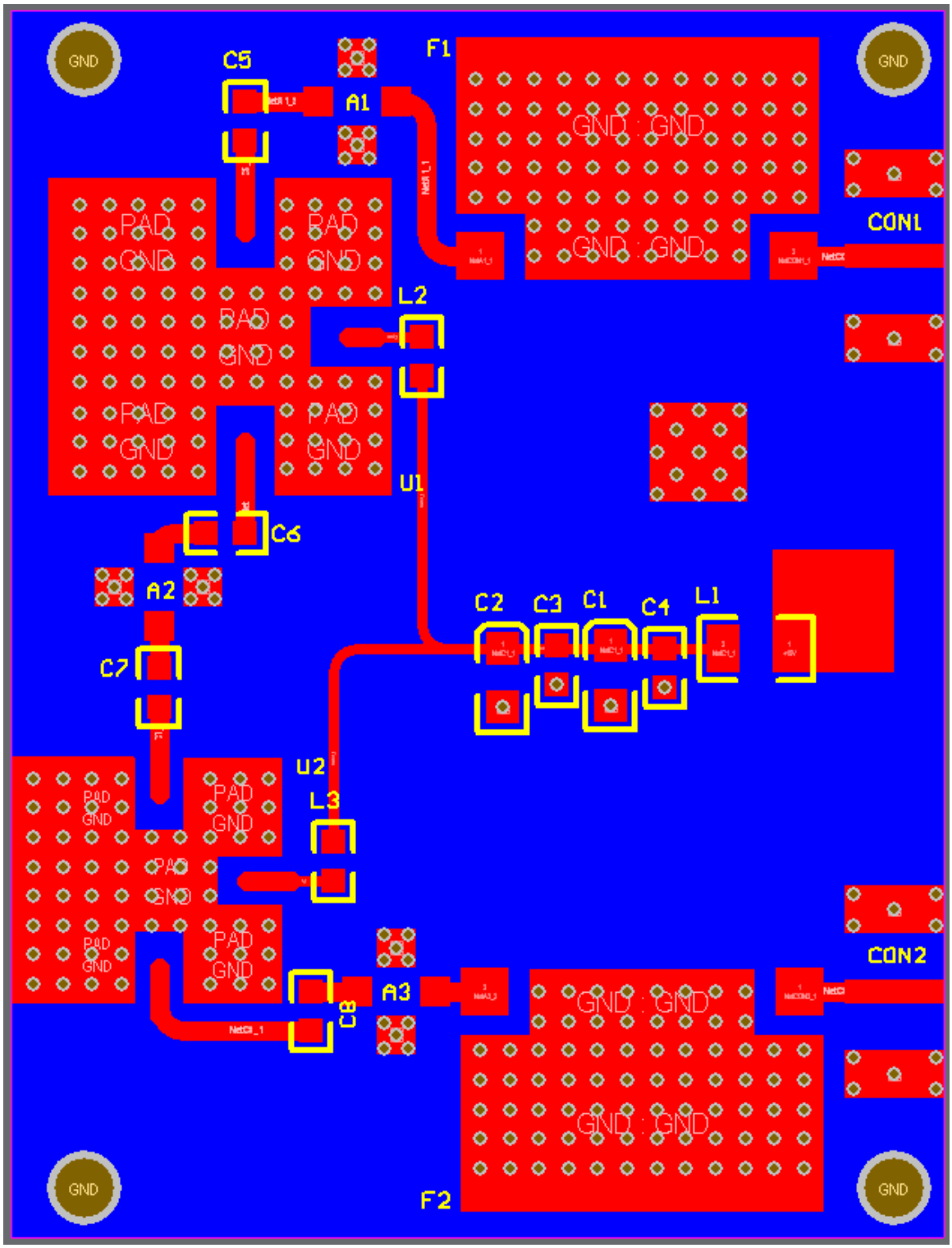

Figure 16. RF transmitter driver amplifier stage board layout.

All the components are connected using 50-Ω microstrip traces. Circuits are often designed for 62 mil (0.062 inch) thick FR4 (relative dielectric ≈ 4.35); however, this results in a

microstrip trace width of roughly 100 mils for a controlled impedance of 50 Ω when using FR4 clad with one ounce copper at 750 MHz (center frequency of the 600-900 MHz operational band). The wide trace width makes compact circuit construction difficult. To overcome this limitation, 20-mil thick FR4 was a better substrate choice to allow for thinner RF traces and minimal cost. Other substrate materials such as Rogers Duroid can also be used, but are often more expensive than FR4 and are not necessary in this case since the operational frequencies are below 1 GHz. The final trace thickness used was 40 mils. The trace width was calculated using ADS LineCalc and verified using the microstrip equations provided in [19, Appendix C]. A second verification was made using the simplified trace width calculator provided in Altium Designer. The calculations can be found in the appendix of this document.

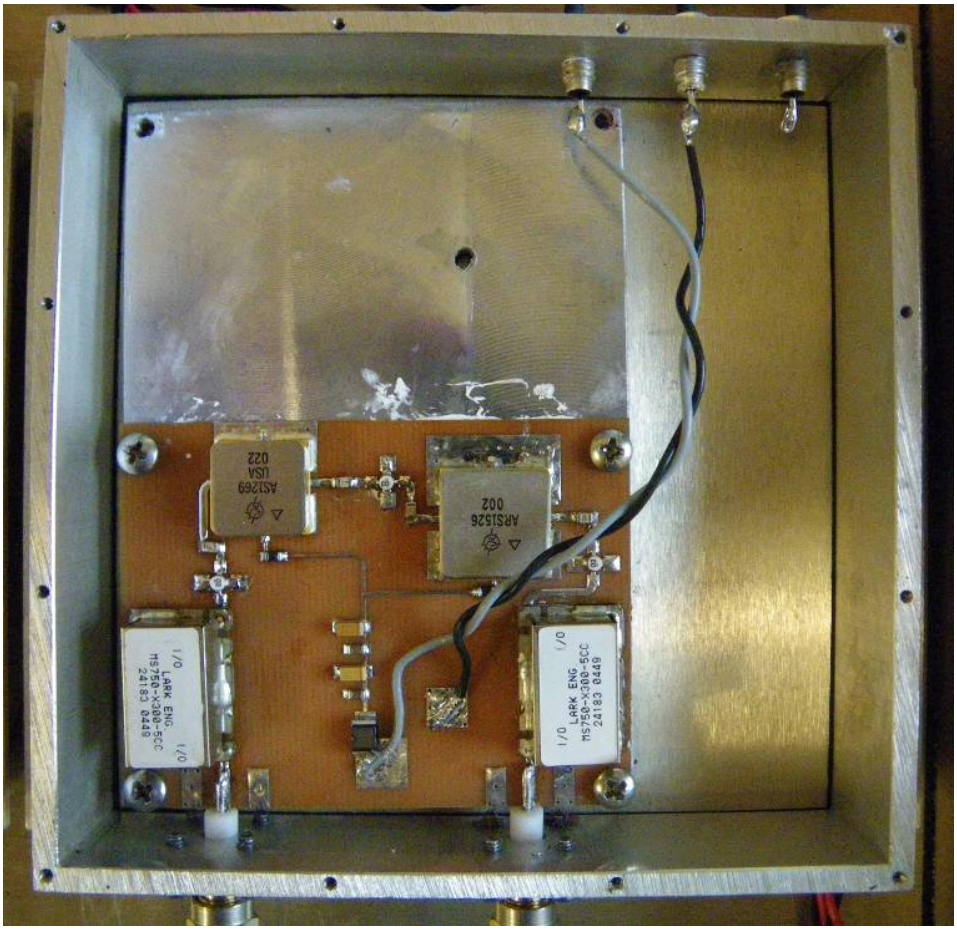

Figure 17. Photograph of the transmitter driver amplifier stage enclosure.

The driver amplifier stage is housed in a separate 4” by 4” Compac-RF EMI suppressing enclosure. This enclosure is designed to provide at least 80 dB isolation from external radiating noise sources, according to the manufacturer’s specification. Figure 17 shows the layout of this enclosure. This enclosure is nested within another EMI-suppressing enclosure, shown in Figure 18. This nesting provides at least 160 dB isolation between the transmitter driver amplifier stage and external radiating noise sources. This isolation is assuming both the internal and external enclosures meet the manufacturer’s specification. A more thorough discussion of the EMI-suppressive enclosures and design considerations is included in the Appendix of this document.

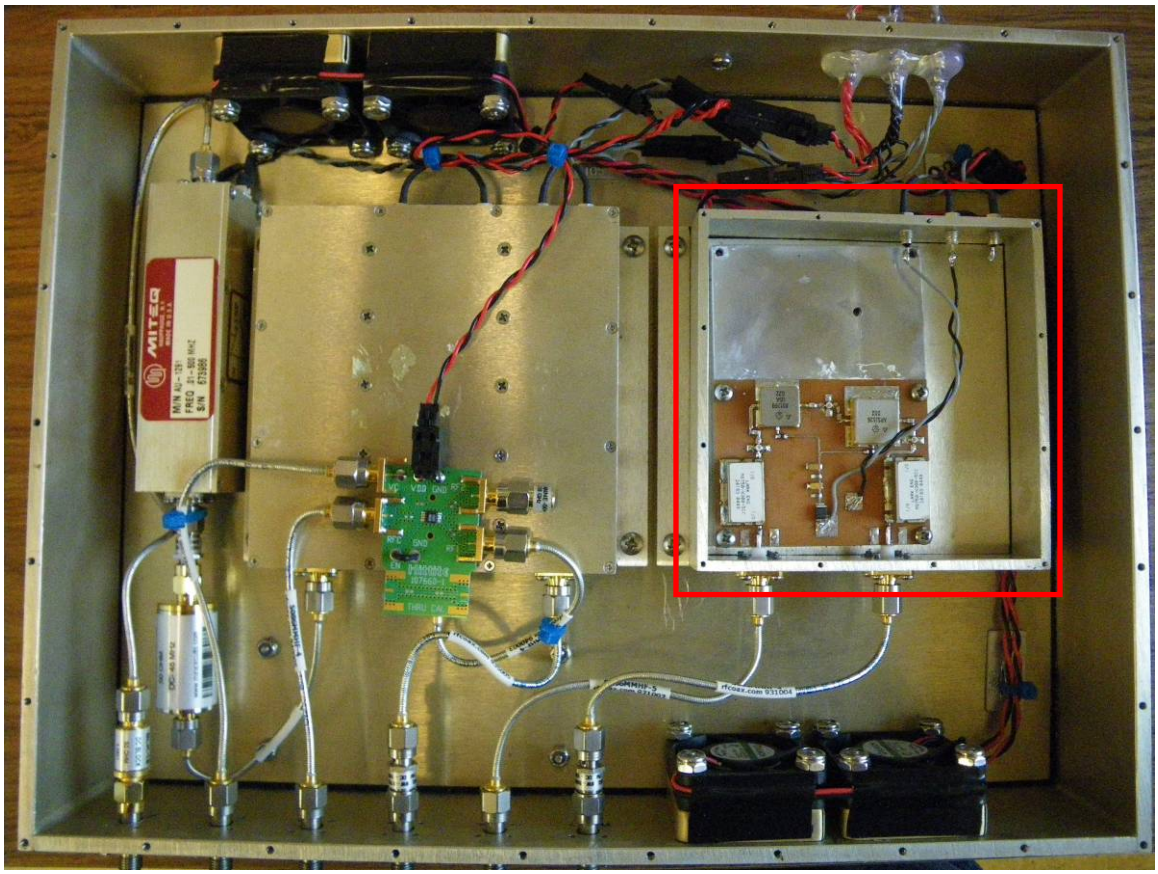

Figure 18. Photograph of the RF enclosure. Transmitter driver amplifier stage has been highlighted.

3.3.2.2 Power Amplifier Stage

The output of the driver amplifier stage is amplified using a high power amplifier (MiniCircuits ZHL-900A-10W). This amplifier has a gain of 26 dB with a 1-dB compression level of +40 dBm. Accounting for attenuators and filter losses, it amplifies the signal to provide a power output of +38 dBm.

3.3.2.3 T/R Switch Stage

Finally, the transmit signal passes through a transmit/receive (T/R) switch assembly based on the Hittite HMC784MS8GE chip. The measured loss through this assembly is roughly 1 dB; combine with the 3-dB attenuator added between the switches within the assembly, the transmit signal power delivered to the antenna is +34 dBm or 2.5 W. The T/R switch assembly consists of two high-power switches connected in cascade, a 3-dB attenuator, and two isolators (Raditek RADI-600-900M-S3-5WR-M1), as shown in the transmitter block diagram above.

Each switch provides at least 30 dB of isolation between each RF path. Each isolator provides roughly 15 dB of reverse isolation. The first isolator and first switch provide isolation between the transmitter and receiver. The second switch allows for the use of a single antenna, switching the antenna between the transmitter and the receiver. The second isolator protects the second switch from any mismatches between the receiver and the second switch. An additional isolation switch exists at the front end of the receiver, providing additional isolation between the transmitter and the receiver. This switch provides at least 60 dB of isolation when open; therefore there is at least 90 dB of isolation between the transmit path and the receiver input during transmit. This switch is discussed in more detail in the receiver section of this document. During receive, the first switch connects to a 50-Ω load, the second switch connects the antenna

to the receiver, and the receiver isolation switch conducts. This configuration provides 60 dB of isolation between the receiver input and any amplified noise from the transmitter.

Custom circuit boards were designed for the high-power switches to accommodate the circuitry necessary to drive the switch control inputs. A Hittite HMC784 SPDT RF switch was chosen for its power handling ability (10 W), low insertion loss (0.4 dB), and high-speed switching (40 ns). While the HMC784 can operate with a bias voltage (Vdd) between +3 V and +8 V, it is necessary to operate using a bias voltage of +8V in order to achieve an input compression point of 10 W or more (1-dB compression point greater than 40 dBm) [16]. The HMC784 requires complimentary control signals. Since the control voltages must be at least Vdd (+8 V) for the "high" state, a simple pair of inverters cannot be used to drive the HMC784 control lines. A pair of MAX4659EUA high-speed SPDT switches, capable of being driven using TTL logic, was employed to supply the necessary +8 V to the HMC784. The schematic of the T/R module is shown in Figure 25.

The MAX4659 switch was chosen since a switch driver circuit had already been designed for the power amplifier controller of another radar, and extra components were readily available. Hindsight shows that this was not an ideal choice. The MAX4659 switch is designed to provide high current; this is not necessary for the GaAs FET architecture of the HMC784 which requires very low gate currents. Using the MAX4659 may result in transients on the RF ports of the HMC784. Future revisions will replace the MAX4659 with a higher switching speed, CMOS analog switch with lower transients.

A single square-wave control signal is provided by digital system. This control signal passes through a pair of inverters to generate a copy of the control signal and its complement. Each inverter output is used to drive the control input of each MAX4659 separately. Each

MAX4659 has two inputs and one output. The output of one MAX4659 is tied to the "A" control input on the HMC784, and the output of the other MAX4659 is tied to the "B" control input on the HMC784. One input on each MAX4659 is tied to +8 V and the other inputs are tied to ground. A logic-high input to this circuit provides a logic-low (ground) to control "A" on the HMC784 and a logic-high (+8 V) to the control "B" on the HMC784; this connects the common port (RFC) of the HMC784 to the RF1 port. Conversely, a logic-low input to this circuit would connect RFC to RF2.

As part of the total system characterization, the switching characteristics of the T/R switch were investigated. The total path for the control signals used to switch the HMC784 includes the signal inverters (74HCT04), the voltage controlling switches (MAX4659) and the switching delay of the HMC784 itself. The delay through each inverter is stated to be ~8 ns [22]. The switching delay of the MAX4695 is stated to be ~120 ns. The switching delay of the HMC784 is stated to be ~15 ns. This would give an expected switching delay of ~150 ns. A set of signal generators and an oscilloscope were employed to quantify the delay of the manufactured board; Figure 19 shows a block diagram of this test setup.

Figure 20 shows views of the oscilloscope for both the turn on delay and the turn off delay. The turn on delay was measured to be ~160 ns and the turn off delay was measured to be ~130 ns; these correspond well with the expected 150 ns stated in the data sheet. To avoid damage of the switch this test was performed with an RF power of 1 mW (0 dBm). This is significantly lower than the full-power operation of the 10 W (40 dBm) maximum. Under full-power operation we would expect to see much larger transients. These larger transients do not appear to affect the expected switch operation. The larger transients can be seen in Figure 28.

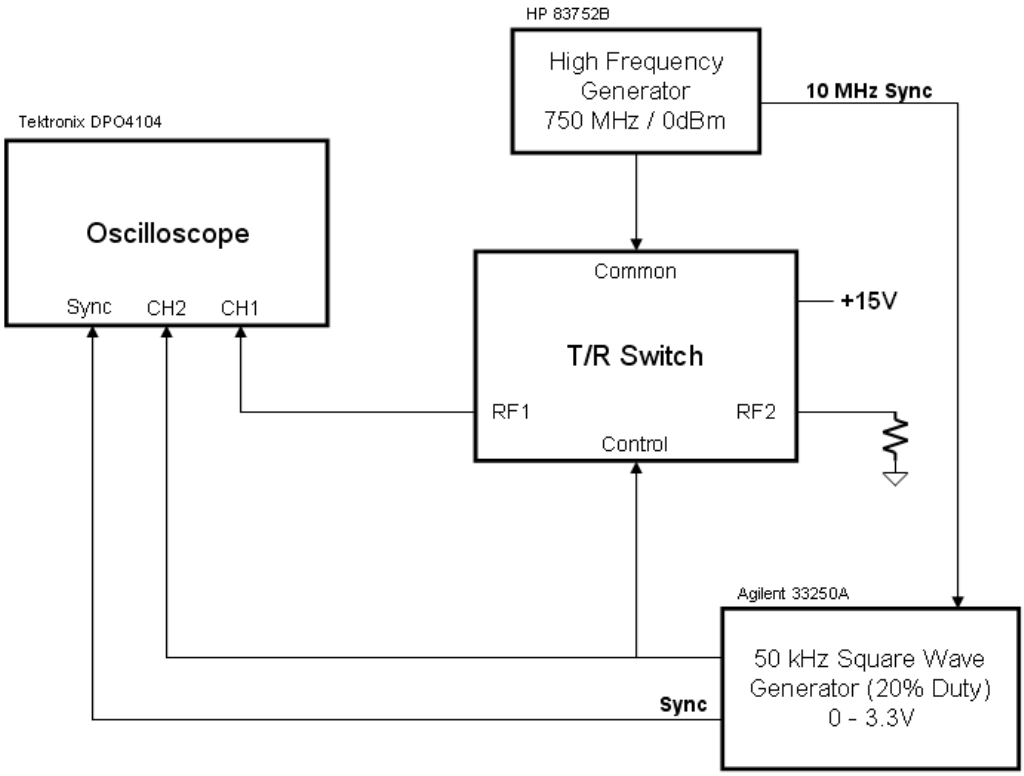

Figure 19. Block diagram of the T/R switch switching time test setup.

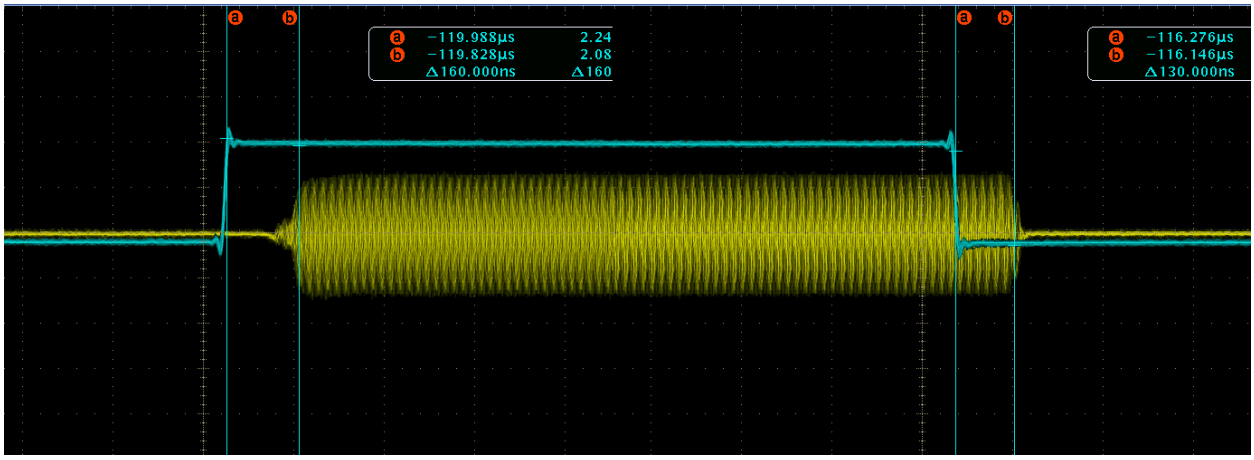

Figure 20. T/R switch switching delay measured on a high-speed multi-channel oscilloscope.

Additionally, the loss and isolation characteristics of the T/R switch were measured using an Agilent N5230C Microwave Network Analyzer at a drive level of -10 dBm. Figure 21 shows the RF Common to RF Output loss for both RF outputs. Loss through both outputs is nearly the same, with an acceptable average of ~0.5 dB and maximum of ~0.7 dB.

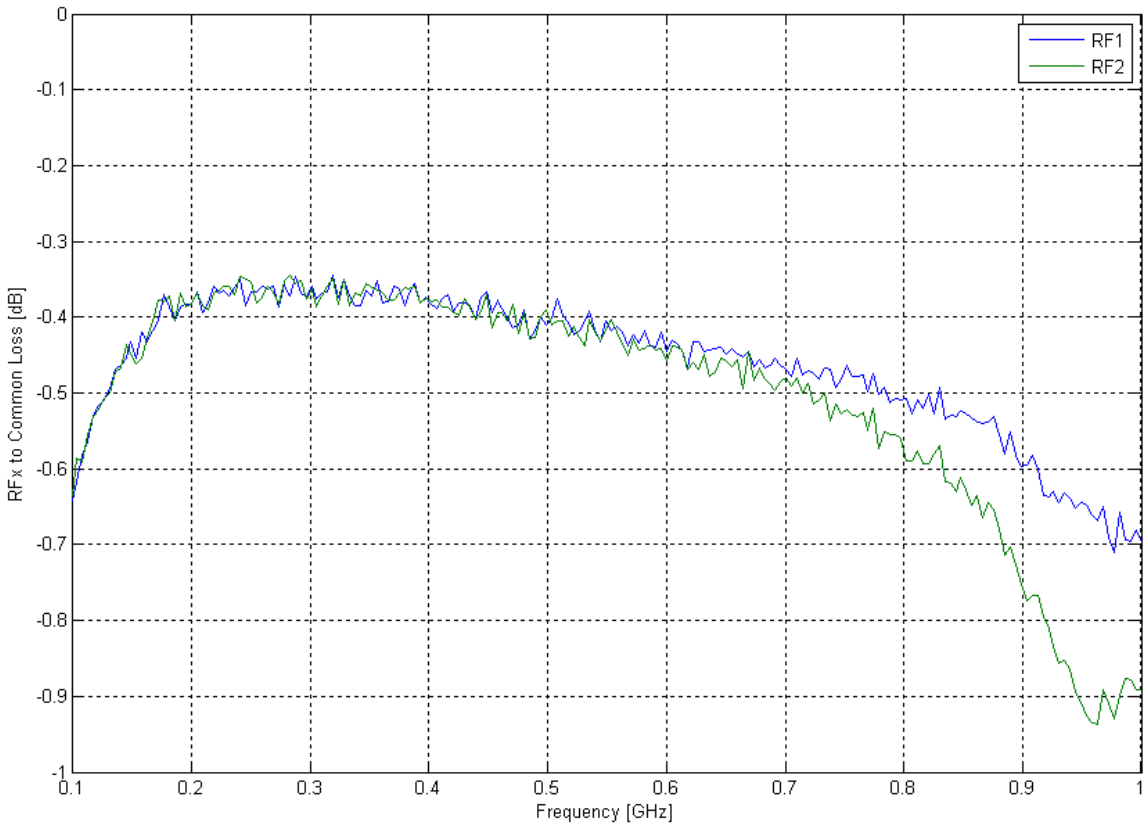

Figure 21. Measured T/R switch RFx to Common Port loss.

Figure 22 shows the measured inter-channel isolation combinations. It can be seen that the switch provides at least 30 dB of isolation between the RF Common and each RF Output when the respective output is off. The switch also provides at least 30 dB between each of the RF Outputs regardless of the switch position.

Figure 23 shows the measured port impedances for both conducting and open (non-conducting) states. This plot confirms the reflective nature of the switch ports when in an open state; this is common for high-power switches. When in receive mode, the input port of a single switch would be reflecting any amplified noise from the power amplifier since this amplifier is always powered during both transmit and receive. To prevent leakage of this amplified noise into the receive path and to protect the power amplifier output from reflected power from the open switch port, a dual switch configuration was implemented. This

configuration directs the amplified noise from the transmitter into a 50-Ω load during receive. During operation, it was found that the interaction between the two switches in the T/R switch assembly were generating undesired spectral components that marred the IF signal. If the two switches are not toggled precisely at the same time (and they are most certainly not), it is possible that one switch port may see the open circuit port of the other switch; this mismatch could generate a standing wave oscillation between them. The addition of a 3-dB attenuator between these switches seeks to damp these oscillations. Testing results discussed in Chapter 4 support this analysis.

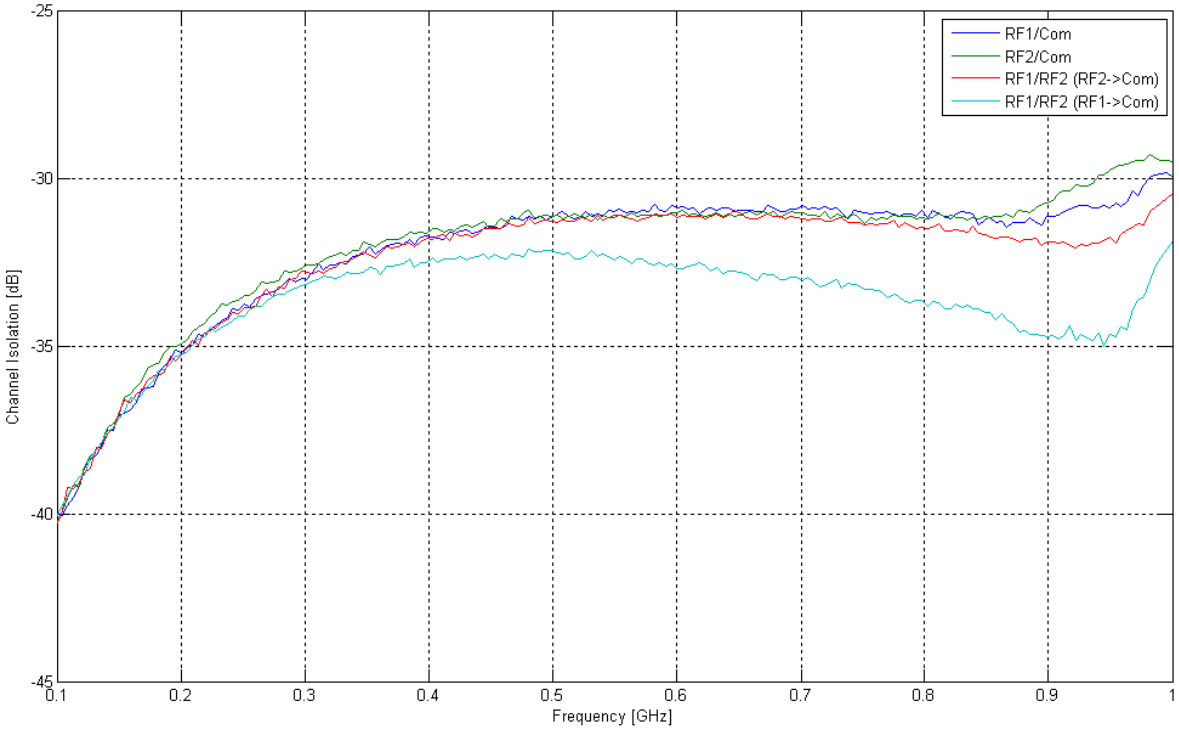

Figure 22. Measured T/R switch inter-channel isolations.

As with the other circuit board designs, Altium Designer was employed for schematic and board layout. Since the requirement for impedance-controlled RF traces was minimal, a grounded coplanar waveguide trace structure was chosen to improve inter-channel isolation.

This trace structure was greatly simplified (in terms of trace width and gap spacing) by using a four layer boar design with a 13-mil FR4 substrate between the top traces and the internal ground plane; for the RF traces, the board is effectively 13 mil thick.

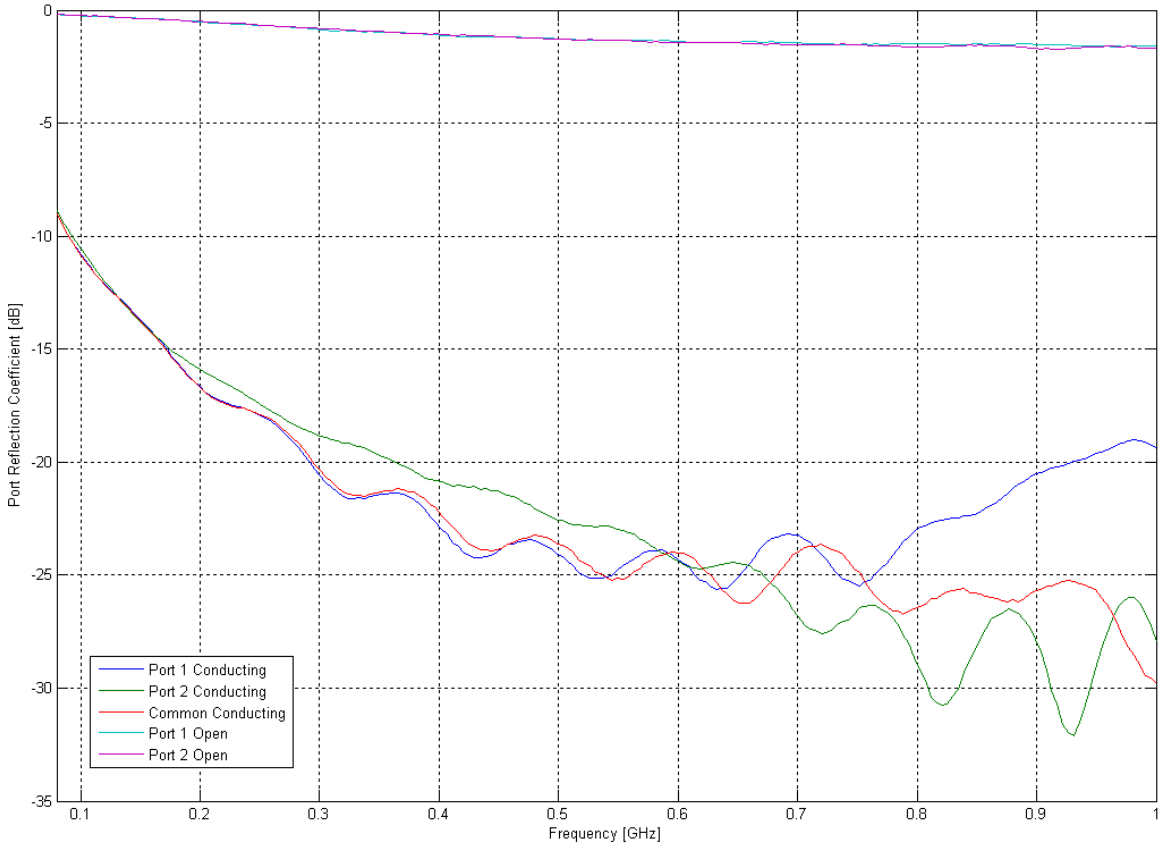

Figure 23. Measured T/R switch port reflection coefficient.

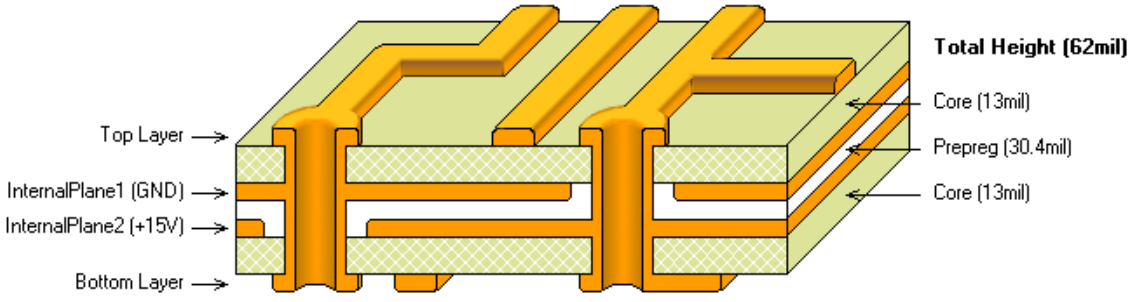

Figure 24. Illustration of T/R switch circuit board layer stack.

The board dimensions were dictated by the enclosure choice: a 2”x 3” Compac-RF box. An all-inclusive design approach was taken; the high-power switch, control signal drivers, and necessary voltage regulators were all placed on the same circuit board. To simplify the power

requirements of the circuit and provide an additional layer of protection against conducted EMI, linear regulators were employed to produce the needed +12 V, +8 V, and +5 V supplies from a single +15 V source. Figure 26 shows the board layout for the T/R switch; the grounded coplanar waveguide trace structure is visible on the upper half of the board. Figure 27 shows a photograph of the assembled T/R switch circuit board in its housing.

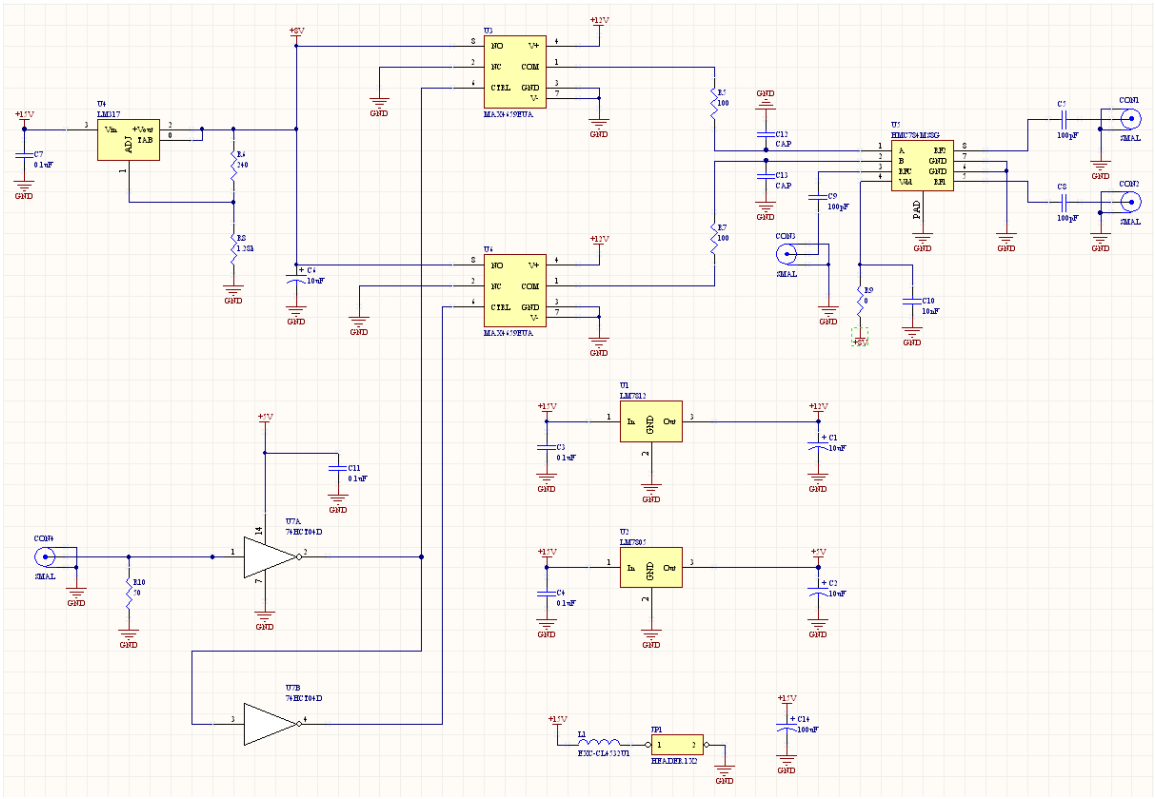

Figure 25. High power T/R switch schematic.

Both high power T/R switches are toggled using TTL logic lines provided by the FPGA within the digital subsystem. These TTL logic lines are phase locked to the logic outputs of the FPGA that drive the DDS outputs. A logic low connects the transmitter to the antenna. A logic high connects the first switch to a 50-Ω load and allows the second switch to connect the antenna to the receiver input. These control lines are programmed to switch from transmit to receive mode roughly 100 ns following the end of the transmit chirp. The control lines remain high for

the next 9.5 µs (dedicated receive window) before toggling low during the DDS reprogramming stage.

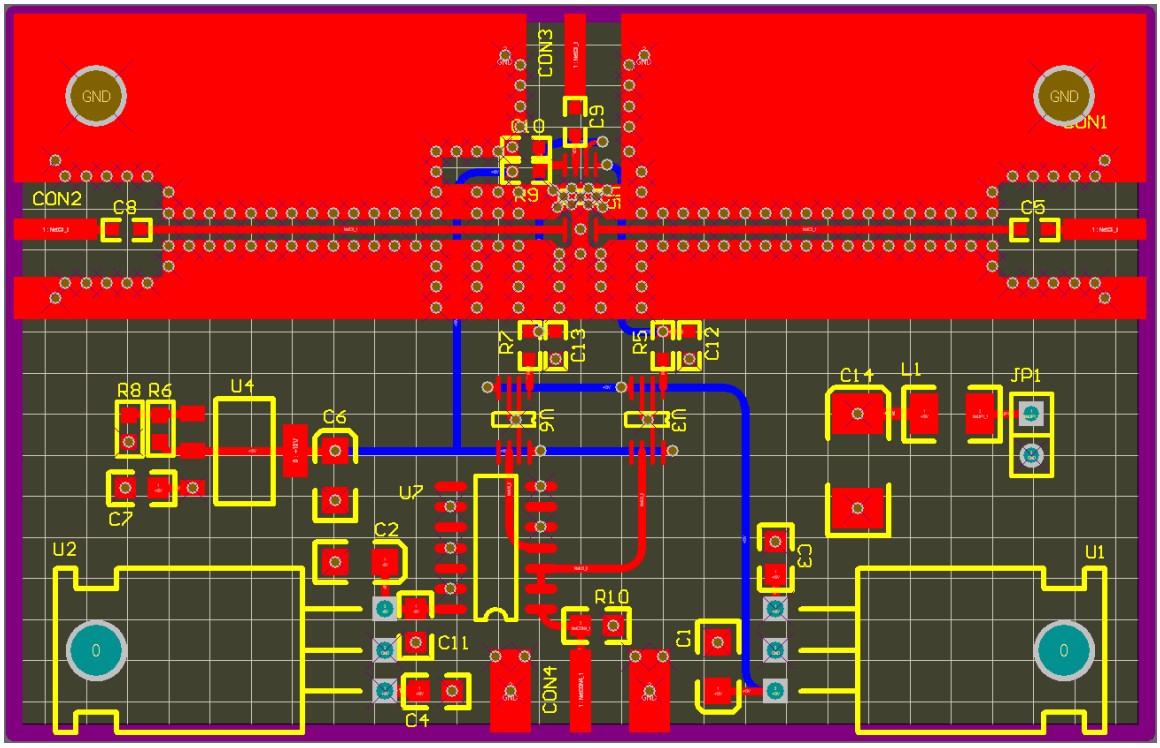

Figure 26. High power T/R switch board layout.

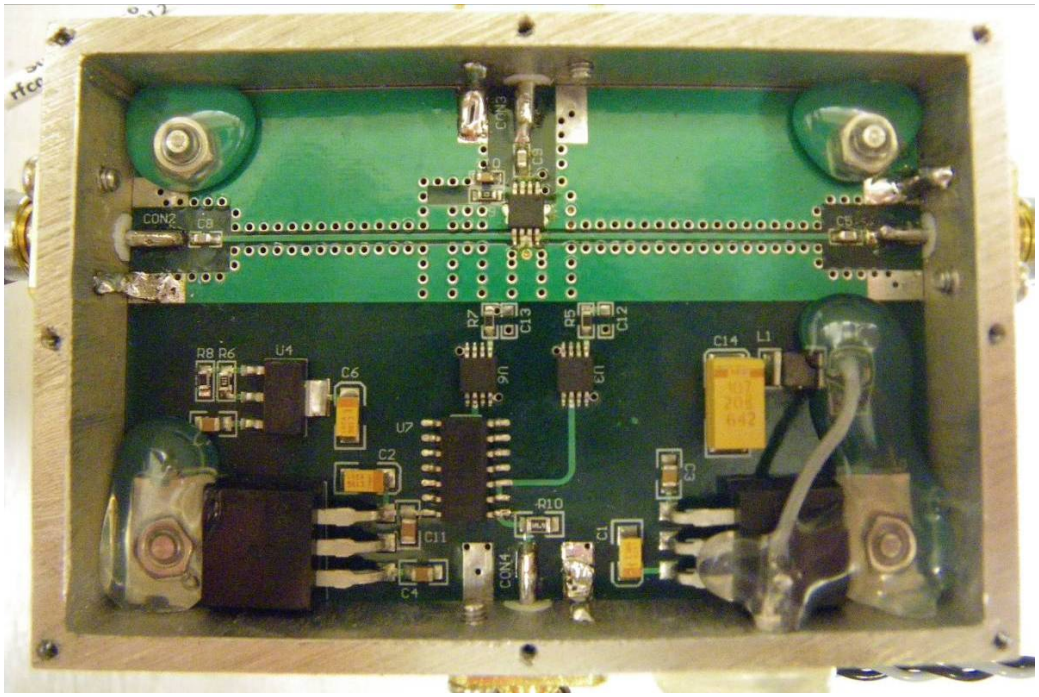

Figure 27. Photograph of the manufactured high power T/R switch enclosure.

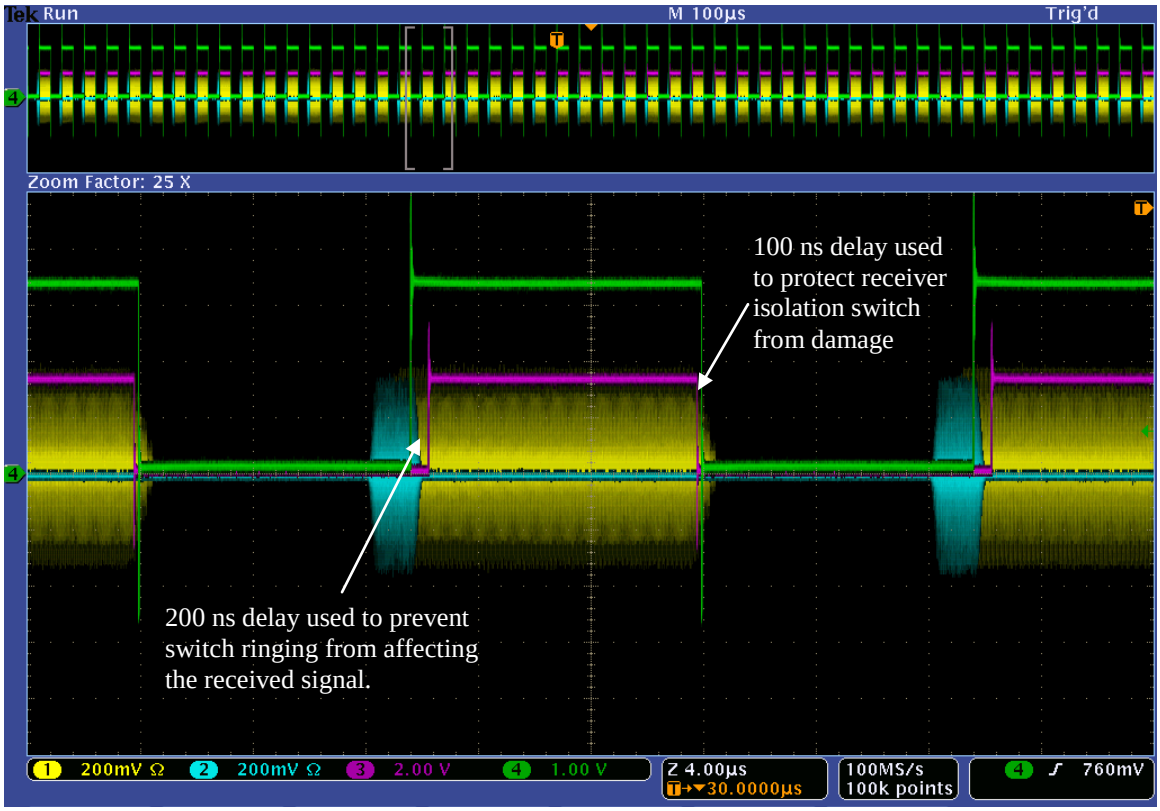

Figure 28. Measured T/R switch and receiver isolation switch control signal timing. Yellow: LO tone, Blue: transmit chirp, Purple: T/R switch control signal, Green: receiver isolation switch control signal.

A logic low was chosen for the reprogram stage for two reasons: to limit the receive window so as to only see returns from less than 300 m in ice at the nominal flight altitude of 500 m, and to avoid dumping too much power into the 50-Ω load connected to the first switch since the DDS will output spikes during reprogramming. Refer to Figure 28 for a graphical explanation of the switch timing.

3.3.3 RF Receiver

The purpose of the receiver hardware is three-fold: amplify weak return signals, filter these signals so they only contain frequencies in the band of interest, and down-convert these frequencies to fall within the bandwidth of the digital acquisition hardware (DAQ). The most complex of these operations is the down-conversion: translating the frequency content that exists in each received waveform (50 MHz of bandwidth) from the UHF frequency (between 600 and

900 MHz) range to the bandwidth of the DAQ hardware: 5-55 MHz. This operation is accomplished by mixing the received signal with a stable, phase-coherent reference tone generated by a second DDS output, a local oscillator signal (LO) that changes with each waveform so that the received signal is mixed down to the same IF bandwidth (5-55 MHz). This is easily accomplished since the DDS is reprogrammed between each waveform in preparation for the next.

For the first waveform, the Channel 1 output of the DDS is a 2-μs long, 600-650 MHz chirp, and the Channel 2 output is a tone at 606 MHz. The received signal and this reference tone are mixed together in the receiver, converting the received signal to baseband where it falls within the bandwidth of the DAQ. For the second waveform, the Channel 1 output is a 620-670 MHz chirp and the Channel 2 output is a tone at 626 MHz. This again converts the received signal to baseband. This pattern continues for the remaining 14 waveforms.

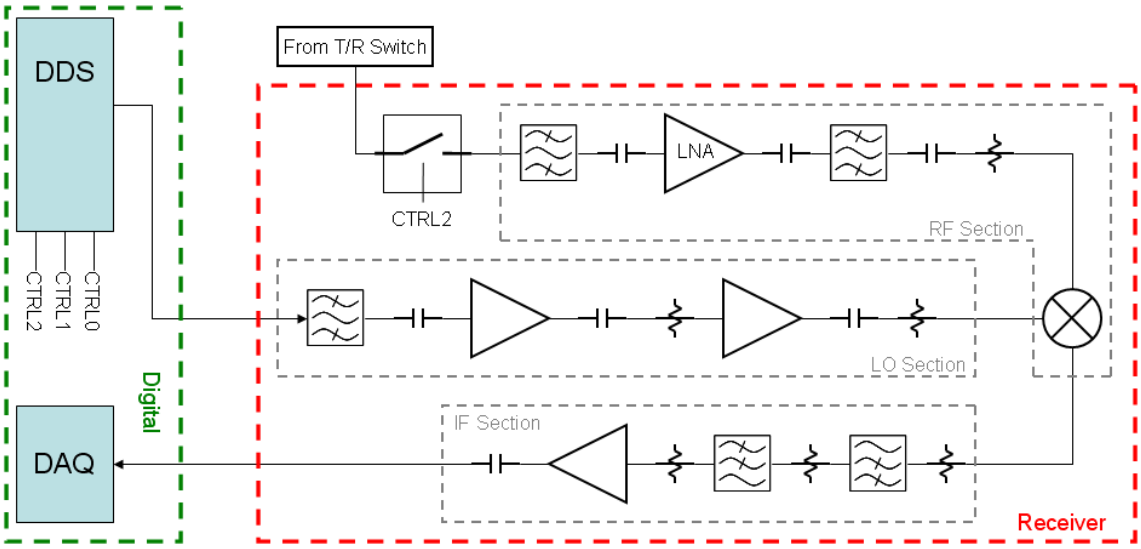

Figure 29. Winter 2009-2010 accumulation radar receiver block diagram.

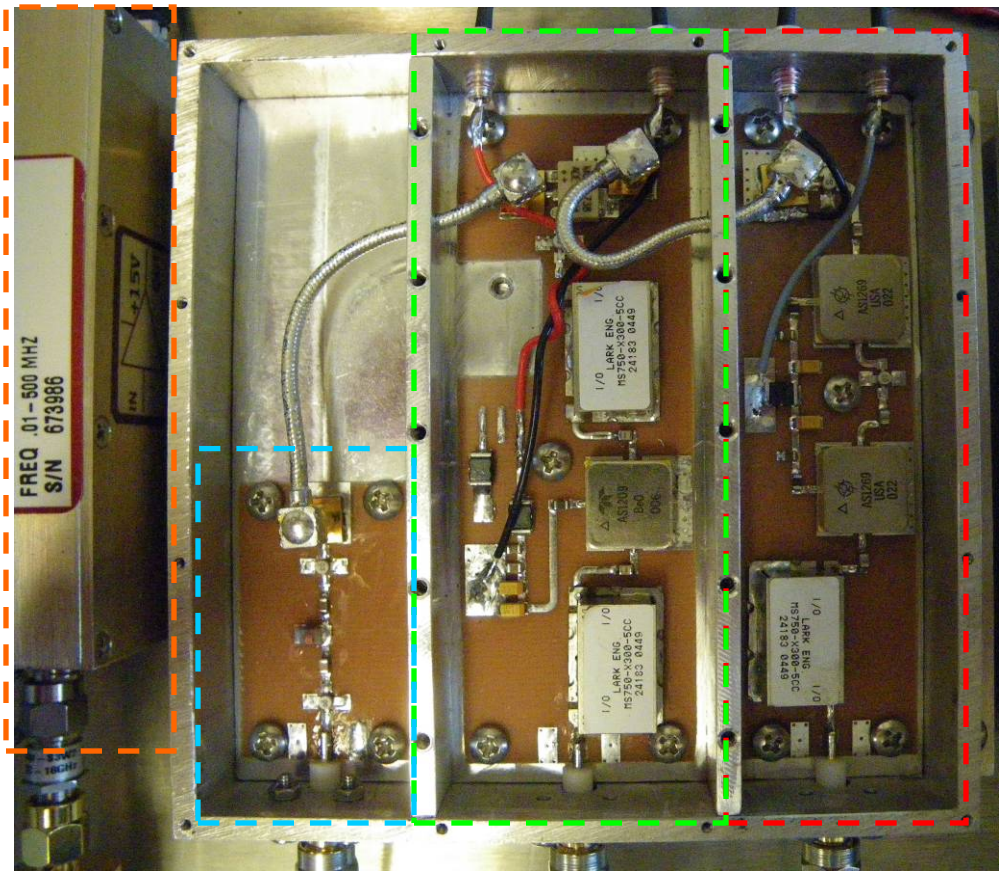

Figure 30. Photograph of the receiver enclosure. Orange: IF amp, Blue: IF Filter, Green: RF Section, Red: LO Section.

Figure 29 shows a block diagram of the accumulation radar receiver. There is an additional isolation switch preceding the LNA, as discussed in the T/R section of the transmitter. The receiver RF hardware is divided into three subsections: radio frequency (RF), local oscillator (LO) and intermediate frequency (IF). Figure 30 shows the majority of the RF hardware housed in a 4" by 4" Compac EMI-suppressive enclosure similar to the transmitter; however, this enclosure is subdivided to provide additional isolation between each subsection of the receiver. The additional isolation helps reduce contamination of the received RF signal and the converted IF signal by the higher power LO signal.

3.3.3.1 Receiver RF Subsection

The receiver RF subsection is responsible for amplifying and conditioning the UHF band received signals. This section is preceded by the receiver half of the T/R switch discussed above, including the additional receiver isolation switch. This switch, a Hittite HMC349, is used to provide additional isolation of about 60 dB between the transmitter and receiver during transmission. When conducting in receive mode, the insertion loss is roughly 0.8 dB. Since this switch was added to the system after the initial enclosure design stage, a Hittite evaluation board was used and connected to the exterior of the receiver enclosure. Since this switch still resides inside the larger RF enclosure (Figure 40), sufficient isolation exists between the switch and external noise sources.

This switch is toggled using a TTL output from the DDS. This control signal differs slightly in timing compared to the T/R switch control signals (Figure 28). The receiver isolation switch is toggled to close roughly 200 ns before the T/R switch is toggled to receive to allow any ringing that may occur during switching to subside before the received RF signal is applied. Also, the toggle to open the receiver isolation switch is delayed roughly 100 ns following the toggle of the T/R switch so as to avoid directly applying a signal to the receiver isolation switch input. When the receiver isolation switch is open, its input is connected to an internal 50-Ω load, which is only capable of dissipating 1 W. While the signal incident on the receiver isolation switch is not expected to exceed 1 W, this timing delay was implemented as a precaution to prevent damage to the switch.

Following the receiver isolation switch is a Lark 600-900 MHz bandpass filter (the same bandpass filter used in the transmitter, refer to Figure 14 for the frequency response), used to reduce the out-of-band noise and spurious signals. Next is a Teledyne Cougar AS1209

low-noise amplifier (LNA) with 28 dB of gain, +19.8 dBm 1-dB compression point, a 1-dB noise figure, and 40 dB reverse isolation. This amplifier is followed by another Lark 600-900 MHz filter, used to further reduce any out-of-band spectral components. A 3-dB attenuator is used between this filter and the RF port of the down-conversion mixer to reduce reflections between these two devices caused by mismatched port impedances; the RF port of the mixer has a VSWR of ~1.7. The down-conversion mixer is a MiniCircuits ADE-R5LH+. This mixer was chosen for its relatively low conversion loss (~7.2 dB) and high inter-channel isolation (~65 dB LO/RF and ~50 dB LO/IF). The overall gain of this stage is 16.4 dB, including the conversion loss of the mixer. DC-blocking capacitors are used around each active component in order to maintain separate DC biases.

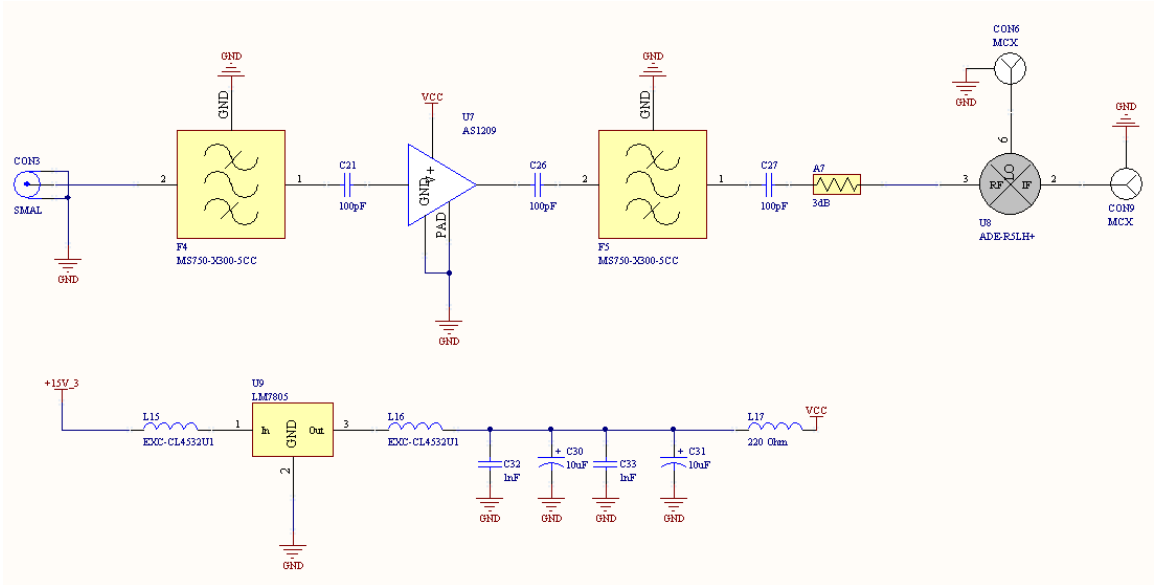

Figure 31. Receiver RF section schematic.

Figure 31 and Figure 32 show the schematic and board layout for the RF section of the receiver, respectively. Just like the transmitter driver amplifier board, 20-mil FR4 was utilized in order to allow for smaller width 50-Ω traces. Originally, the entire RF section (transmitter and receiver) was designed to run from a single power supply: +15 V. Since some components (such as the AS1209 on the receiver RF board) require +5 V, the use of regulators was required. This

explains the presence of a regulator on the board layout below. It was later decided that separate +15 V and +5 V supplies would be more convenient; therefore this regulator was not populated (Figure 30). Grounded co-planar waveguide was used on the LO and IF ports of the mixer; this was done to reduce potential coupling between the LO, RF, and IF ports.

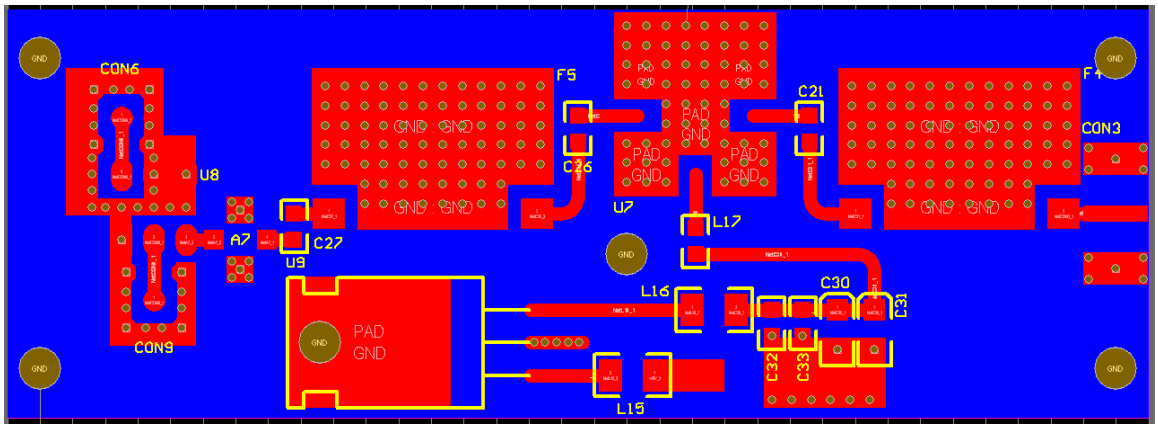

Figure 32. Receiver RF section board layout.

An important characteristic of any RF receiver is its noise figure. The noise figure is a measure of the degradation in the SNR between the input and output of a device or cascade of devices [32]. We are often interested in capturing and amplifying very weak signals from the target with a radar receiver, such as signals that are often near or below the ambient noise floor. Because of this, it is critical to understand and minimize the addition of noise into the receive path by those components in the receive path (especially the active components); consequently, the overall receiver front-end noise figure was calculated.

Table 3. Receiver front-end component gains and noise figures.

Component	Gain [dB]	Noise Figure [dB]	Gain	Noise Figure
HMC784 Switch	-0.6	0.6	0.87	1.15
Raditek Isolator	-0.6	0.6	0.87	1.15
HMC349 Switch	-1.1	1.1	0.78	1.29
1st Filter	-0.7	0.7	0.85	1.17
AS1209	28	1	631	1.26
2nd Filter	-0.7	0.7	0.85	1.17
3 dB Attenuator	-3	3	0.5	2
ADE-R5LH+	-7.2	7*	0.19	5

* Using the rule-of-thumb that a mixer's noise figure is roughly equivalent to the conversion gain.

$$F = F_1 + \frac{F_2 - 1}{G_1} + \frac{F_3 - 1}{G_1 G_2} + \frac{F_4 - 1}{G_1 G_2 G_3} + \frac{F_5 - 1}{G_1 G_2 G_3 G_4} + \frac{F_6 - 1}{G_1 G_2 G_3 G_4 G_5} + \cdots$$

$$F = 1.15 + \frac{1.15 - 1}{0.87} + \frac{1.29 - 1}{0.87(0.87)} + \frac{1.17 - 1}{0.87(0.87)(0.78)} + \cdots = 2.55 \rightarrow 4.06\ dB \quad (15)$$

Table 3 lists each component in the receiver path, its gain/loss, and noise figure. Using the equation for the noise figure of a cascaded system (15), the overall noise figure of the receiver front-end was found to be ~4.06 dB. This means we can expect the overall SNR of the received signal to be degraded by roughly 4 dB. In equation 15 above, F_n denotes the noise figure of a particular component and G_n denotes the gain of a particular components where n is the position of the component in the chain starting with one as the first component as listed in Table 3.

3.3.3.2 Receiver LO Subsection

The LO section is responsible for filtering and amplifying the LO tone from the DDS used to drive the receiver down-conversion mixer. Filtering the output of the DDS is essential, just as before, to remove all frequency components except those of interest in the 2nd Nyquist zone. The LO drive level needs to be above a specific threshold (10 dBm for the MiniCircuits ADE-R5LH+) to minimize conversion loss and noise figure. Mixing will occur at drive levels below this threshold, but the conversion efficiency and noise figure may not meet the manufacturer stated specifications and may not satisfy the design requirements. Figure 33 shows the unfiltered LO (Channel 2) output of the DDS.

The first component in the LO section is a Lark 600-900 MHz bandpass filter, used to filter out the baseband and higher-order harmonics in the DDS output while preserving the second Nyquist band. Two cascaded amplifiers (Teledyne Cougar AS1269) follow this filter. Each of these amplifiers has about 21 dB of gain with a 1-dB compression point of +21 dBm.

The two amplifiers are separated by a 3-dB attenuator in order to reduce multiple reflections caused by port impedance mismatches. The final component before the LO port of the mixer is another 3-dB attenuator, again to reduce multiple reflections caused by port impedance mismatches. DC-blocking capacitors are used around each active component to isolate bias voltages of these devices. The output of the DDS Channel 2 is set to about -22 dBm; accounting for gains and losses in the LO chain, we would expect the power level at the input of the mixer to be roughly +13 dBm. This power level is sufficient to adequately drive the mixer without saturating either of the amplifiers.

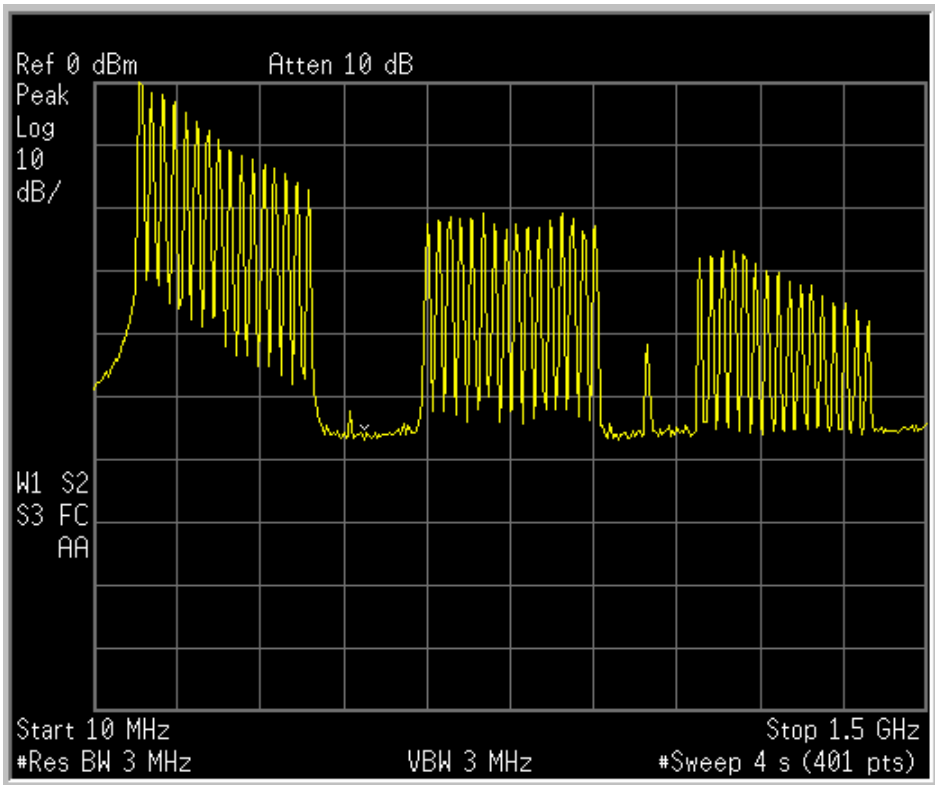

Figure 33. Unfiltered spectrum of the LO signal (Channel 2) at the output of the DDS.

Figure 34 and Figure 35 are the schematic and board layout for the LO section circuit board, respectively. This circuit is manufactured using 20-mil FR4 in order to reduce the necessary trace width while maintaining 50 Ω.

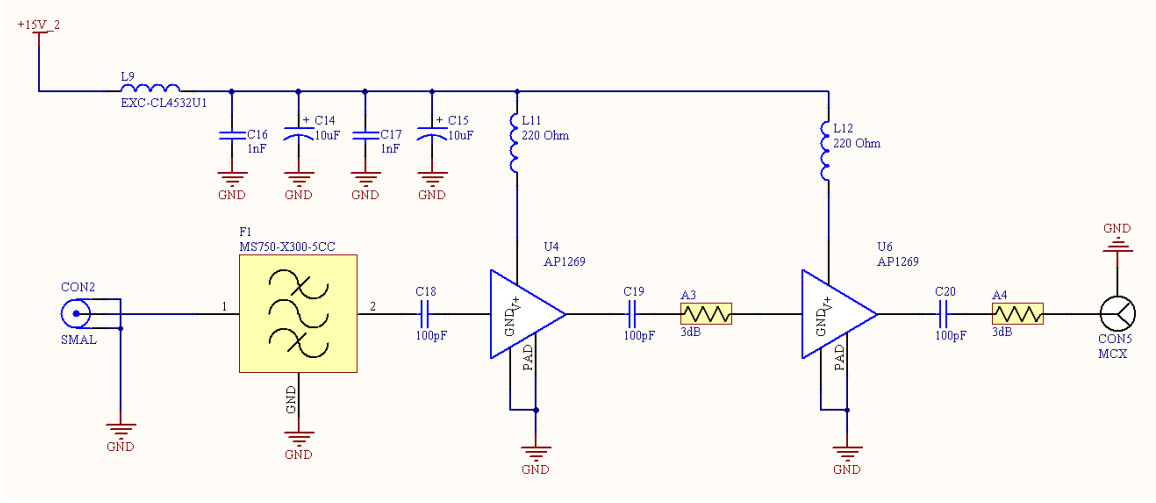

Figure 34. Receiver LO section schematic.

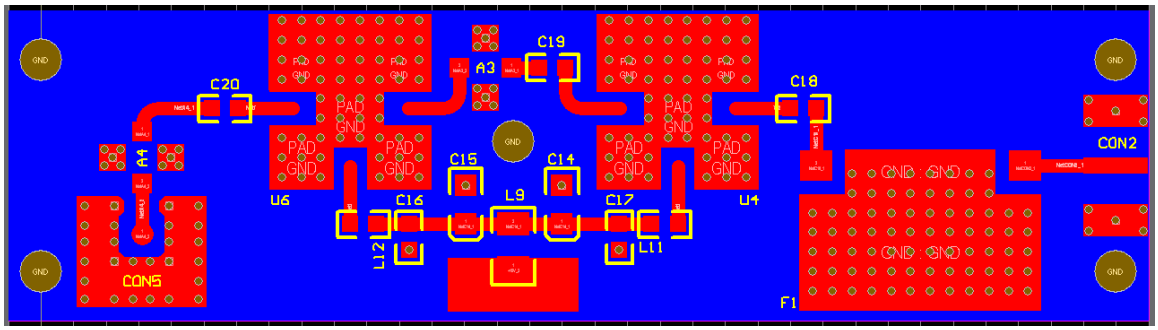

Figure 35. Receiver LO section board layout.

3.3.3.3 Receiver IF Subsection

The IF section of the receiver can be viewed in two sub-sections: those components that are inside the receiver enclosure and those connectorized components that are outside the receiver enclosure (but still within the RF enclosure). Figure 36 and Figure 37 are the schematic and board layout for the components inside the receiver enclosure, respectively. Again, 20-mil FR4 was used as the substrate.

The IF section within the receiver enclosure consists of matching attenuators and the IF high-pass filter (HPF). The first 3-dB attenuator is used to reduce the effect of impedance mismatches between the IF port of the mixer and the HPF. The second 6-dB attenuator is used

to minimize the effect of impedance mismatches between the HPF and the following low-pass filter (LPF) as well as reduce the IF signal power level to prevent saturating the IF amplifier. The IF section high-pass filter was designed using Genesys.

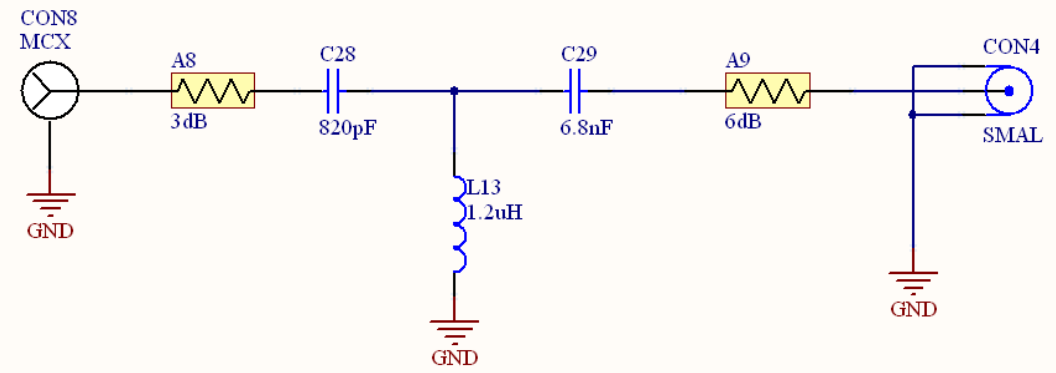

Figure 36. Receiver IF section HPF schematic.

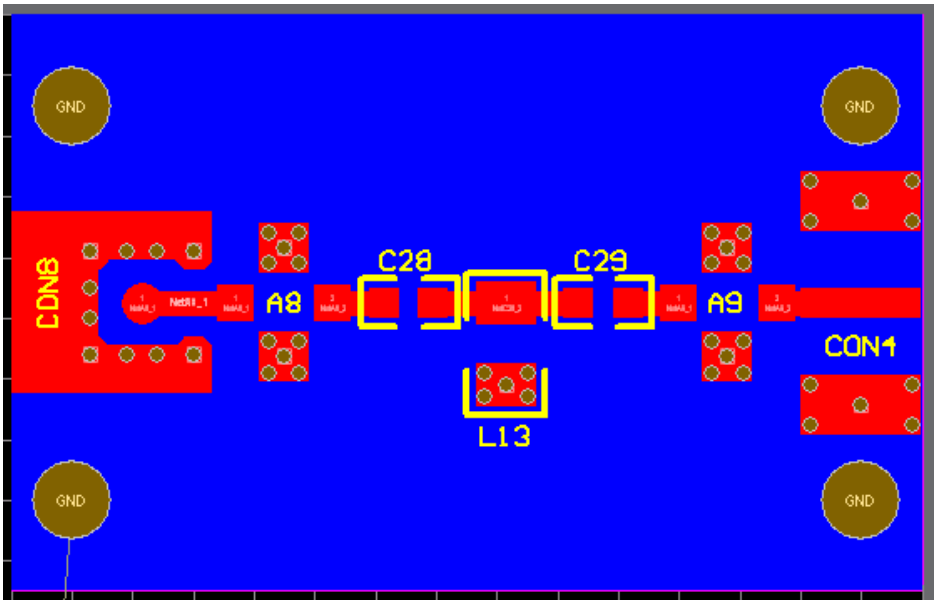

Figure 37. Receiver IF section HPF board layout.

Figure 38 and Figure 39 show the simulation schematic and simulation results for the filter design using real component S-parameter files. The design goal was to achieve a 3-dB cutoff near 5 MHz. Optimizing component values led to a design with a 3-dB cutoff at 4 MHz; this was deemed acceptable.

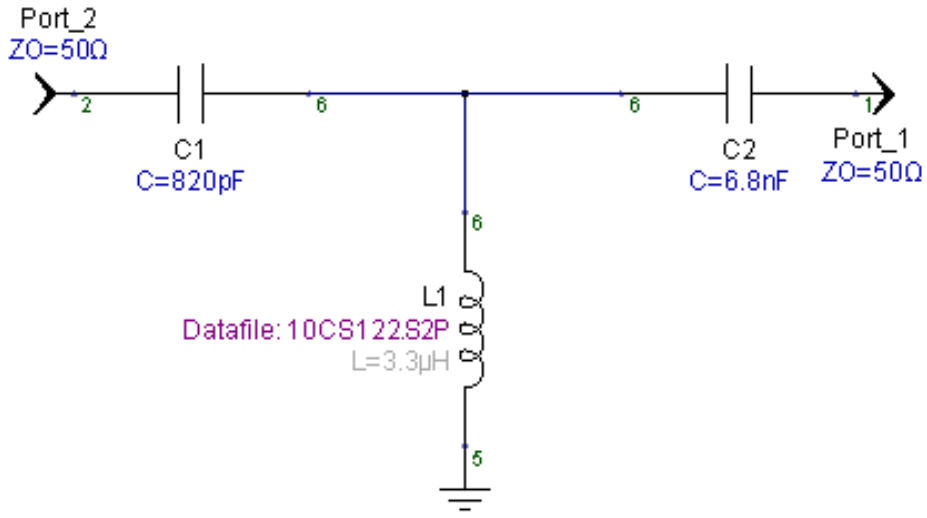

Figure 38. Receiver IF HPF schematic. Genesys used for simulations.

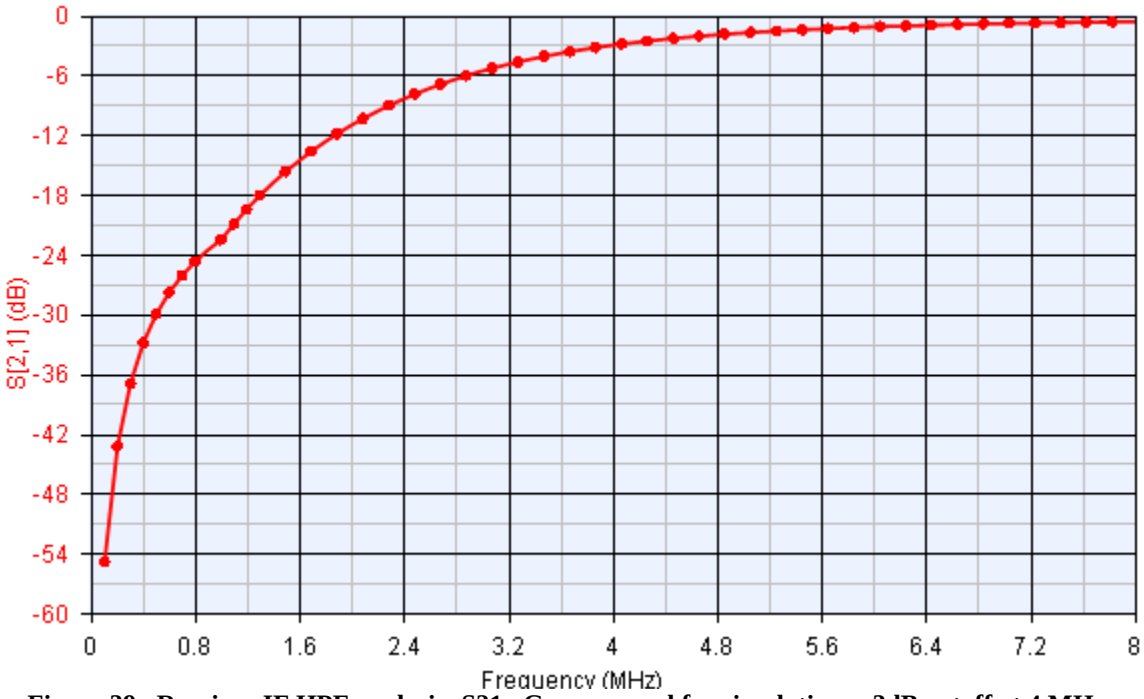

Figure 39. Receiver IF HPF analysis: S21. Genesys used for simulations. 3dB cutoff at 4 MHz.

It was chosen to use a connectorized low-pass filter (LPF) so that it could be easily swapped if the IF bandwidth needed to be changed during a field experiment. This filter directly follows the output of the IF HPF section. Since the initial design requirements called for an IF 3-dB bandwidth of 5-55 MHz, a connectorized SLP-50+ MiniCircuits LPF was utilized. This filter has a 3-dB cutoff of 55 MHz and a 1-dB cutoff of 48 MHz [24]. Following the LPF is a

3-dB attenuator; as with other attenuators, this is used to reduce ringing between components due to impedance mismatches. This is followed by the IF amplifier, a connectorized amplifier (Miteq AU-1291). This amplifier has 62 dB of gain, +11.5 dBm 1-dB compression point, 1.2 dB noise figure, -85 dB reverse isolation, and -12 dB input/output return losses within the band of interest [25]. The final component of the IF section is a connectorized DC block used to ensure DC isolation between the output of the IF amplifier and the input of the DAQ. Figure 40 shows the layout of the receiver within the RF enclosure.

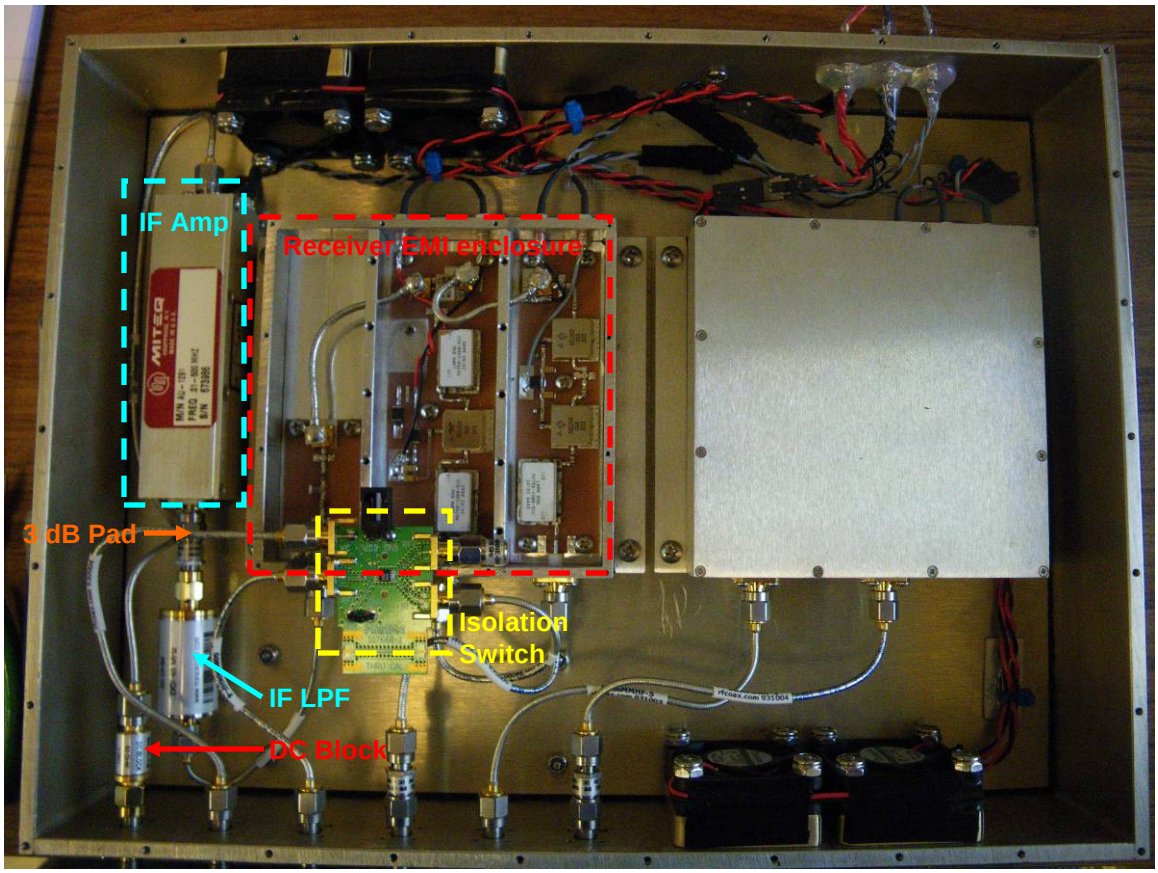

Figure 40. Photograph of the RF enclosure with receiver components highlighted. Red: Receiver enclosure, Yellow: Receiver isolation switch, Blue: IF amplifier.

3.3.4 Antenna

The available space on the DHC 6 Twin Otter platform used for the 2009-2010 CReSIS Antarctic Survey mission was the driving force behind the antenna choice for the accumulation radar. Figure 41 is a specification document from Kenn Borek Air Ltd. and shows the location and size of the available nadir port openings available for the accumulation radar antenna array.

The available port is an oval-shaped opening 21" (53 cm) long (forward-to-aft) and 19" (48 cm) wide (port-to-starboard). It was chosen to use an array of Vivaldi antennas since their wide bandwidth and smaller size (in comparison to other wide bandwidth antennas that are physically larger, such as printed circuit board elliptical dipoles) allowed for used of more elements.

The radiating structure chosen for the Twin Otter platform was a tapered slot, or Vivaldi [6]. The original design by Panzer [28] was taken as a base design. Additional design steps were taken to develop a smaller, lighter version of this antenna, fabricating it out of aluminum [4].

Figure 42 and Figure 43 show the 3-D AutoCAD model and fabricated element, respectively. This smaller antenna is roughly 8" x 8" x 1/8". Since weight was not a critical factor for the array to be used on the Twin Otter, the elements were manufactured out of brass to ease milling and soldering. Each element was fed using an 18" coaxial cable. The outer conductor was soldered into a groove milled into one face of the antenna with the center conductor exposed across the feed-gap and soldered to the opposite side. A close-up view of the feed point can be seen in Figure 44.

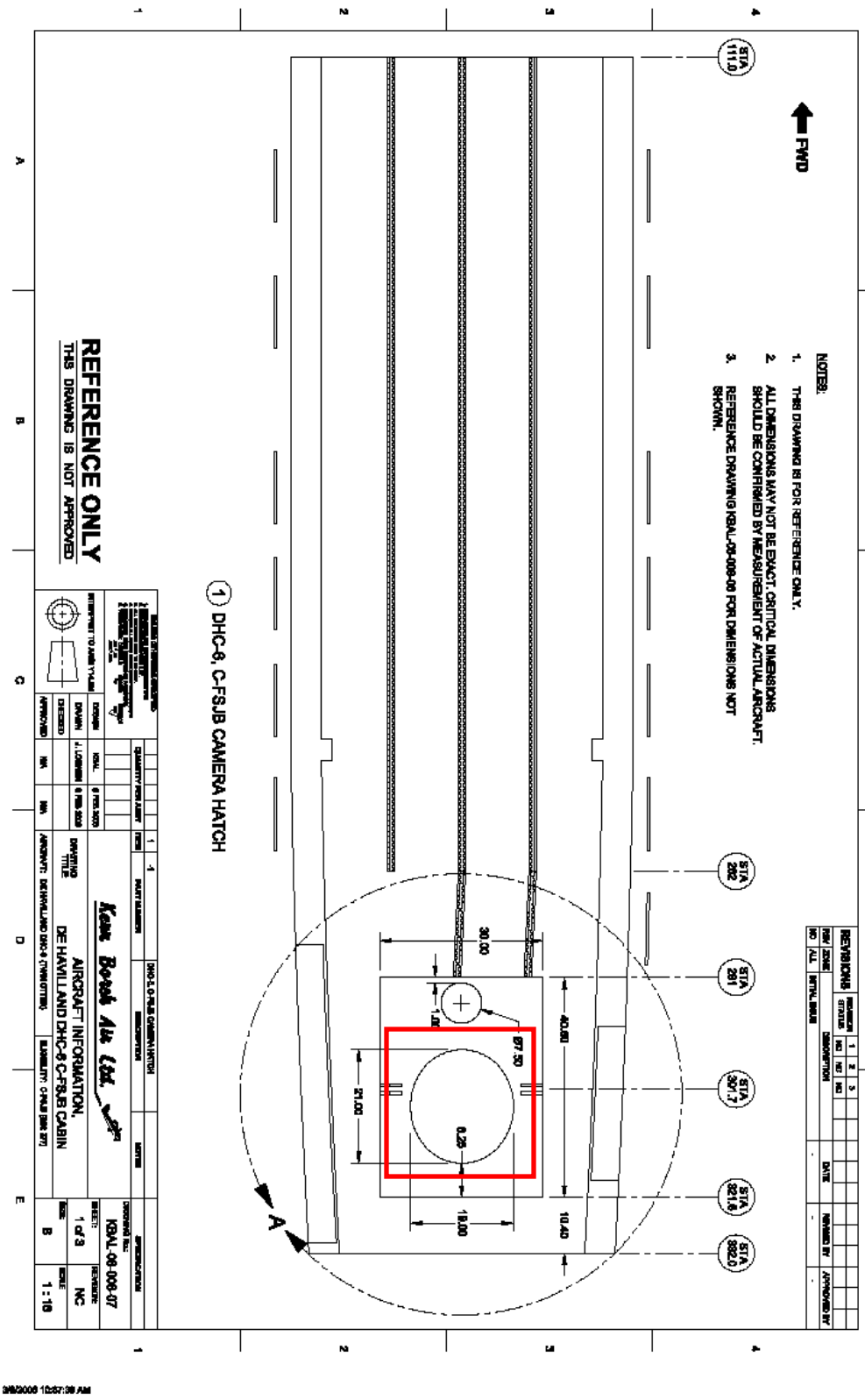

3/6/2009 10:57:39 AM

Figure 41. DHC-6 Twin Otter floor layout. Available nadir port highlighted.

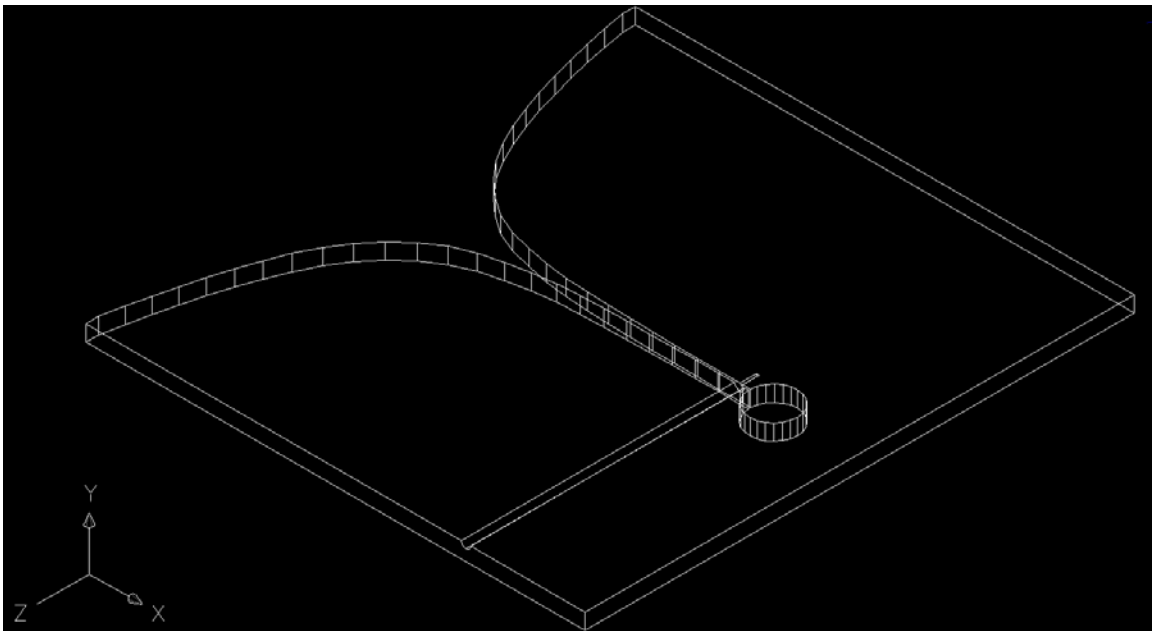

Figure 42. 3-D CAD model for the single element Vivaldi.

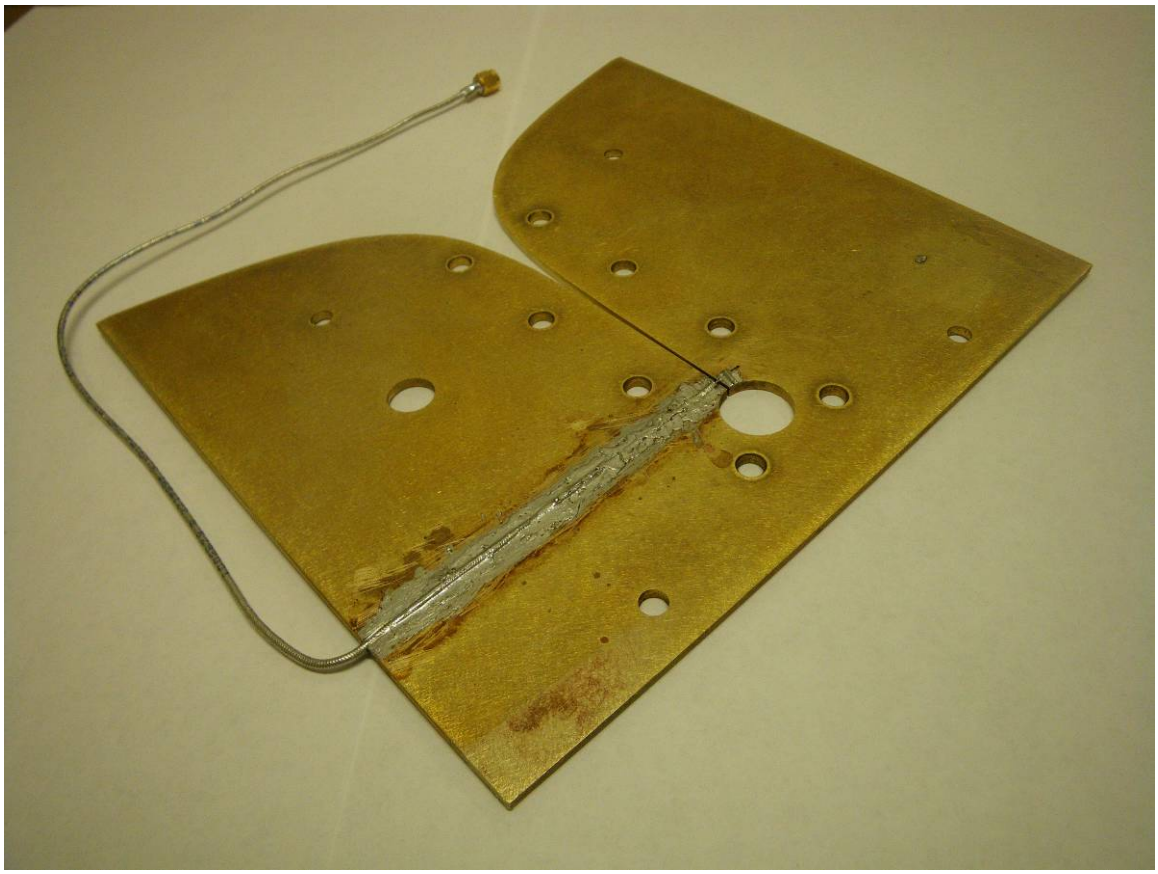

Figure 43. Photograph of the manufactured all-metal Vivaldi (material: brass).

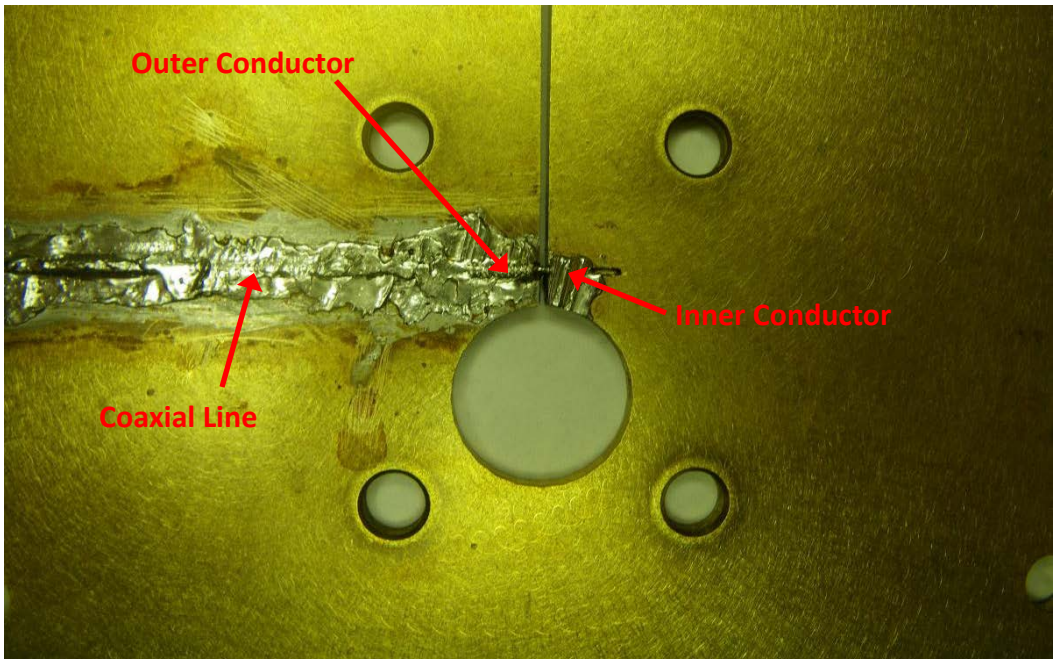

Figure 44. Close-up view of the all-metal Vivaldi feed point.

Figure 45 shows the standard array configurations for the Vivaldi antennas (or any tapered slot antenna). Given the space constraints and to maximize the number of elements, an H-plane array configuration was chosen. It is necessary to space the elements less than a wavelength (λ) at the lowest frequency of interest in order to avoid grating lobes in the array radiation pattern. Ideally an array would be spaced at λ/2 at the lowest frequency of interest for the best balance between main lobe beamwidth and relative sidelobe amplitude. It was also chosen to space the elements at λ/4 at the lowest frequency of interest (600 MHz) in order to maximize the number of elements and therefore maximize array gain.

$$\frac{\lambda}{4} = \frac{3x10^8\ {}^{m}/_{s}}{4 * 600\ MHz} = 12.5\ cm \tag{16}$$

$$\frac{\lambda}{2} = \frac{3x10^8\ {}^{m}/_{s}}{2 * 600\ MHz} = 25\ cm \tag{17}$$

$$D_{{\lambda}/{4}} \approx 2N\frac{d}{\lambda} = 2(4)\frac{{\lambda}/{4}}{\lambda} = 2(dimensionless) = 3\ dB \tag{18}$$

$$D_{\lambda/2} \approx 2N\frac{d}{\lambda} = 2(2)\frac{\lambda/2}{\lambda} = 2(dimensionless) = 3\ dB \tag{19}$$

Equation 16 shows that λ/4 is 12.5 cm; this allows for an array of four elements (N = 4). Using the equation for broadside directivity (D) [3], Equation 18 shows the gain of this array to be 3 dB above that of an isotropic radiating element. However, Equation 19 shows us that this array of four elements spaced at λ/4 has the same broadside directivity as a two-element array (N = 2) spaced at λ/2. Since these elements are driven with a power splitter, it would have been a better solution to use the two-element configuration since a practical (non-ideal) 1-to-2 splitter would likely exhibit less insertion loss, phase unbalance, amplitude unbalance and would likely exhibit better inter-channel isolation compared to the 1-to-4 splitter that was used for this application.

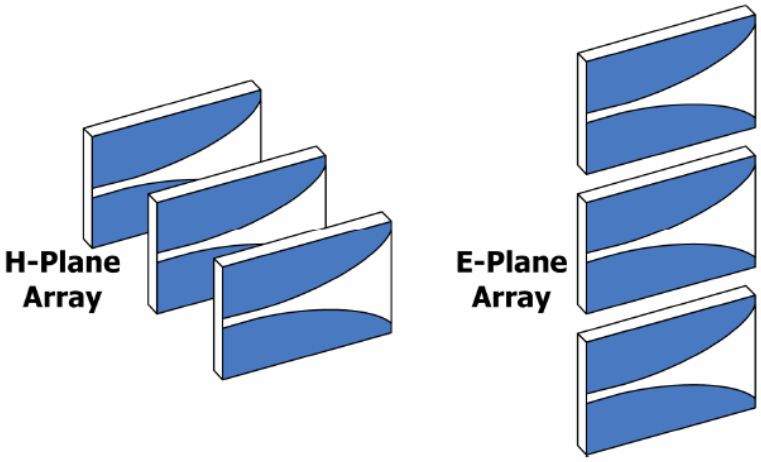

Figure 45. Standard array configurations [28].

In fact, this is the case when considering the Midisco MDC2423 broadband 1-to-4 splitter used and the Midisco MDC2223 broadband 1-to-2 splitter that would have been used for a two-element array. Table 4 shows the relevant parameters. Given the selected element type, space constraints, and directivity analysis, the best solution would have been a three-element array spaced at λ/2. This would have taken up the same space as the four-element, λ/4-spaced array, and the additional element would have provided roughly 1.8 dB more array gain compared

to the two- or four-element options previously discussed. Equation 20 shows the directivity calculation of the three-element array. Specifications on a selected 1-to-3 splitter (MiniCircuits ZA3PD-1) shows that this additional gain would not necessary be lost to non-ideal device characteristics; relevant parameters are included in Table 4 for comparison.

$$D_{\lambda/2} \approx 2N\frac{d}{\lambda} = 2(3)\frac{\lambda/2}{\lambda} = 3(dimensionless) = 4.77\ dB \tag{20}$$

Table 4. Splitter specification comparison. Data collected from the component's data sheet.

Device	Split (Ideal Loss)	Isolation [dB]	Insertion Loss* [dB]	Amplitude Unbalance [dB]	Phase Unbalance [deg]
MDC2223	2 (3 dB)	22	0.2	0.2	2
MDC2423	4 (6 dB)	20	0.4	0.4	4
ZA3PD-1	3 (4.77 dB)	22	0.4	0.4	0.5

* Insertion loss is defined as loss above the ideal splitter characteristic.

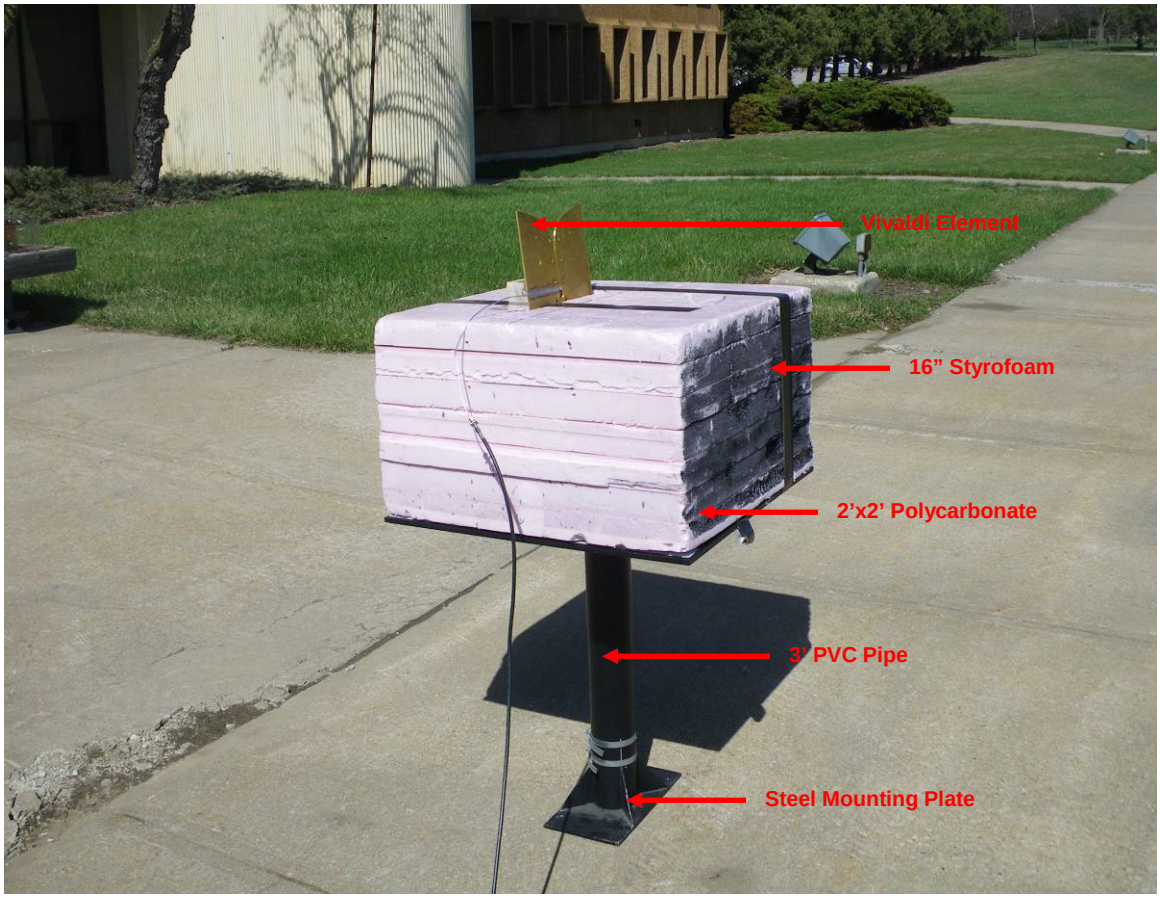

Figure 46. Photograph of Vivaldi element return loss measurement testing rig.

Return loss measurements were performed on both the individual elements and the four-element array. Broadside gain measurements were also performed on the four-element array. Individual elements were tested following manufacture. The test rig shown Figure 46 used was similar to the rig used to test other planar antennas developed in house (e.g. [28]). This rig consists of a steel mounting plate, 3' of PVC, a 2' x 2' sheet of polycarbonate, and 16" of Styrofoam. Return loss measurements were performed outdoors to reduce the possibility of multi-path effects.

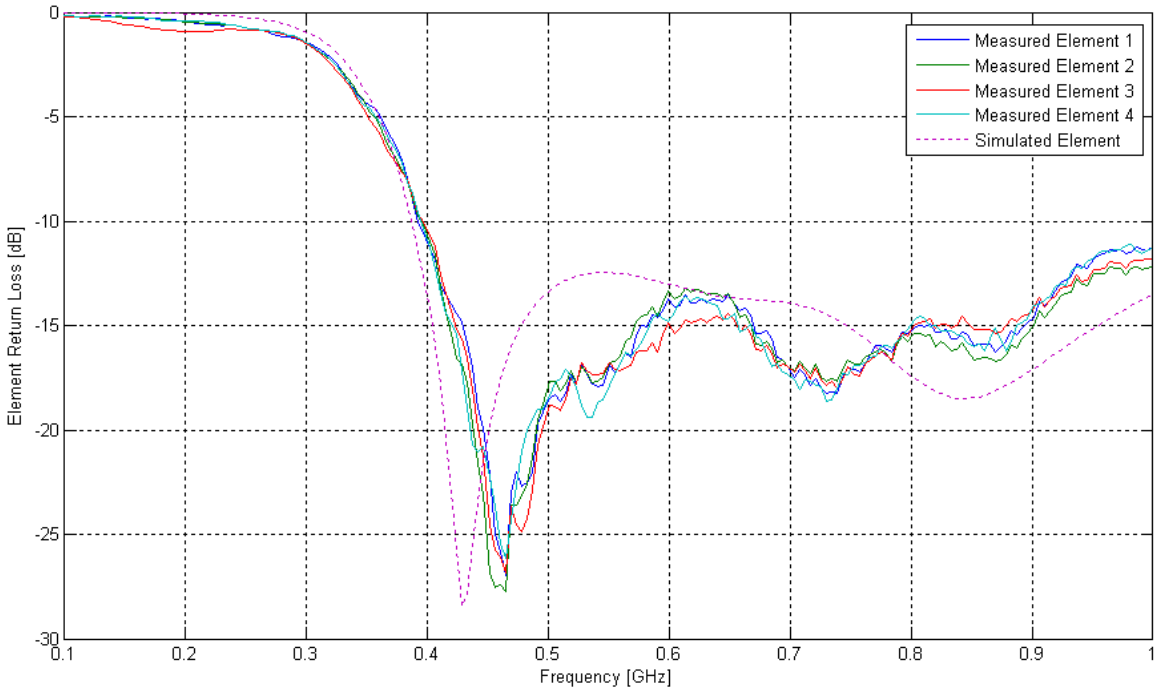

Figure 47. Return loss measurements for individual Vivaldi elements and simulation results.

Figure 47 shows the return loss measurement results for an individual element. The individual elements exhibited excellent return loss characteristics from roughly 430 MHz up to the top of the measurement range (1 GHz). These measurements were compared with simulation results obtained via Ansoft HFSS. Details about the simulation setup can be found in the Appendix. Figure 47 shows reasonable correlation between the simulated antenna and the measured antennas. The difference in position of the resonance seen at roughly 420 MHz in the

simulation and at roughly 470 MHz in the measured results is likely due to manufacturing precision, specifically at the mouth of the element. Overall the manufactured element performed better than the simulation across most of the frequencies of interest.

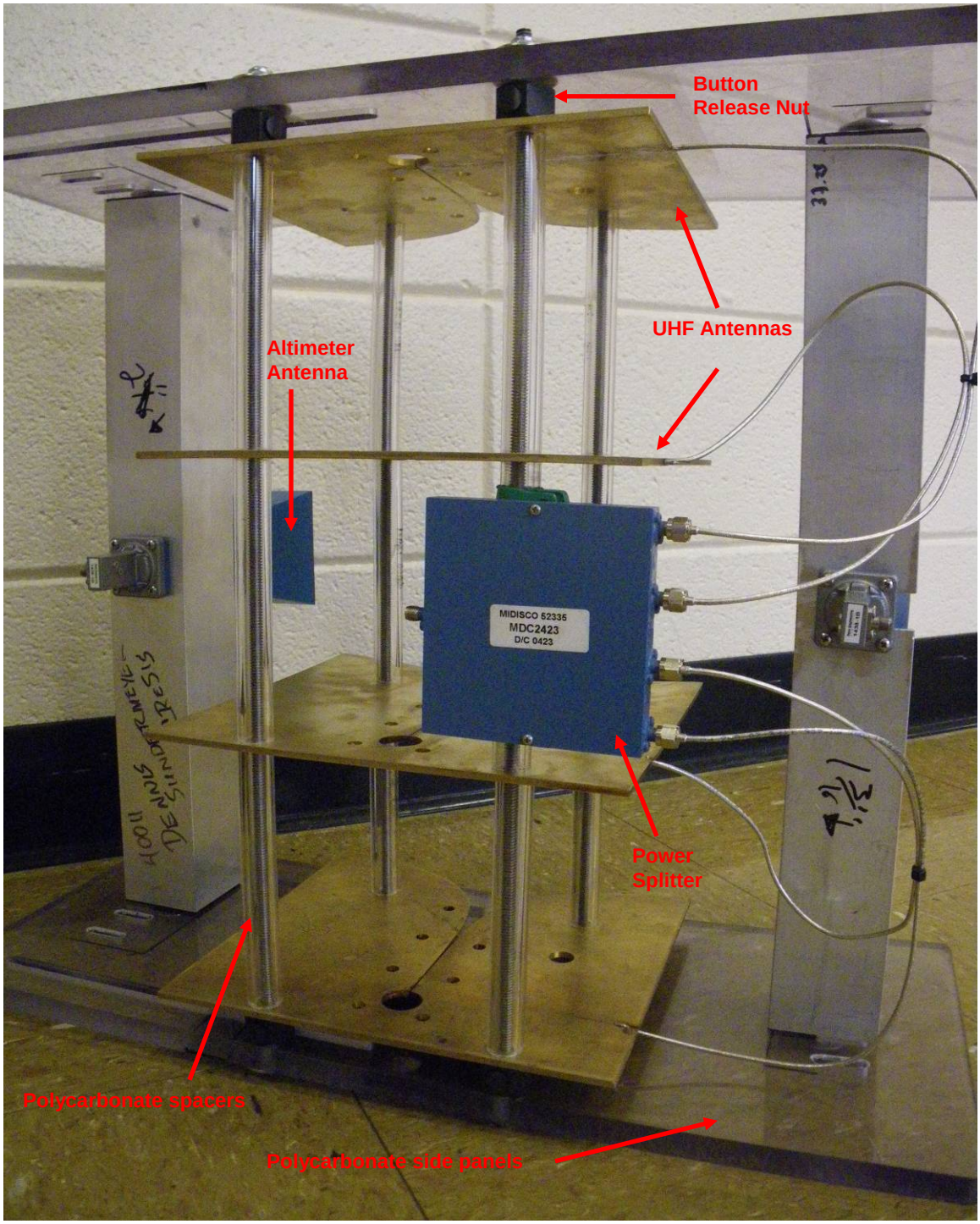

Figure 48. Photograph of the assembled Vivaldi array used on the 2009-2010 Twin Otter Antarctic survey mission.

After the acceptable operation of the individual elements was confirmed, they were combined into the array configuration discussed above: four-element H-plane array spaced at 12.5 cm. Figure 48 shows the assembled array. The blue horn antennas included in this assembly are the transmit and the receive antennas for the Ku-band altimeter, which was operated simultaneously during the 2009-2010 CReSIS Antarctic survey. The blue component attached to the support structure is the Midisco MDC2423 1-to-4 splitter discussed above.

The array was assembled using threaded steel rods, rigid polycarbonate tubing spacers, and button release nuts. Polycarbonate panels were added to the side in order to accommodate the addition of the Ku-band altimeter antenna as well as provide a solid structure for mounting inside the aircraft. Details regarding installation-specific hardware attached to the array assembly are discussed in the Chapter 5.

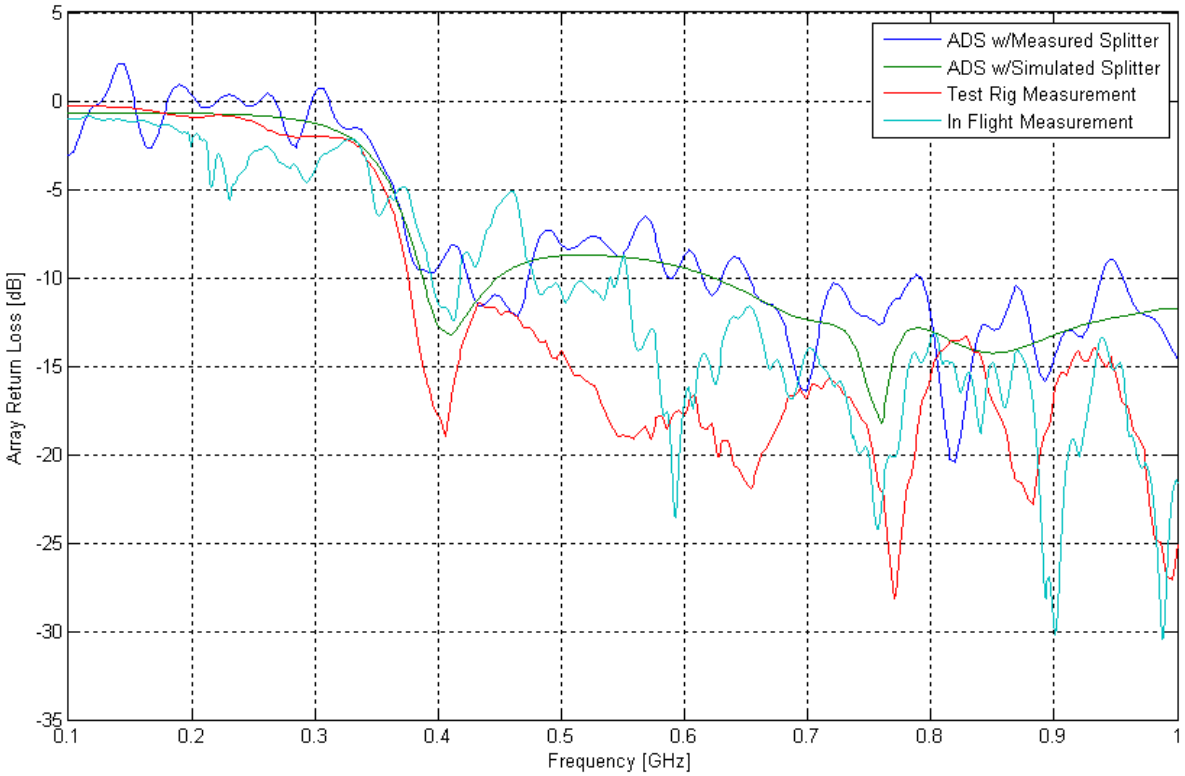

Figure 49. Vivaldi array return loss comparisons.

The Vivaldi array was measured both on the test rig and during flight in the Twin Otter while over thick ice in Antarctica. Both of these measurements were compared to ADS simulations. Figure 49 shows these measurements.

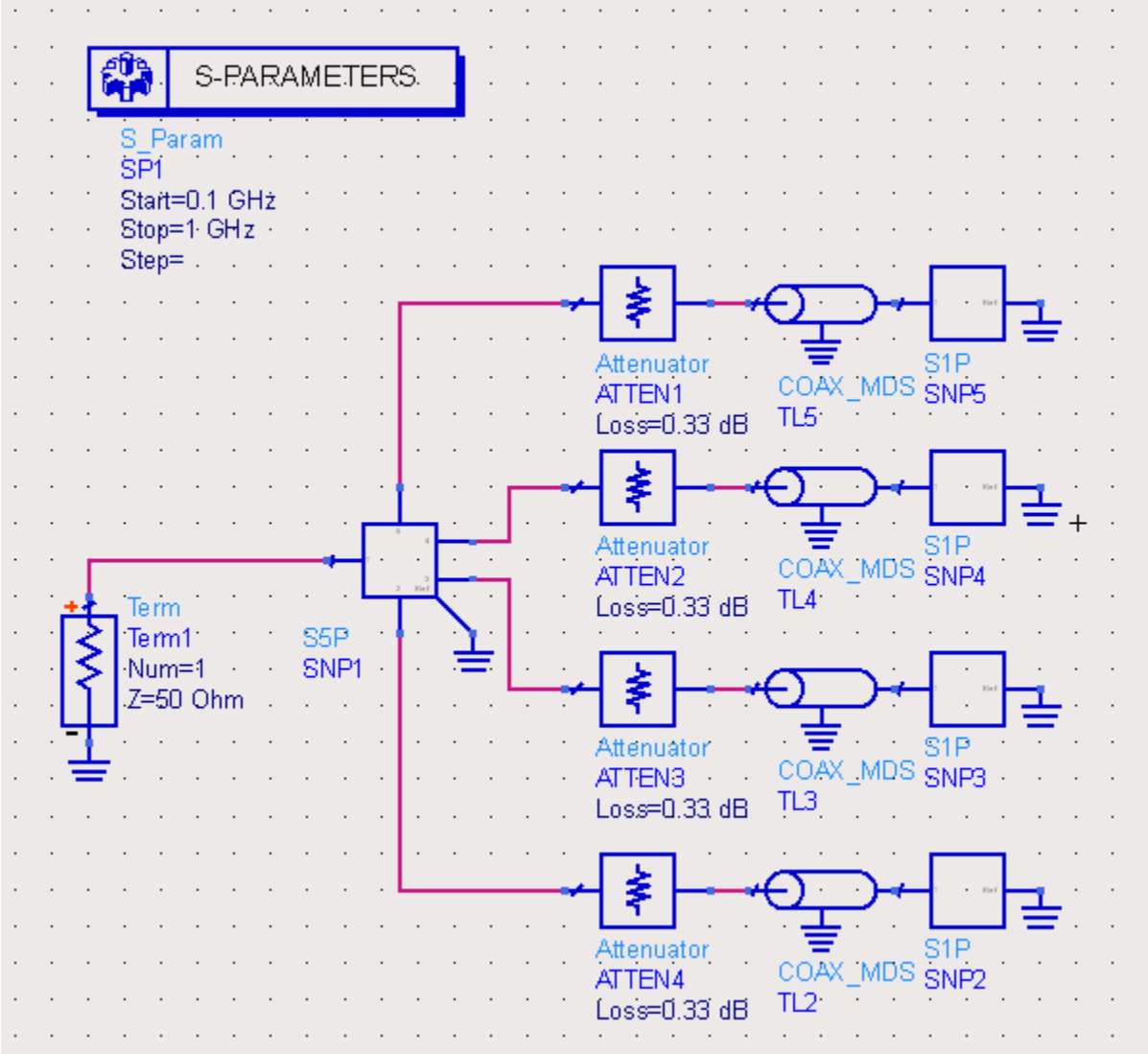

Figure 50. ADS Vivaldi array simulation setup with real splitter.

ADS simulations were performed by combining the s-parameters obtained through HFSS simulations with simulated cables and both simulated and measured s-parameters of the splitter. Figure 50 and Figure 51 show the ADS simulation setups using the measured splitter and simulated splitter, respectively. The splitter simulation was the only difference between the presented ADS simulations. It was chosen to perform separate simulations to judge the effect of

the non-ideal nature of the splitter on the return loss of the antenna, compared to the operation of the array fed using an ideal splitter. A network analyzer was used to characterize the 4:1 splitter. Figure 49 shows that the real splitter adds a ±3 dB ripple to the ideal response across most of the frequency range of interest.

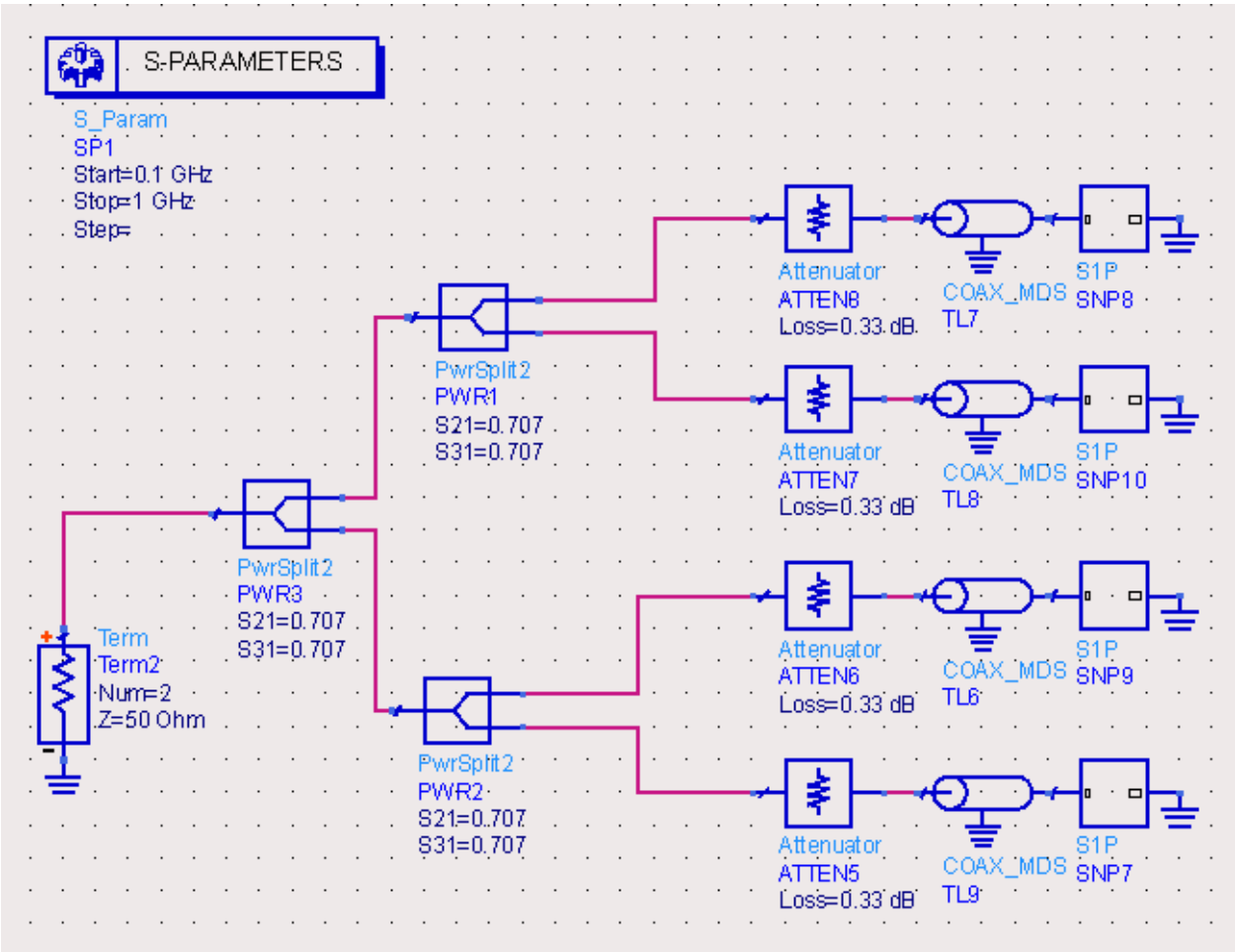

Figure 51. ADS Vivaldi array simulation setup with simulated splitter.

Both simulations used ideal coaxial lines between the splitter and the antenna ports to simulate the delay introduced by the real 18" long cables. Attenuators were added to simulate the loss of the cables. The antennas were simulated using HFSS; details on this simulation setup can be found in the Appendix. The four-element HFSS simulation produced four S11 measurements that were used to supply the ADS simulation. Both simulation results produced an acceptable performance (-10 dB return loss or better) within the frequency range of interest.

Figure 49 shows that the actual antenna array performance, both on the test rig and aboard the aircraft, performed better than simulation. This is likely due to geometry estimations made in the HFSS simulations. Performance differences between the test rig and the airborne array, mainly resonance shifts, may be attributed to the presence of the Kydex radome and the proximity of the antenna array to the metal edges of the nadir port opening of the aircraft. In the end, these differences arise because the simulations do not include the entire antenna and aircraft structure.

Chapter 4: Lab Testing and Results

While laboratory measurements have been presented in proceeding sections, it is useful to provide a succinct summarization of these key measurements and a comparison to the specification ideal outlined in 3.1.

4.1 Transmitter Measurements

The DDS is responsible for producing five signals: the RF chirps, the LO tones, two copies of the T/R switch control signal, and one copy of the receiver isolation switch control signal. The switch control signals were presented in Figure 28 and will not be discussed any further in this section. Measurements of the AC outputs of the DDS were captured using a spectrum analyzer.

Figure 52 shows the output of the DDS RF port as measured with a spectrum analyzer (Agilent E4407B); the ideal -17 dBm output specification window is included. The nearly ±4 dB deviation from the specification; this is due to the chosen predistortion. The waveform is predistorted in order to achieve as level an output as is possible at the antenna port; additional components exist between the output of the DDS and the antenna port.

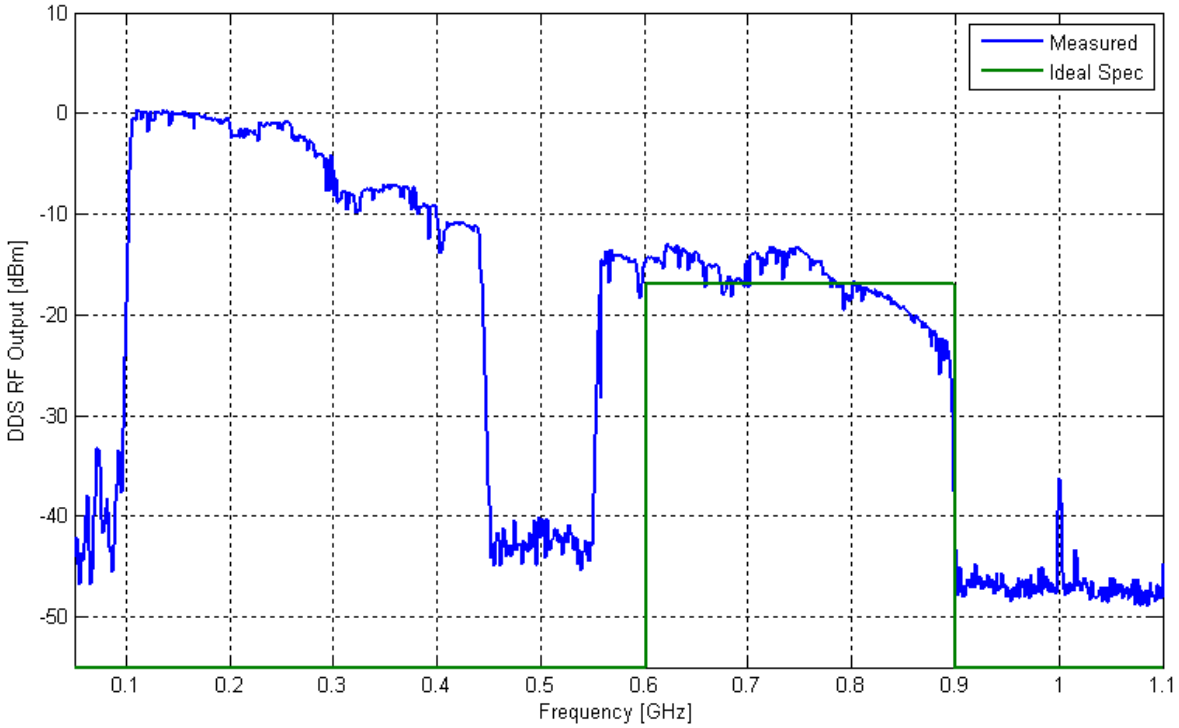

Figure 52. Measured DDS RF output with ideal spec for reference.

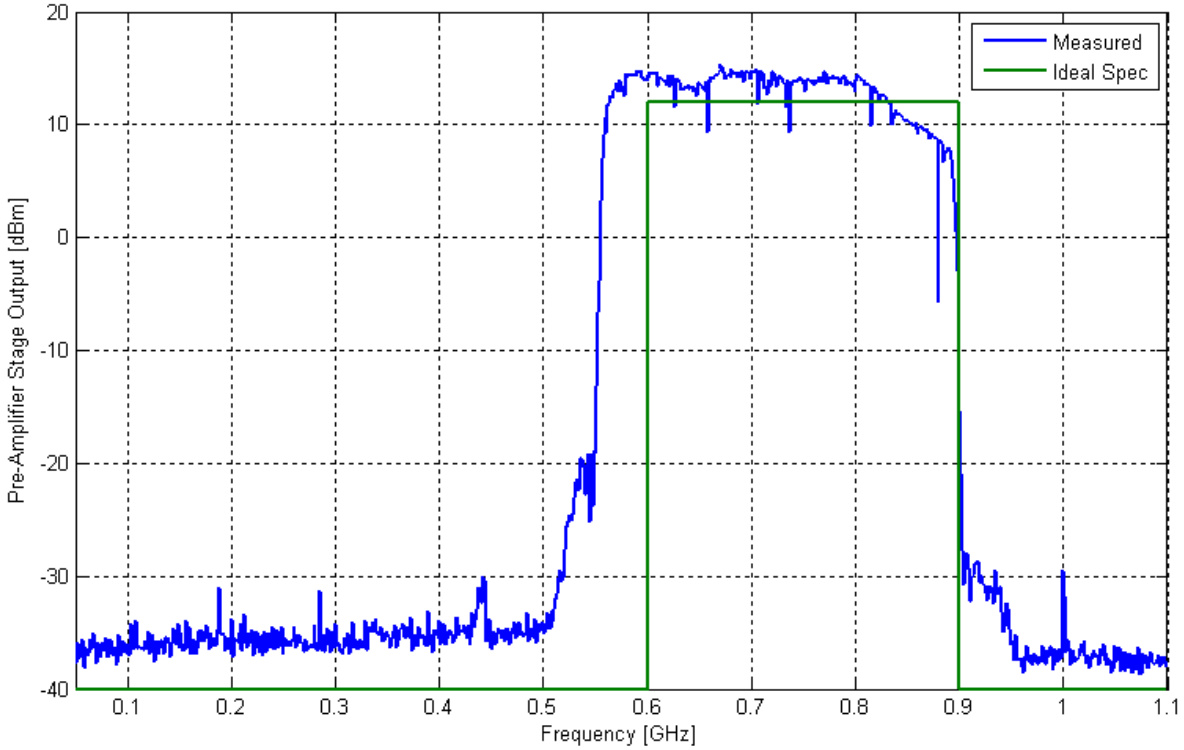

Figure 53. Measured driver amplifier stage output with ideal spec for reference.

As discussed in 3.3.2.1, the expected output of the driver amplifier section is +12 dBm. Figure 53 shows the output of the driver amplifier stage as measured with the spectrum analyzer. As with the DDS output, the ±4 dB of variation is caused by the predistortion; the distortion at this stage is less than at the input to the driver amplifier stage. Dramatic deviations, as seen at 890 MHz, are caused by inaccuracies in the spectrum analyzer measurement due to the chosen sweep rate.

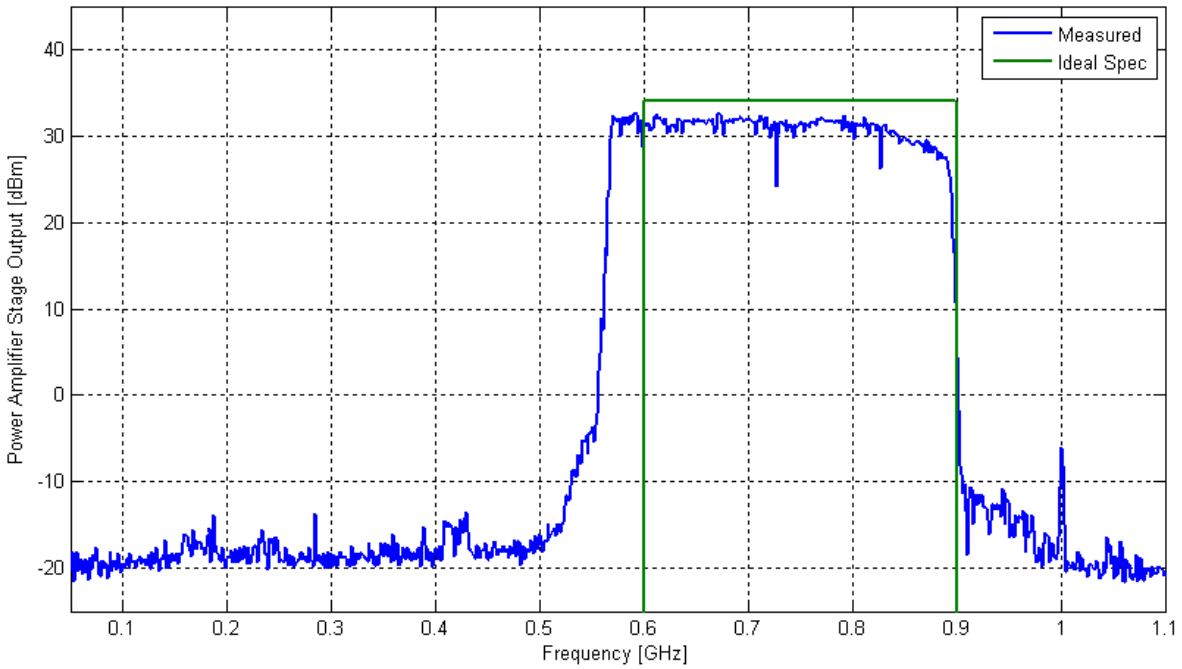

Figure 54. Measured power amplifier stage output with ideal spec for reference.

Figure 54 shows the output of the power-amplifier stage at the antenna port as measured with the spectrum analyzer. This response includes the T/R switch. This output is about 2 dB lower than the ideal specification (34 dBm); this may be due to a lower than expected gain from the power amplifier or higher than expected loss from the isolator.

Amplitude modulation (AM) within the transmit waveform (or within the LO signal used to mix the received signal to baseband) results in the presence of sidelobes in the demodulated return signal [29] [30]. This is essentially what happens when performing ground penetrating

radar (GPR) measurements. Sidelobes created by the presence of amplitude modulation in the transmit signal are unwanted and may mask weak signals or may falsely be interpreted as layers. To assess the tolerability of amplitude modulation, the following equation can be used to determine the sidelobe level with respect to the carrier power level as a function of the amplitude ripple [30]:

$$sidelobe = 20log\left(10^{x/20} - 1\right) \tag{21}$$

where x is the amplitude ripple of the transmit waveform. Figure 55 is a graphical representation of the above equation.

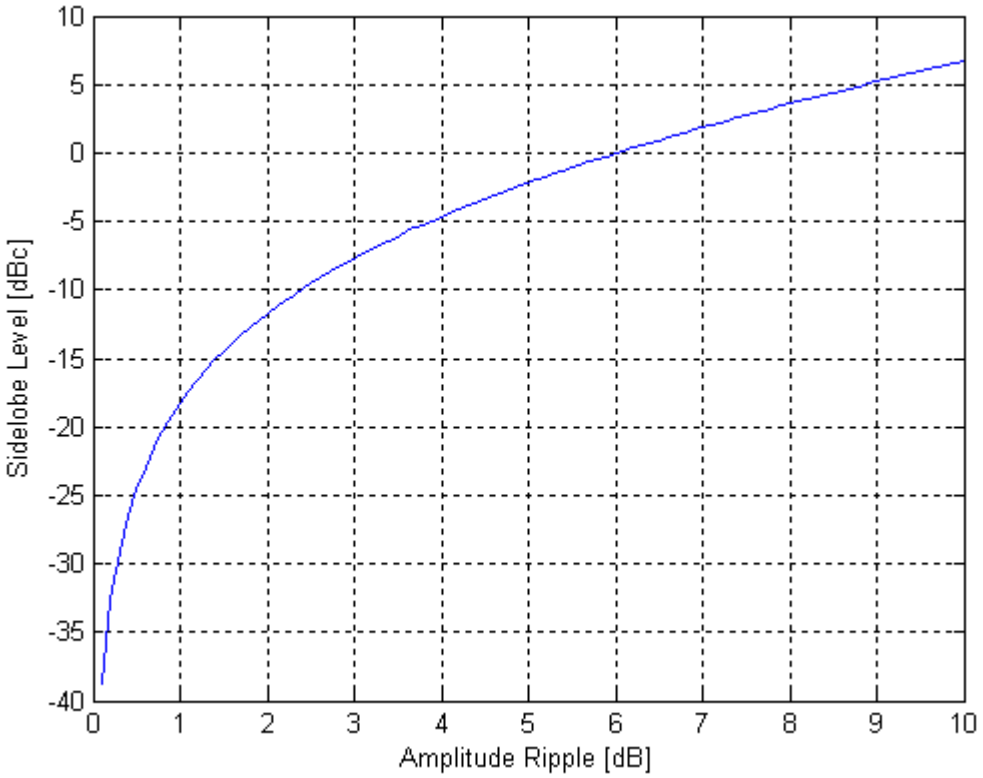

Figure 55. Sidelobe level as a function of amplitude ripple.

Figure 55 shows that for a 2-dB ripple, we would expect sidelobes at roughly -12 dBc; this could pose a problem for layers close to the strong surface return. Since a chirp is defined by its change in frequency over time, the amplitude ripple that exists in the frequency domain is proportional to the envelope ripple in the time domain. The frequency of this envelope ripple in

the time domain determines the spacing of the sidelobes, with respect to the main lobe, in the IF signal; a higher frequency ripple translates to a wider sidelobe spacing.

Currently, a single value is used to define the amplitude level of each sub-chirp; the amplitude may still vary significantly across the 50 MHz bandwidth of each chirp. Precise amplitude leveling, requiring the use of multiple values per chirp, will be necessary to prevent these sidelobes from masking layers; this will be a focus of future revisions.

4.2 Receiver Measurements

Receiver measurements were performed using an optical delay line to simulate a specular target and propagation through 500 m of air and 200 m of ice. Details on the loop-back experimental setup can be found in Appendix C.

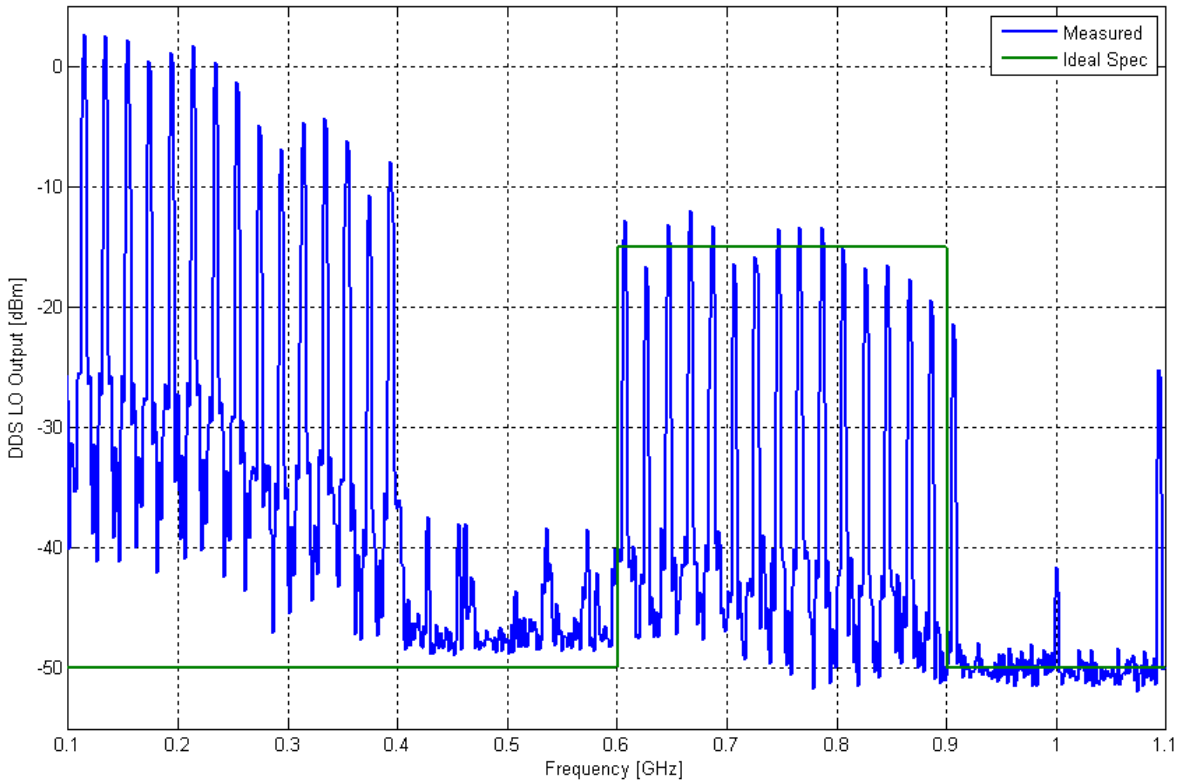

Figure 56. Measured DDS LO output signal with ideal spec for reference.

Figure 56 shows the local oscillator (LO) output from the DDS as measured with the spectrum analyzer. Accounting for gains and losses in the LO driver stage of the receiver, the ideal specification is -15 dBm to achieve +13 dBm at the LO input to the mixer. As with the transmitter, considering the non-ideal response of components as a function of frequency, a tolerance of ±3 dB around the ideal spec is considered acceptable. It is important that the amplitude across the tones be constant at the LO input to the mixer. Figure 56 shows that the tones above 840 MHz fall outside of the acceptable specification. The input power to the LO port of the mixer can be as low as +7dBm and still operate normally; however, the conversion loss, isolation, and input VSWR are inferior in comparison to the device performance at higher power levels [23].

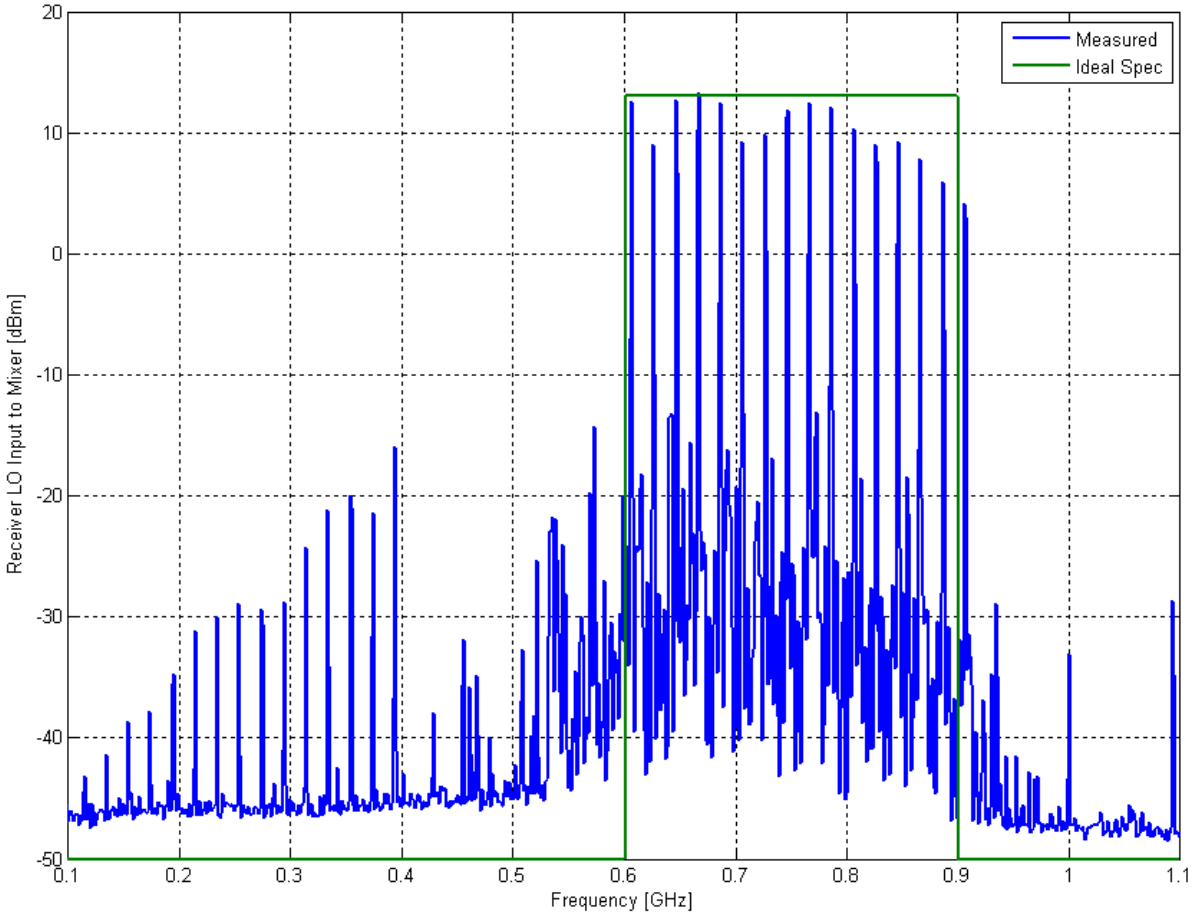

Figure 57. Measured LO input signal to mixer with ideal spec for reference.

Figure 57 shows the measured spectrum of the LO input to the receiver mixer. As discussed above, the ideal specification is +13 dBm for optimal mixer operation. The single LO driver stage bandpass filter was able to reduce the baseband signals by nearly 30 dB. The two closest tones occurring at the same time are the 606 MHz and 394 MHz tones. Since these tones are separated by more than the IF bandwidth (50 MHz) we do not need to worry about first order mixing products from the baseband leakage (394 MHz) mixing with the received signal aliasing on top of the IF signal of interest. Future designs would call for improved filters or multiple filters to further reduce the power level of these baseband signals to prevent unwanted mixer products.

Just as was done with the transmit chirps, the LO tones should be amplitude leveled to reduce the presence of sidelobes in the demodulated received signal. Unfortunately, the current software does not allow for the LO tones to be leveled separately from the RF chirps; this is apparent in Figure 57. It can also be seen that the power level input to the mixer is less than ideal, especially for frequencies above 840 MHz. Waveform leveling in processing currently seeks to minimize the sidelobes produced by the amplitude modulation. Future designs will seek to provide an amplitude-leveled set of tones to the mixer.

As discussed before, the receiver mixer is used to move the frequencies of interest to baseband for digitization instead of performing hardware pulse compression. Figure 58 shows the measured output spectrum of the IF stage just before entering the DAQ. Ideally, this is expected to be a 50-MHz band-limited signal between 5 and 55 MHz. With the 34 dBm output, about 118 dB of loss within the loop-back components, and about 63 dB of gain in the receiver chain, the expected IF output should be about -21 dBm. Initially, this response had pairs of spikes centered at 20 MHz, 40 MHz, and 60 MHz, spaced 4 MHz apart (2 MHz on either side of

the center frequency). Further investigation found that these oscillations (spectral components) could be attributed to the T/R switch; removal of the T/R switch from the loop resulted in no visible oscillations. Each switch within the T/R switch assembly was tested individually; oscillations were not observed. It was suspected that port mismatches between the two switches were responsible; a 3-dB attenuator was placed between the switches (Figure 13). The addition of this attenuator appeared to eliminate these oscillations. It is still possible that very low-level or out-of-band oscillations exist. As discussed in the T/R switch design section, the reflective nature of these switch, combine with imprecise control signal timing are likely for the development of these oscillations.

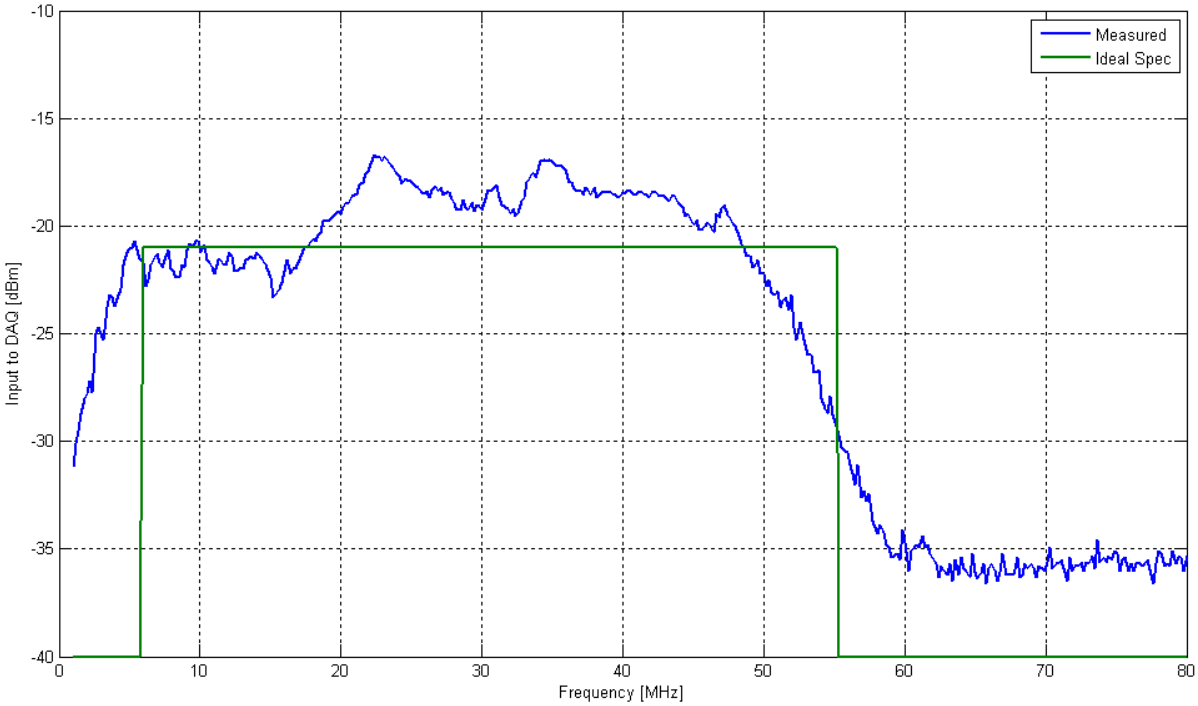

Figure 58. Measured DAQ input with ideal spec for reference.

Figure 59 shows the measured spectrum of the received signal after pulse compression in software. The delay within the radar and delay line would translate to an expected return near roughly 842 m. Software-controlled delays within the ADC introduce an offset to this delay of roughly 237 m; this would result in an expected return near roughly 605 m. This return is found

at 617 m, acceptably close to the calculated distance. Details about the above delays and offsets can be found in Appendix C.

Figure 60 shows a zoomed in view of the return signal showing the first sidelobe level to be roughly -16 dBc. It was shown that roughly -12 dBc would be expected. This 4-dB improvement is likely due to an attempt at amplitude-leveling during signal processing.

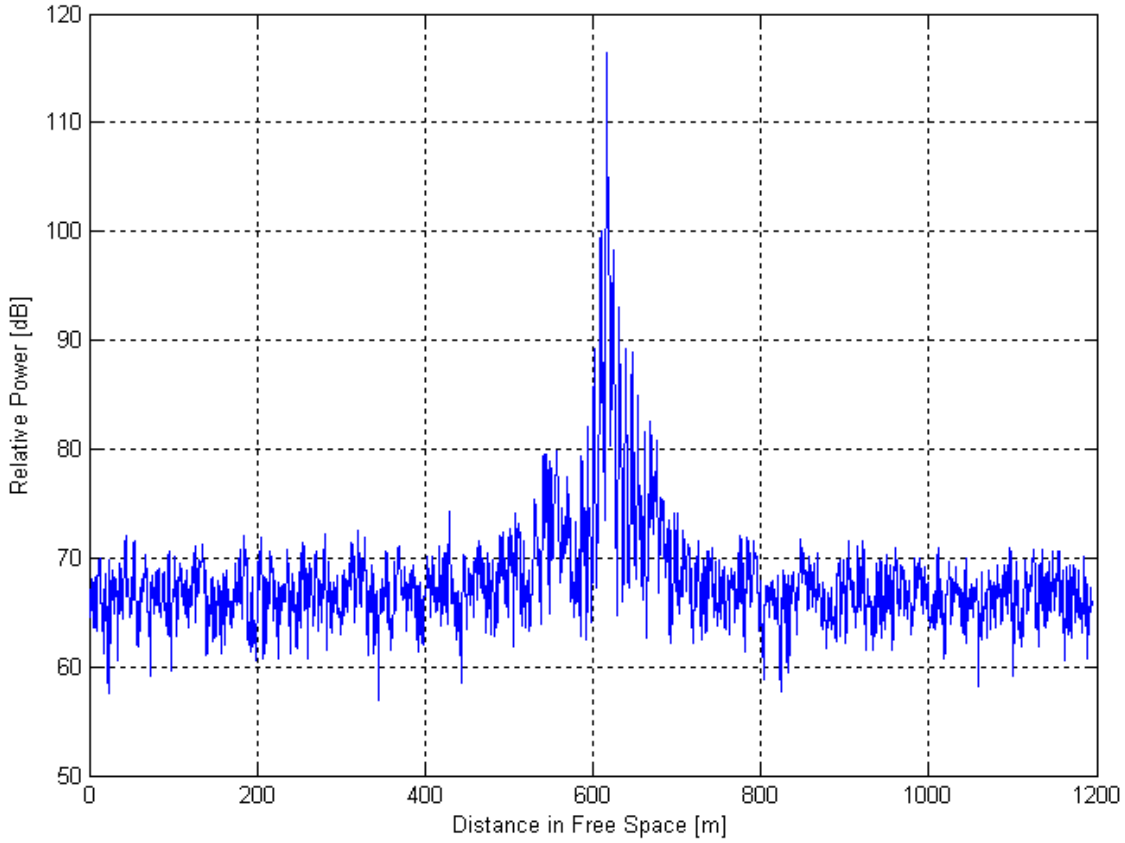

Figure 59. Delay line received signal.

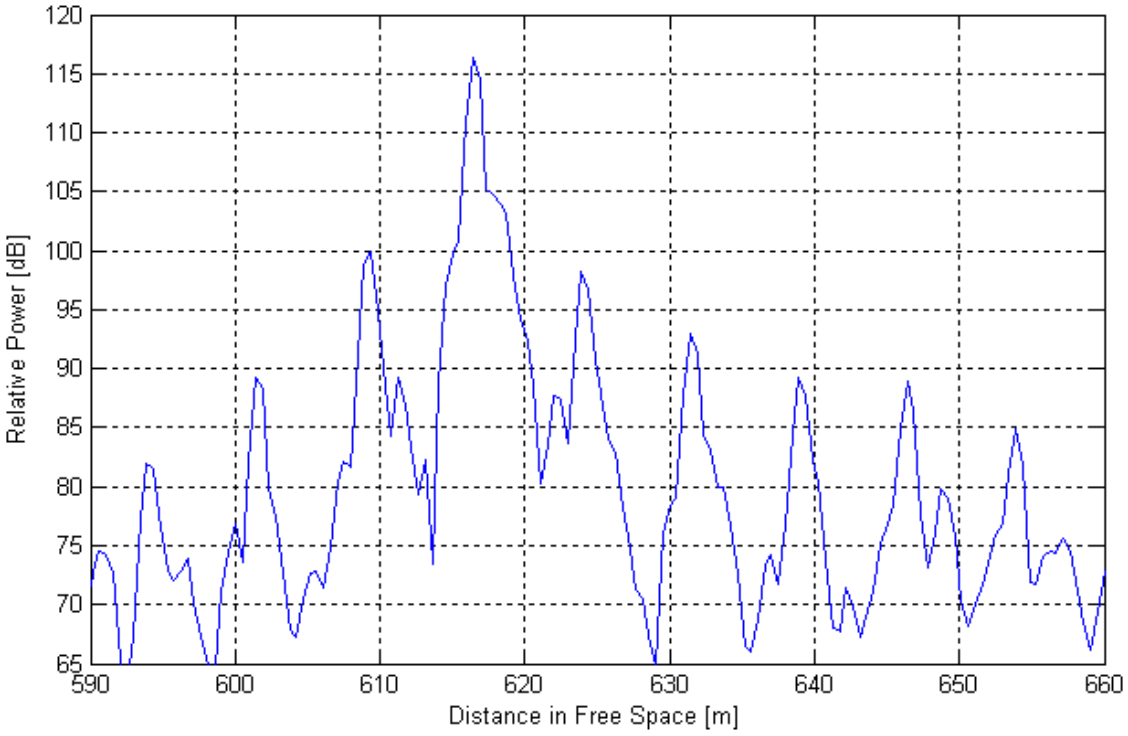

Figure 60. Delay line received signal, zoomed in.

Chapter 5: Installation and Test Flights

As discussed previously, a DHC-6 Twin Otter was the chosen aerial platform for both the spring and winter 2009 field campaigns (Figure 61). The National Science Foundation (NSF) contracted on behalf of CReSIS to obtain flight time and crew time to perform our surveys with Kenn Borek Air Limited, based in Calgary, AB. Additionally, the current system was installed, tested, and operated on the NASA P-3 Orion as a part of the spring 2010 Operation Ice Bridge (OIB) campaign.

The scope of this discussion will be limited to the installation and testing of the current radar system on a Borek Twin-Otter for the winter 2009-2010 CReSIS Antarctica Survey, as well as the installation and testing of the current radar system on the NASA P-3 for the spring 2010 OIB Survey. Only the antenna changed between these two missions. The elliptical dipole

array used for the NASA OIB mission is considered beyond the scope of this thesis, but details are included in the appendix for completeness.

Figure 61. Photograph of the Kenn Borek DHC-6 Twin Otter on Pegasus Field apron near McMurdo, Antarctica.

5.1 Winter 2009-2010 Survey

For this mission, installation and testing was performed twice: once in Calgary as the Kenn Borek facility, and once in McMurdo, Antarctica. The first installation and test in Calgary was necessary to evaluate the fit and performance of the radar system before shipping it to Antarctica, as resources to perform modifications or repairs in Antarctica can be difficult and expensive when considering the harsh climate and remote location. Since the space inside the aircraft is needed to accommodate fuel for the transit from Calgary to Antarctica, the radar

equipment was removed and reinstalled once the airplane reached McMurdo. Test flights were performed following installation in Calgary, as well as following reinstallation in McMurdo.

Figure 62. Photograph of the installed empty equipment racks inside the Twin Otter aircraft. Nearest rack houses the accumulation radar and KU-band altimeter.

Specialized aircraft equipment racks were employed to mount the radar hardware inside the Twin Otter. These racks were bolted to the starboard floor grounding rails as well as the starboard wall for stability. Horizontal rails were added to these racks to support the weight of the equipment and the front plates of the radar chasses were bolted to the front of the racks for a secure installation. Figure 62 shows the installed empty racks. Figure 63 shows the installed radar equipment. The accumulation radar only needs nine standard rack units (9U) worth of space; the relevant radar equipment is highlighted in Figure 63.

A/C power is supplied to each radar component using a Tripplite 1200 VA uninterrupted power supply (UPS). A/C power is provided to the UPS using a voltage inverter connected to the airplane 28 VDC supply via a switch/breaker box. This switch/breaker box is used to protect

the inverter and UPS from high-voltage transients that occur on the +28 VDC supply bus during the aircraft power-up procedure. Figure 64 shows a block diagram of the power connections to the aircraft 28 VDC bus.

Figure 63. Photograph of the installed accumulation radar (highlighted).

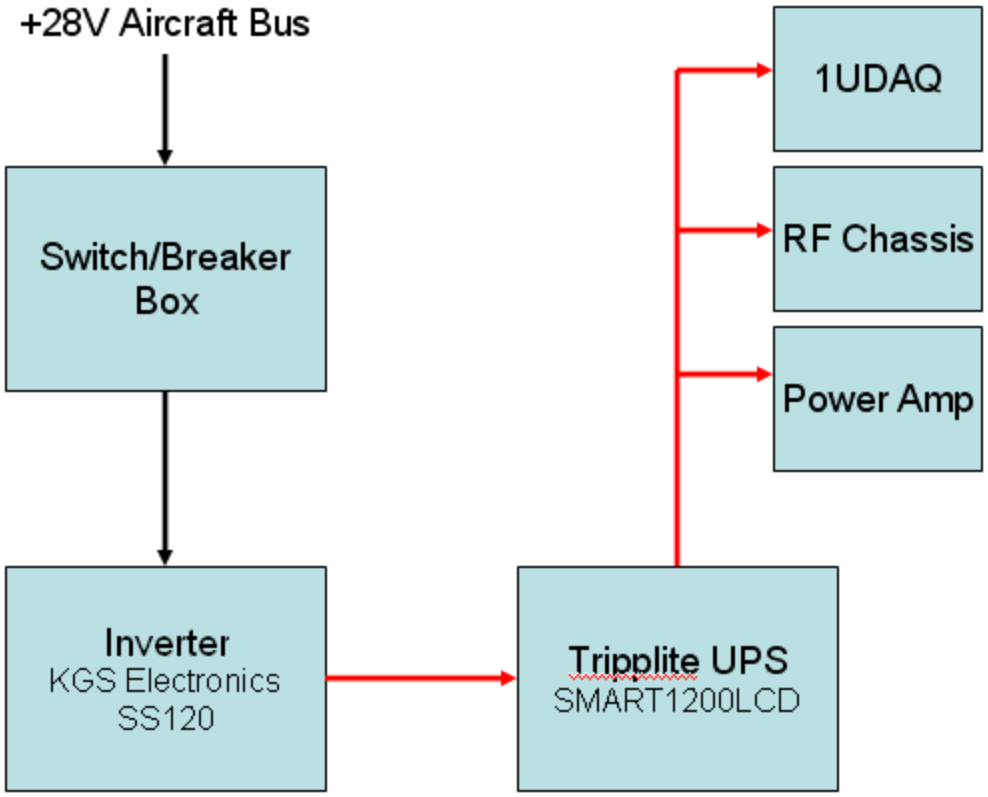

Figure 64. Rack wiring block diagram. (Black arrow: +28VDC, Red arrow: 115VAC, 60Hz)

As discussed earlier, the antenna array was installed in the nadir port, roughly six feet aft of the radar rack (Figure 41). Figure 65 shows the installed array.

There are only a few suitable mounting points in the nadir port. It was decided to mount the array using aluminum "wings" bolted to the polycarbonate side panels of the array structure (Figure 48). The "wings" were slid into the available floor joist slots and bolted into place. The aft end of the array structure (specifically, the polycarbonate side panels) was allowed to rest on the floor of the bay. Visual inspection during and after the test flight in Calgary showed that this installation method proved sturdy enough for field operations, as vibrations were minimal. A single 10-foot coaxial cable (LMR-240, with an expected loss of 8 dB/100 ft at 1 GHz) was used to connect the splitter of the array to the antenna port on the radar chassis. This cable was passed through a notch in the corner of the wooden floor panel. As Vivaldi antennas exhibit minimal

back radiation, a rear metallic ground plane ("rear" would be above the array seen in Figure 65) was not employed. The array edges are in close proximity to the metal edges of the nadir port opening.

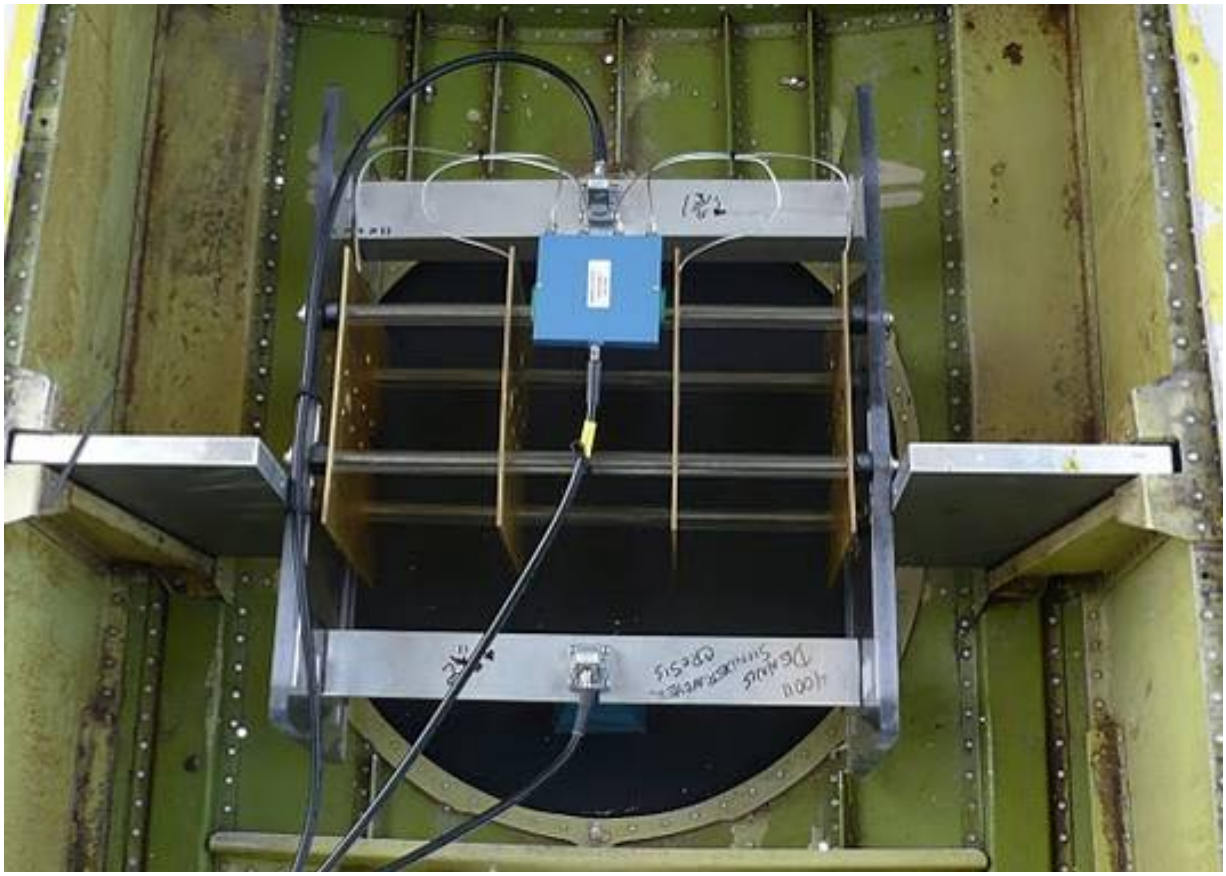

Figure 65. Installed antenna array.

During installation, it was found that the proximity of the array to the edges of the opening did not significantly affect the return loss of the array. It is unknown how the antenna position affected the field properties of the antenna (i.e. along-track and cross-track beamwidths, relative sidelobe levels, grating lobe distribution, etc.). In an attempt to minimize these effects, the array was placed as close to the center of the opening as possible. The addition of electromagnetic absorbing foam (Eccosorb AN) placed between the antenna and the metal edge of the opening was not found to have a discernible effect on the array return loss; therefore, it was not employed for this mission.

The nadir port was not covered during the test flights because a proper radome material had not been purchased yet. Following the tests flights, a number of radome materials were tested. It was found that 0.060" thick Kydex 100 had a minimal effect on the antenna's return loss and was strong enough to resist significant "oil-canning." A sheet of this material was cut to match the size of the nadir port opening and attached during installation in Antarctica.

Bench loop-back tests were performed prior to installation and performed again following installation in the plane. Details regarding the setup and operation of loop-back testing can be found in Appendix C.

Two test flights were flown over lakes near Calgary at a nominal altitude of 1500 ft. The first test flight revealed a damaged T/R switch; therefore, no viable data were collected. The damaged T/R switch was replaced with an operational backup. An additional 20-dB attenuator was used between the output of the power amplifier and the T/R switch to prevent any damage until additional testing could be performed on the T/R switch in the laboratory. It was later found that a dual T/R switch configuration was necessary; this final design proved successful upon use during the Antarctic mission.

The second test flight proved successful; specular returns from the lake surface were observed with an SNR of 60 dB at 1500 ft above the lake. A sample of the collected data can be seen in Figure 66. Two prominent, horizontally-consistent returns can be seen in the echogram. The first return, seen at zero depth, corresponds to the lake surface. The second return, seen at 450 m corresponds to a multiple reflection of the surface caused by the transmitted signal reflecting off of the lake surface, then reflecting off of the bottom of the airplane, then reflecting off of the lake surface a second time before being received. Range hyperbolae are also visible; these are likely caused by relatively electromagnetically bright objects on the lake surface (i.e.

boats), the shoreline, objects on the shoreline (i.e. trees), or the steep hillsides near the shoreline. Additionally, weaker horizontally-consistent returns are also visible in the echogram at depths 25 m, 50 m, 100 m, 130 m, 150 m, and 175 m. These are either side lobes of the surface return caused by saturation of the RF receiver chain or returns caused by multi-path effects.

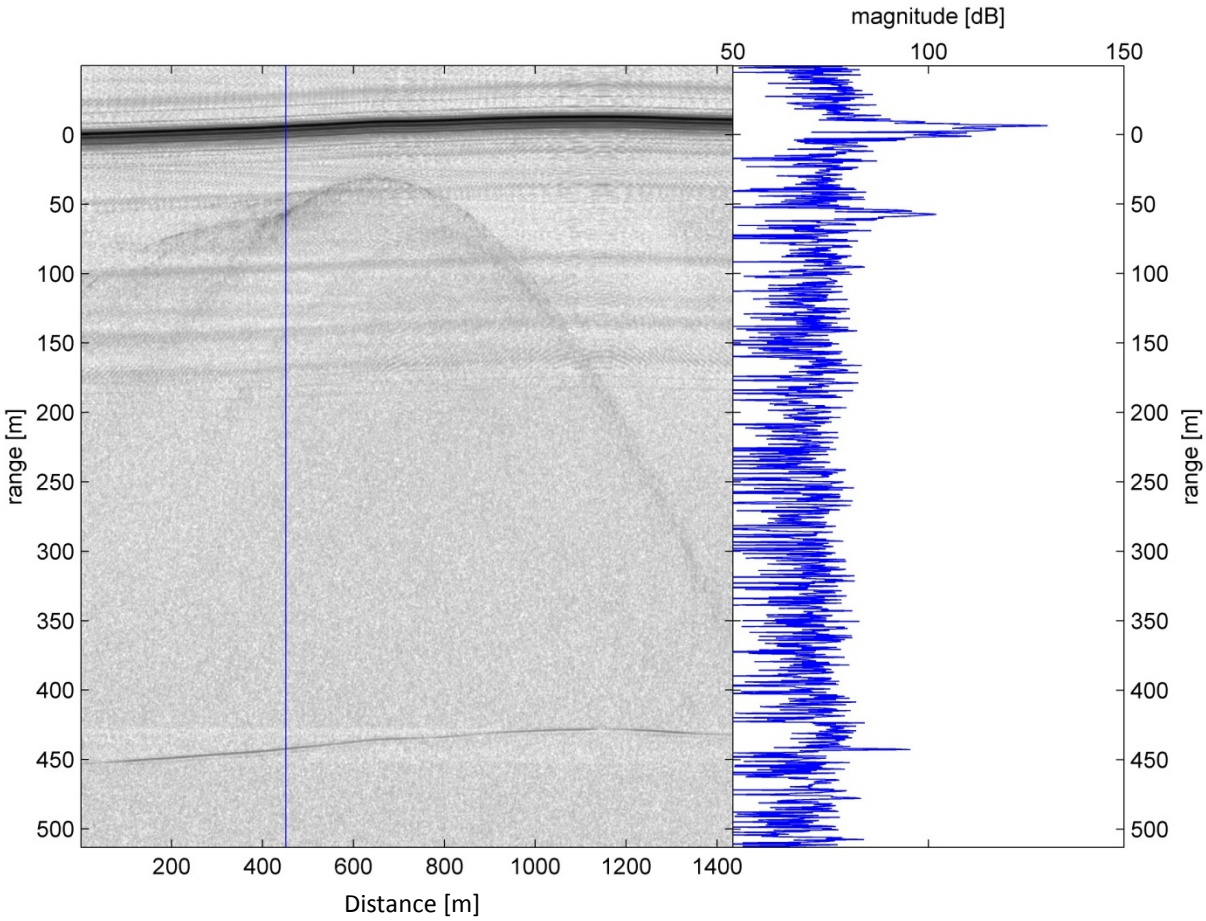

Figure 66. Data sample from second test flight. Left: echogram, right: a-scope, position indicated by the blue line in the echogram.

Left and right rolls, to a maximum of 30 degrees, were performed to evaluate the antenna pattern. No discernable difference was observed in the return signal during each roll; it was concluded that the main lobe of the antenna pattern was nearly constant within ±30 degrees of roll. A map of the flight path is seen in Figure 67.

Figure 67. Google Earth map of Calgary test flight lines over the Spray Lakes Reservoir.

The radar systems and antennas were uninstalled following the second test flight. This was required for the aircraft to be ferried to Antarctica. The radar equipment was shipped to Antarctica separately. The radar systems were reinstalled in McMurdo, Antarctica. Test flights were flown over the nearby Ross Ice Shelf and neighboring glacial ice.

Figure 68 shows a sample echogram of data collected during the test flights in Antarctica. Figure 69 shows the flight line map; the sample echogram region is highlighted in blue. Internal layering can be seen distinctly to approximately 50 m below the surface of the ice shelf. Multiple strong base returns can also be seen. These are likely a combination of nadir returns from the bottom of the ice shelf where it interfaces with the ocean below and off-nadir reflections from the bedrock of the nearby Ross Island.

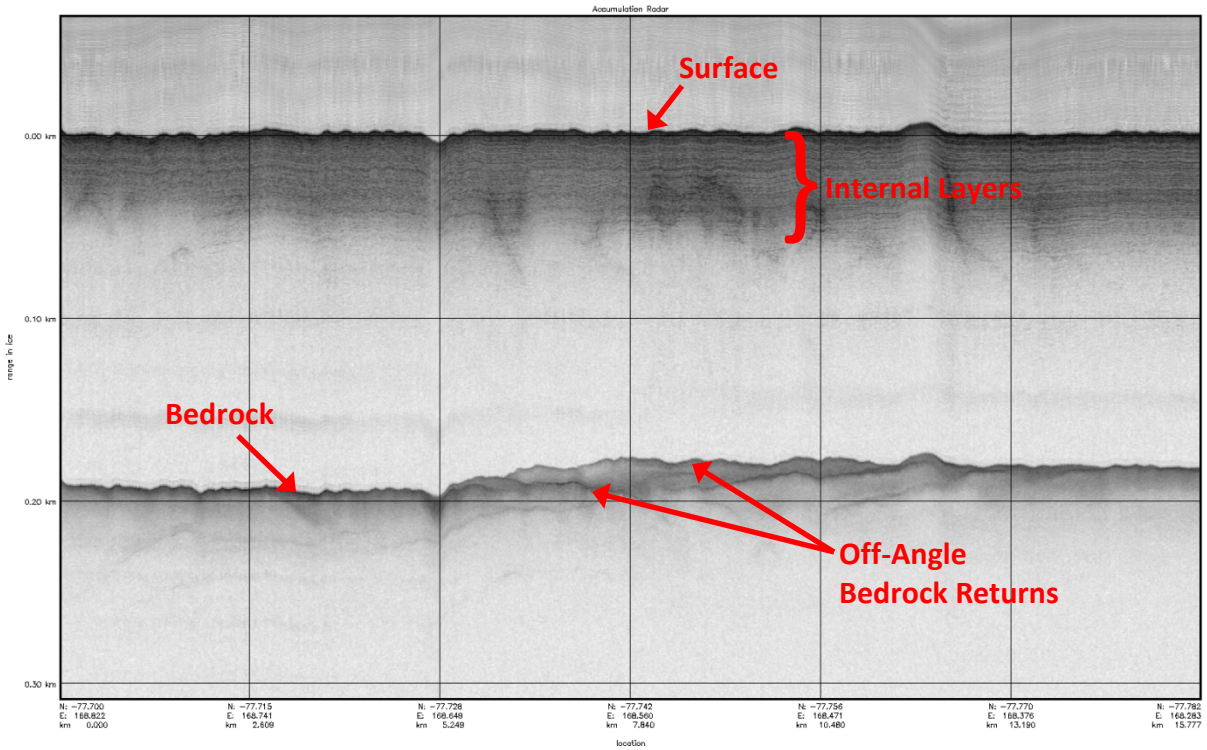

Figure 68. Sample echogram from test flight near McMurdo, Antarctica.

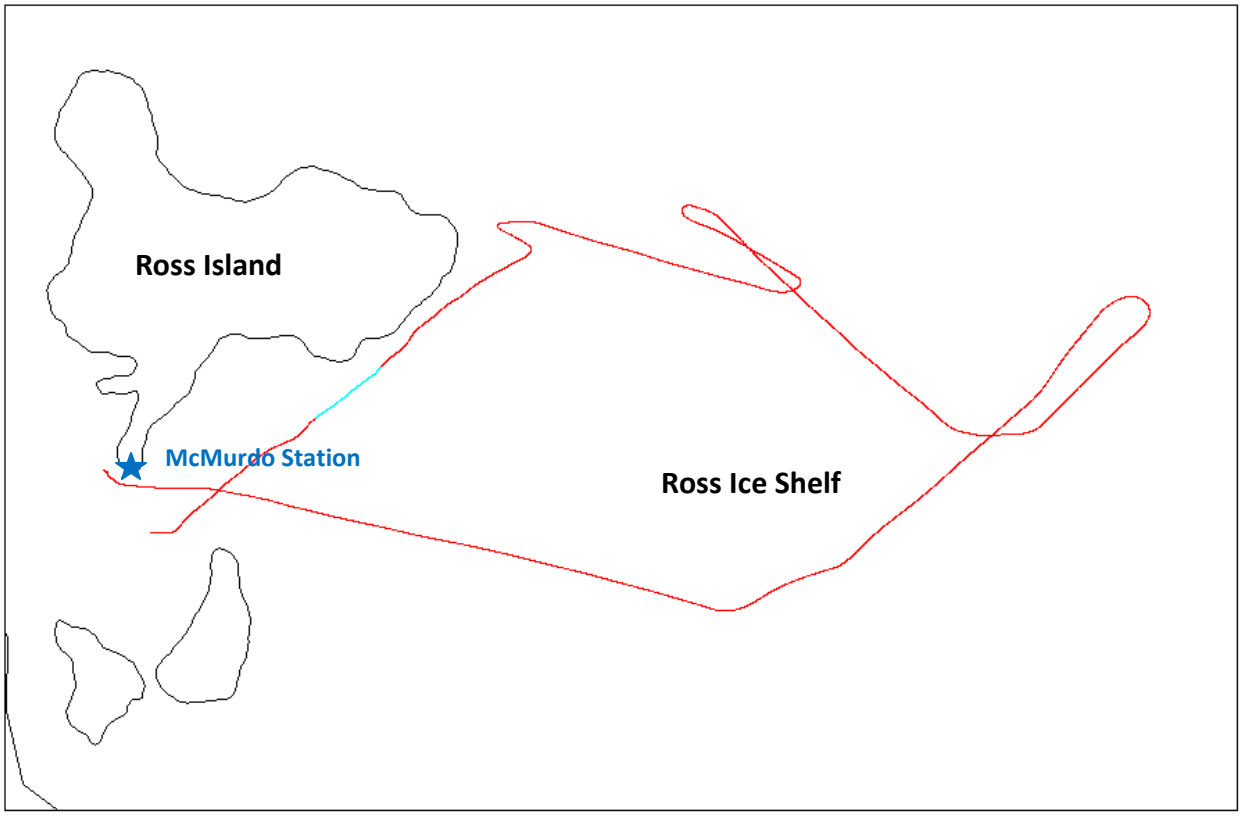

Figure 69. Flight line from test flight near McMurdo, Antarctica. Echogram region highlighted in blue.

5.2 Spring 2010 Survey

The same accumulation radar hardware used during the winter 2009-2010 Antarctica survey was used during the spring 2010 NASA Operation Ice Bridge (OIB) Greenland survey campaign. The spring 2010 OIB experiment platform was a Lockheed Martin P-3 Orion. Figure 70 shows a picture of the aircraft on the apron at Thule Air Base in northern Greenland. The radar hardware was installed into an aircraft specific rack positioned aft of the first-class/coach bulkhead. Figure 71 shows both the front and back the populated rack.

Figure 70. P-3 Orion on the apron at Thule Air Base in northern Greenland. Red arrow indicates the approximate position of the accumulation radar antenna array within the forward bomb bay.

A new antenna array was designed for this survey; details about this antenna array and the elements themselves are discussed in the appendix. The antenna array used was a four-by-two array of printed circuit board elliptical dipoles.

Results from the test flight performed off the Virginia coast confirmed that the radar operated as expected with comparable SNR to the operation observed during the Twin Otter installations and deployments. Figure 72 shows a sample echogram from data collected during

transit from Virginia to Kangerlussuaq. These data were collected over southern Greenland. Significant range sidelobes are present near the surface return. These sidelobes can be attributed to amplitude imbalance between the sub-chirps used to synthesize the needed bandwidth; this is essentially the same sidelobe response expected from amplitude modulation of a single waveform. Amplitude imbalances between tones produced for the LO stage of the receiver are also suspect. These amplitudes were changed between the 2009-2010 Antarctic mission and the spring 2010 Greenland mission, possibly explaining why these sidelobes were not as apparent in the Antarctica data. Amplitude matching techniques will be applied in post-processing to help eliminate these sidelobes.

Figure 71. Front (left) and back (right) of accumulation radar rack on P-3.

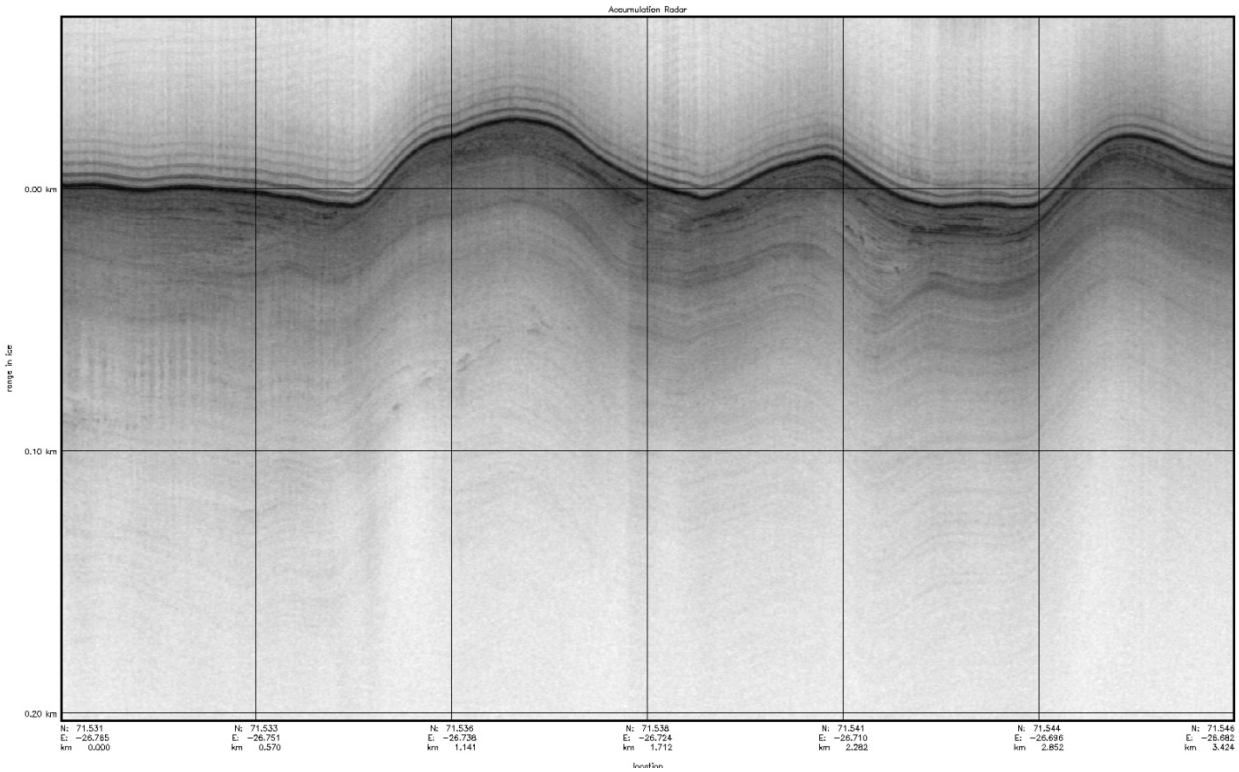

Figure 72. Sample echogram from tests flights over southern Greenland.

Chapter 6: Field Data Collection and Results

6.1 Winter 2009-2010 Survey

As discussed thoroughly in previous sections, a deHavilland DHC-3 Twin Otter was the selected platform for this survey. Areas of interest were identified by Dr. Sridhar Anandakrishnan of Penn State University, Dr. Ian Joughin of the University of Washington, Dr. Cornelis van Der Veen of the University of Kansas, and others based on science requirements. The areas included Ellsworth Land, Pine Island Glacier, Thwaites Glacier seismic up and down locations, and remote coastal regions of Marie Byrd Land. Flight lines were planned based on these areas of interest. Originally these flight lines were planned based on six hours of flight time between refueling; this required the installation of an extra fuel tank within the passenger compartment. Canadian regulation did not grant the use of such a tank with this survey;

consequently, flight lines were revised to accommodate the four-hour flight time limit of the aircraft. This, coupled with available fuel, drastically changed the planned flight lines. A map of the original flight lines can be seen in Figure 73. Winter 2009-2010 Antarctic survey original flight plan. Background coloring represents satellite derived ice velocities; some flight lines focus along areas of higher velocity (blue to purple).

The first portion of the science team arrived in Antarctica on November 16, 2009. Additional members arrived November 25, 2009. Installation began shortly after Thanksgiving; weather delays prevented access to the airplane before this time. Ground tests and test flights were performed during the first two weeks of December 2009. Surveys were conducted in two parts. One grid was flown near McMurdo over the Antarctic Geological Drilling (ANDRILL) location on the Ross Ice Shelf. This grid is not included in Figure 73 or Figure 74. This grid was flown on December 12, 2009, prior to deployment to Byrd Surface Camp. The second portion of the survey mission was conducted from Byrd Surface Camp. Deployment to the camp occurred on December 16, 2009. Survey work began on December 21, 2009 and continued through January 19, 2010. Often two four-hour missions were flown daily, weather permitting.

Flight lines were grouped based on their scientific priority. Flight lines for NSF mission I-157 (black polygons) and fine resolution grids over Thwaites Glacier seismic locations (red grids) were considered primary objectives. Additional lines over remote coastal Marie Byrd Land (green grids) were considered secondary. Grids over coastal Marie Byrd Land were redefined to maximize coverage based on the available fuel reserves at the I-189 fuel cache. Course resolution grids over Thwaites Glacier (blue grid) and grids near Siple Dome (left green grid) were abandoned for this survey due to time constraints and fuel limitations.

All the primary missions were completed. Roughly 50% of the secondary missions were completed. Figure 74 shows the flight lines map from the 2009-2010 Antarctic survey. The green region is land mass as defined in the Matlab atlas files. Blue lines denote regions where accumulation radar data were collected. Example echograms are presented below; the locations of these echograms are highlighted on the map using different colors. These images have been corrected for aircraft altitude; vertical variations reflect actual variations in the ice.

Figure 75 shows an echogram from data collected over remote Ellsworth Land (upper Thwaites glacier) during transit from WAIS Divide to the I-157 fuel cache on January 6, 2010. This echogram shows consistent layering to nearly 300 m of depth; this implies that this area of the ice sheet is fairly stable.

Figure 76 shows an echogram from data collected over upper portions of the Pine Island glacier on January 11, 2010. The deformation seen is likely caused by a vertical gradient in ice velocity in this region. This implies that this area of the ice sheet is under stress and may be moving significantly.

Figure 77 shows an echogram from data collected over lower portions of the Pine Island glacier on January 11, 2010. The vertical streaking is caused by open crevasses oriented perpendicular to the aircraft motion. Clutter from the crevassing and increased attenuation due to warmer ice temperatures near the coast lead to a reduction in the depth of prominent layering returns.

Figure 78 shows an echogram from data collected over coastal Marie Byrd Land on January 17, 2010. As with Figure 75, consistent layering to depths of at least 300 m shows a fairly stable section of the ice sheet.

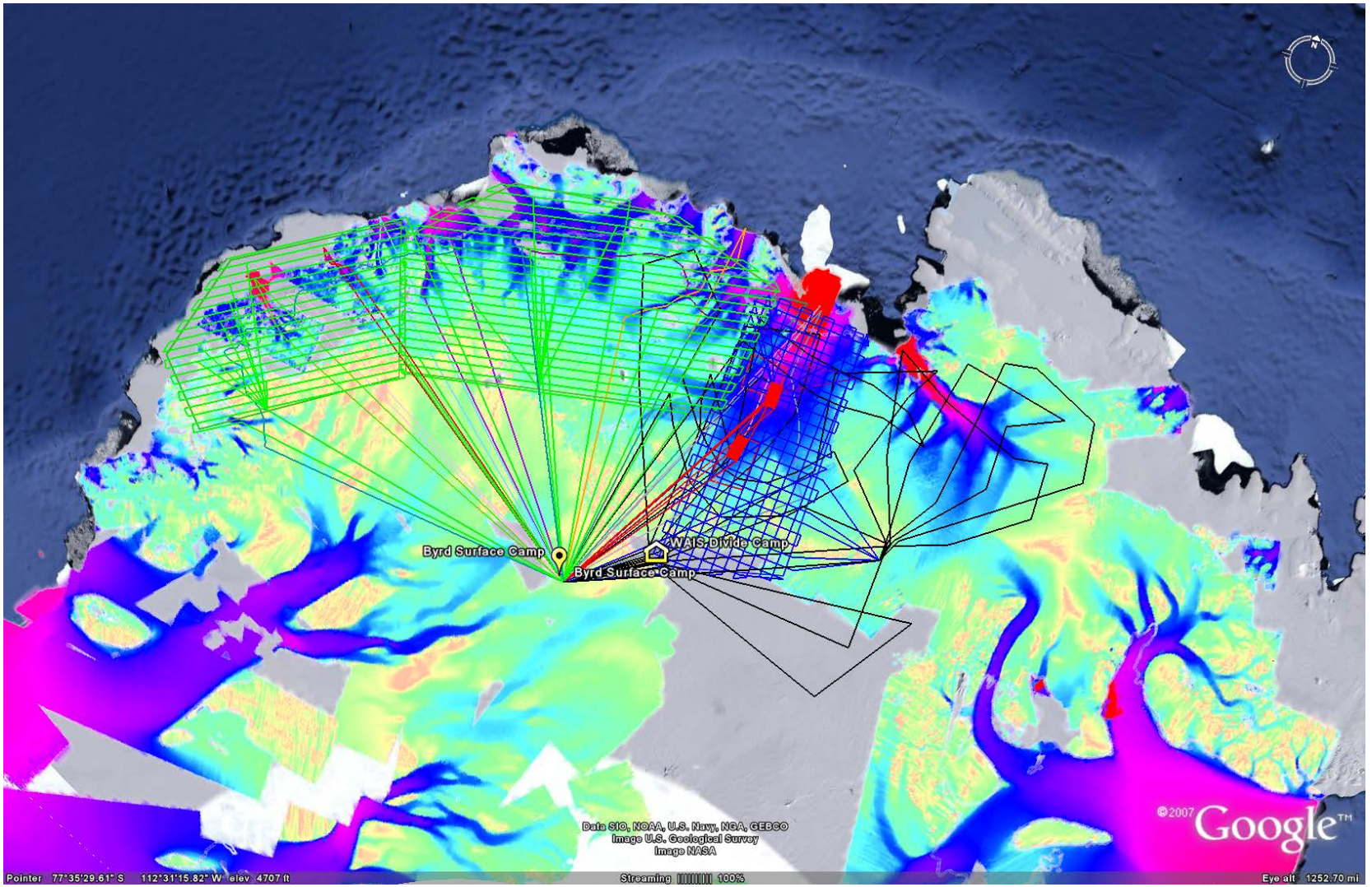

Figure 73. Winter 2009-2010 Antarctic survey original flight plan. Background coloring represents satellite derived ice velocities; some flight lines focus along areas of higher velocity (blue to purple).

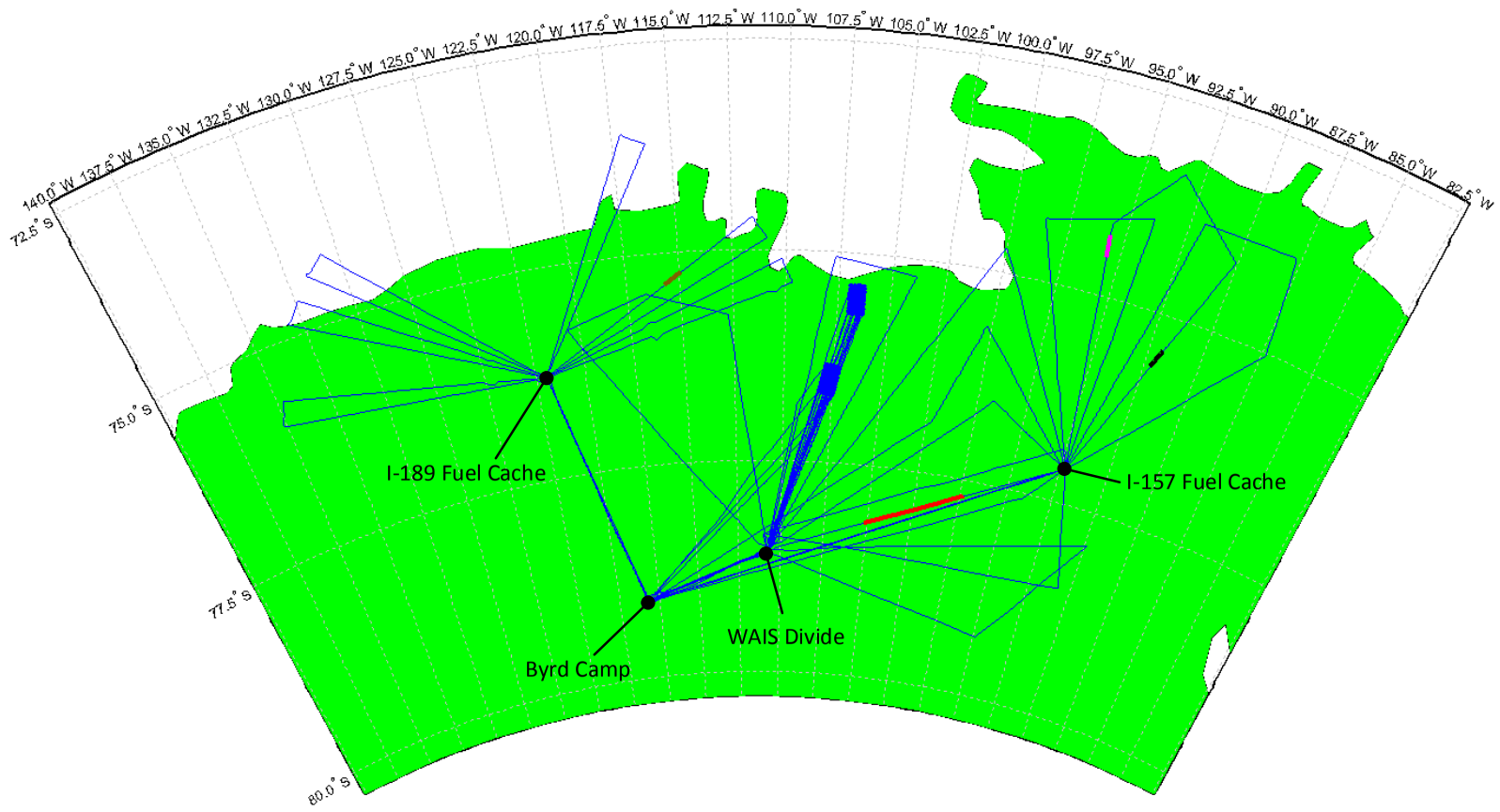

Figure 74. Winter 2009-2010 Antarctica survey lines for which accumulation radar data exists. Specific echogram locations are highlighted.

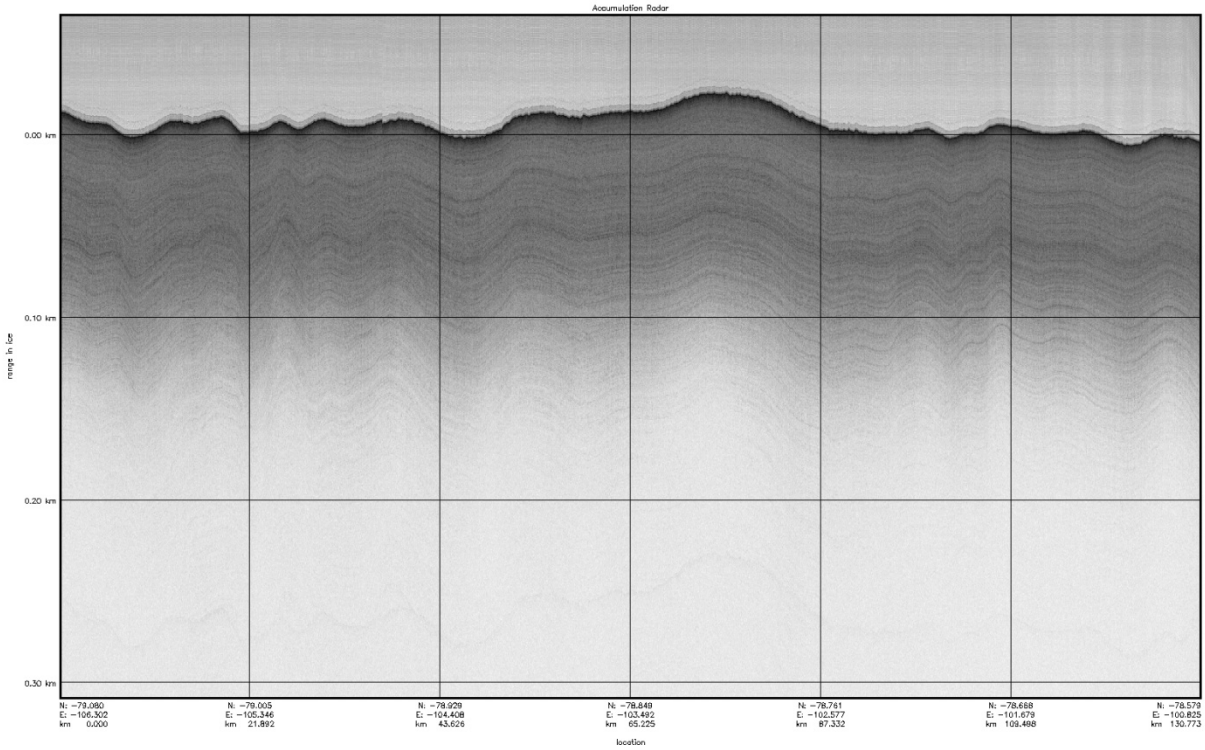

Figure 75. Echogram from Jan 6, 2010 flight over remote Ellsworth Land between WAIS Divide and the I-157 fuel cache. Highlighted in red on map (Figure 74).

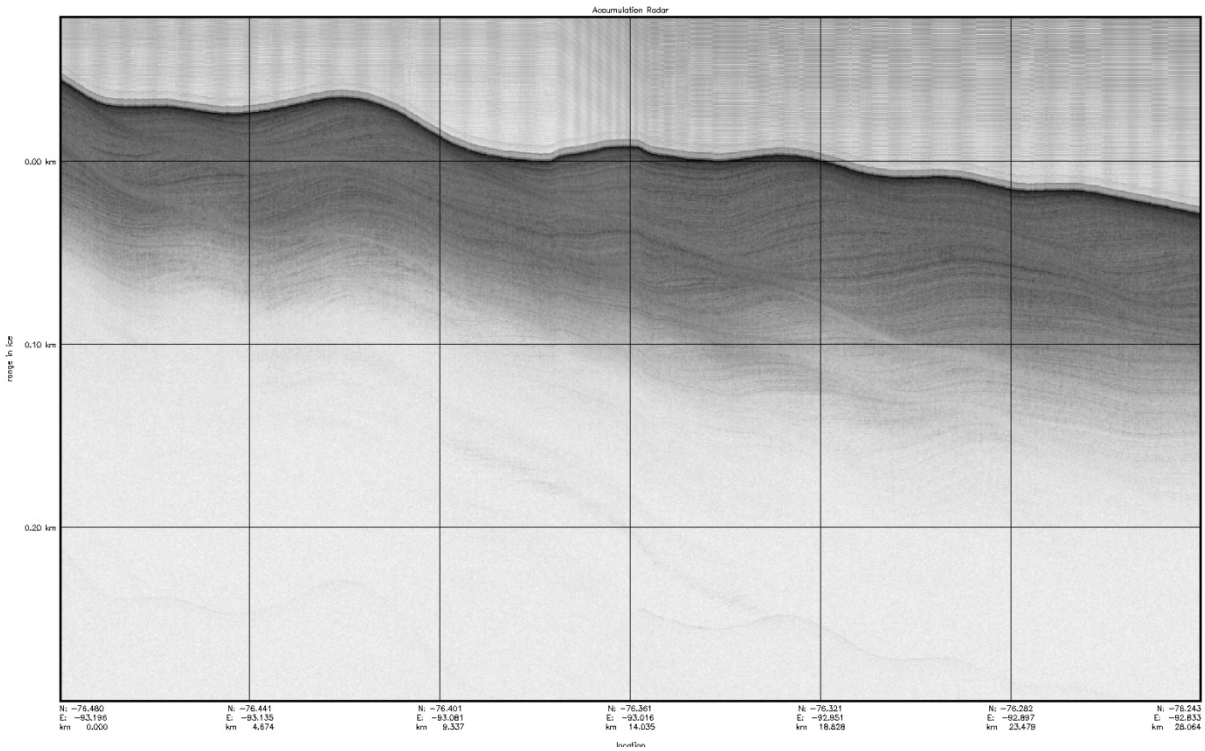

Figure 76. Echogram from Jan 11, 2010 flight over upper Pine Island glacier. Highlighted in black on the map (Figure 74).

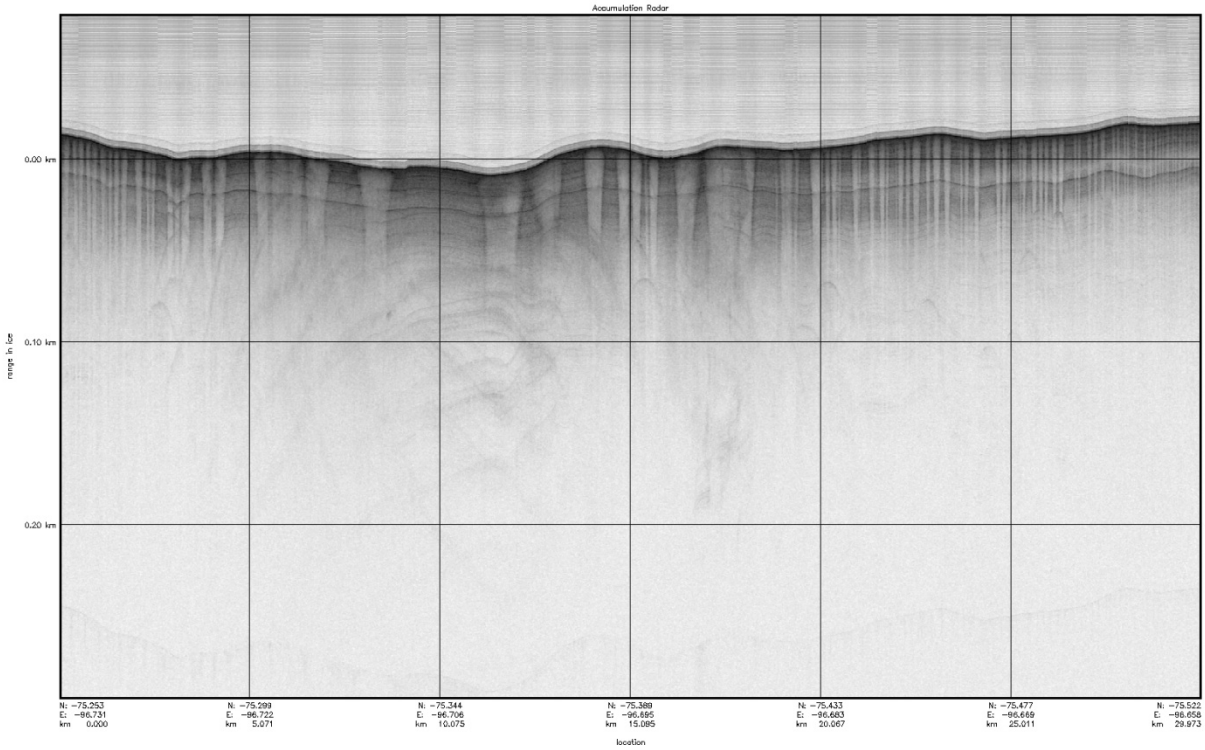

Figure 77. Echogram from Jan 11, 2010 flight over lower Pine Island glacier. Highlighted in magenta on the map (Figure 74).

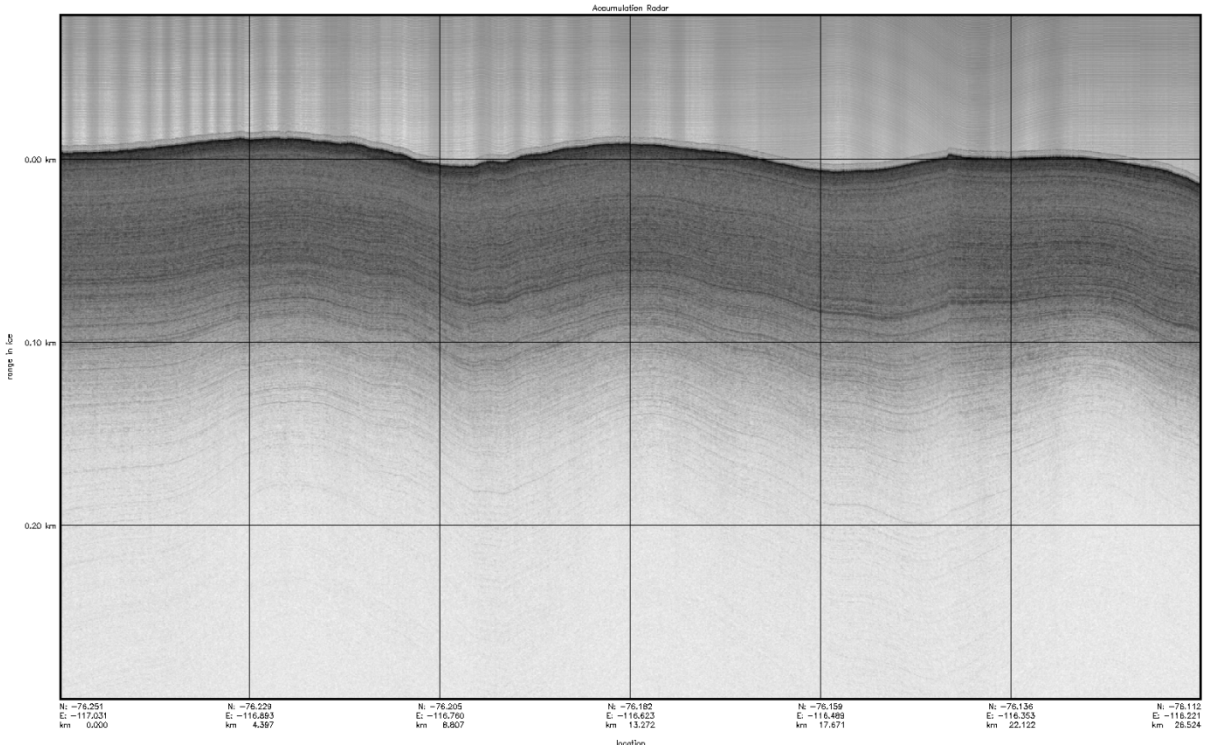

Figure 78. Echogram from Jan 17, 2010 flight over coastal Marie Byrd Land. Highlighted in brown on the map (Figure 74).

6.2 Spring 2010 Survey

As discussed previously, the spring 2010 Greenland survey was conducted under contract with NASA as part of Operation Ice Bridge (OIB). Surveys were conducted aboard a P-3 Orion between May 7, 2010 and May 26, 2010. Thirteen missions were flown, each averaging eight hours. Seven missions were flown from Kangerlussuaq over portions of southern Greenland; this included six primary missions and one secondary mission. Six missions were flown from Thule Air Base over portions of northern Greenland; five missions were considered primary and three additional missions considered secondary. One secondary mission was flown, but was cut short due to equipment issues; the remaining two secondary missions were not flown due to time and weather constraints. All primary missions were completed.

Figure 79 shows a flight line map for all survey lines flown during the campaign. Focuses included glaciers along the southeast cost, dry snow zones along the southeast coast, glaciers near Nuuk, glaciers near Kangerlussuaq, the Russell Glacier near Kangerlussuaq, the Jakobshavn Glacier near Ilulissat, glaciers along the northwest coast, dry snow zones along the northwest coast, glaciers in extreme northeast Greenland, and central areas of the ice sheet where accumulation data is sought after. Accumulation radar data were collected during all missions.

Three sample echograms were selected, one from southern Greenland, one from central Greenland, and one from northern Greenland. Locations were chosen within the dry snow zone. The images have been corrected for aircraft altitude; vertical variations reflect actual variations in the ice. Percolation zones and outflow glaciers proved to be a challenge to effectively image due to high clutter and wet snow surfaces; receiver saturation and sub-chirp amplitude imbalances created range sidelobes that masked weak layer returns. These sidelobes are present

in all the data, including those collected over the dry snow zone. Sub-chirp amplitude balancing will be necessary to correct these sidelobes; this balancing will also need to account for the amplitude imbalance present in the LO tones as well.

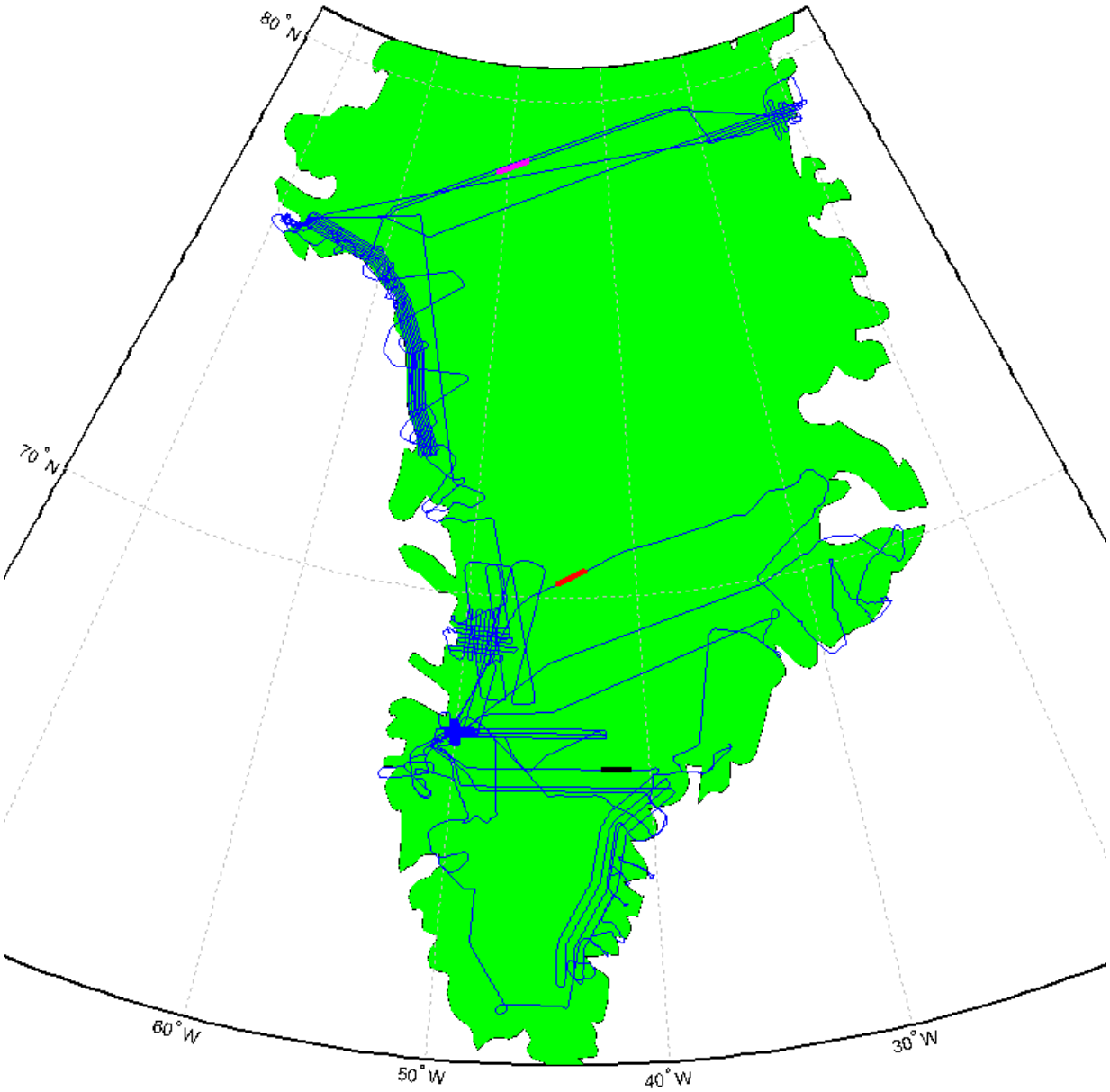

Figure 79. Spring 2010 Greenland survey lines. Specific echogram locations are highlighted.

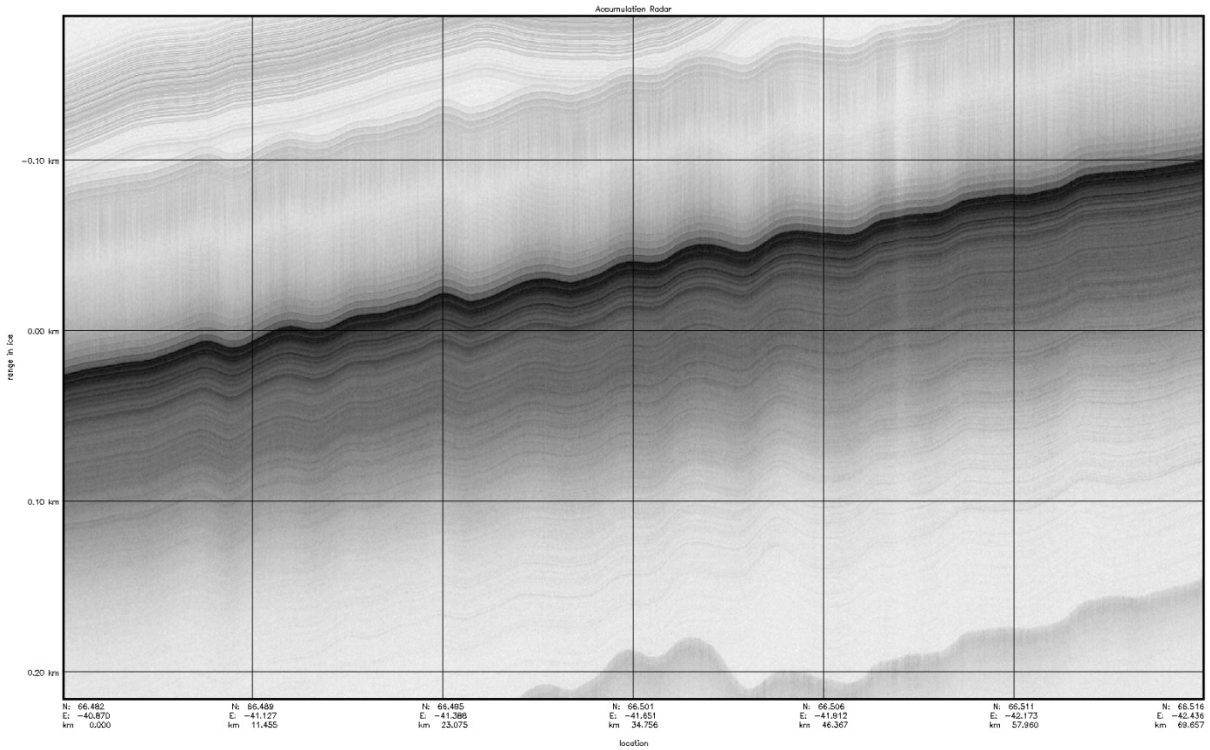

Figure 80. Echogram from May 12, 2010 flight over south central Greenland. Highlighted in black on the map (Figure 79).

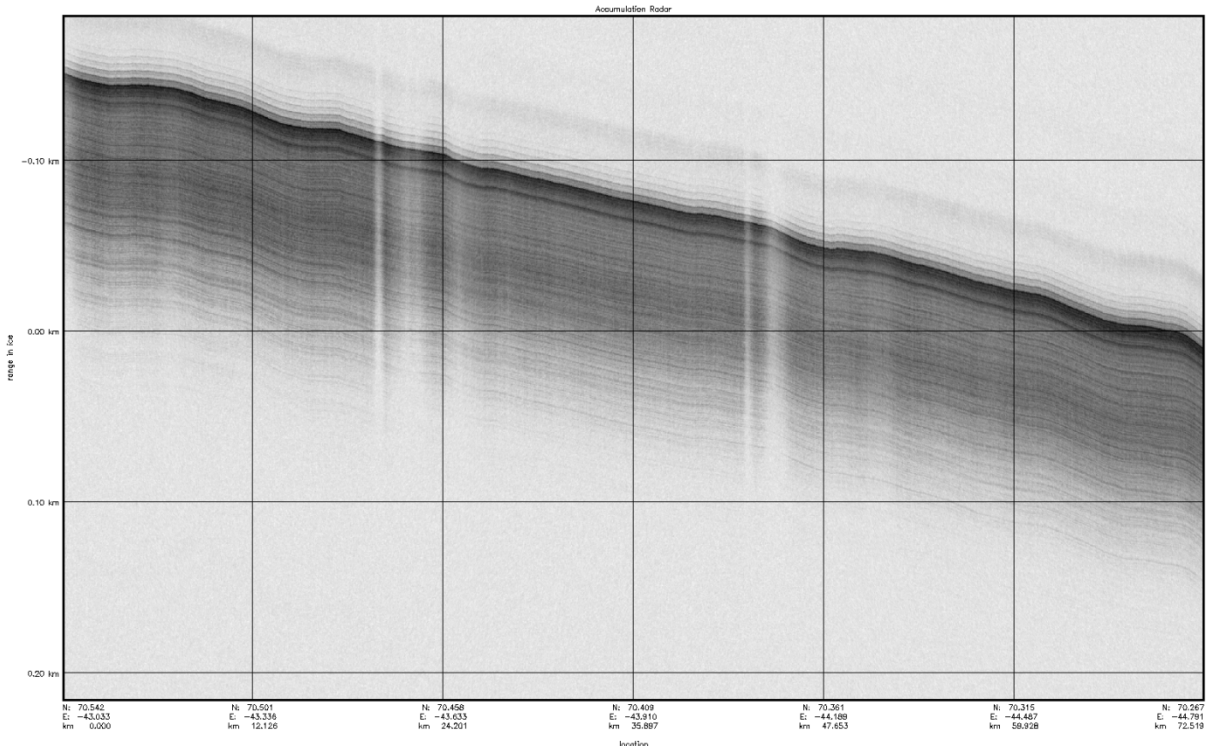

Figure 81. Echogram from May 7, 2010 flight over west central Greenland. Highlighted in red on the map (Figure 79).

Figure 80 shows an echogram collected May 12, 2010 over south central Greenland. Prominent layering can be seen to a depth of at least 200 m. Figure 81 shows an echogram collected May 7, 2010 over west central Greenland. Prominent layering is only seen to a depth of roughly 150 m; this shallower imaging is likely due to the presence of warmer ice.

Fading in Figure 81 may be related to the presence of ice near the freezing point (32°F) or small areas of surface water; both conditions lead to high signal attenuation. Figure 82 shows an echogram collected May 26, 2010 over north central Greenland. Prominent layering can be seen to a depth of at least 150 m with spotty weak layer returns to a depth of 200 m.

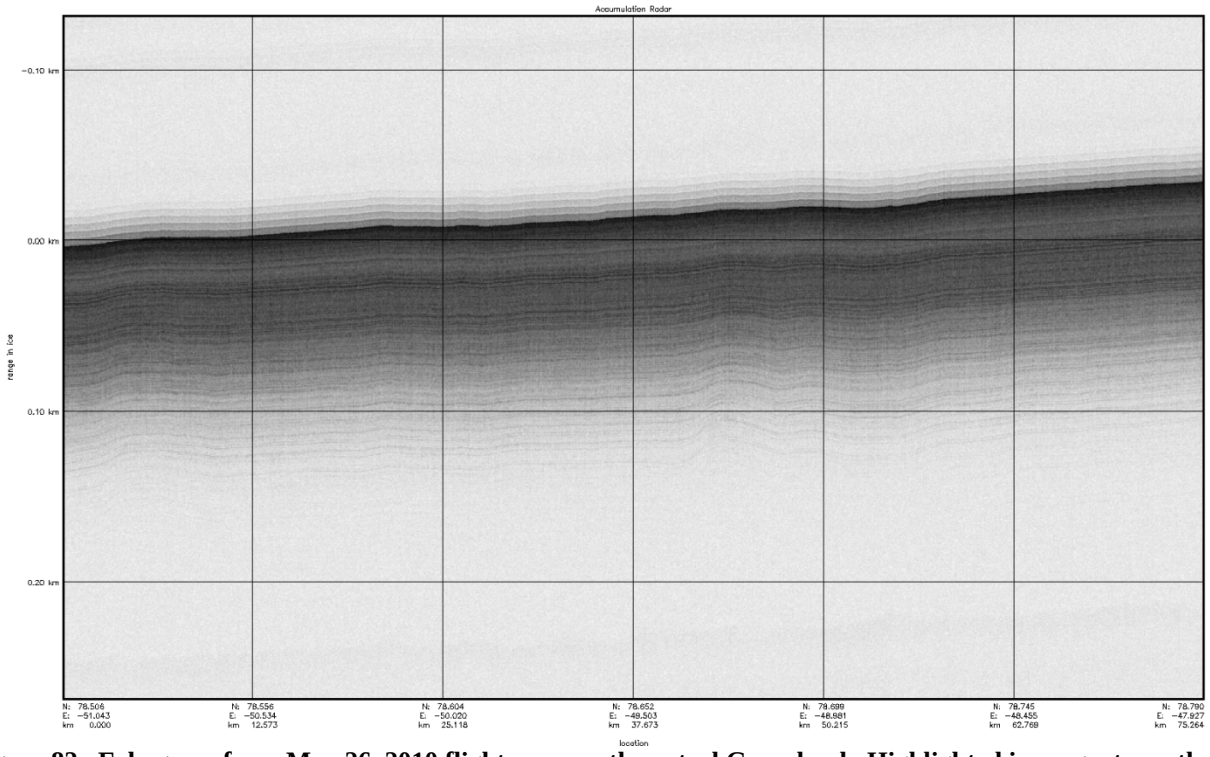

Figure 82. Echogram from May 26, 2010 flight over north central Greenland. Highlighted in magenta on the map (Figure 79).

Chapter 7: Conclusions

7.1 Summary

The design, construction, testing, and fielding of a wideband UHF radar was presented in this document. Changes and improvements were incorporated into an existing prototype design to reduce component count (and cost) and improve sensitivity. Additional goals included modifications for operation on a DHC-6 Twin Otter and additional field work to confirm operability in the Antarctic. New circuit boards and custom EMI suppressive housings were designed and constructed to meet the new design requirements. Advanced waveform techniques and T/R switches were designed and utilized to support single-antenna operation. The radar system was fielded to collect data during both the winter 2009-2010 Antarctic Twin Otter survey and the spring 2009 Greenland NASA OIB P-3 survey. Results from both surveys showed that all initial design constraints were satisfied and that the radar is capable of imaging layers to a depth of at least 200 m in the dry snow zone of both central Greenland and West Antarctica. The results from both campaigns show the need for focus on sub-chirp and LO tone amplitude leveling to improve range sidelobes. As discussed in [29], a multi-channel receiver system is necessary to collect viable data from high clutter zones, especially outlet glaciers.

7.2 Achievements and Contributions

As with all research, the work presented in this document seeks to contribute to the knowledge of the field. Many of the goals of this project seek to further the development of the existing accumulation radar platform:

1. Increased transmit power and increased receiver sensitivity (unsaturated receiver gain and comparatively lower noise figure) led to layer mapping below 200 m in most cases, as well as thickness mapping of ice shelves.
2. Development of a T/R switch for single antenna configuration and operation on board a DHC-6 Twin Otter.
3. Application of a CReSIS-designed, all-metal Vivaldi antenna; allowed for increased antenna gain (via array) within a small available footprint (Twin Otter camera port).
4. First extensive, specific accumulation measurements using a CReSIS radar in West Antarctica.

7.3 Future Work

While both lab and field results showed that the described system met the design requirements, these results also showed areas where improvement is necessary and beneficial. The following areas will undergo major improvement for the next version of the radar, focusing mainly on sensitivity and footprint reduction:

1. The current system uses a single value to define the amplitude across an entire sub-chirp; this same value is used to define the amplitude of the corresponding LO tone. This limits the ability to accurately control the amplitude across the entire bandwidth. Future systems will rely on an array of values for each sub-chirp to compensate for amplitude imbalance within and between chirps based on lab measurements of the transmitter. A separate LO amplitude array will be utilized to compensate for amplitude inter-tone imbalance.

2. Figure 14 shows that the response of the current bandpass filters provide only 15 dB of suppression at ±100 MHz offset from the band of interest. While this has proved to be adequate thus far, additional suppression of base-band chirps (100-400 MHz), the clock frequency (1 GHz), and its harmonic (500 MHz) will need to be accomplished (to at least 30 dB) to improve sensitivity.
3. The current system relies on a single-channel receiver architecture. While this has proved adequate for layer mapping within the dry snow regions, it is not adequate within high-clutter areas near the edges of the ice sheet. A multi-channel receiver system is necessary to allow for the application of clutter rejection schemes in processing and post-processing. Multiple receivers will also allow for 3-D tomography images of near-surface layers to be constructed. Tomographic techniques have been successfully demonstrated using multiple receiver systems at lower frequencies for a surface based system [27].
4. Continued focus on developing smaller, lighter-weight modules. This includes the continued miniaturization of the single channel system for use on uncrewed aerial vehicles (UAVs) and the development of CPCI cards for use within a National Instruments PXI Express chassis (i.e. NI PXIe-1082).
5. Perform extensive EMI/EMC testing. Rigorous calculations required for proper circuit layout and EMI filter design, as well as Faraday shielding is needed.

References

[1] Analog Devices. "AD9640 Datasheet." Revision B. 2009.

[2] Analog Devices. "CN0050: Stable Closed-Loop Automatic Power Control for RF Application." Circuit Note. 2008.

[3] Balanis, C. A. Antenna Theory: Analysis and Design. 3rd Edition. Wiley-Interscience, 2005. pp. 313-318.

[4] Bowen, J. W. "Astigmatism in tapered slot antennas." *International Journal of Infrared and Millimeter Waves*, Vol. 16, No. 10, pp. 1733-1756, 1995.

[5] Box, J. E. "Greenland ice sheet surface mass-balance variability: 1991-2003." *Annals of Glaciology*, Vol. 42, pp. 90-94, 2005.

[6] Chio, T. H. and Schaubert, D. H. "Parameter study and design of wide-band widescan dual-polarized tapered slot antenna arrays." *IEEE Transactions on Antennas and Propagation*, Vol. 48, No. 6, pp. 879-886, 2000.

[7] Douglas, B., Kearney, M. S., and Leatherman, S. P. Sea Level Rise: History and Consequences. *International Geophysical Series*, Vol. 75, 2001.

[8] EMI Filter Company. "B8C104A Filters, EMI, Standard, 8-32 Threaded Body Datasheet." Revision B.

[9] EMI Filter Company. "B8P753A Filters, EMI, Standard ("Pi") Circuit, 8-32 Threaded Body Datasheet." Revision B.

[10] Forester, R. R., Jezek, K. C., Bolzan, J., Baumgartner, F., Gogineni, S. P. "Relationships between radar backscatter and accumulation rates on the Greenland ice sheet." *International Journal of Remote Sensing*, Vol. 20, No 15 & 16, pp. 3131-3147, 1999.

[11] Fujita, S., Matsuoka, T., Ishisa, T., Matsuoka, K., and Mae, S. "A summary of the complex dielectric permittivity of ice in the megahertz range and its application for radar sounding of polar ice sheets." *Physics of Ice Cores*, pp. 185-212, 2000.

[12] Hanna, E., McConnell, J., Dah, S., Cappelen, J., and Stephens, A. "Observed and Modeled Greenland Ice Sheet Snow Accumulation, 1958-2003, and Links with Regional Climate Forcing." *Journal of Climate*, Vol. 19, pp. 344-358, 2005.

[13] Hansen, J. E. "Scientific reticence and sea level rise." *Environmental Research Letters*, Vol. 2, No. 2, 024002, 6 pages, 24 May 2007.

[14] Harris, F. J. "On the Use of Windows for Harmonic Analysis with the Discrete Fourier Transform." *Proceedings of the IEEE*, Vol. 66, No. 1, pp. 51-83, 1978.

[15] Harrison, C. H. "Radio echo sounding of horizontal layers in ice." *Journal of Glaciology*, Vol. 12, No. 66, pp. 383-397, 1973.

[16] Hittite Microwave Corp. "HMC784MS8GE Datasheet." Version 00.0808. 2008.

[17] Johnson, H. High-Speed Digital Design: A Handbook of Black Magic. Prentice Hall, 1993.

[18] Kanagaratnam, P. "Airborne Radar for High-Resolution Mapping of Internal Layers in Glacial Ice to Estimate Accumulation Rate." PhD. Dissertation, University of Kansas, February 2002.

[19] Kanagaratnam, P. "High-Resolution Backscatter from Sea Ice and Range-Gated Step-Frequency Radar Using the FM-CW Concept." Master's Thesis, University of Kansas, December 1995.

[20] Kingsley, S. and Quegan, S. Understanding Radar Systems. Mendham, NJ: SciTech Publishing, 1999, pp. 15.

[21] Ledford, J. "Development of an Eight Channel Waveform Generator for Beam-forming Applications." Master's Thesis, University of Kansas, February 2009.

[22] Maxim Integrated Products. "MAX4659 Datasheet." Revision 0. 2001.

[23] Mini-Circuits. "ADE-R5LH+ Datasheet." 2009.

[24] Mini-Circuits. "SLP-50+ Datasheet." Revision B. 2009.

[25] Miteq Corp. "AU-1291 Datasheet." 2007.

[26] Nazli, H., Bicak, E., Turetken, B., and Sezgin, M. "An improved design of planar elliptical dipole antenna for UWB applications." *IEEE Antenna and Wireless Propagation Letters*, Vol. 9, pp. 264-267, 2010.

[27] Paden, J., Akins, T., Dunson, D., Allen, C., and Gogineni, P. "Ice-sheet bed 3-D tomography." *Journal of Glaciology*, Vol. 56, No. 195, pp. 3-11, 2010.

[28] Panzer, B. "Development of an Electrically Small Vivaldi Antenna: The CReSIS Aerial Vivaldi (CAV-A)." Master's Thesis, University of Kansas, December 2007.

[29] Parthasarathy, B. "Design and Development of an Airborne Multi-Channel FMCW Radar for High Resolution Mapping of Internal Layers in Glacial Ice." Master's Thesis, University of Kansas, December 2005.

[30] Parthasarathy, R. "Fine Resolution Radar for Near-Surface Layer Mapping." Master's Thesis, University of Kansas, August 2004.

[31] Paul, C. R. Introduction to Electromagnetic Compatibility. Second Edition. Hoboken, NJ: Wiley-Interscience, pp. 856, 2006.

[32] Pozar, D. Microwave Engineering. 3rd Edition. Hoboken, NJ: John Wiley and Sons, 2005.

[33] Robin, G. de Q., "Radio-echo sounding – Glaciological interpretations and applications." *Journal of Glaciology*, Vol. 15, No. 73, pp. 49-63, 1975.

[34] Schurter Electronic Components. "KFA Power Entry Modules with Linear Filter Datasheet."

[35] Solomon, S., Qin, D., Manning, M., et al. "Climate Change 2007: The Physical Science Basis. *Working Group I Contribution to the Fourth Assessment Report of the IPCC*. September 2007.

[36] Thierauf, S. C. High-Speed Circuit Board Signal Integrity. Norwood, MA: Artech House, 2004.

[37] Thomas, R., Frederick, E., Krabill, W., Manizade, S., and Martin, C. "Progressive increase in ice loss from Greenland." *Geophysical Research Letters*, Vol. 33, L10503, 4 pages, 2006.

[38] Ulaby, F. T., Moore, R. K., and Fung, A. K. Microwave Remote Sensing: Active and Passive. Volume I. Norwood, MA: Artech House, 1981.

[39] Ulaby, F. T., Moore, R. K., and Fung, A. K. Microwave Remote Sensing: Active and Passive. Volume II. Norwood, MA: Artech House, 1982.

[40] Velicogna, I., Wahr, J., Hanna, E., and Huybrechts, P. "Short term mass variability in Greenland, from GRACE." *Geoscience Research Letters*, Vol. 32, L05501, 4 pages, 1 March 2005.

[41] Yi, D., Zwally, J., and Sun, X. "ICESat Measurements of Greenland ice sheet surface slope and roughness." *Annals of Glaciology*, Vol. 42, No. 1, pp. 83-89, 2005.

[42] Zhang, J. P., Xu, Y. S., and Wang, W. D. "Ultra-wideband microstrip-fed planar elliptical dipole antenna." *Electronic Letters*, Vol. 42, No. 3, pp. 144-145, 2006.

Appendix A: PCB Trace Calculations

Microstrip Calculations

Table 5 lists the relevant parameters for printed circuit board trace calculations. FR4-specific parameters were obtained from the AP Circuits website (circuit board manufacturer of choice).

Table 5. AP Circuits' FR4 specifications for microstrip configuration.

Parameter	Value
Relative Permittivity (ε_r)	4.34
Relative Permeability	1
Substrate Thickness (h)	20 mil
Trace Thickness (t)	1.4 mil (1 oz copper)
Accepted Trace Width (w)	40 mil
Conductivity (copper)	59.6×10^6 S/m
Loss Tangent	0.014
Solution Frequency	750 MHz

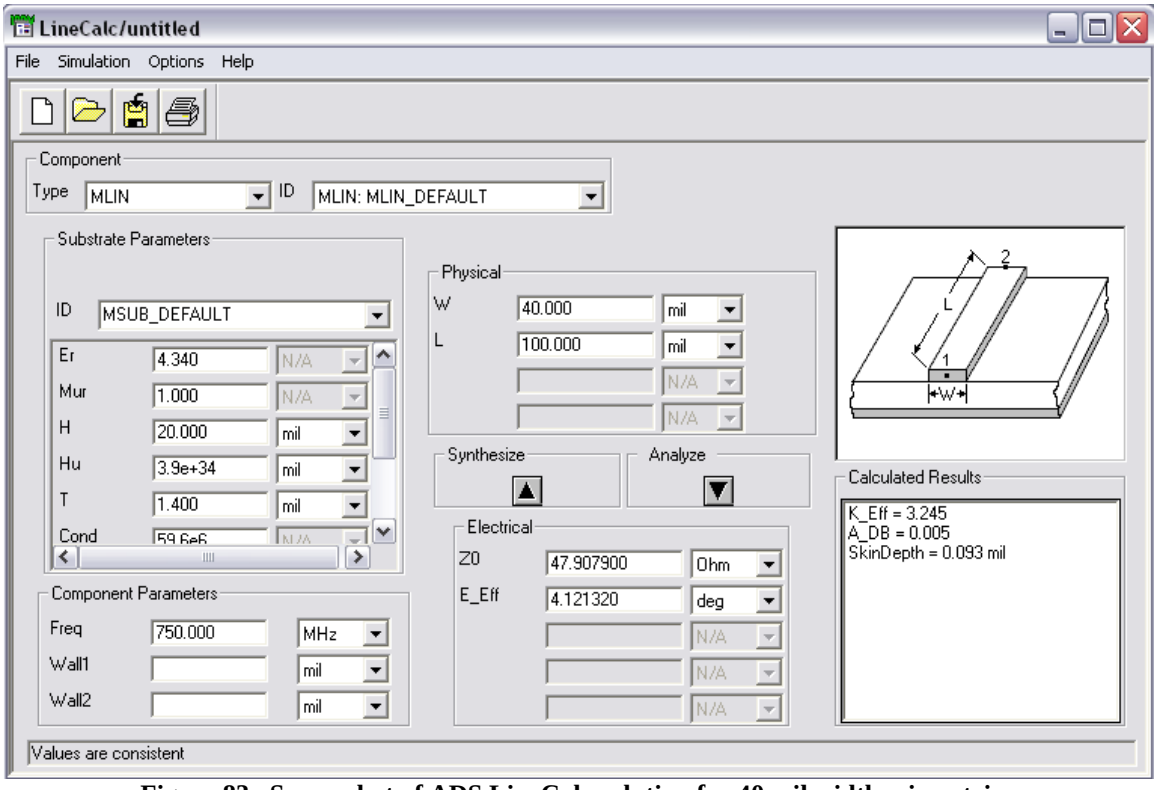

Figure 83. Screenshot of ADS LineCalc solution for 40 mil width microstrip.

Figure 83 is a screenshot of the ADS LineCalc dialog window showing the relevant parameters and the calculated trace impedance for a 40-mil trace. The impedance calculator found an impedance of 47.9 Ω for the selected trace width; this was deemed acceptable.

$$Z_{micro}(h,w,t,er) = \frac{Z_{wide}(h,w,t)}{\sqrt{EEFF(h,w,t,er)}} \tag{A1}$$

$$Z_{wide}(h,w,t) = \frac{120\pi}{\frac{WE_{wide}(h,w,t)}{h} + 1.393 = 0.667ln\left[\frac{WE_{wide}(h,w,t)}{h} + 1.444\right]} \tag{A2}$$

$$WE_{wide}(h,w,t) = w + \frac{1.25t}{\pi}\left[1 + ln\left[\frac{2h}{t}\right]\right] \tag{A3}$$

$$EEFF = \frac{er+1}{2} + \left[\frac{er-1}{2}\right]\left[1 + \frac{12h}{w}\right]^{-0.5} - \frac{(er-1)\left(\frac{t}{h}\right)}{4.6\sqrt{\frac{w}{h}}} \tag{A4}$$

```
% Accum radar circuit board microstrip calculations
% Based on equation in Appendix C of High-Speed Digital Design by Howard
Johnson
% Coded by Cameron Lewis

% Parameters
er = 4.34;
h = 20/1000;
t = 1.4/1000;
w = 40/1000;

% Effective relative permittivity
EEFF = ((er+1)/2) + ((er-1)/2)*(1+(12*h/w))^(-0.5) - ...
    (((er-1)*(t/h))/(4.6*sqrt(w/h)));

% Effective trace width
WE = w + (1.25*t/pi)*(1+log(2*h/t));

% Effective trace impedance
Z_w = (120*pi)/((WE/h)+1.393+0.667*log((WE/h)+1.444));

% Trace impedance
Z = Z_w/sqrt(EEFF);
```

Given the complexity of the microstrip equations presented in Appendix C of *High-Speed Digital Design* by Howard Johnson [17], Matlab was employed to facilitate these calculations.

The necessary equations and Matlab code are presented above. These equations are considered valid for "wide" traces; that is, traces where the width is larger than the thickness of the substrate and for substrates with a relative permittivity $0 < \varepsilon_r < 16$. Our parameters meet these conditions.

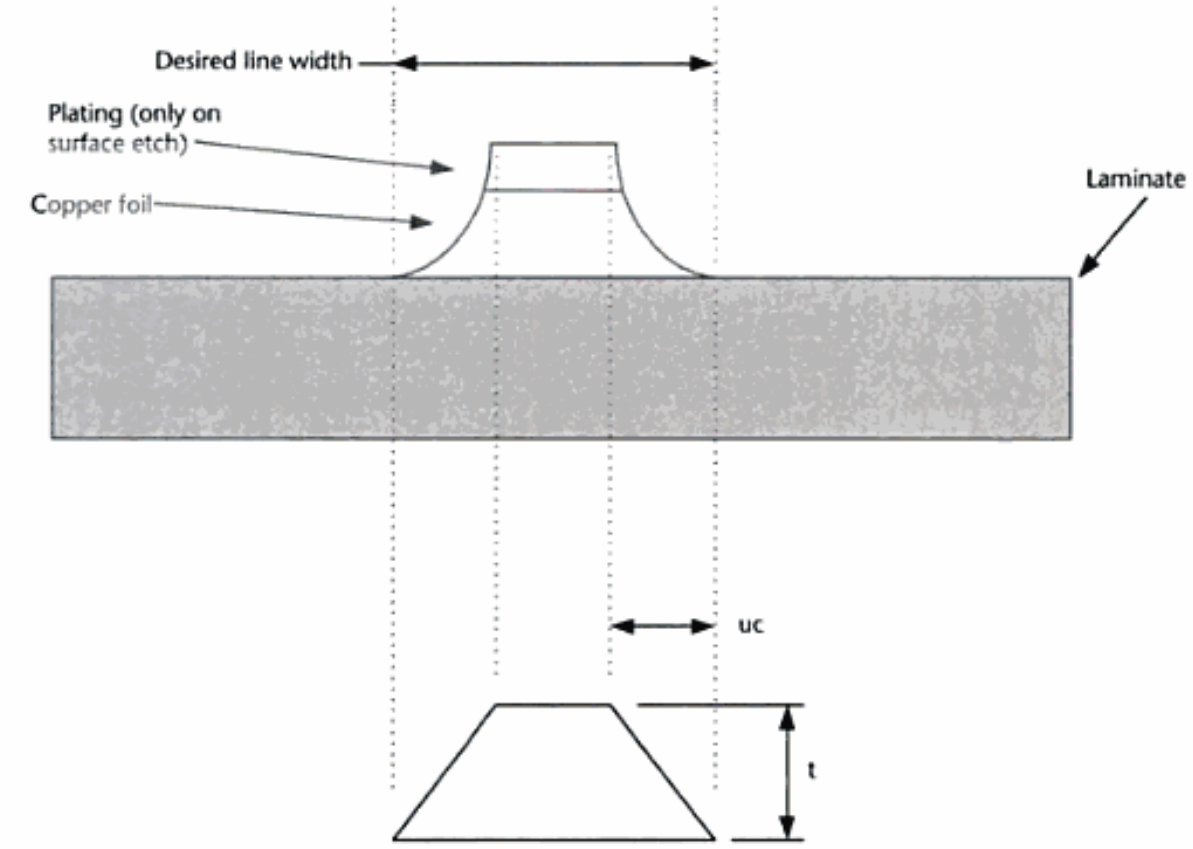

Figure 84. Trace over-etch cross-section [36].

Using the parameters provided in Table 5, these equations produced a trace impedance of 47.8 Ω. Finally, the simplified microstrip impedance equation provided in Altium Designer was used. This equation is presented below.

$$Z_{micro} = \frac{87}{\sqrt{er + 1.41}} ln\left[\frac{5.98h}{(0.8w) + t}\right] \quad \text{(A5)}$$

Using the parameters provided in Table 5, this equation produced a trace impedance of 46.3 Ω. Table 6 summarizes these calculations.

Table 6. Calculated trace impedances versus method.

Method	Result
ADS LineCalc	47.9 Ω
High-Speed Digital Design	47.8 Ω
Altium Designer	46.3 Ω

It was found that a trace width of 37 mil would produce a trace impedance of nearly 50 Ω via all calculation methods. It was accepted that the etching process used by the circuit board manufacturer will likely lead to trace over-etching. Over-etching leads to a trace that has a trapezoidal cross-section (Figure 84). This over-etching effectively reduces the width of the trace, increasing its impedance. Coupled with possible inaccuracies in manufacturing (accepted at ±1 mil) it was decided to stay with a trace width of 40 mil.

Grounded Co-planar Waveguide Calculations

ADS LineCalc was employed to determine the trace width and gap spacing. Figure 85 is a screenshot of the LineCalc dialog window. Table 7 presents the trace and substrate parameters used for this calculation. Given a trace width of 20 mil and gap of 15 mil, the trace impedance was found to be 53.3 Ω.

Table 7. AP Circuits' FR4 specification for grounded co-planar waveguide configuration (GCPW).

Parameter	Value
Relative Permittivity (ε_r)	4.34
Relative Permeability	1
Substrate Thickness (h)	13 mil
Trace Thickness (t)	1.4 mil (1 oz copper)
Accepted Trace Width (w)	20 mil
Accepted Trace/Ground Gap (g)	15 mil
Conductivity (copper)	59.6×10^6 S/m
Loss Tangent	0.014
Solution Frequency	750 MHz

Fixing the gap to 15 mil, it was found that a trace width of 22.5 mil would produce a trace impedance of 50 Ω. To simplify the board layout procedure, the trace width was rounded down to the nearest 5 mil. In hindsight, given the manufacturing inaccuracies discussed in the microstrip calculation section, it would have best to round up to 25 mil instead of down to 20 mil.

This is because over-etching leads to a smaller trace width and larger trace-to-ground gap. Table 8 lists the trace impedance for several width/gap combinations.

Given manufacturing inaccuracies, clearly an over-sizing of the trace width dimension would have likely led to more ideal trace impedances. Since the operation of the switch was acceptable and met the design constraints, this level of accuracy in the trace impedance may not be necessary, but the analysis has been included here for completeness.

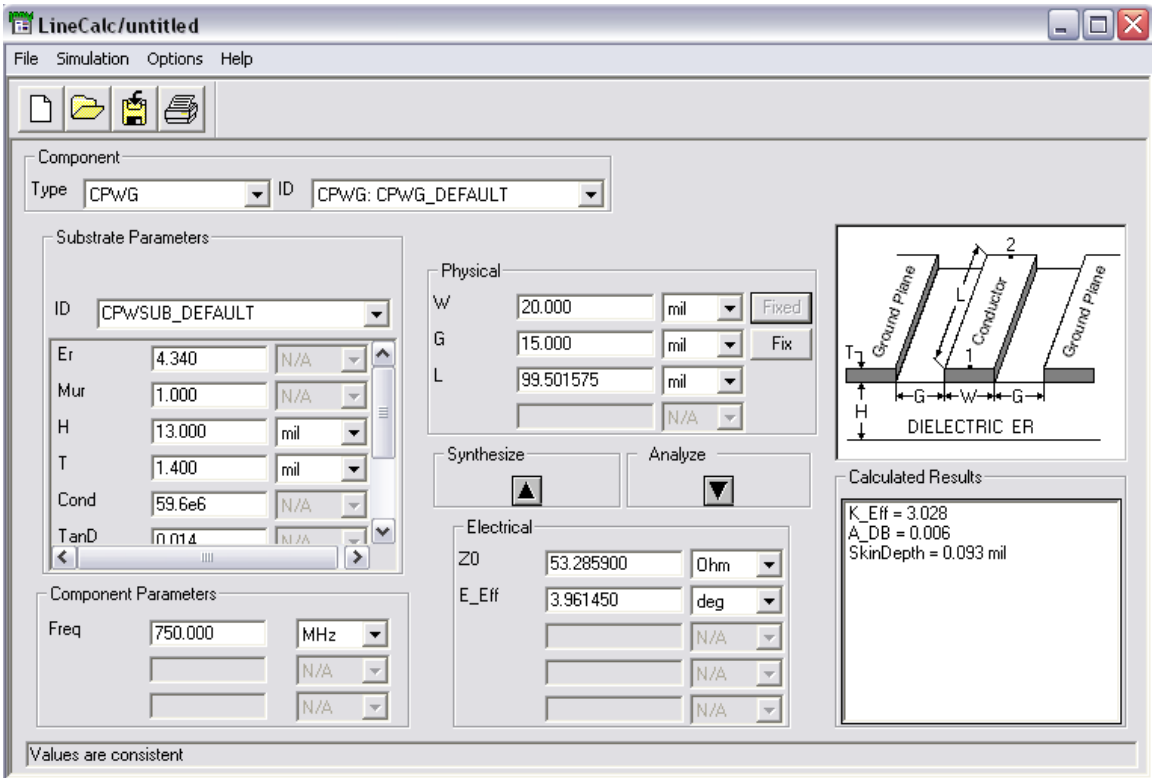

Figure 85. Screenshot of ADS LineCalc solution for GCPW.

Table 8. GCPW calculated trace impedances.

Trace Width [mil]	Trace/Ground Gap [mil]	Description	Trace Impedance [Ω]
22.5	15	Ideal design	50
20	15	Used in current design	53.3
18	16	Over-etching of current design	56.7
25	15	Round up width of ideal design	47.1
23	16	Over-etching of rounded up width	49.8

Appendix B: Radar Operation Manual

The following operation manual was generated during the installation and testing of the accumulation radar during the fall of 2009. This operation manual was designed to provide the user with all the needed information to properly install the radar, make all necessary power and RF connections, properly power up and shutdown the radar and software, and properly record data during flight. Loop-back testing, necessary during installation and before field operation, is discussed in Appendix C.

Needed Materials

- 1 Accumulation RF chassis
- 1 Accumulation Power Amp chassis
- 1 Accumulation 1U DAQ
- 1 Accumulation Delay line
- 1 Accumulation Antenna assembly (Vivaldi array for Twin Otter installation)
- 1 Tripplite SMART1200LCD uninterrupted power supply
- 1 16’ LMR-300 cable (antenna cable)
- 3 Male BNC - Female SMA adapters
- 2 10” RF cables SMA/SMA
- 6 6” RF cables SMA/SMA
- 4 Computer power cables (IEC-C13)
- 1 USB cable (type A to B)
- 1 Serial cable
- 1 Serial to USB converter (Keyspan brand highly recommended)
- 2 Isolators (Raditek RADI-600-900M-S3-5WR-M1)
- 1 40 dB coupler (10 W minimum)
- 1 20 dB high power attenuator (10 W minimum)
- 3 20 dB SMA attenuators
- 5 RF test cables (at least 2’ long)

Rack Installation

The rack mount chasses are designed for mounting into standard 18” wide aircraft equipment racks (Figure 63 or Figure 71). For ease of operation and cabling, it is suggested that the chasses be installed from bottom to top in the following order (Figure 86):

- Tripplite UPS
- Accumulation Delay Line
- Accumulation Power Amp Chassis
- Accumulation RF Chassis
- Accumulation 1U DAQ

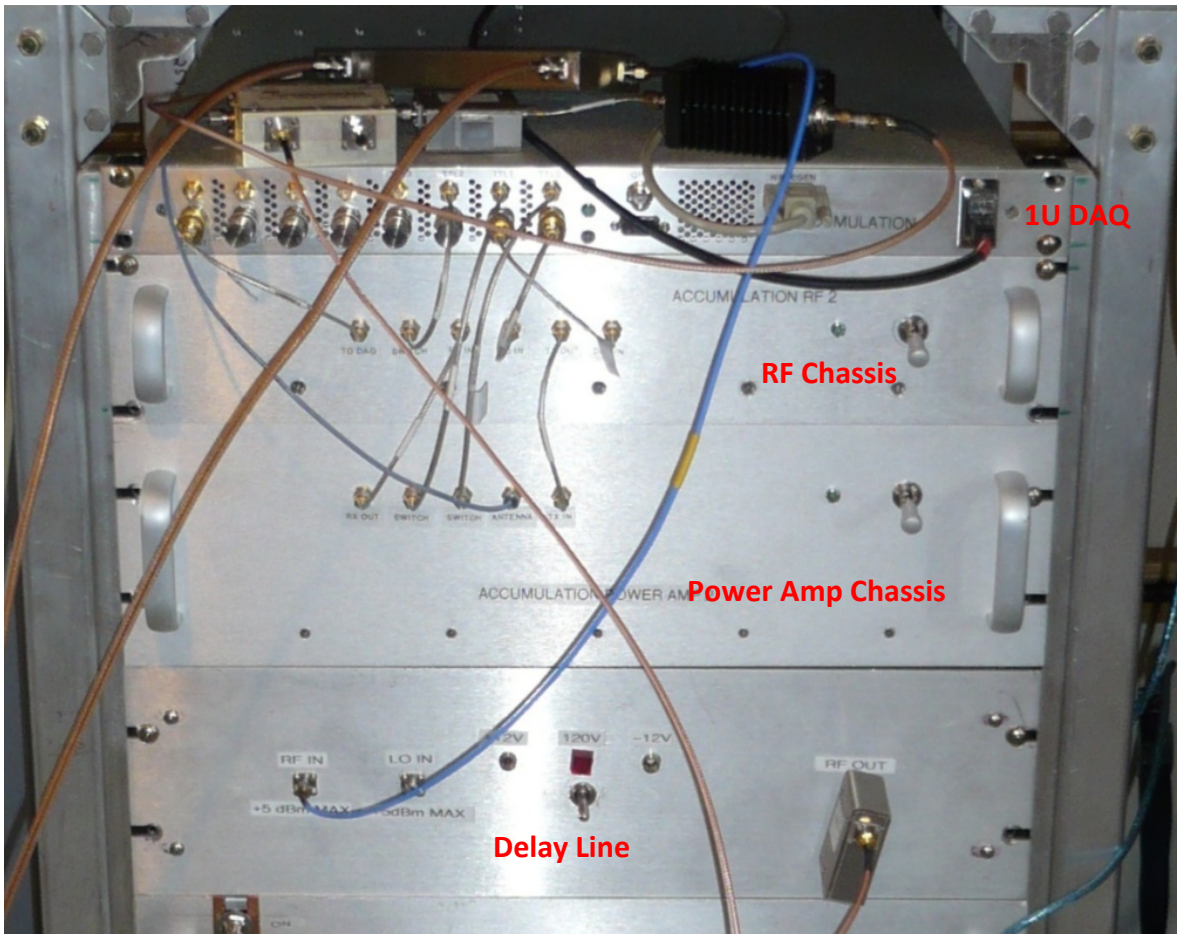

Figure 86. Photograph of the radar component stack-up.

Antenna Installation

As discussed in the installation section, the antenna assembly is installed in the nadir port of the Twin Otter. The assembly replaces the removable strut. Two bolts are used to secure the assembly through holes near the top of the strut supports (yellow arrows in Figure 87). The porthole is covered using the Kydex-100 radome. The assembly is installed so that the horn antennas (for Ku-band altimeter) are resting against the radome. One end of the 16' LMR-300 antenna cable is connected to the power divider (red circle in Figure 87). The other end of the antenna cable is connected to the Antenna port on the front of the Power Amp chassis.

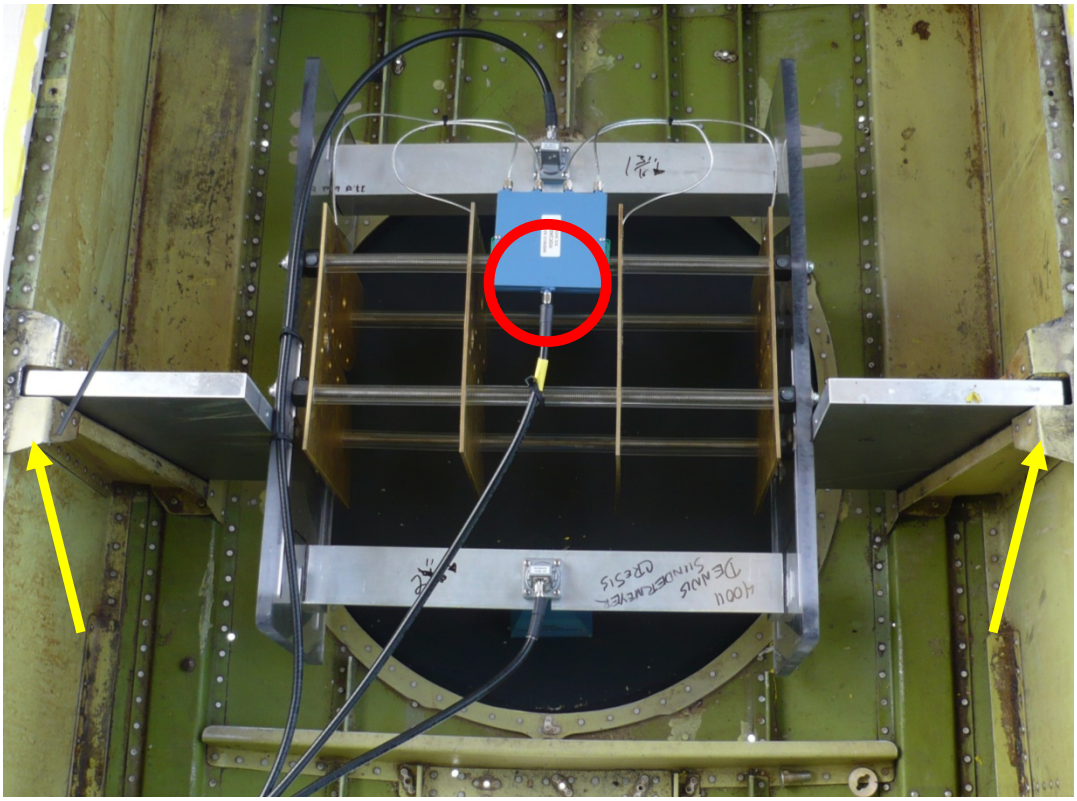

Figure 87. Installed antenna assembly. Yellow arrows show tie down points. Red circle shows where accumulation antenna cable is connected.

Connections

All alternating current (A/C) power connections are on the back of each chassis (as shown in the right half of Figure 71) using IEC-C13 compatible A/C power cables (consumer computer power cables). Each power cable is routed from the back of each radar chassis to one of the "protected" power plugs on the back of the Tripplite UPS located at the bottom of the rack. The UPS is connected to the aircraft A/C power bus. Figure 64 illustrates the aircraft power bus configuration for the Twin Otter. A/C power drops are supplied directed to each rack on the P-3 Orion. The user is encouraged to safely route and zip-tie the power cables as shown in Figure 71 to allow for easy access and troubleshooting. The user is also encouraged to attach snap-on ferrite beads, if they are available, to each power cable as close to the radar as possible; this helps reduce conducted electromagnetic interference.

The following connections are to be made on the front of the radar chasses:

- Connect the BNC/SMA adapters to the following 1U DAQ ports:
  - DAQ1
  - WFG1
  - WFG2

- Use 10" RF SMA/SMA cables to make the following connections:
  - TTL0 on DAQ → Switch on Power Amp chassis
  - TTL1 on DAQ → Switch on Power Amp chassis

- Use 6" RF SMA/SMA cables to make the following connections:
  - DAQ1 on DAQ → To DAQ on RF chassis
  - WFG1 on DAQ → DDS In on RF chassis
  - WFG2 on DAQ → LO In on RF chassis
  - TTL2 on DAQ → Switch on RF chassis
  - TX Out on RF chassis → TX In on Power Amp chassis
  - RX Out on Power Amp chassis → RX In on RF chassis

- Use the 16' LMR-300 antenna cable to make the following connection:
  - Antenna on Power Amp chassis → Power divider on antenna assembly

Software Operation, Data Recording, and Shutdown

The following steps should be followed exactly in order to prevent damage to the radar hardware or corruption of field data:

- Start the accumulation radar laptop, choose RHEL operating system
- Login as root (standard radar root password)
- Open a terminal window, type: `tail –f /var/log/messages`
- Mount the data drive, type: `mount /dev/sdX1 /mnt/1/`, where X is the drive letter of the data drive to mount
- Open another terminal window, type:
  - `cd /lprojects/fx2drv/`
  - `insmod fx2.ko`
  - `cd ../accum/`
  - `idl` (idl opens, confirm there are no license errors)
- Turn on the radar components in the following order:
  - Delay line (if performing a loop-back test)
  - Power Amp chassis
  - RF chassis
  - 1U DAQ
- Confirm in the log terminal window that the fx2 driver found the DAQ; just look for the word "Ready."
- On the IDL command line, type:
  - `dlm_register,'./serial_idl/serial_idl.dlm'`
  - `serial_open`
  - `.run mod_ddsreg.pro`
  - `.run wavegen.pro`
- A series of commands will echo to the screen, the IDL prompt will return after this process is complete. Confirm that "wrapped" echoes appear in the log terminal window.
- Open a third terminal window, type:
  - `dlm_register,"../dlm/fx2/fx2_idl.dlm"`
  - `dlm_register,"../dlm/serial/serial_idl.dlm"`
  - `dlm_register,"../dlm/shrmem/shrmem_idl.dlm"`
  - `daq_gui`
- The DAQ GUI program will open, click Update, then choose "0" from the channel menu.
- The a-scope window will open, confirm proper radar operation, then choose "on" from the record menu, confirm the echo "Record Event" on the log terminal window.
- From here the additional settings in the DAQ GUI program can be utilized to view different transformations of the received radar data.
- To shutdown:
  - Choose "off" from the record menu.
  - Choose "none" from the channel menu.

- On the second IDL terminal window (used to start the waveform generator), type: `.run wavestop.pro`
- When the program has finished echoing, the radar components can be shut off in the following order:
  - 1U DAQ
  - RF chassis
  - Power Amp chassis
  - Delay line (if used)
- Unmount the data drive.
- Shut down the laptop as normal.

Appendix C: Loop-back Testing

Loop-back testing, also referred to as delay-line testing, is a radar system testing method that mimics a single point target at a known distance. A loop-back test often includes a known attenuation, which simulates the spherical spreading loss of radiated waves, and a delay line (often optical), which mimics the time delay incurred due to the physical separation between the radar and the target of interest. For a radar with separate transmit and receive antennas, a simple loop can be created by passing the output of the transmitter through an attenuator, then through a delay line and feeding the output of the delay line into the receiver. For a radar with a single antenna (and T/R switch), the setup becomes more complicated. Figure 88 shows the loop-back test setup for the single-antenna configured radar.

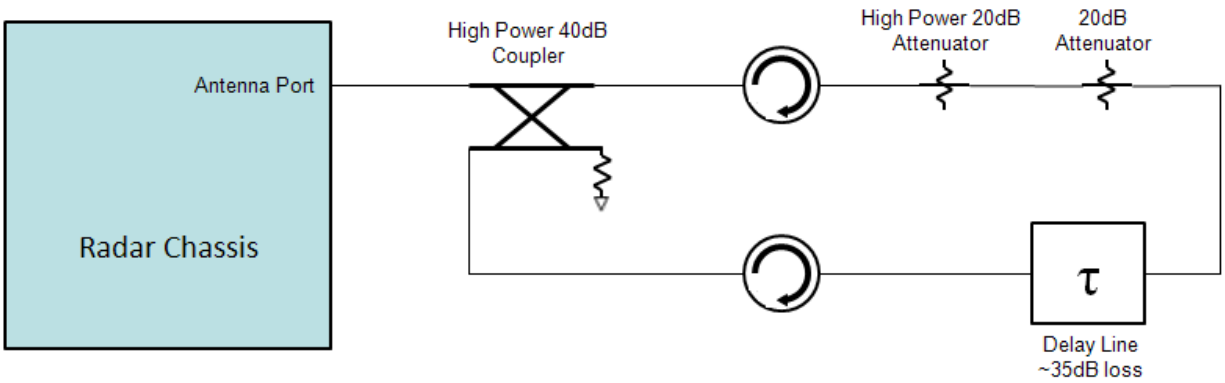

Figure 88. Loop-back test setup for single antenna configuration.

With a single-antenna configuration, a natural "loop" in the system is not physically apparent; it is closed by the presence of the T/R switch. To perform a loop-back test on a single-antenna configuration, an artificial "loop" must be created, taking advantage of the time delay introduced by the delay line in conjunction with the T/R switch timing to simulate a return signal. For this case, a coupler and isolators were used to create a loop. The output of the transmitter is connected to the input port of a high-power coupler (HD Comm Corp, 200 W, 40 dB coupling). The output port of the coupler is connected to a high-power isolator (Raditek

RADI-600-900M-S3-5WR-M1-b). This isolator protects the radar (and the coupler) from reflected energy due to impedance mismatches at the input of the delay line. The first isolator is followed by attenuators; in this case, a 20-dB high-power attenuator and 20-dB low-power attenuator. The attenuators are followed by the optical delay line. Figure 89 shows the delay line loss as a function of frequency. It is accepted that the loss across the 600-900 MHz spectrum is roughly 35 dB.

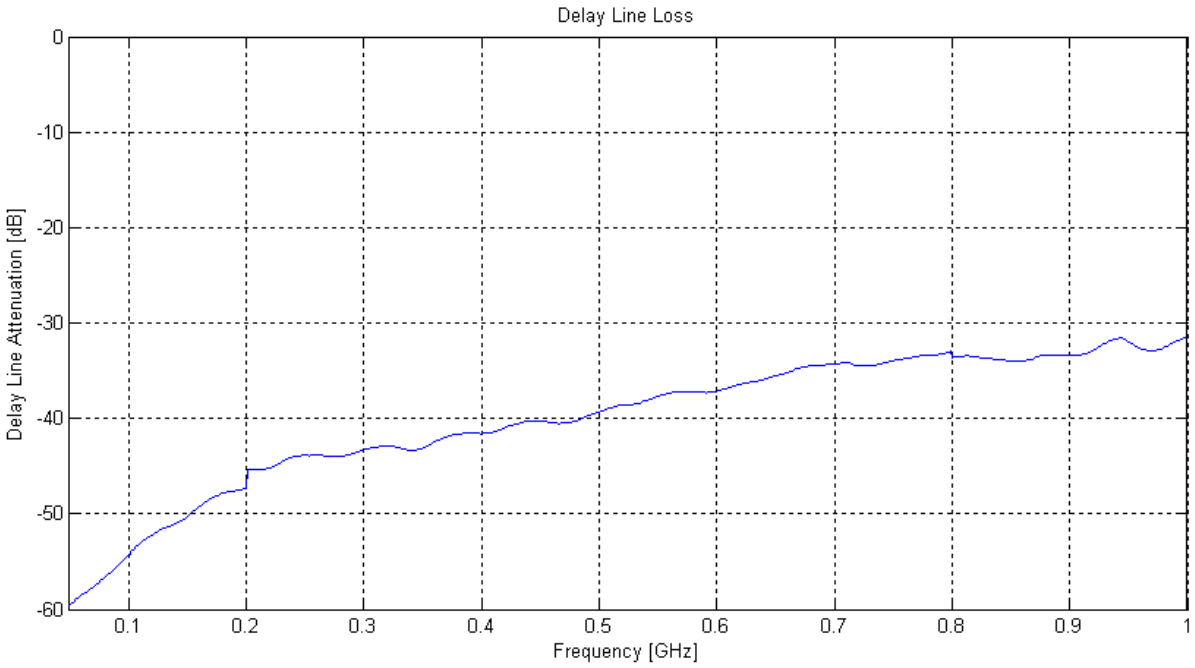

Figure 89. Measured delay line loss.

The delay line is followed by an additional isolator. Since some of the transmit signal will be coupled into the backward direction of the delay-line loop, this isolator is used to prevent the signal from damaging the output of the delay-line. Since the coupler has 40 dB of coupling and the isolator provides at least 15 dB of isolation, the maximum signal power impinging on the output of the delay line is roughly -15 dBm. Following this isolator, the delayed transmit signal is fed into the coupled port of the coupler where the signal is passed back to the radar chassis and to the receiver chain. Accounting for minimal loss within the coupler mainline and the isolators,

the total loss within the loop is about 118 dB. This is comparable to the actual loss expected as calculated in Section 3.1, shown in Table 1.

In order to simulate a point target return at a distance of 500 m (nominal platform altitude), an available 1067 m fiber optic delay line was used. Since the refractive index of fiber optic cable is typically 1.48, we would expect the total delay through this fiber spool to be 5.26 µs. Measuring the delay using a signal generator and oscilloscope, the total delay through the delay-line chassis was found to be roughly 5.15 µs, acceptably close to the expected value. To this delay we must add any additional delay incurred as the signal passes through the transmitter and receiver. Delay through the transmitter was negligible (<10 ns). Figure 90 shows the measured receiver delay is roughly 460 ns. This is a total loop delay of roughly 5.61 µs, a free space distance of 1683 m or a one-way travel distance of 842 m.

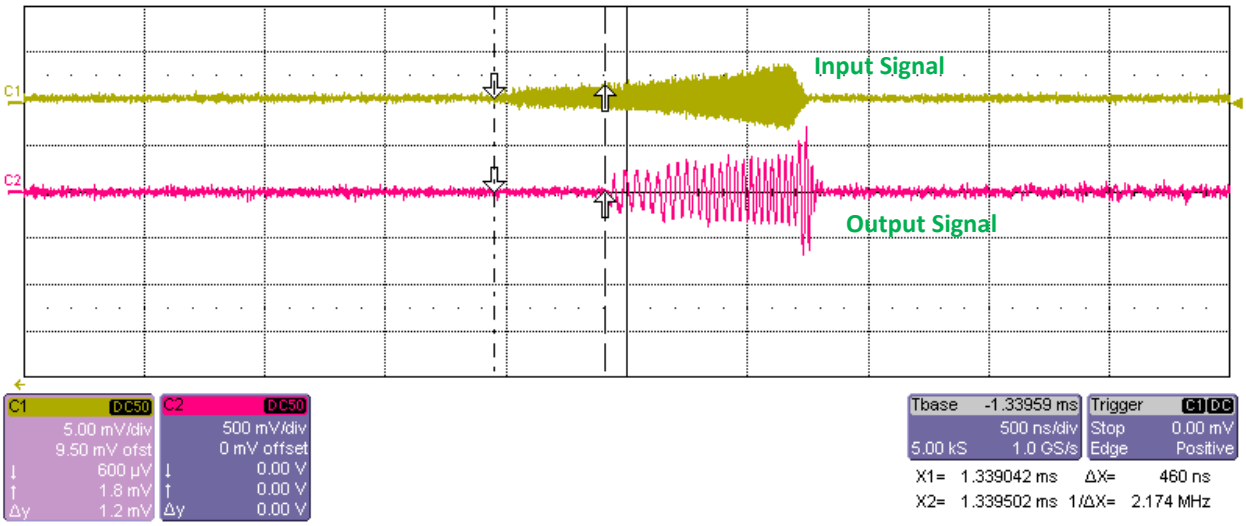

Figure 90. Measured receiver delay.

Settings within the digital hardware determine when the transmit waveform starts and when the receiver listen window starts. These delays are set to 500 samples and 1300 samples, respectively; this means there is a period of 500 samples between the start of the transmit chirp and the start of the receive window. Using the ADC clock of 125 MHz, this window is 6.4 µs. As calculated above, 5.61 µs of this window is occupied by the travel time of the waveform

through the loop, leaving 790 ns of delay before the ADC begins recording the impinging waveform. This delay means that the initial 790 ns of the waveform will not be recorded. Said another way, it will appear as if the return signal is 790 ns or 237 m closer to the receiver. Accounting for record delay, we would expect the return to appear at roughly 605 m instead of 842 m. The test data were recorded using the DAQ system using the setup described above.

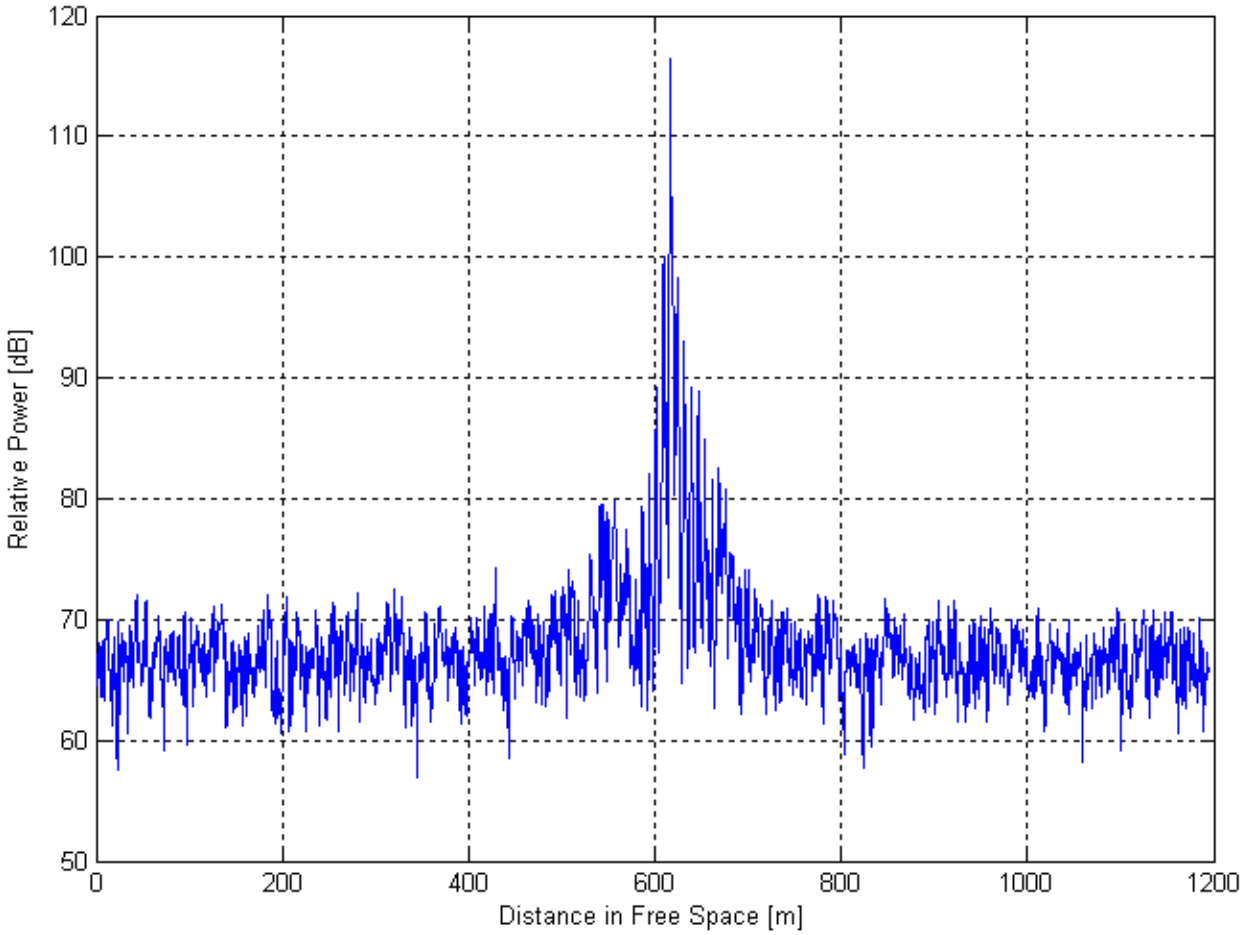

Figure 91. Delay line received signal.

Figure 91 shows the return signal at roughly 617 m, which is acceptably close to the calculated 605 m. The 12 m difference could be attributed to inaccuracies in the delay measurements and jitter in the ADC clock.

Appendix D: Chassis Construction

Great care was given to the design and construction of the radar chassis to minimize volume and weight, provide adequate cooling, and provide adequate EMI suppression. Two separate metal chasses were designed and constructed to house the radar components. One chassis houses the radar transmitter, receiver, and necessary linear power supplies. The other chassis houses the power amplifier, T/R switches, and necessary power supplies. These chasses house custom-designed, EMI-suppressive enclosures. In this appendix, we will present each custom-designed enclosure, comparing the model to the actual manufactured component.

RF Rack Chassis

The RF components are housed in a 24” by 17” by 3.5” aluminum enclosure. Since the layout of the RF rack chassis only contains the RF enclosure and two power supplies, an Inventor model was not created. Figure 92 shows the interior of the RF rack chassis, with the front of the enclosure facing to the right. The front panel includes a power switch, a power indication LED, and six SMA bulkhead connectors. The back panel contains the AC inlet filter. Black, white, and green wires are used to run AC power, using black for hot, white for neutral, and green for ground. AC power is run through the switch on the front panel before being passed to each power supply in parallel. The front panel switch is used to break the hot line only; a black wire is run from the rear inlet filter to the front switch and back to the power supplies. The neutral and ground lines are run directly from the rear inlet filter to the power supplies. Since the outer metal jacket of the AC inlet filter is in physical contact with the outer chassis at all times, a chassis ground connection was not installed. This chassis contains both a +15VDC (Acopian A15NT200) and a +5VDC (Acopian A5NT350) linear power supply. The

outputs of each of these power supplies are wired to the RF enclosure using a quick release C-Grid connector, using black wire for ground, red wire for +5VDC, and gray wire for +15VDC. The DC ground lines are tied together to establish a common ground. The front panel LED is powered from the +5VDC output, with a 100Ω 1/4W resistor in series. The six connectors of the RF enclosure are passed to the front panel of the chassis using 6" SMA-SMA jumper cables. The power wires are zip-tied together and to the chassis where necessary to ensure organization and prevent vibration that could lead to a connection failure.

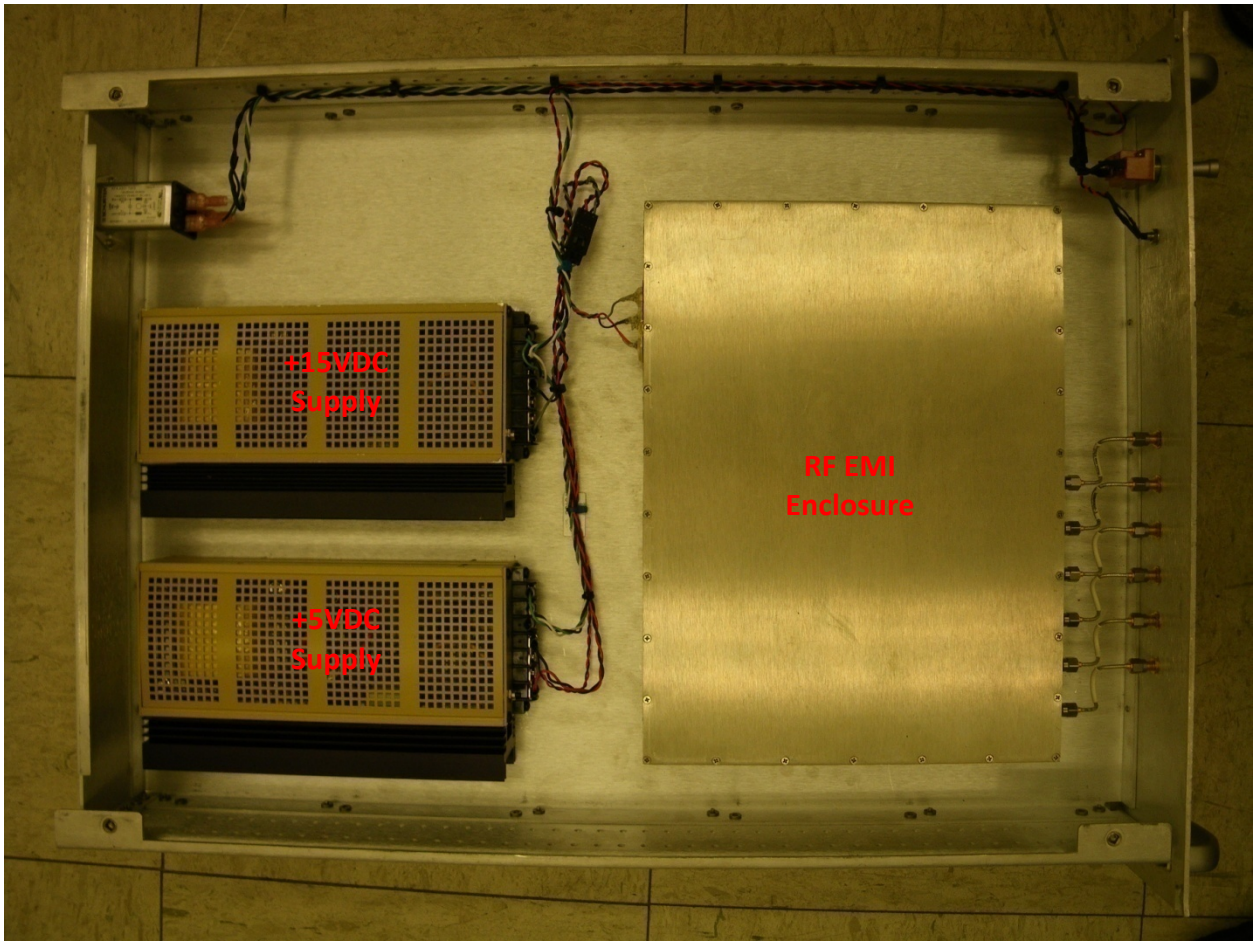

Figure 92. Photograph of the manufactured RF Rack Chassis, lid removed.

RF Enclosure

Figure 93 and Figure 94 compare the modeled to manufactured RF enclosures. The computer-aided drafting (CAD) modeling was done using Autodesk Inventor. This model was created to ensure that all the needed components would fit in the selected 12” by 9” by 1.75” enclosure. Four fans were installed (two pulling air in from the front and two pushing air out the back) to provide adequate cooling. DC power was wired to each device separately using multi-pin connectors (Molex 50-57-94XX) to allow the user to connect power to individual components during testing.

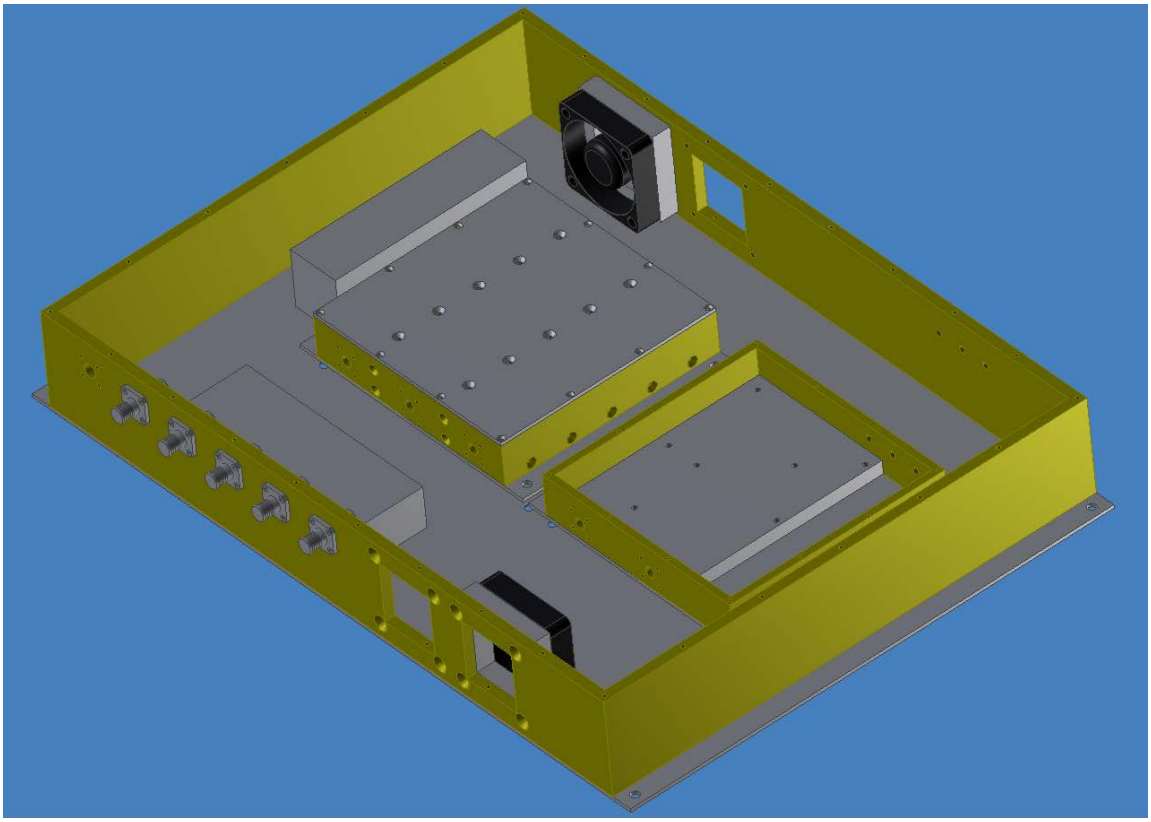

Figure 93. RF enclosure CAD model.

Four square openings, each with four threaded, countersunk mounting holes were milled into the enclosure shell to accommodate the fans and associated honeycomb EMI-suppressive grills. Six SMA bulkhead connector holes, each with four threaded, mounting holes were also

milled into the enclosure shell to accommodate the SMA pass-through connectors (transmitter in, transmitter out, LO receiver in, RF receiver in, IF receiver out, and receiver isolation switch control). Finally, three threaded holes were milled on the back face of the enclosure shell to accommodate the power inlet pins (+15VDC, +5VDC, and ground). Additional holes were milled into the bottom plate to accommodate mounting of the transmitter enclosure, receiver enclosure, and the IF amplifier.

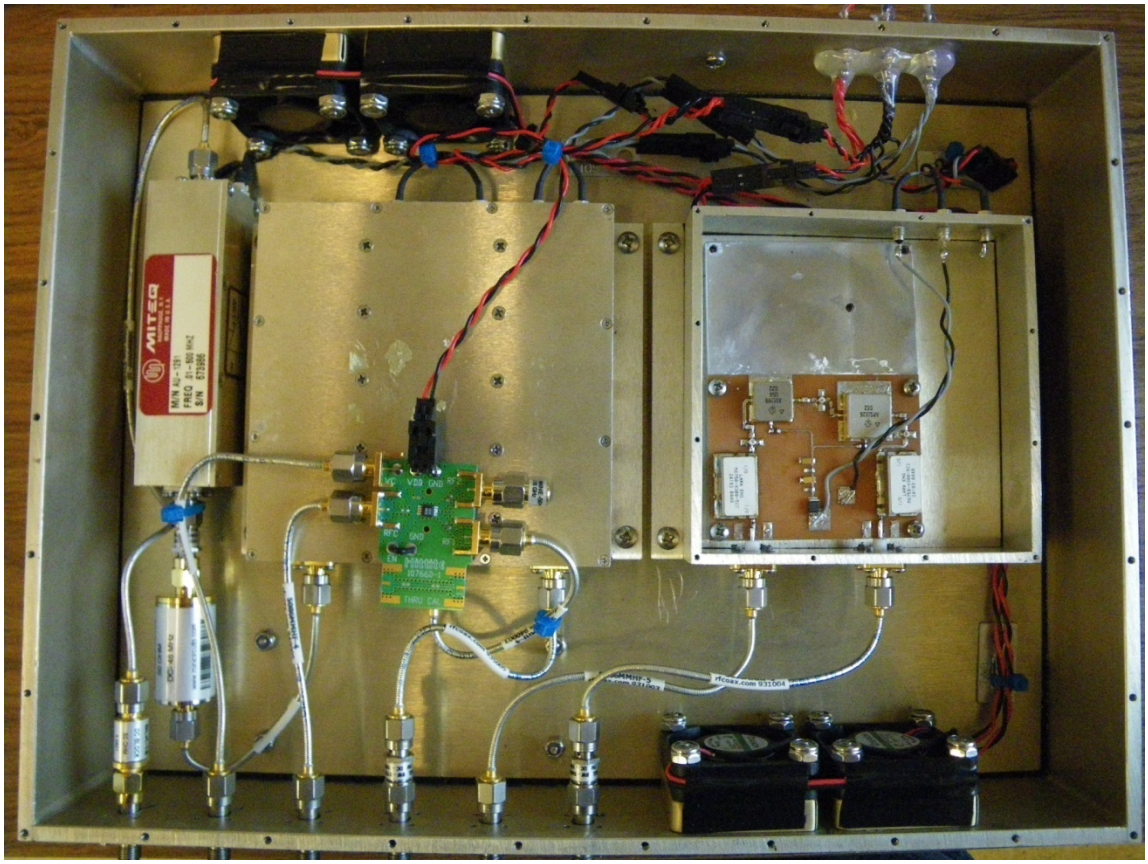

Figure 94. Photograph of the manufactured RF enclosure, lid removed.

Shrink tube and hot glue were used where necessary to cover exposed solder joints on power pins. Wires and cables were zip-tied both together and to clips on the chassis to ensure organization, prevent vibration, and to keep cables from interfering with fan operation. The receiver isolation switch is exposed; this is because the switch was added to the design after the enclosure was manufactured. This switch will be incorporated into the enclosure during the next

revision. The transmitter enclosure and the receiver enclosure are mounted to the base of the chassis using ¼" metal standoffs; this was done to allow for adequate air flow around both enclosures. SMA-SMA jumper cables are used to connect each component to each other and to the bulkhead connectors on the front of the box. Filters, attenuators, and DC blocks are used inline where called for by design.

Transmitter Enclosure

The transmitter enclosure consists of a 4" by 4" by 0.75" box with a 0.25" thick aluminum block mounted to the bottom plate. Figure 95 shows CAD model and Figure 96 shows the manufactured enclosure.

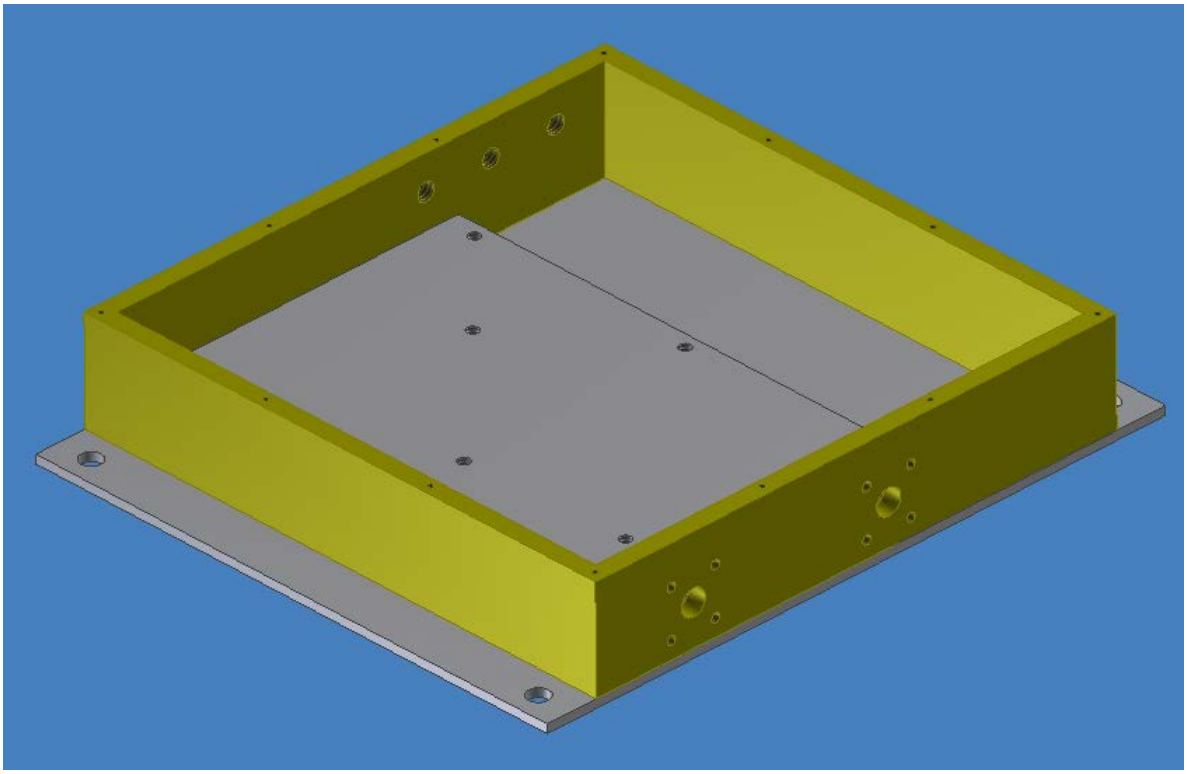

Figure 95. Transmitter enclosure CAD model.

The aluminum block is used to raise the transmitter circuit board off the floor of the enclosure so as to accommodate the SMA connectors and to provide a heat sink for the medium

power amplifiers used in the transmitter circuit. This block was oversized to accommodate a previous transmitter board design. However, a 0.125” gap was left along the connector edge of the board to allow for a portion of insulation to be left on the SMA pass-throughs; this was done to aid impedance matching across the transition from connector to circuit trace. Thermal paste was used in mounting the circuit board to the aluminum block to aid heat transfer. Two SMA bulkhead connector holes, each with four threaded mounting holes, were milled into the enclosure shell to accommodate the SMA pass-through connectors (input and output). Three threaded holes were also milled into the enclosure shell for DC power pins. Only +15VDC was used for this revision; previous designs called for +5VDC and this was left intact in the case it is needed in the future.

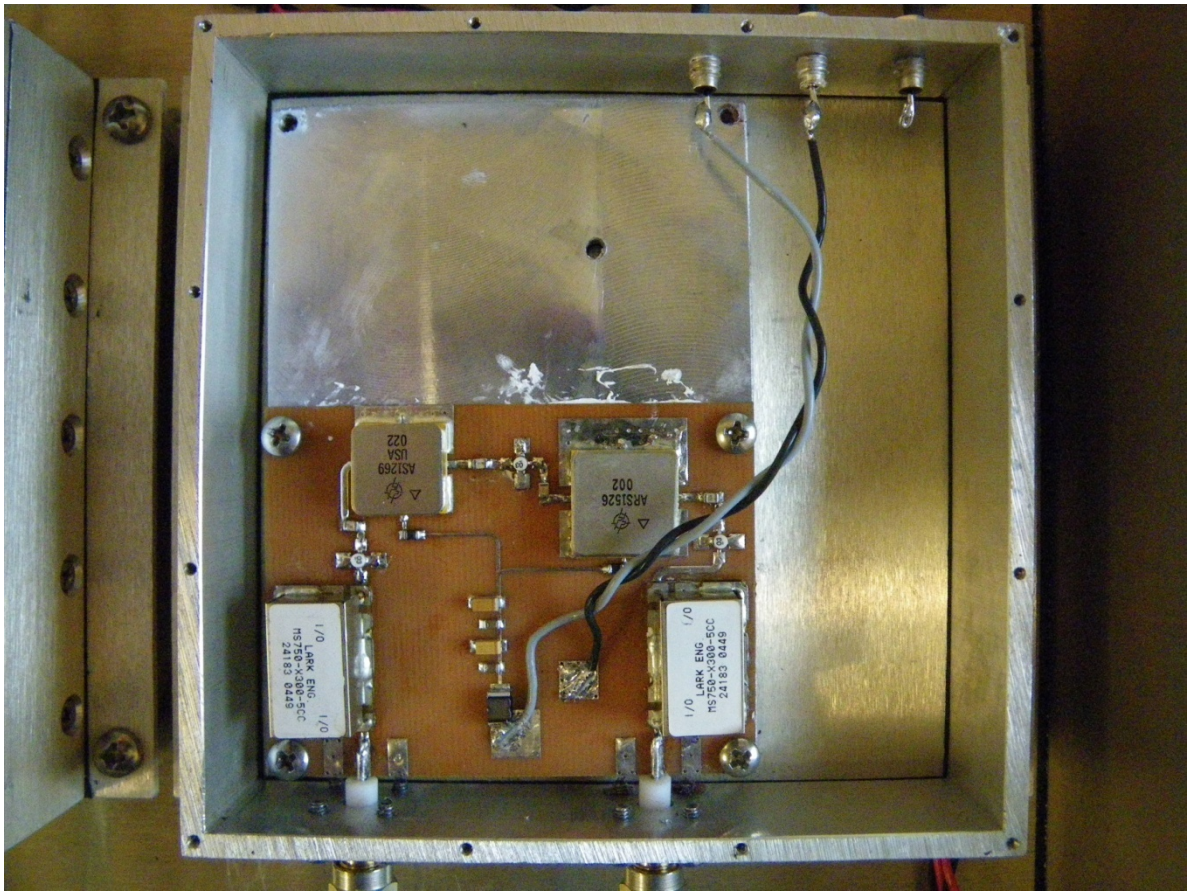

Figure 96. Photograph of the manufactured transmitter enclosure, lid removed.

Receiver Enclosure

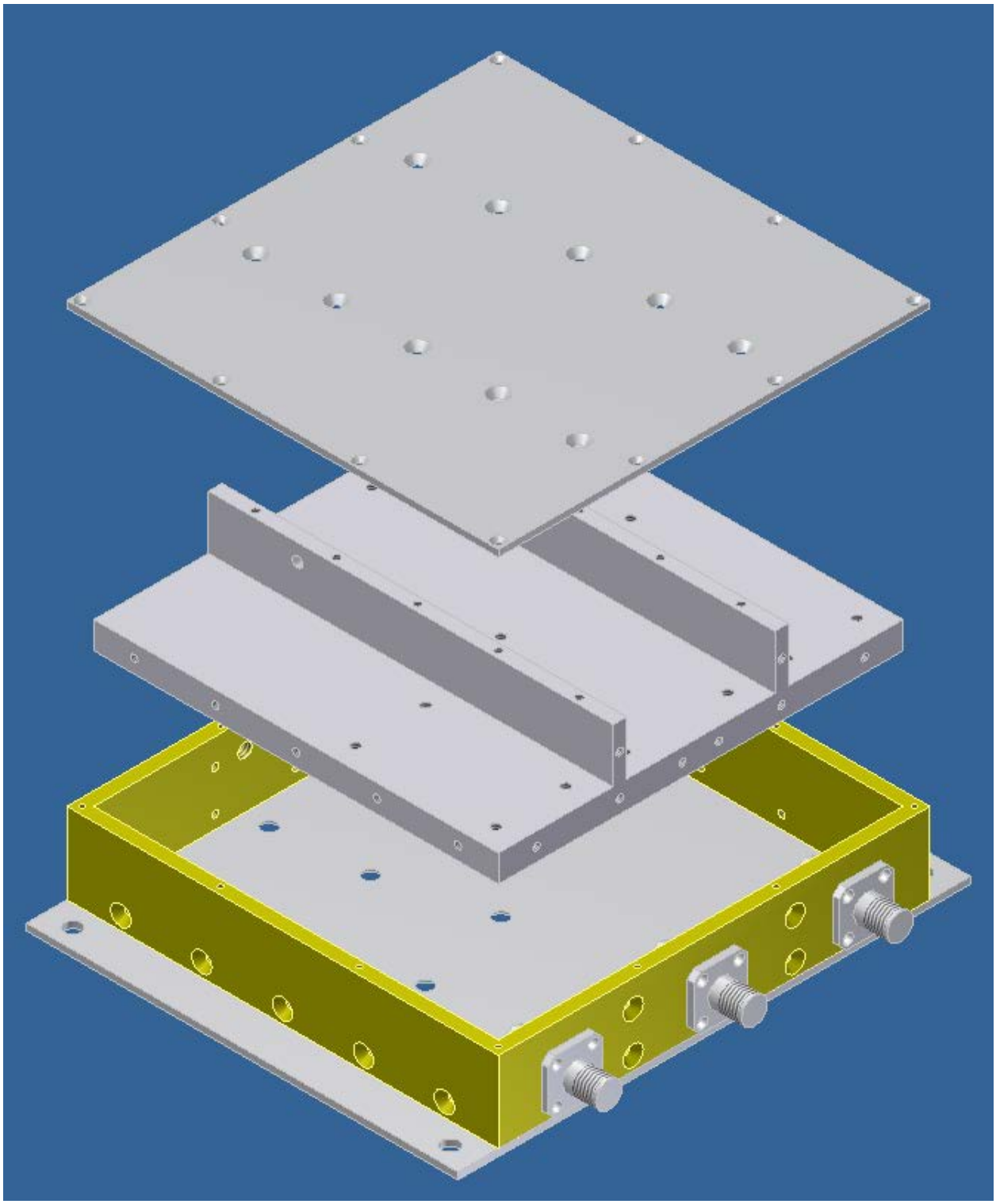

Figure 97. Receiver enclosure CAD model, exploded.

Similar to the transmitter enclosure, the receiver enclosure is also a 4” by 4” by 0.75” box with a 0.25” thick aluminum block mounted inside to provide an elevated mounting surface and heat sink. Due to the need to electromagnetically isolate each of the receiver subsections (i.e. LO, RF, IF), this block includes walls that stretch up to meet the lid of the enclosure.

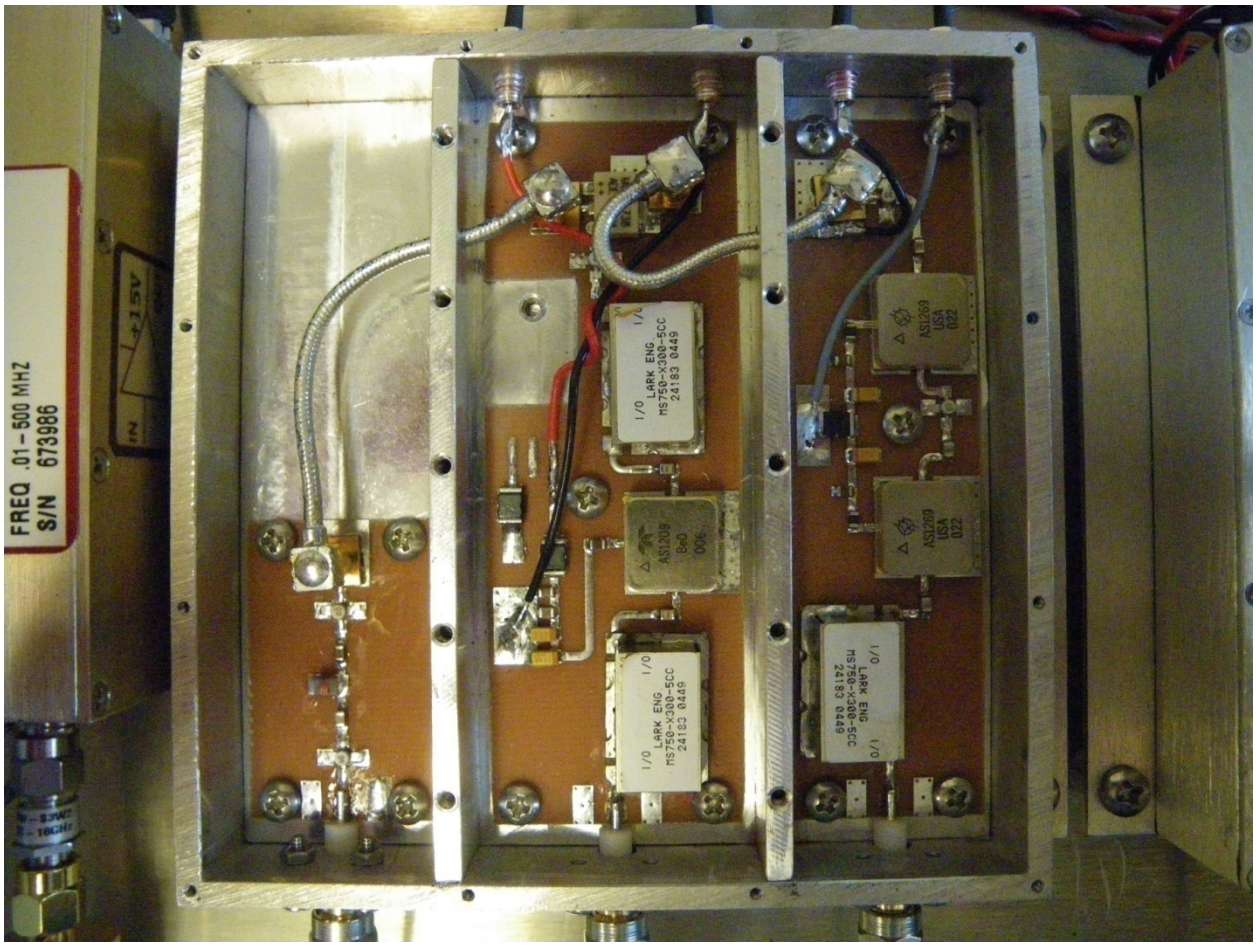

Figure 98. Photograph of the manufactured receiver enclosure, lid removed.

Unlike the block used in the transmitter enclosure, this block fits snuggly within the enclosure to provide sealed compartments for each subsection; the long seams around the edges and the tops of the dividing walls are broken into smaller gaps using screws. The largest gap between screws in this assembly is 1.287 in (0.33 m); this is much smaller than a quarter wavelength of the highest frequency of interest, and therefore electromagnetic leakage or

interference within our frequency band of interest should be minimal. Figure 97 shows an exploded view of the receiver enclosure CAD model.

Three SMA bulkhead connector holes, each with four threaded mounting holes were milled into the enclosure shell to accommodate the SMA pass-through connectors for each subsections (inputs for the LO and RF sections, output for the IF section). Four threaded holes were milled into the enclosure shell (two for the LO section and two for the RF section) to accommodate the DC power pins (+15VDC and ground for the LO section, +5VDC and ground for the RF section). DC power is needed to power the amplifiers. Power is not needed in the IF subsection of the enclosure since all components housed there are passive. Thermal paste was used to the mount the LO and RF subsection circuit boards to facilitate heat transfer to the aluminum block. The subsections are connected using MMCX connectors and exposed ground RG-405 cable. These cables are passed through small holes milled through the vertical walls of the aluminum block and soldered in place to close the gap between the cable and the hole's edge.

Power Amplifier Rack Chassis

The power amplifier components are housed in a 24" by 17" by 5" aluminum enclosure. As with the RF rack chassis, the AC power enters the chassis through an inlet filter mounted on the back panel and the hot line is run to a switch on the front of the box before being routed to each power supply. Neutral and ground are run directly from the inlet filter to each power supply. To provide extra cooling to the power amplifier, an AC fan is installed on the right side panel; this fan is spliced into the AC power lines after the switch.

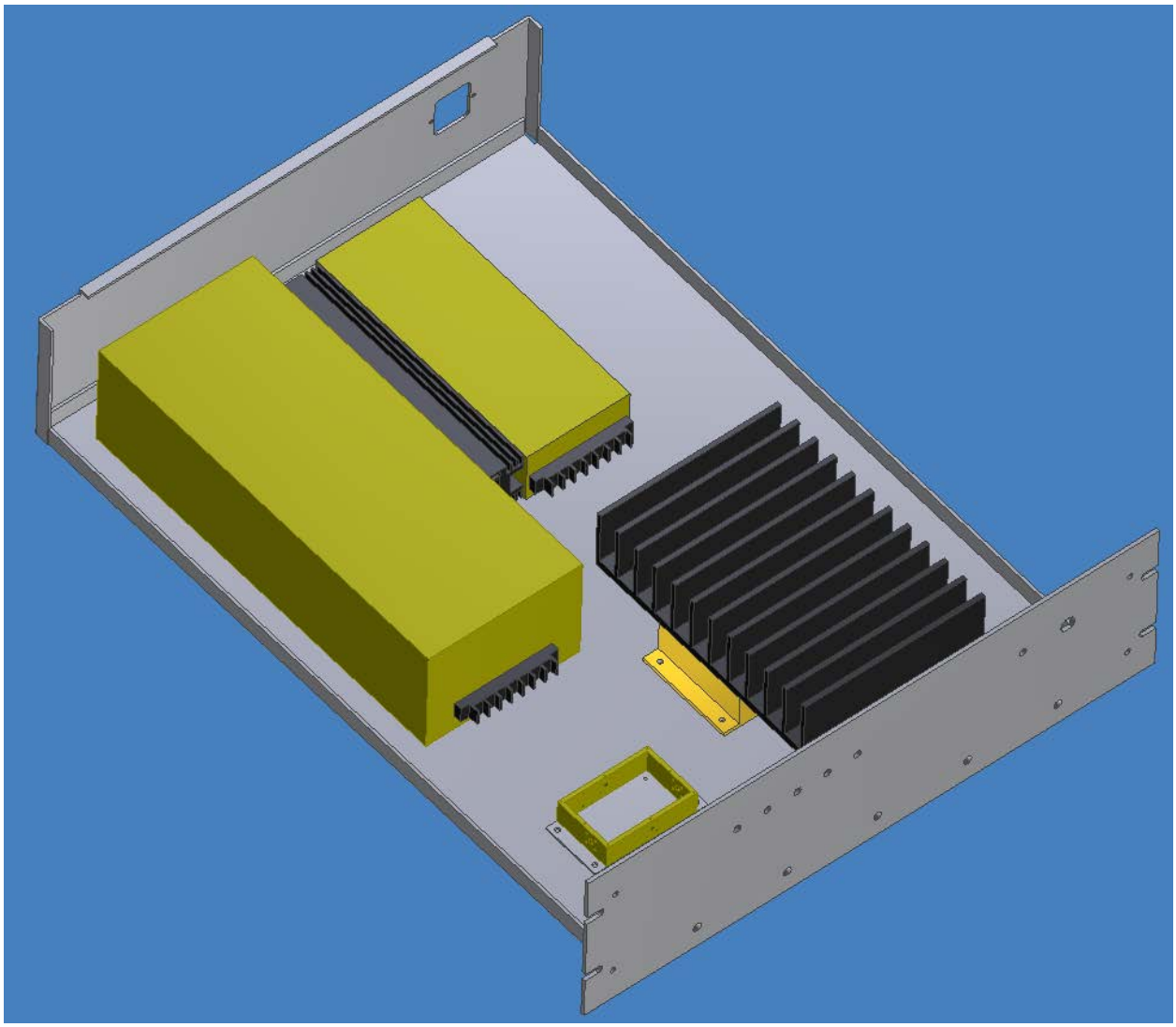

Figure 99. Power amplifier rack chassis CAD model.

A +15VDC power supply (Acopian A15NT200) is used to provide DC power to the T/R switches. A +24VDC power supply (Acopian A24MT550) is used to provide DC power to the power amplifier. A power indication LED is mounted on the front panel next to the switch and is connected to the DC output of the +15VDC supply with a 470Ω, 1W resistor in series. Five SMA bulkhead connector holes were milled in the front panel to accommodate the nessary RF and switch control connections (power amp in, two switch control lines, antenna, and out to receiver).

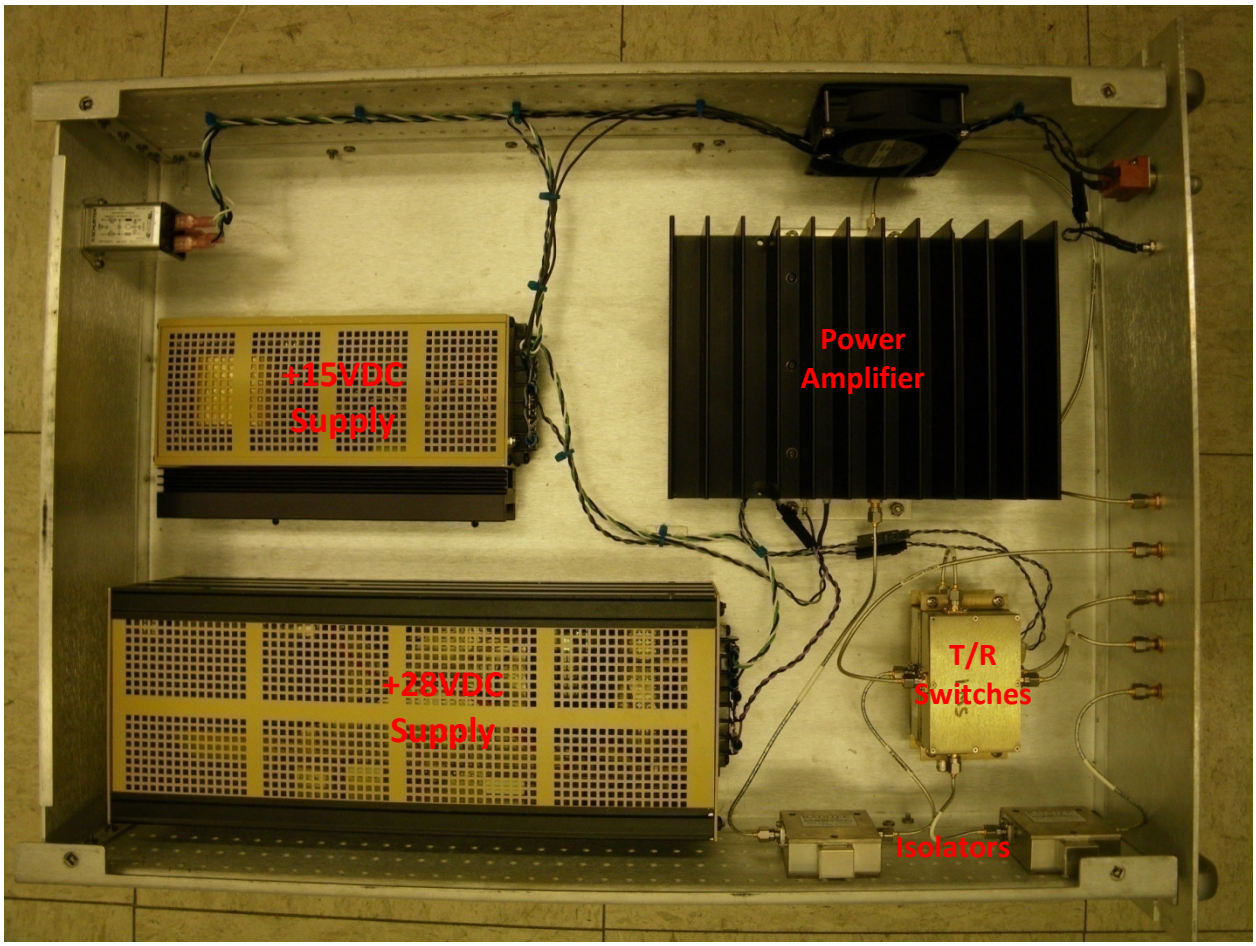

Figure 100. Photograph of the manufactured power amplifier chassis, lid removed.

To save space, the T/R switches were stacked using stand offs. Since the isolators were added to the design after the layout was finalized, they were attached to the side of the enclosure. SMA-SMA jumper cables were used to connect both between components and between components and the front panel. As with the RF enclosure, cables and power wires were routed neatly and zip-tied to each other, the enclosure floor, or the walls to prevent vibration and damage.

T/R Switch Enclosure

Each T/R switch assembly was housed within a 2” by 3” by 0.75” case. The circuit board was designed to fit snuggly within the inside of this box. Four SMA bulkhead connector holes

were milled into the enclosure wall to accommodate all three switch ports and a control line port. Two additional holes were milled to accommodate the DC power pins (+15VDC and ground). The circuit board was secured to the bottom plate using stand offs; washers were inserted to fine tune the vertical placement of the board to match the position of the connectors. Due to space constraints, the +15VDC power line was brought in and soldered to the top of the circuit board (gray wire in Figure 102), while the ground line was brought in and soldered to the bottom of the circuit board (unseen). The two lower mounting screws were also used to secure the voltage regulators into place while providing a heat sink. Hot glue was used to secure nuts and wires to prevent vibration damage.

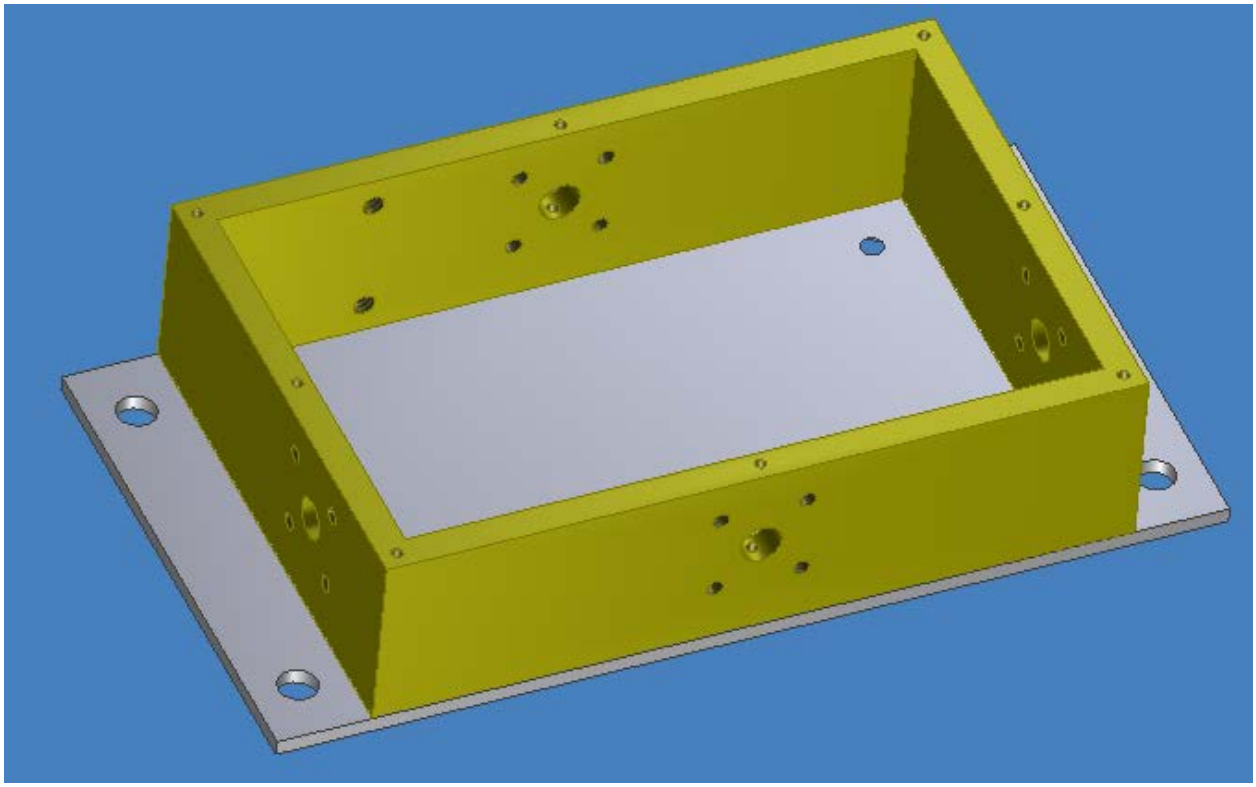

Figure 101. T/R switch module CAD model.

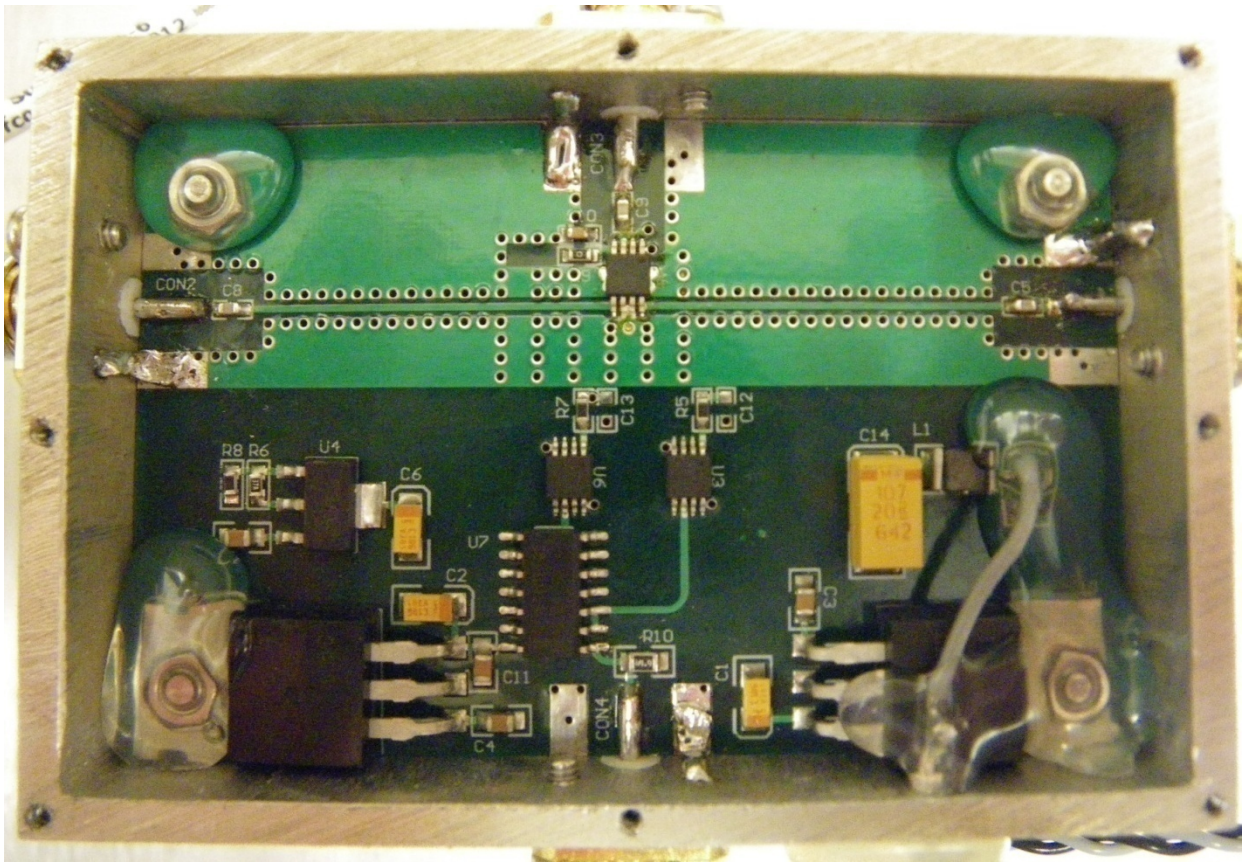

Figure 102. Photograph of the manufactured T/R switch module.

The use of a copper braid is to ensure proper grounding at each connector. This copper braid is sandwiched between the connector and the outer face of the enclosure, passed through one of the screw holes, and soldered to a ground pad. This was done after testing revealed issues related to inconsistent ground connections. Special ground pads with treaded screw receptacles will be incorporated into future designs.

Appendix E: EMI Considerations

This radar system often (if not always) operates in the field in conjunction with many other electrical and electronic systems including, but not limited to: a VHF depth sounding radar, a 2-6.5 GHz snow accumulation radar, a Ku-band radio altimeter, a laser altimeter, aircraft avionics, direct current aircraft electrical systems, alternating current electrical systems, and personal computers. All of these devices are capable of producing what this radar would see as noise within its receiver's frequency bands of interest (600-900 MHz RF band and 5-55 MHz IF band). Additionally, this radar system is capable of producing frequency content that would be seen as noise by these neighboring systems; and for this design process we will consider these other systems to be susceptible to this noise, regardless of their actual susceptibility. The goal is three-fold: reduce the amplitude of conducted and radiated emissions coming into this system, reduce the amplitude of conducted and radiated emissions between components within this system, and reduce the amplitude of conducted emissions (and somewhat of radiated emissions) leaving this system. While extensive analysis is beyond the scope of this document, basic "rules of thumb" were applied during design and construction; these instances will be presented. Extensive EMI analysis and testing is to be considered future work for this system.

Conducted and radiated emissions/susceptibility will be discussed in separate sections. Additionally, internal susceptibility will be discussed. Paths for emission/susceptibility will be presented and then implemented solutions will be discussed. This discussion will be limited to the RF components of this radar; the emission/susceptibility of the digital hardware, including the personal computer used for operating the radar and saving data, is considered beyond the scope of this document.

Conducted Emissions

Conducted emissions are controlled using filters on both AC and DC voltage lines. On the AC voltage side emission control is accomplished by using power entry modules with built in line filters. Each radar chassis has its own power entry module; a Schurter KFA 4301.7005 was chosen. This module (Figure 103) is rated to 10 A and provides at least 20 dB of common mode and differential mode at frequencies above 1 MHz [34].

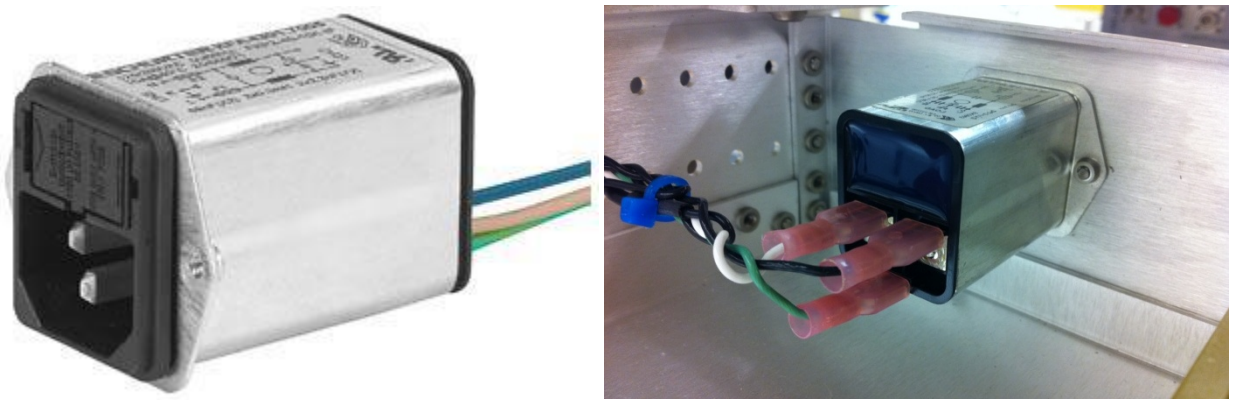

Figure 103. Photograph of the Schurter power entry module (right image: installed).

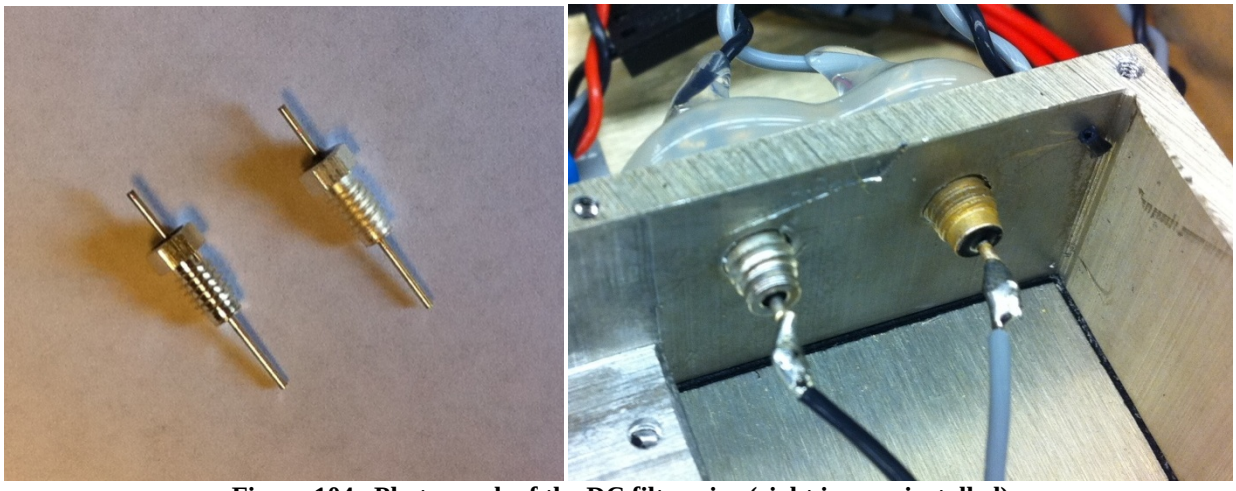

Figure 104. Photograph of the DC filter pins (right image: installed).

Filter pins were used on all DC voltage (and associated ground) lines each time it passes through a case wall. The pins are encapsulated capacitor and "pi" circuit filters built into 8-32 threaded bodies made by EMI Filter Company (Figure 104). Capacitor pins were used for all ground lines (B8C104A) and are rated for 50 VDC at 10 A. These pins provide an insertion loss

of at least 22 dB above 1 MHz, 47 dB above 100 MHz, and 65 dB above 1 GHz [8]. "Pi" circuit (shunt capacitor, series inductor, shunt capacitor) pins were used for all DC voltage lines (B8P753A) and are rated for 50 VDC at 10 A. These pins provide an insertion loss of at least 27 dB above 1 MHz and 90 dB above 100 MHz [9]. The insertion loss specifications of both the capacitor and the "pi" circuit pins exceed the specifications (provide more isolation) of the RF and IF filters used to reduce noise within the frequency bands of interest (RF: 600-900 MHz, IF: 5-55 MHz).

Additional filter networks are built into each circuit board. These filters were implemented as low-pass "T" filters (series inductor, shunt capacitor, series inductor). These networks were used to supplement the presence of external DC filtering networks. Typical component values were chosen: capacitors: 10 μF and 1 nF, ferrite beads: 100 Ω and 220 Ω at 100 MHz. Simple ADS simulations of this filter network showed attenuation values of 100 dB or more for frequencies above 5 MHz.

Radiated Emissions

Many measures were taken to reduce radiated emission propagation and susceptibility. These measures can be divided into two different groups: methods used to the reduce susceptibility of cabling and methods used to confine circuitry within Faraday shields.

While the use of filters on AC and DC wiring and circuit board filter networks were used to help prevent conducted emissions, all AC and DC wiring was constructed as sets of twisted pair (or twisted group for three wire AC). Twisting a voltage line with its associated ground return helps eliminate inductive coupling [31]. Additionally, coaxial cables were used for all RF connections between assemblies and external connectorized components. Coaxial cables were also employed to connect subsections of the receiver. The use of properly grounded (with

properly torqued connectors) coaxial cables confines signals to the inner conductor and prevents external EM field incident on the cable from influencing the signals traveling on the inner conductor. External coaxial connections were made with prefabricated 0.086" diameter hand-formable SMA cables from RF Coax. Internal connections (with the receiver) were made in-house using hand-formable RG-405 cables and MCX connectors.

All RF circuitry is housed within EMI-suppressing enclosures. The goal of these enclosures is to suppress the amplitude of electromagnetic fields incident on the enclosures for frequencies of 1 GHz and lower. 1 GHz was chosen because the radar related digital equipment uses a 1 GHz clock and much of the high-power aircraft communication equipment uses frequencies below 1 GHz. Additionally, all of the signals of interest produced by this radar are below 1 GHz.

Ideally, to achieve the manufacture's isolation specification the largest dimension of an opening in the EMI enclosure (i.e. connector or lid) should be much smaller than a wavelength at the highest frequency of interest. An opening dimension of $\lambda/10$ at 1 GHz would be preferred, but having all openings smaller than $\lambda/4$ at 1 GHz is acceptable; this dimension is 7.5 cm. The longest opening dimension of any enclosure is the lid gap between screws in the RF enclosure (Figure 94); this is 3.73 cm, or roughly $\lambda/8$ at 1 GHz. All other opening or seams are smaller than 3.73 cm.

As seen in the chassis construction section above, all exposed circuit boards are housed within these EMI-suppressing enclosures. The receiver isolation switch is considered partially exposed as it does not reside within the dedicated receiver enclosure, but it does reside within the RF enclosure. This circuit board is protected from external noise sources, but may still be subject to any signal leakage from the transmitter enclosure or any of the connectorized

components within the RF enclosure. A nested enclosure design approached was used. The circuit boards of the transmitter and receiver were housed within separate enclosures. Within the receiver enclosure, additional chambers were created to separate the RF, LO, and IF sections to reduce cross-contamination of frequency content between each section (especially the RF and LO sections with both operate at 600-900 MHz, but have different signal contents).

The transmitter enclosure, receiver enclosure, IF connectorized components, and cooling fans are housed within a larger enclosure for additional EMI suppression and organization. Large openings were created in the sides of this enclosure to accommodate proper air flow. Honeycomb vents (equipped with finger gaskets) were employed between these openings and the fans to reduce the electrical size of these openings. These vents are specified to suppress plane waves up to 1 GHz at least 115 dB. Brushless fans were used to prevent of high frequency noise generation.

The current design uses one common ground: chassis ground. This means that chassis ground is also used as the signal return path for many components, including the transmitter and receiver circuit boards. This common ground may make these circuits susceptible to unwanted signals present on the chassis ground, defeating the EMI-suppressive techniques discussed above. Future revisions will seek to solve this concern.

Appendix F: HFSS Antenna Simulations

Ansoft HFSS was used to perform electromagnetic simulations the of all-metal Vivaldi antennas. Initial simulations were performed on scaled single elements [28]. These simulations were adjusted to match the current design requirements and verify operation. This simulation was extended to a four-element array. Results for both the single-element and the array were compared with measured results, as seen in Figure 47 and Figure 49.

Single Element Simulation

Figure 105 shows the HFSS model for the single Vivaldi element. The original geometry is defined in [28]. Basic parameters are defined in Table 9. The dimensions used for the all-metal Vivaldi are exactly one-third of the dimensions used for the original depth sounder Vivaldi designed for the Meridan UAV [28]. Perfect electrical conductor (PEC) material was chosen for this all-metal simulation. A vacuum-filled solution airbox was placed around the antenna model with 60 cm added to the existing antenna dimension in each direction; this exceeds the rule of thumb that the airbox boundary should be at least one-half wavelength away from the structure at the lowest frequency of interest (for this case 600 MHz, $\lambda/2 = 25$ cm).

The element was simulated from 100 MHz to 1 GHz in steps of 10 MHz; these results are shown in Figure 47. Default mesh settings were used since the airbox definition is much larger than necessary. Figure 106 shows a close-up of the port definition used to excite the element. This limped port is defined using a sheet spanning the entire width and length of the element's throat placed at a distance of 3.5 mm from the edge of the circular resonator. The integration line was defined in the Y dimension; its direction is arbitrary. This choice defined the E-field to be in the plane of the antenna, which is optimal for propagation using a Vivaldi element [28].

Table 9. All-metal Vivaldi geometry parameters.

Parameter	Value
Overall Z dimension (length)	20 cm
Overall Y dimension (width)	22 cm
Overall X dimension (thickness)	3 mm (1/8”)
Mouth opening	21 cm
Throat width	0.83 mm
Circle resonator diameter	19.17 mm
Distance from resonator to excitation point	3.5 mm

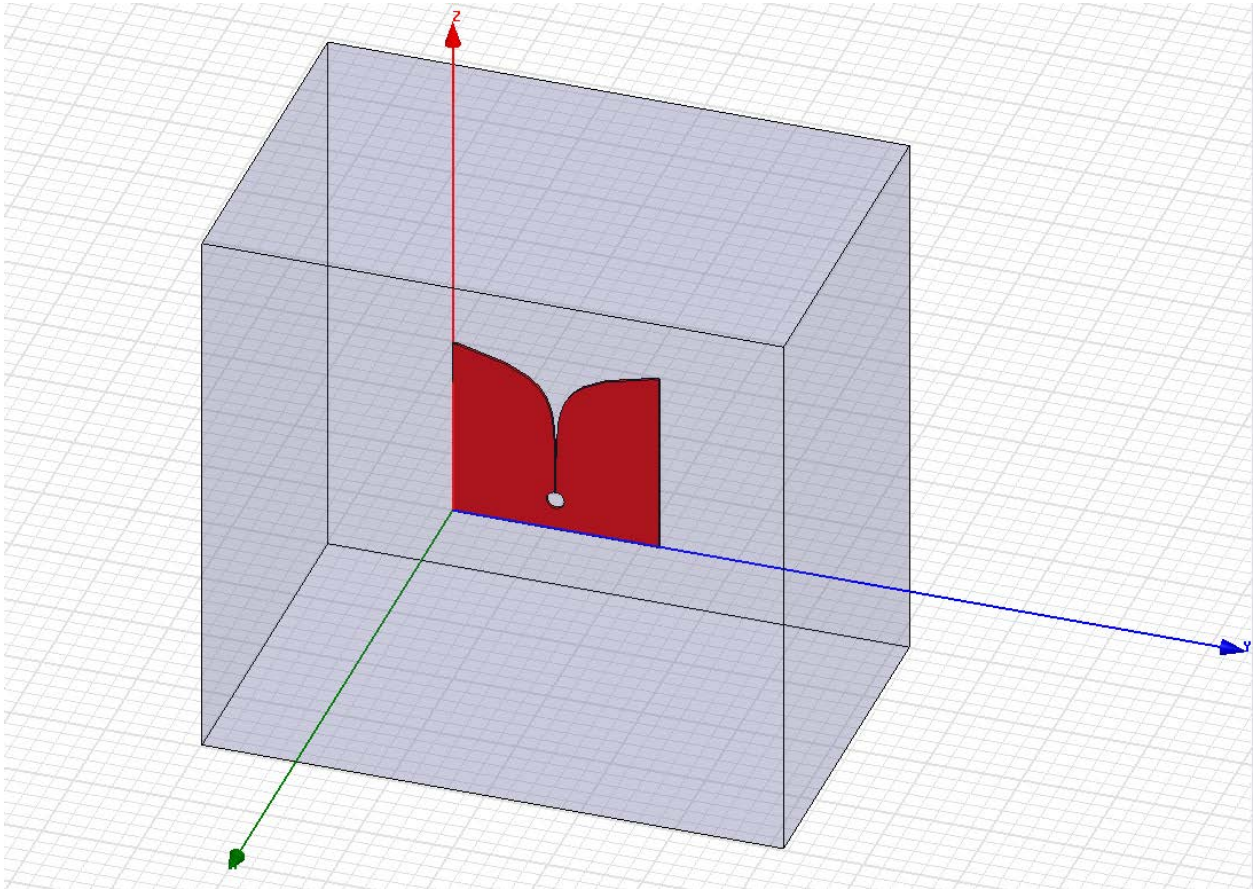

Figure 105. HFSS model of single Vivaldi element.

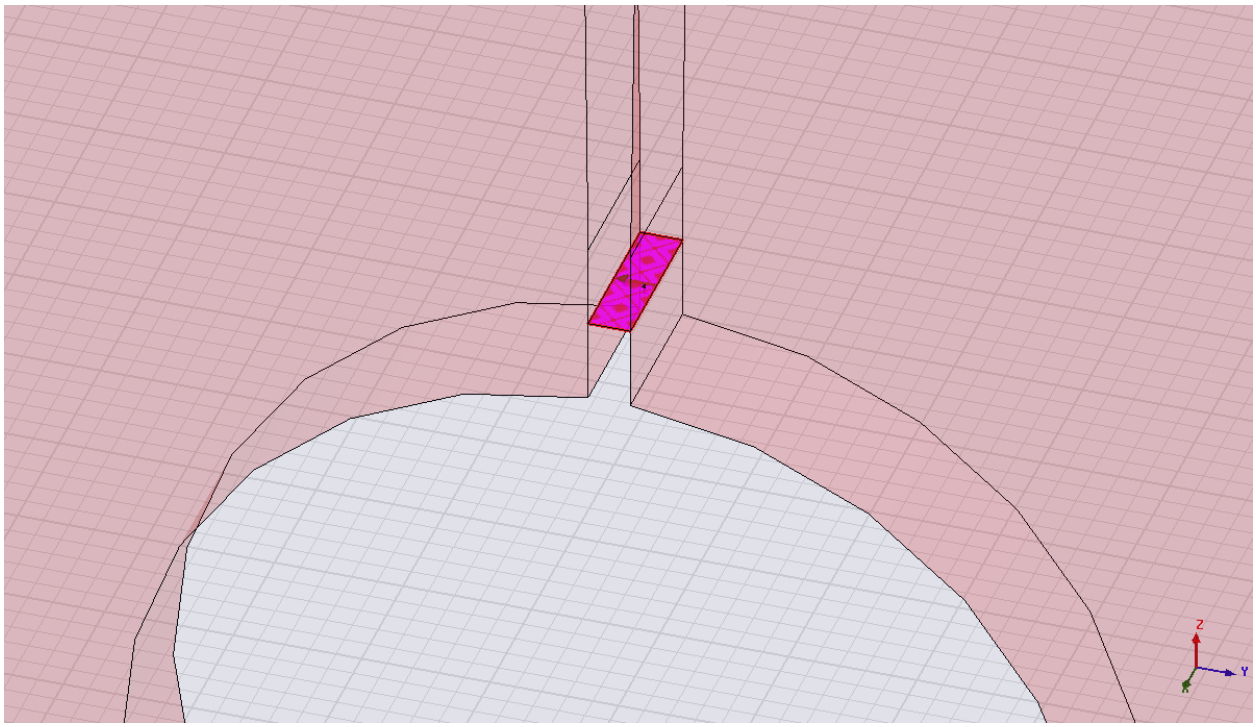

Figure 106. HFSS Vivaldi port definition.

Array Simulation

This simulation was extended to include four identical elements in an H-plane array configuration. This model was constructed by array-copying the element and airbox of the original model, merging the resulting four airboxes to create one solution box, and redefining each port to be independent. The same simulation parameters were used. Four S11 measurements resulted; these were fed into the ADS simulations discussed in Section 3.3.4. Care was taken to make sure that the integration lines on each port were defined in the same direction so as to excite each element correctly, in an additive manner. Figure 107 shows the model layout for the array simulations. Results from these simulations are included in Figure 49.

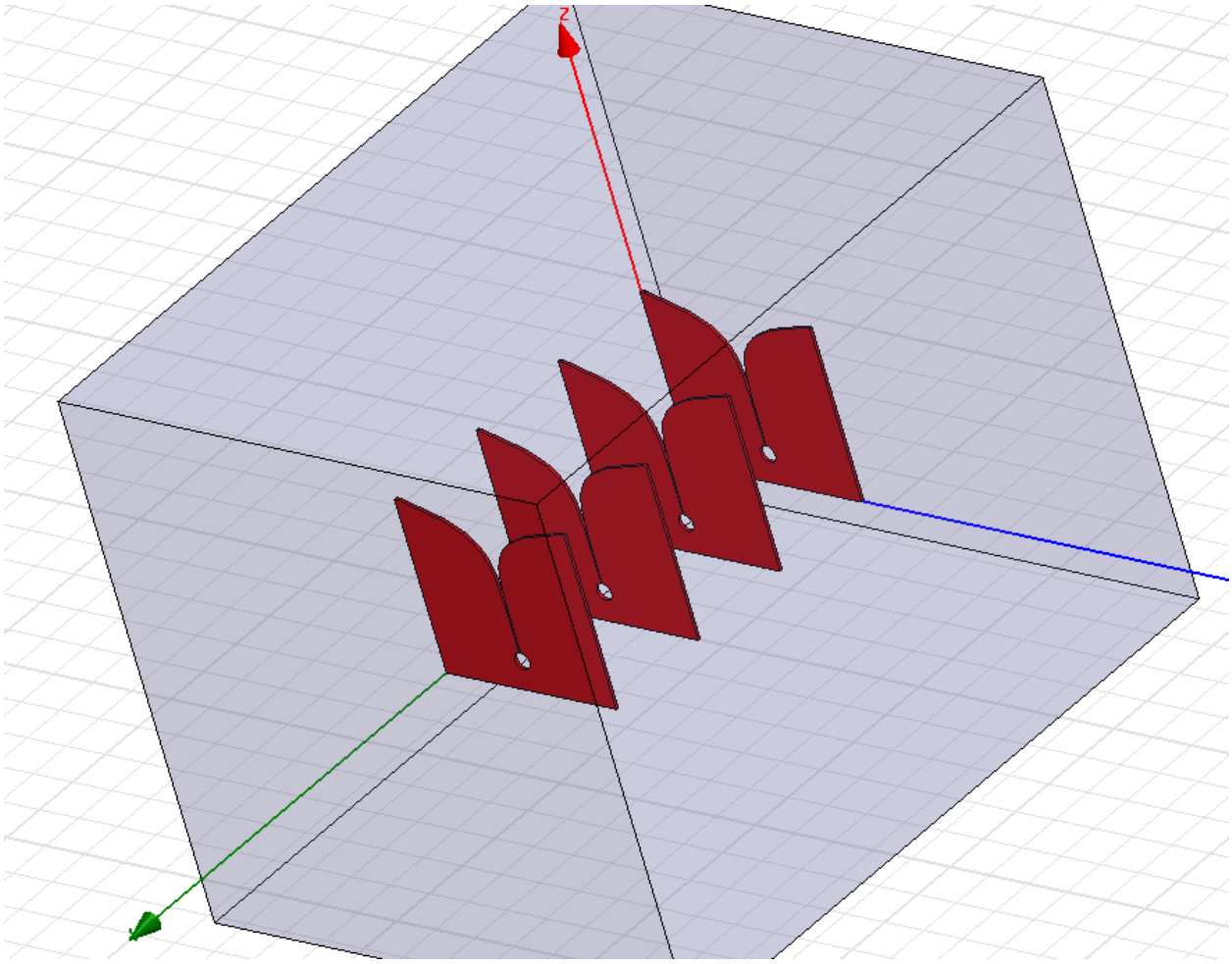

Figure 107. HFSS Vivaldi array model.

Appendix G: P-3 Antenna Array

Since considerably more space was available for antennas on the NASA P-3 Orion compared to the Twin Otter used in the winter 2009-2010 survey, it was decided that a different antenna array would be designed and used. The key concern was to design and build an array that would provide more gain than the small four-element Vivaldi array used on the Twin Otter. Space within the P-3 bomb bay allowed for the development of a two-element by four-element elliptical dipole array.

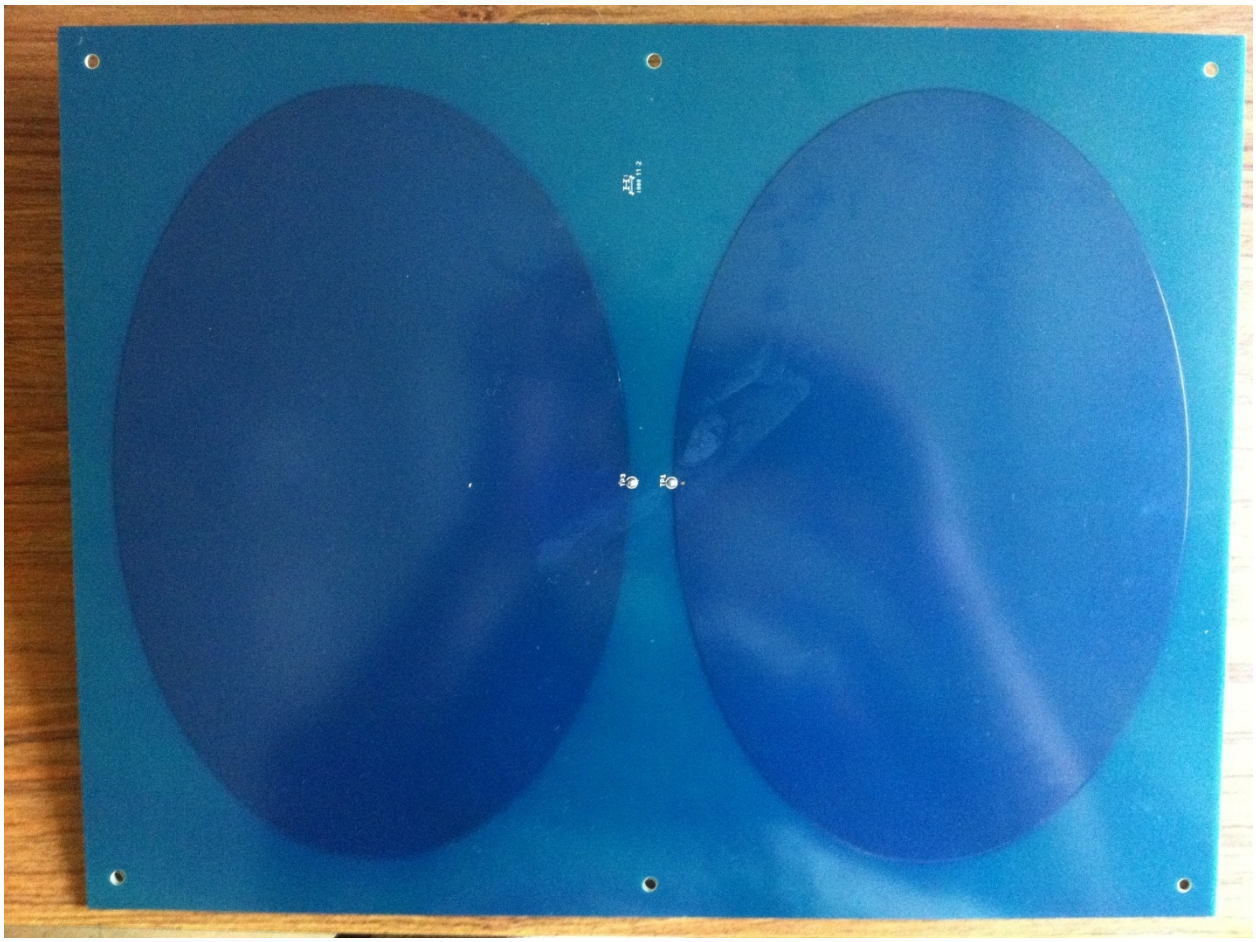

Figure 108. Photograph of an elliptical dipole element.

An elliptical dipole was chosen for its ease of design and known wide bandwidth characteristic [26] [42]. Figure 108 shows the bottom side of a single element. The two elliptical copper regions are visible. HFSS was used to tune the major and minor axis

dimensions as well as the spacing between each half, and the distance between the element and the ground plane.

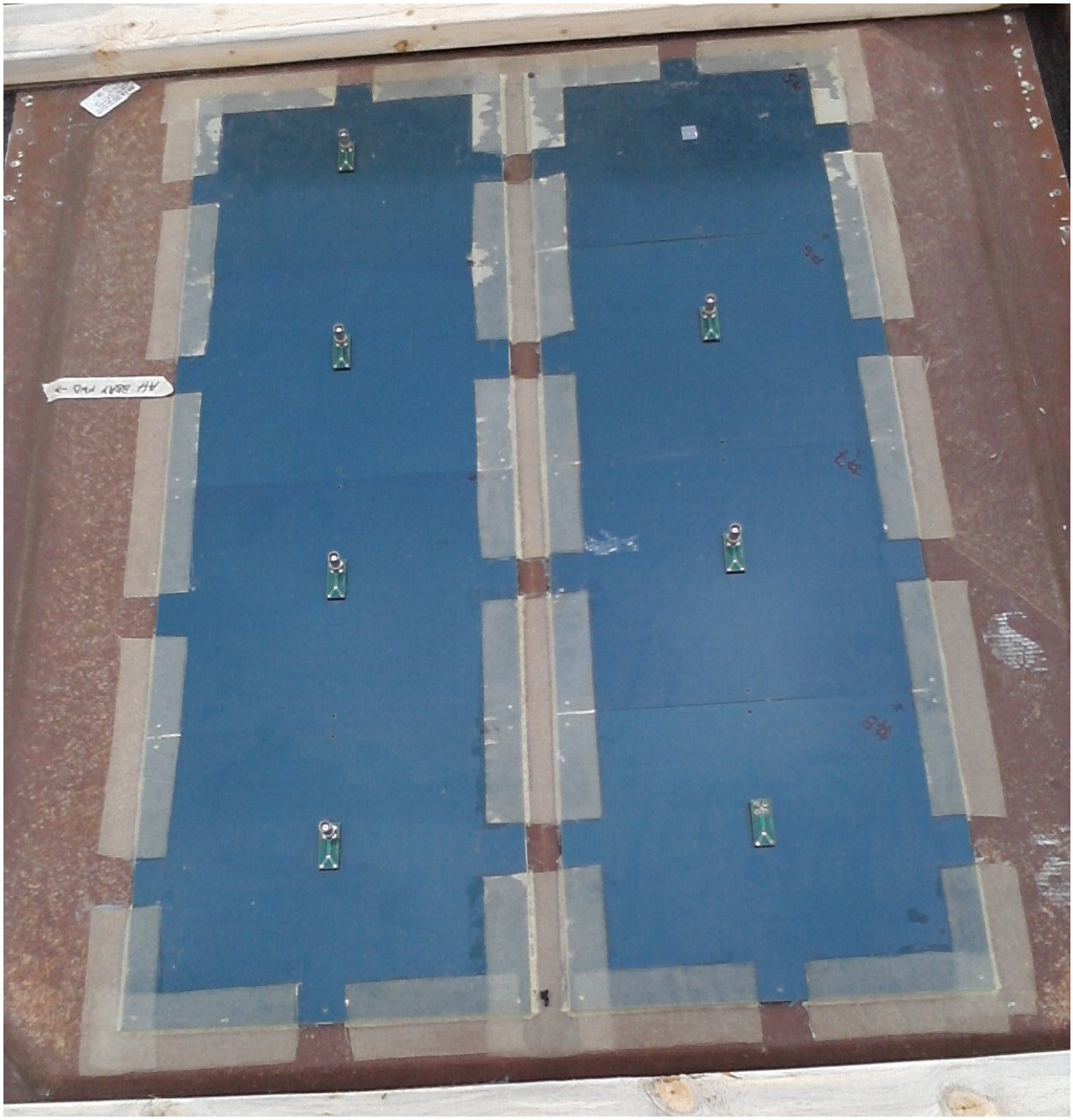

Figure 109. Photograph of the elliptical dipole array mounted on P-3 panel.

Figure 109 shows the eight elements mounted on the aircraft radome panel. The panel was designed and fabricated by the KU Aerospace Engineering department. It consists of multiple layer of fiberglass with foam sandwiched between to provide rigidity (to prevent

"oil-canning" during flight). Strips of aluminum were sandwiched between the fiberglass layers around the perimeter to allow for sturdy mounting to the aircraft. The elements were fiberglassed into place. Experimental measurements showed that a 3 cm gap between the two rows of elements improved the return loss of the element over having them butt against each other. This gap also allowed for considerably less fiberglass to be used to mount the antennas to the panel.

Figure 110 shows the close-up view of the balun and connector board used to feed each element. A BNC connector was chosen for easy installation. A 50 Ω trace feeds a 50 Ω RF transformer (balun, MiniCircuits TCN2-122+). 50 Ω traces are used to connect the unbalanced side of the transformer to metal posts that pass through the antenna board to connect to the copper patches on the bottom side. Since this balun board lies between the radiating elements and the ground plane (the ground plane can be seen in Figure 111), its presence does affect the return loss of the element (and the return loss of the array). It was found that increasing the distance between the balun board and the antenna board reduced this influence. A couple pieces of foam tape were used to elevate the balun board. Simulations revealed that a spacing of 10 cm between the antenna array and the ground plane would be ideal. Lab measurements showed that this distance was acceptable between 8 cm and 12 cm, with slight improvement closer to 12 cm. A 12 cm spacing was chosen for the final installation.

Figure 111 shows the installed ground plane, 1-to-8 splitter, and cables. Figure 112 shows the antenna cables passing through the ground plane and connecting to each element. Positioning of the holes in the ground plane was chosen so that each cable could pass vertically between the ground plane and the antenna element; this was done to minimize the effect of the

cable on the element (and array) return loss. Rubber grommets and brackets were used to secure the cables, preventing vibration that may damage the fragile balun board during flight.

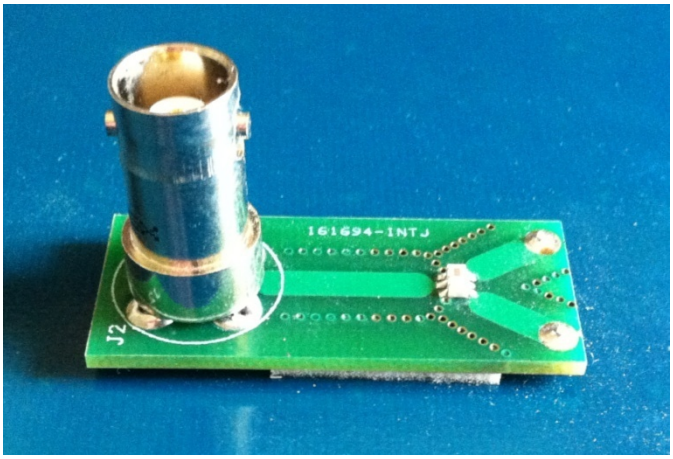

Figure 110. Photograph of the elliptical dipole balun (mounted).

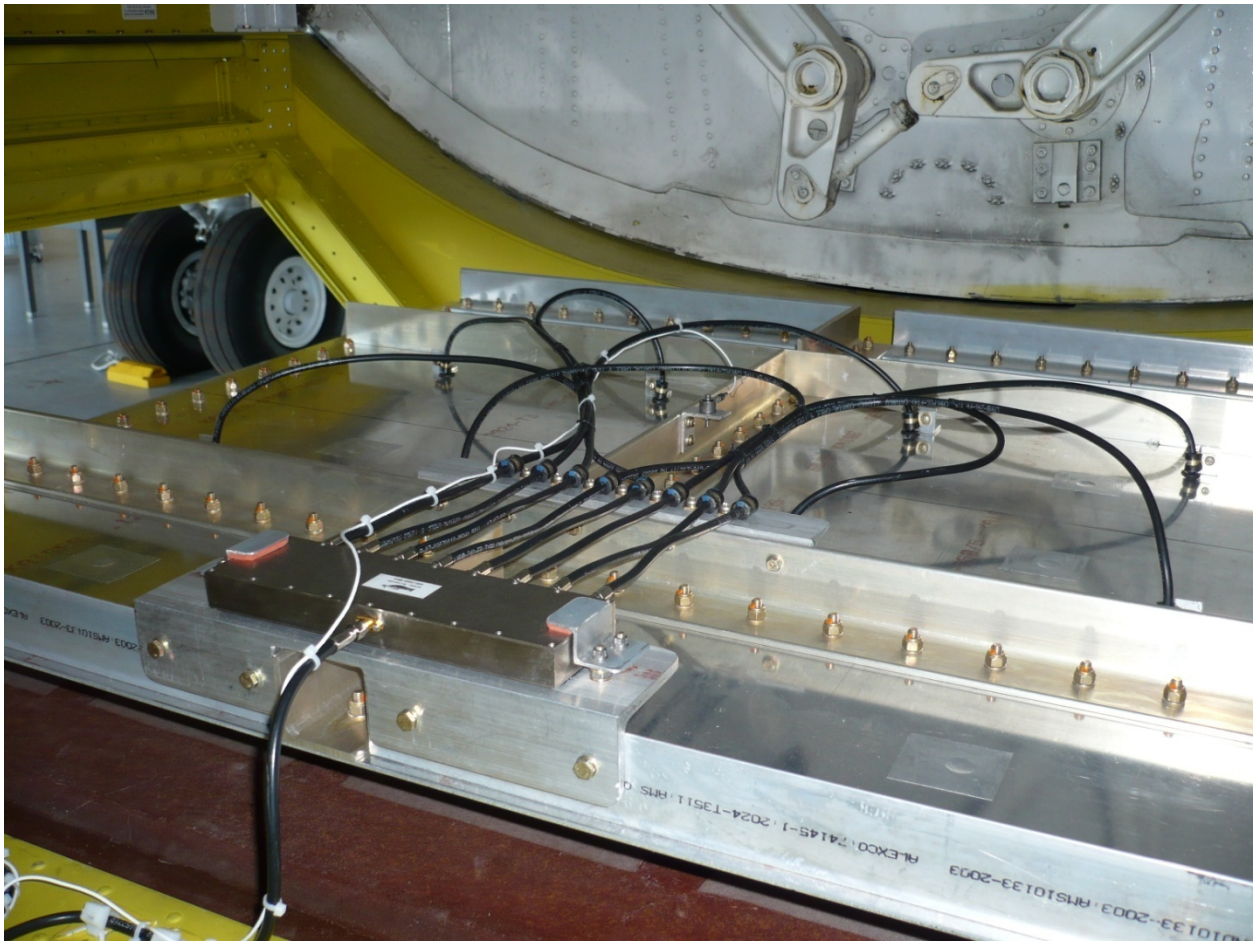

Figure 111. Photograph of the elliptical dipole array ground plane and splitter (installed).

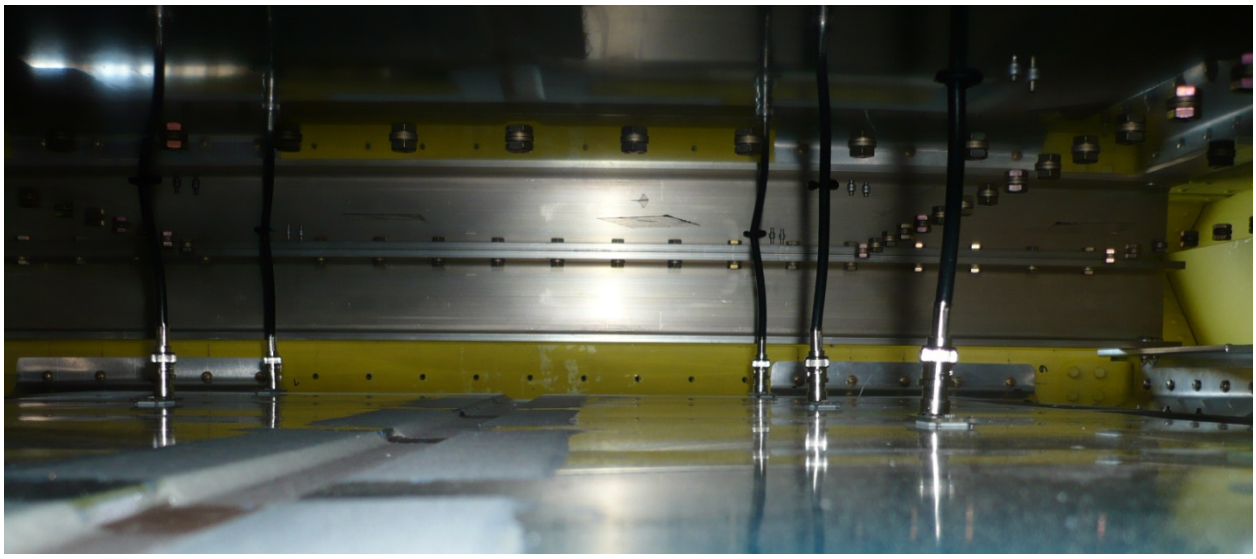

Figure 112. Photograph of the elliptical dipole array installed, cables passing through ground plane and connected to elements.

Figure 115 shows the return loss of each elliptical dipole element as measured in the laboratory using a vector network analyzer (VNA). These measurements were taken with the elements mounted on the radome panel, positioned upside down (pointing skyward) with a ground plane spaced 12 cm from the elements and elevated roughly 1 m off the ground. Figure 113 shows a drawing of this test setup. Figure 114 shows a diagram of the element layout on the radome; element numbers are referenced to the traces in Figure 115. Each element in the array was measurement separately. The VNA was connected to the feed cable of the element under test. Unused elements were terminated with 50-Ω loads. It was found that each element exhibited more than 1.4 GHz of bandwidth (-10 dB) between ~500 MHz and ~1.9 GHz.

These elements were measured together, using a 1-to-8 splitter (Broadwave Technologies 151-040-008). Figure 116 (blue trace) shows the return loss measured at the input to the splitter. The additional ripples in the response are caused by resonances within the splitter (likely a result of the distributed element design). While small jumps in the return loss within the band of interest (600-900 MHz) above -10 dB occur, these jumps did not exceed -8 dB; the electrical performance of this array was deemed acceptable.

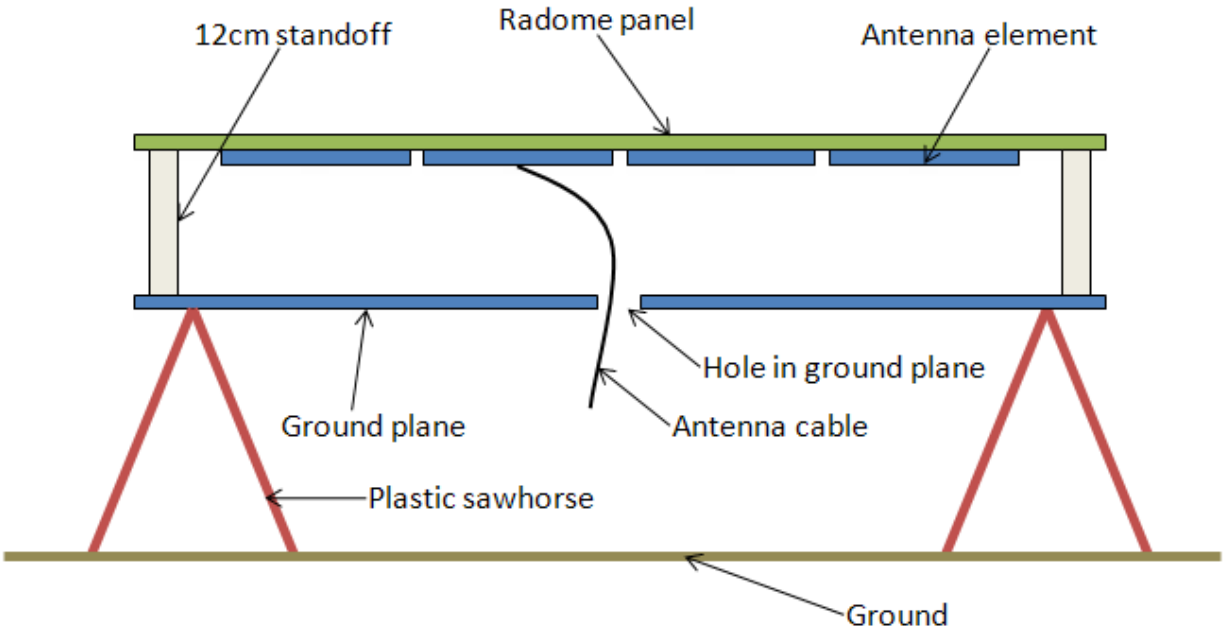

Figure 113. Elliptical dipole measurement setup.

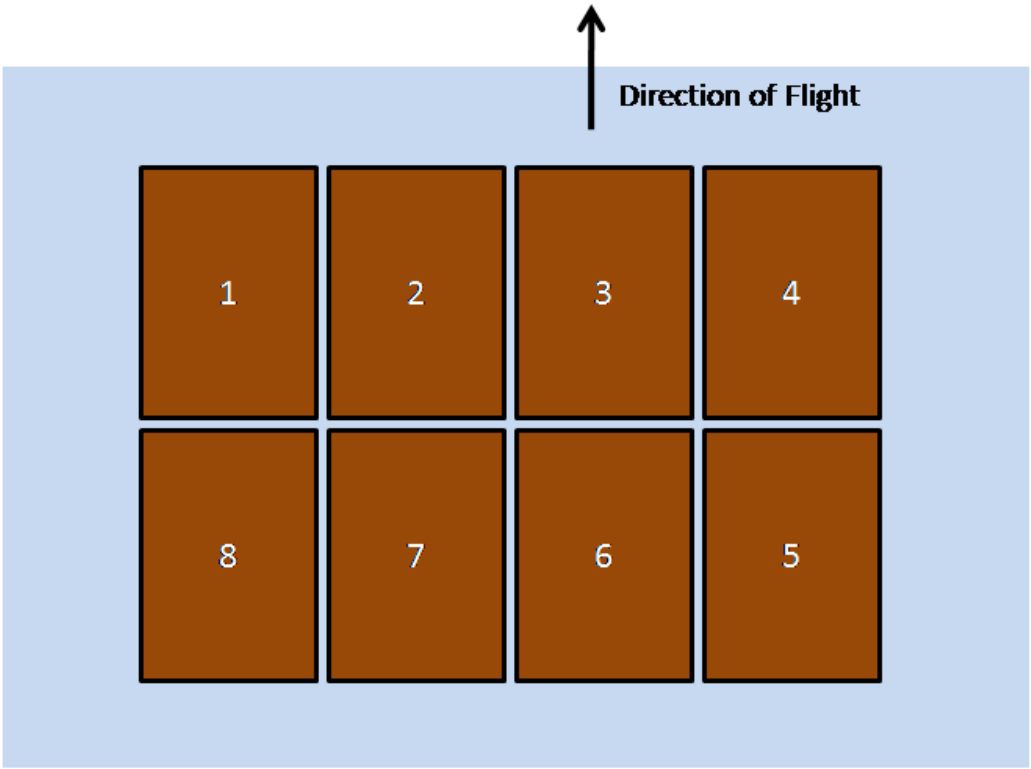

Figure 114. Elliptical dipole array layout looking from the top. Element number matches with trace in Figure 115.

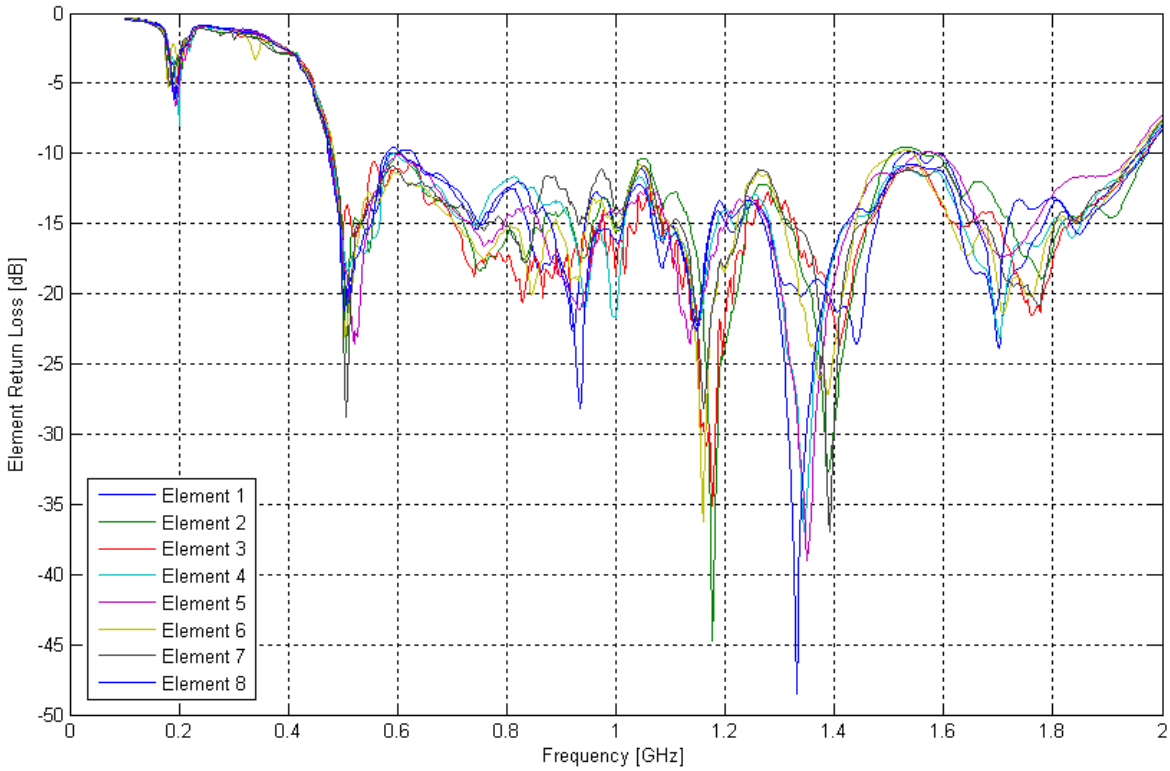

Figure 115. Measured return loss for individual elliptical dipole elements.

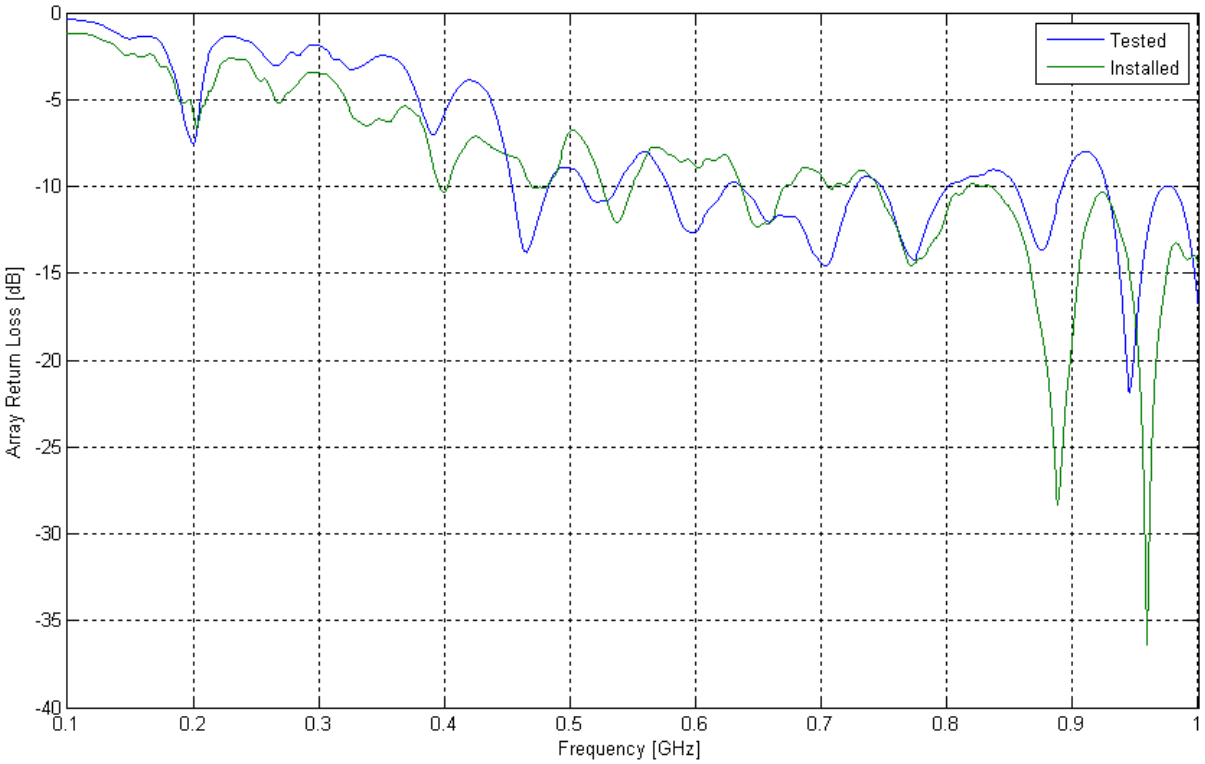

Figure 116. Measured elliptical dipole array return loss (at splitter).

Changes to the elements and optimization of the array configuration, including the use of a splitter with lower insertion loss and lower port-to-port phase imbalance, will improve the response for future missions. Figure 116 also shows the array return loss measured after installation in the aircraft (green trace). The response improved at higher frequencies, but worsened slightly near 600 MHz. Over all the response below -8 dB and is considered acceptable.